



Universität
Bremen

Near Surface Seismic Inversion: Quantitative Interpretation of the Physical Properties of Unconsolidated Sediments

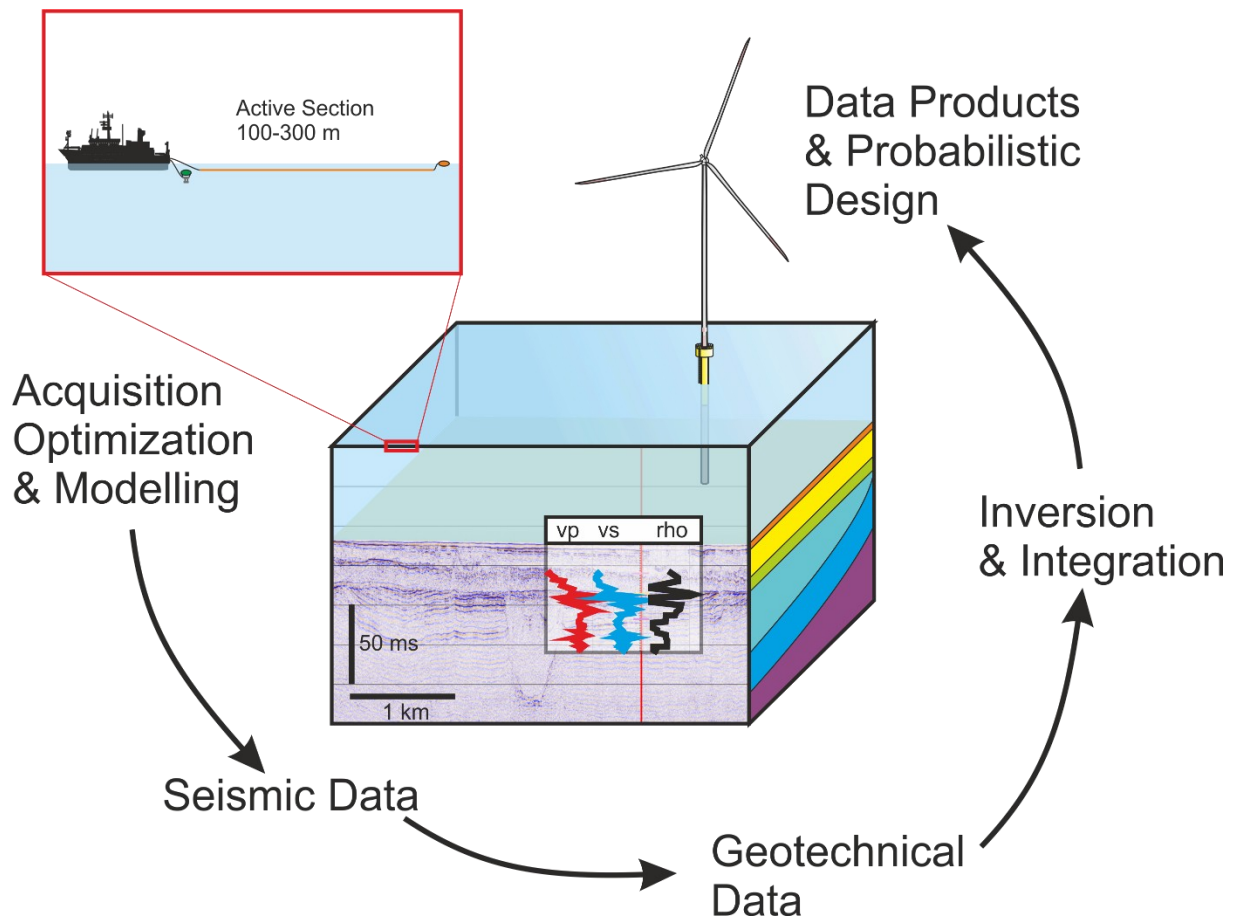
Dissertation

zur Erlangung des Doktorgrades
der Naturwissenschaften
(Dr. rer. nat.)

am Fachbereich Geowissenschaften
der Universität Bremen

vorgelegt von
Nikolas Römer-Stange

Bremen, Deutschland
Dezember 2024



Diese Promotionsarbeit wurde in der Zeit von April 2020 bis Oktober 2023 in der Arbeitsgruppe MeeresTechnik / Umweltforschung am Fachbereich 05 Geowissenschaften der Universität Bremen angefertigt.

This doctoral thesis was conducted from April 2020 to October 2023 in the working group Marine Technology / Environmental Research at the Faculty 05 Geosciences of the University of Bremen.

Reviewers

Prof. Dr. Volkhard Spieß

University of Bremen, Germany

Prof. Dr. Serge A. Shapiro

Freie Universität Berlin, Germany

Colloquium

18 January 2024

Zusammenfassung

Das reflexionsseismische Verfahren mit künstlichen Signalquellen bietet einmalige Möglichkeiten Strukturen unterhalb der Erdoberfläche abzubilden. Seismische Bilder können unter Zuhilfenahme von Inversionstechniken sogar noch um quantitative Abschätzungen ergänzt werden, was die Interpretation seismischer Daten eindeutiger macht. Auch können so weitere, für die angewandte und technische Forschung wichtige Parameter abgeschätzt werden. Bisher lag der Hauptfokus eher auf tief liegenden Erkundungszielen in Festgesteinskörpern, die mit niederfrequenten seismischen Signalen erkundet werden. Die zu diesem Zweck etablierten technischen Anwendungsarten und Methoden können allerdings nicht ohne Weiteres auf unverfestigte Sedimente und hochauflösende seismische Studien übertragen werden. Die wenigen Fallstudien in diesem Bereich der hochauflösenden Seismik haben die generelle Machbarkeit der Erkundung unverfestigter Sedimente nahe des Meeresbodens bewiesen und so auch das Industrieinteresse geweckt, z. B. für die Vorerkundung von Offshore-Windparks. Die bisher genutzten Methoden erfordern jedoch zumeist Feldvergleichsdaten oder basieren nicht nur auf dem reflektierten Wellenfeld oder aber andere methodische Einschränkungen verhindern eine breitere Anwendung.

Zur Inversion mariner oberflächennaher seismischer Daten konzentrierte sich diese Studie auf die Optimierung der Datenerfassung und die Entwicklung von Inversionsmethoden, die ausschließlich auf Reflexionen von P-Wellen basieren und durch an unkonsolidierte Sedimente angepasste empirische Beziehungen unterstützt werden. Für die Optimierung der Datenerfassung werden die verschiedenen Typen von unverfestigten Sedimenten charakterisiert und detaillierte Analysen zweier typischer Weise genutzten seismischen Quellen durchgeführt. Auf dieser Grundlage werden numerische Modelle und Inversionsansätze entwickelt, um Konfigurationen zur Datenerfassung zu testen und das Potenzial der verschiedenen Inversionsansätze u. a. für die Schätzung von Schereigenschaften zu untersuchen. Anhand dieser Modelle wird ein Anforderungskatalog für die Datenerfassung entwickelt und es werden mögliche Anwendungseinschränkungen aufgezeigt. Als Nachweis der Machbarkeit von Impedanzinversionen wurden seismische Daten aus der Nord- und Ostsee in Offshore-Windparkgebieten invertiert. Zu diesem Zweck wurden Algorithmen verbessert und implementiert für die Abschätzung und Korrektur der inelastischen Dämpfung, die Erzeugung niederfrequenter Trends durch Intervallgeschwindigkeitsschätzung und Konvertierung zu Dichte, die Inversion bandbegrenzter Impedanzprofile, die Zusammenführung niederfrequenter Trends mit bandbegrenzter Impedanz sowie die Tiefenkonvertierung. Die sich daraus ergebenden Impedanzprofile stellen eine erhebliche Verbesserung für die quantitative Interpretation geologisch komplexer Gebiete dar, indem sie Interpretationsfehler reduzieren und

lithologische Variationen innerhalb einer Einheit sowie Eigenschaftsgrenzen erfassen, die auf seismischen Amplitudenbildern nicht erkennbar sind. Es wird gezeigt, dass die Impedanz gut mit Cone Penetration Test-Messungen korreliert und dass der Soil Behaviour Type auf der Grundlage der Impedanz klassifiziert werden kann. Somit verbessern diese seismischen Inversionsergebnisse die Extraktion wichtiger Sedimenteigenschaften, z. B. für technische Zwecke. Für die Schätzung der Schereigenschaften wird ein Pre-Stack-Inversionsalgorithmus mit einem Gradientenverfahren zur Optimierung und einem Faltungsvorwärtsmodell auf der Grundlage von Zoeppritz P-Wellen Reflexionskoeffizienten entwickelt und getestet. Das Ausgangsmodell für die Pre-Stack Inversion basiert auf Impedanzinversionsergebnissen und angepassten empirischen Beziehungen. In der Machbarkeitsstudie, die mit Daten aus der Nordsee durchgeführt wurde, konnten mit diesem Inversionsansatz S-Wellen Geschwindigkeiten, im Vergleich zu den verfügbaren Cone Penetration Test-Daten, erfolgreich vorhergesagt werden, obwohl die Empfindlichkeit für niedrige S-Wellen Geschwindigkeiten begrenzt ist. Eine Sensitivitätsanalyse mit synthetischen Testdaten zeigt, dass dieser Mangel an Sensitivität eine allgemeine Einschränkung der Inversion von P-Wellen Reflexionsdaten ist.

Kurz zusammengefasst wird in dieser Arbeit aufgezeigt, wie marine oberflächennahe reflexionsseismische Daten erfasst und invertiert werden müssen, um quantitative Informationen abzuleiten, die über qualitative Standardinterpretationsergebnisse hinausgehen und diese ergänzen.

Abstract

Active reflection seismic data offer unprecedented possibilities to image structures in the Earth's interior. Employing inversion techniques, those images can be complemented by quantitative information making seismic interpretation less ambiguous and enabling the deduction of subsurface properties of relevance for applied research or engineering purposes. Mostly deep targets in lithified sediments or rocks have been targeted with seismic inversion studies and employed low resolution seismic sources. Constraints and methods established for this purpose are not applicable to the marine near surface, which is mainly comprised of unconsolidated sediments, and for which high resolution seismic signals are required. The comparatively few high resolution studies focussing on the marine near surface proofed the general feasibility of marine near surface seismic inversion, which sparked industry interest, e.g., for offshore wind farm investigations. However, the methods often require additional ground truthing data, or are not only based on the reflected wavefield, or methodological limitations impede a general application.

To invert marine near surface seismic data, this study focused on the optimization of data acquisition, and the development of inversion methods based exclusively on P-Wave reflection seismic data aided by empirical relations fitted to unconsolidated sediments. For the data acquisition optimization, the different types of unconsolidated sediments are characterized and detailed analyses of two types of near surface seismic sources are conducted. On this basis, numerical models and inversion trials are developed to test acquisition set-ups and to investigate the potential of the different inversion approaches for, among others, shear property estimation. These tests are then used to develop a catalogue of requirements for data acquisition and possible limitations are indicated. As a proof of concept for impedance inversion, seismic data from the North Sea and the Baltic Sea in offshore wind park areas have been inverted. For this purpose, algorithms have been improved and implemented for attenuation estimation and correction, low frequency trend generation by interval velocity estimation and conversion to density, band limited impedance inversion, merging of low frequency trends with band limited impedance as well as depth conversion. The resulting impedance profiles resemble a significant improvement for quantitative interpretation of geologically complex areas reducing interpretation biases and capture intra-unit lithologic variations and property boundaries which are not evident on seismic amplitude images. It is demonstrated that the impedance correlates well to Cone Penetration Test measurements and that the Soil Behaviour Type can be classified based on the impedance. Thus, these seismic inversion results improve the extraction of important sediment properties, e.g., for

engineering purposes. For the estimation of shear properties, a pre-stack inversion algorithm with a steepest descent optimization scheme and a convolutional forward model based on unconstrained Zoeppritz P-Wave reflection coefficients is developed and tested. The initial model for the pre-stack inversion is based on impedance inversion results and fitted empiric relations. In the feasibility study conducted with data from the North Sea, the inversion scheme successfully predicted S-Wave velocities compared to available Cone Penetration Test ground truthing data, although the sensitivity for low S-Wave velocities is limited. A sensitivity analysis with synthetic test data indicates that this lack of sensitivity is a general limitation of P-Wave reflection data inversion.

In summary, in this thesis it is disclosed how marine near surface P-Wave reflection seismic data have to be acquired and inverted to deduce quantitative information reaching beyond and complementing qualitative standard interpretation results.

Content

Zusammenfassung	VII
Abstract	IX
Content	XI
Thesis Outline and Author Contributions	XIII
Chapter 1 Introduction.....	1
1.1 Marine Near Surface Seismics	1
1.2 Quantitative Interpretation	14
1.3 Motivation and Objectives.....	25
Chapter 2 Material and Methods	30
2.1 Seismic Data	30
2.2 Seismic Inversion.....	39
Chapter 3 Data Acquisition Requirements and Limitations for Near Surface Reflection Seismic Inversion.....	51
Keywords	51
Abstract	52
3.1 Introduction	53
3.2 Material and Methods	57
3.3 Results	61
3.4 Discussion.....	70
3.5 Conclusion	84
Chapter 4 From Interface to Unit Characterisation: Stochastic Near Surface Seismic Impedance Inversion in the German North Sea	86
Keywords	86
Abstract	87
4.1 Introduction	88
4.2 Geological Setting.....	92
4.3 Material and Methods	93
4.4 Results	104
4.5 Discussion.....	118
4.6 Conclusion	126
Chapter 5 Pre-Stack Inversion on Near Surface Reflection Seismic Data	128
Keywords	128
Abstract	129
5.1 Introduction	130

5.2	Material and Methods	131
5.3	Results	138
5.4	Discussion.....	144
5.5	Conclusion.....	146
Chapter 6 Post-Stack Acoustic Impedance as a Reliable Indicator of Variation in Lithologic and Geo-technical Properties in Southern Arkona Basin – Assessment of Two Near-Surface Impedance Inversion Approaches Using Stationary Wavelets..... 148		
	Keywords.....	148
	Abstract.....	149
6.1	Introduction	150
6.2	Geological Setting.....	151
6.3	Material and Methods	152
6.4	Results	156
6.5	Discussion.....	163
6.6	Conclusion.....	169
6.7	Acknowledgements of Opeyemi Ogunleye	170
Chapter 7 Synthesis..... 171		
7.1	Summary of the Conclusions	171
7.2	Outlook	174
Acknowledgements..... 177		
References		
180		
List of Figures		
208		
List of Tables		
222		
Appendix		
224		
	A Abbreviations and Nomenclature	224
	B Additional Manuscript: Is it too loud? Approximations for Underwater Noise Impact Assessments and Reporting for Near Surface Seismic Campaigns.....	227
	C Supplementary Material to the Manuscripts.....	241
	D Certificate of Participation in a Good Scientific Practice Course.....	263
	E Publication List.....	264
Versicherung an Eides Statt / Affirmation in Lieu of an Oath		
267		

Thesis Outline and Author Contributions

This cumulative doctoral thesis includes seven chapters and begins with a general introduction to near surface seismic inversion, to the main study site in the German North Sea and the scientific objectives in Chapter 1. In Chapter 2 the material and methods used are described. Those introductory chapters are also aimed to be general enough to provide context to the scientific publications for the project partners in the interdisciplinary, overarching project SynCore.

The scientific objectives are addressed with four manuscripts (Chapter 3 to 6) that are recommended for publication with major revisions (Chapter 3), submitted (Chapter 4) and in preparation (Chapter 5 and Chapter 6) to international and peer reviewed journals. The manuscripts are arranged in chronological order of preparation. The connection between the manuscripts will be discussed in Chapter 7. References are found at the end of the thesis, while supplementary data and an additional manuscript about the underwater noise impact by near surface seismic surveys are provided in the Appendix

Except for Chapter 6, Nikolas Römer-Stange is the principal author to all manuscripts and all figures. Writing the original drafts, only the methodological section about Cone Penetration Tests were contributed by Natasha Morales. As a cruise participant, he was significantly involved in the data acquisition, curated the data for the research purposes and performed the formal analysis. The data processing scheme and inversion approach are developed by the author with support of some co-authors. Commercial software has been used for standard seismic data processing, while the inversion algorithms have been developed and programmed by the author. The developed software has been documented and prepared for release to ensure reproducibility. The author contributions according to the CRediT scheme (<https://credit.niso.org/>) are outlined in tabular form below.

Chapter 3: Data Acquisition Requirements and Limitations for Near Surface Reflection Seismic Inversion

Author Name	Statement of Contribution
Nikolas Römer-Stange	Conceptualisation, Data Curation, Formal Analysis, Investigation, Methodology, Software, Validation, Visualization, Writing Original Draft
Hanno Keil	Conceptualisation, Data Curation, Funding Acquisition, Investigation, Project Administration, Resources, Supervision, Review & Editing
Stefan Wenaus	Validation, Review & Editing
Maximilan Merl	Investigation, Resources, Review & Editing

Aisgo Oguro	Methodology, Validation
Carlos Ramos Córdova	Methodology, Validation
Volkhard Spieß	Conceptualisation, Funding Acquisition, Project Administration, Supervision

Chapter 4: From Interface to Unit Characterisation: Stochastic Near Surface Seismic Impedance Inversion in the German North Sea

Author Name	Statement of Contribution
Nikolas Römer-Stange	Conceptualisation, Data Curation, Formal Analysis, Investigation, Methodology, Software, Validation, Visualization, Writing Original Draft
Natasha Morales	Data Curation, Formal Analysis, Writing Original Draft (Section on Cone Penetration)
Hanno Keil	Conceptualisation, Data Curation, Funding Acquisition, Project Administration, Resources, Supervision, Review & Editing
Normal Ettrich	Conceptualisation, Methodology, Project Administration, Validation, Review & Editing
Sigrid Wilhelm	Validation, Review & Editing
Stefan Wenaus	Validation, Review & Editing
Aisgo Oguro	Methodology, Validation
Maximilian Merl	Investigation, Resources, Validation
Carlos Ramos Córdova	Methodology, Validation
Lennart Siemann	Validation, Review & Editing
Taisiya Pein	Formal Analysis
Patrick Arnold	Conceptualisation, Project Administration
Volkhard Spieß	Conceptualisation, Funding Acquisition, Project Administration, Supervision

Chapter 5: Pre-Stack Inversion on Near Surface Reflection Seismic Data

Author Name	Statement of Contribution
Nikolas Römer-Stange	Conceptualisation, Data Curation, Formal Analysis, Investigation, Methodology, Software, Validation, Visualization, Writing Original Draft
Natasha Morales	Data Curation, Formal Analysis, Writing Original Draft (Section on Cone Penetration)
Norman Ettrich	Conceptualisation, Methodology, Project Administration, Validation, Review & Editing
Hanno Keil	Data Curation, Funding Acquisition, Investigation, Project Administration, Resources, Supervision
Volkhard Spieß	Conceptualisation, Funding Acquisition, Project Administration, Supervision

Chapter 6: Post-Stack Acoustic Impedance as a Reliable Indicator of Variation in Lithologic and Geo-technical Properties in Southern Arkona Basin — Assessment of Two Near-Surface Impedance Inversion Approaches Using Stationary Wavelets

Author Name	Statement of Contribution
Opeyemi Ogunleye	Conceptualization, Data Curation, Methodology, Software, Validation, Formal Analysis, Investigation, Resources, Writing Original Draft, Writing Review and Writing, Visualization, Funding Acquisition Research Placement at Norwegian Geotechnical Institute in Oslo
Nikolas Römer-Stange	Data Curation, Formal Analysis, Methodology, Software, Validation, Writing Original Draft (Methodology)
Guillaume Sauvin	Data Curation, Formal Analysis, Methodology, Software, Validation, Formal Analysis, Writing Original Draft
Maarten Vanneste	Data Curation, Resources, Writing Original Draft, Project Administration
Volkhard Spieß	Conceptualisation, Investigation Methodology, Resources, Writing Review and Editing, Funding Acquisition, Project Administration, Supervision

Chapter 1 Introduction

1.1 Marine Near Surface Seismics

Conducting research in general and geoscientific research in particular, important societal duties are performed, which are essential for prosperity and sustainable progress (DFG, 2023). On the one hand, there is basic research satisfying the curiosity about the processes that formed and still shape the Earth and possibly leading to new discoveries. On the other hand, applied geoscientific research has been necessary, e.g., to ensure access to resources (Dragoset, 2005; Sirgue et al., 2010; Petterson et al., 2021), assess and mitigate hazards (Vardy et al., 2012; Clare et al., 2017; Provenzano et al., 2018; Kaminski et al., 2020; Smith & Bricker, 2021), plan infrastructure installations (Whiteley, 2005; Lesny et al., 2014; Fischer et al., 2019; Masoli et al., 2020), and conserve the environment (Pereira et al., 2021; IPCC, 2022; Stewart et al., 2023). These targets of geoscientific research are reflected in the deeds from the foundation stone of the Geoscience Faculty of the University of Bremen formulated by Prof. Kertz on 07. November 1986:

„To perceive our Earth both in detail and holistically, to benefit humanity, and protect nature shall be the aim of all members of the Faculty of Geosciences.” (free translation of the German original)

In this context, the study of the marine near surface and the active reflection seismic method are of special importance, which is explored in the following. Furthermore, it is investigated how near surface seismic inversion can improve subsurface studies.

1.1.1 The Marine Near Surface

The uppermost 50-100 m down to a maximum of 300 m of the seafloor are commonly described as the marine near surface, which is the highly dynamic part of the Earth's crust with most direct interactions (Butler, 2005). In terms of chemical processes, the upper sediment layers often show greater changes than the overlying water column and are an important driver of the Earth's biogeochemistry (Boudreau, 2000 and references therein). As shown in Figure 1-1, the near surface is highly diverse in both morphology and sediment cover. Today, less than 20% of the surface of the ocean floor has been sampled for depth (Mayer et al., 2018; see www.gebco.net or seabed2030.org for updated numbers).

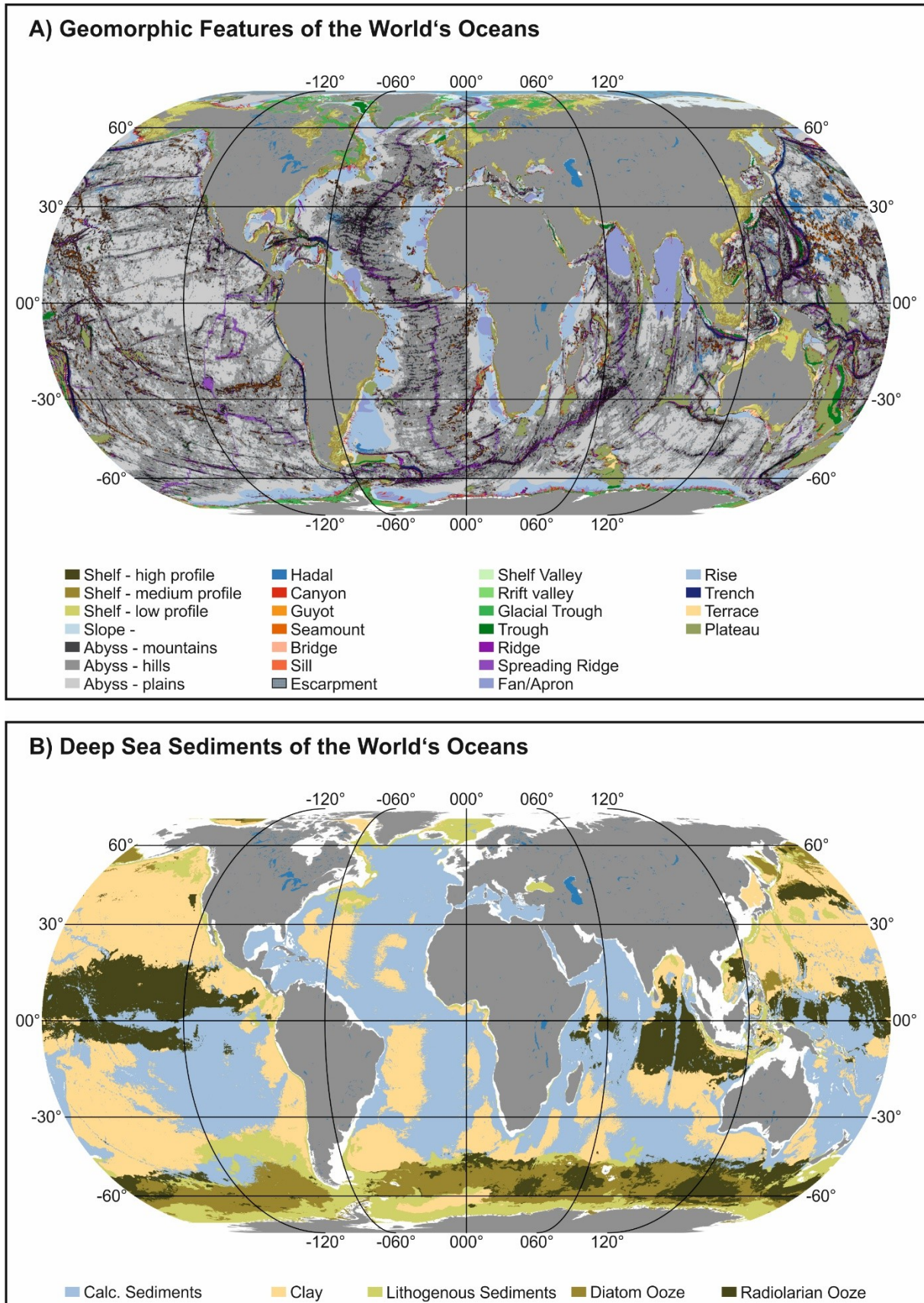


Figure 1-1: Overview of the marine near surface (equal area Eckert IV projection; ESRI 54012). A) Geomorphic features of the world's ocean redrawn and modified from Harris et al. (2014). B) Deep sea sediments of the world's oceans redrawn and modified from Diesing (2020).

But from the basic research perspective, this realm is critical to study, e.g., present day processes to understand the geologic record, the younger geologic history as exemplified in the following section for the North Sea (“1.1.2 The Near Surface of the North Sea”), or aspects of the carbon cycle, as marine surface sediments are a major sink for carbon. So, the largest stocks of buried carbon in the world are below the ocean floor (Atwood et al., 2020). About 80% of the buried carbon are deposited on the shelves (Bauer et al., 2013), whose extent is shown in Figure 1-1A. Marine sediments are also the greatest sink of undissolved, anthropogenic carbon (Friedlingstein et al., 2022) and thus play a vital role for the assessment and mitigation strategies of climate change (IPCC, 2022). Contrastingly, marine sediments are also a source of carbon via biogeochemical processes (IPCC, 2021). The geologic setting such as abyssal plains, continental margins, shelves or seamounts, and processes like hydrothermal or cold venting manifested in the near surface also greatly influence in general the interactions of the biosphere with the geosphere and the biodiversity (Borland et al., 2021; Paulus, 2021). Studies of the near surface are also critical for the understanding of submarine and potentially disastrous landslides (Masson et al., 1998, 2006, 2010; Canals et al., 2004).

Typically, the marine near surface has not been considered to host major resources. Oil or gas reservoirs are found in the deeper subsurface. Therefore, near surface surveys in the Oil+Gas Industry are typically conducted to identify possible sources of operational hazards such as man-made features, archaeological remains, gas hydrates, water flow, gas charges, faults, etc. (Guigné & Blondel, 2017; OGP, 2017; Lebedeva-Ivanova et al., 2018). Also in the deeper subsurface below about 800-1000 m depth, depleted oil and gas reservoirs, coal or saline formations are in discussion for underground geological storage of carbon dioxide for the purpose of greenhouse-gas emission reduction (IPCC, 2005). In this context, near surface exploration is important to assess and monitor possible leakage pathways from wells, geologic faults or seals (Cevatoglu et al., 2015; Römer et al., 2021), whose integrity can be risked by induced seismicity (Zoback & Gorelick, 2012). In recent years, some resources embedded in the near surface gained more interest. Mineral resources in the near surface include polymetallic massive sulphides, ferromanganese crusts and polymetallic nodules (Miller et al., 2018), as well as aggregates including sand, gravel and crushed stone (M. Bendixen et al., 2021). Due to the use of sand and gravel mainly in the construction industry but also, e.g., for glass or semiconductor production, aggregates have become heavily exploited (Bonne, 2010; M. Bendixen et al., 2021) and a possible starting points of conflicts (Kräutner et al., 2022). Deposits of polymetallic nodules found on or just below the seafloor of abyssal plains (ISA, 2010; Hein et al., 2020) may be exploited in the near future to satisfy the demand for critical metals for the green energy transition, e.g., in the Clarion-Clipperton Fracture Zone in the Pacific (Heffernan,

2023). Similarly, polymetallic massive sulphides at inactive hydrothermal sites are a exploration target (Van Dover, 2019). Due to environmental concerns (Miller et al., 2018), Germany has halted further sponsoring of deep-sea mining (BMWK, 2022).

Table 1-1: Examples of offshore structures updated from Richards et al. (1975) including information taken from Lesny et al. (2014), Nikitas et al. (2020), Owen (2020) and Amaechi et al. (2022). Items marked in red are elements of offshore wind energy generation systems.

<p>Energy Production</p> <ul style="list-style-type: none"> • Offshore Wind Energy Plants • Tidal/ Marine Current Power Plants • Wave Power Plants • Floating Photovoltaic Power Plants • Oil+Gas Wells <p>Anchoring and Mooring Systems</p> <ul style="list-style-type: none"> • Buoys • Cables • Floating Structures • Large Ship Moorings • Pipelines <p>Bottom Installations</p> <ul style="list-style-type: none"> • Habitats • Algalculture Structures • Mariculture Structures • Scientific Instrumentation <p>Cables</p> <ul style="list-style-type: none"> • Communication • Power Transmission Cables <p>Coastal Structures</p> <ul style="list-style-type: none"> • Breakwaters • Causeways • Channels • Jetties and Groins • Navigational Aids • Land Reclamations • Cargo Terminals <p>Dredging</p> <ul style="list-style-type: none"> • Barrow Uses • Channel Maintenance 	<p>Transportation</p> <ul style="list-style-type: none"> • Anchored Buoyant Tunnels • Bridges • Cut-and-Cover Tunnels <p>Islands</p> <ul style="list-style-type: none"> • Airports • Deep-Water Terminals • Nuclear-Power Plants • Renewable Energy Islands <p>Mining</p> <ul style="list-style-type: none"> • Aggregate Uses • Polymetallic Resources • Freshwater Aquifers • Marine Placers <p>Pipelines</p> <ul style="list-style-type: none"> • Effluent outfall lines • Freshwater Aqueducts • Oil+Gas Distribution • Pumping Installations <p>Platforms</p> <ul style="list-style-type: none"> • Drilling and Production Rigs • Storage Systems • Tanker Terminals • Sea Forts • Rocket Launch Platforms • Recreational Platforms/Yachts • Measurement Masts • Converter Platforms (Substation) • Maintenance and Accommodation Platforms • Hydrolysis/Energy Conversion Platforms
--	--

Especially in connection with the renewable energy transition, the near surface has also been put into focus due to the importance for offshore structure installations. In Table 1-1 examples of offshore structures are collected. As already mentioned above, surveys to explore the near surface are conducted for hazard avoidance in the Oil+Gas Industry. Similarly, near surface surveys are performed to plan infrastructure installations such as cargo terminals (Masoli et al., 2020) or the single elements of offshore wind energy systems (Lesny et al., 2014; Terente et al., 2016; Forsberg et al., 2022). Disasters like the 1979 Nice airport landslide, which was probably initiated by an increased load after landfill operations, heavy rainfall, and creep along a sensitive layer (Dan et al.,

2007), stress the importance of such surveys prior to the installation of offshore structures. Yet another example is the 1996 Finneidfjord landslide, which may have been caused by a combination of heavy rain and ground tremors including detonations (Longva et al., 2003).

The seafloor is a highly variable environment and largely covered by sediments of different types, as shown in Figure 1-1. After the deposition, those sediments are subjected to diagenetic processes and eventually lithification depending on the available chemical reactants, the pressure and temperature regime, biological transformation, or geophysical processes (Boudreau, 2000; Hesse & Schacht, 2011; Paraska et al., 2014). Mostly and especially in the case of lithogenous sediments, the sediments in the marine near surface are not or only weakly cemented and are thus unconsolidated (Selley, 2000).

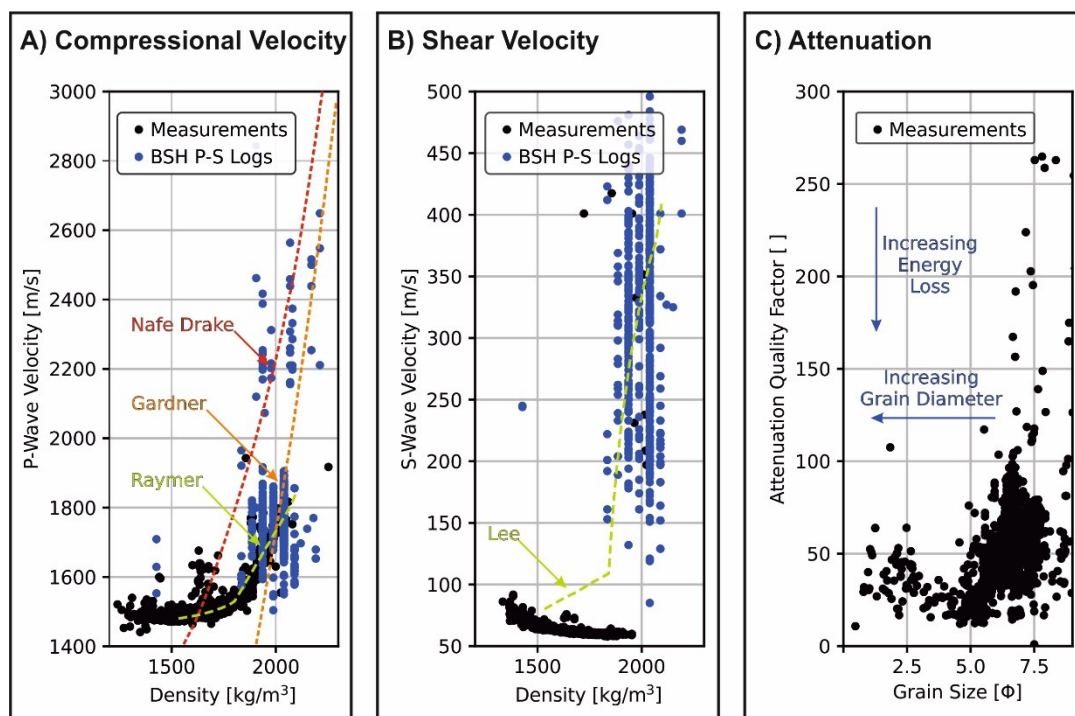


Figure 1-2: Viscoelastic properties of unconsolidated near surface sediments and empirical relations relating the properties reproducing Breitzke et al. (2000) and Pinson et al. (2008). The measurements shown are taken from McCann & McCann (1969), Shumway (1960), Hamilton (1970, 1972), Breitzke et al. (2000), Stevenson et al. (2002), Robb et al. (2006), while the P-S Logging data shown is taken from the BSH Pinta Data Base (2021) for the wind parks N0307, N0308 and O0103. A) Cross-plot of the wet-bulk density and the compressional or P-Wave velocity with an overlay of the empiric density to P-Wave velocity relationship by Raymer et al. (1980), Gardner (1974), and (Ludwig et al., 1970). Below velocities of about 1600 m/s, the variation in density is significantly larger than the velocity variation. B) Cross-plot of the wet-bulk density and the Shear or S-Wave velocity with an overlay of the empiric S-wave velocity estimation by Lee (2006) applied on the fit of the measurements to the Raymer et al. (1980) equation. A clear discrepancy of the P-S Logging data and the measurements as well as the empiric estimation is observed. It is to be noted that only the Breitzke et al. (2000) measurements are shown, as the other measurements lack S-Wave velocity information. C) Cross plot of the grain size and the attenuation quality factor. The grain size is expressed in the Φ -scale according to which the diameter is defined as $D = 1 \text{ mm} \cdot 2^{-\Phi}$ leading to $D(\Phi = 0) = 1 \text{ mm}$, $D(\Phi = 4) = 0.0625 \text{ mm}$, or $D(\Phi = 8) = 0.0039 \text{ mm}$. The quality factor Q is the ratio of the total energy of the seismic wave and the energy lost during one cycle of the wave due to intrinsic attenuation and scattering. Thus, the higher the quality factor, the lower the observed energy loss. So, it is shown in the plot, that attenuation is high for large grain sizes and lower attenuation is expected at small grain sizes.

The viscoelastic properties of those sediments are distinctively different to hard rocks as shown in Figure 1-2 with measurement data from samples, borehole logging and empirical relations interrelating the properties. The compressional, pressure or primary (P) wave speed v_p , the shear or secondary (S) wave speed v_s , wet bulk density ρ as well as the attenuation quality factor Q are shown to describe the viscoelastic properties due to the importance of those parameters for the seismic method (see “1.1.3 Utilization of Seismic Data to Study the Marine Near Surface”). Compressional waves are propagating dynamic disturbances of the elements inside a medium or so-called body waves taking place as oscillating displacements in the spreading direction of the wave and v_p quantifies how fast such a disturbance travels through a medium. For seismic applications, frequencies of this oscillating displacement in the range of 1-2000 Hz are of interest (ten Kroode et al., 2013; ISO 19901-10, 2021). The Gardner (Gardner et al., 1974) and Nafe-Drake (Ludwig et al., 1970) relation in Figure 1-2A are commonly used to relate ρ and v_p of rocks. Although there are discrepancies between the two empiric relationships, both curves show that v_p varies stronger compared to ρ . But the measurements, logging data and the fitted Raymer equation (Raymer et al., 1980) show for the unconsolidated sediments, that the variation of ρ is larger than the variation of v_p , especially for $v_p < 1600$ m/s. In case of S-Waves, the displacement of this type of body wave is perpendicular to the spreading direction. The spreading velocity of shear waves is v_s and it is striking, that the measurements show very low v_s for unconsolidated sediments, which are partially lower than predicted by empirical relations (Lee, 2006). The higher v_s resulting from the logs are to be expected due to the grain size differences. In the measurements, mostly fine-grained sediments were tested, while sandy soils were encountered in the logs. Consolidated sediments and rocks are typically characterized by higher v_s . All measurements shown indicate strong energy loss due to intrinsic attenuation and scattering with $Q < 50$. Thereby, Q is the ratio of the total energy of the wave and the energy lost during one cycle of the wave. Commonly, Q is considered to be frequency independent for seismic applications (Pinson et al., 2008; Morgan et al., 2012). But as high frequent signals cycle more often than low frequent signals during the same time interval, high frequencies are more attenuated. The strongest attenuation is observed at coarse sediments, while Q increases with decreasing grain size. As a comparison, values in the range, e.g., $70 < Q < 280$ are to be expected for granites (Y. Wang, 2008). These observations are in general accordance with the Biot-Stoll model as described in Hovem (1991), Badiey et al. (1998), Dvorkin et al. (Dvorkin et al., 1999), Breitzke (2006). In this model, the sediment is considered to be a fluid saturated frame and an elastic wave passing this system causes displacement of the frame and the fluid. Consequently, attenuation is caused by energy loss by Poiseuille’s flow of the fluid in the sediment frame depending on the viscosity and permeability.

As large, connected pore spaces are encountered in coarse sediments, more fluid flow can occur, and high attenuation is to be expected. According to this model, v_p depends on the bulk properties of the sediment and fluid, while ρ is mainly defined by the porosity, grain size and composition. As the elastic bulk moduli can be considered to be independent of grain size as an approximation (Breitzke, 2006), the grain size effect on ρ is larger than on v_p . Shear displacement is transferred via the sediment frame and thus independent of the fluid, which is essentially inviscid for frequencies in the seismic frequency range. In case very fine grained and unconsolidated sediments are encountered, which behave like a suspension of grains in water, the Biot-Stoll model might not be applicable.

1.1.2 The Near Surface of the North Sea

Due to its importance for the German offshore wind energy industry, a study area has been chosen in the German North Sea north of the island Heligoland in a glaciotectonically influenced area. As confidential CPT data is shown, the exact location of the profile and the CPTs cannot be disclosed. The geologic setting of the study area is described in the following.

Forming an epicontinental basin in the Cenozoic (Ziegler, 1990), the geological setting of the North Sea is defined by the interplay of the formation of accommodation space, the availability of sediment supply and subsequent tectonic deformation or erosion. The accommodation space of the North Sea Basin has been firstly created by subsidence induced thermally with the initialisation of a failed rift and by loading and isostasy in the Mesozoic and Early Cenozoic (Sclater & Christie, 1980; Barton & Wood, 1984). Anomalously high subsidence has been shown for the Quaternary after the rifting (Thorne & Watts, 1989; Kooi et al., 1991). According to Arfai et al. (2018), this high subsidence rate reaching a local maximum value of 480 m/Ma is predominantly due to compaction and load-induced subsidence, while post-glacial collapses, local crustal flow and dynamic topography potentially account for the remaining portion of the subsidence. With the onset of the Quaternary and the intensification of the Northern Hemisphere Glaciations (Batchelor et al., 2019; Ehlers, 2022), those long term trends are superimposed by eustatic sea-level changes resulting in reduced accommodation space in the interglacials (Overeem et al., 2001; Thöle et al., 2014). The glaciations are contextualised and numbered with the Marine Isotope Stages (MIS) derived from the oxygen isotope record of benthic foraminifera as a proxy for the global ice volume (Raymo & Ruddiman, 1992; Lisiecki & Raymo, 2007, 2007). Glacial periods are characterised by low fraction of the heavy oxygen isotope expressed as the difference relative to a standard $\delta^{18}\text{O} < 3 \text{ ‰}$ (Lisiecki & Raymo, 2005) as the heavy isotope is enriched in ice due to equilibrium fractionation (Raymo & Ruddiman, 1992).

In the Paleogene, sediments to the central North Sea were mainly supplied from the west by the British Shield, from the south by the Rhine-Meuse river system and from the northeast by the Fennoscandian Shield to a second depocenter in the north (Anell et al., 2012). In the Neogene, the sediments are supplied by the Eridanos fluvio-deltaic system and the Fennoscandian Shield linked to increased uplift of this shield, the described subsidence and a long-term eustatic sea-level highstand (Overeem et al., 2001; Anell et al., 2012; Thöle et al., 2014). The major transgression caused by the subsidence and the eustatic sealevel rise before the onset of the Eridanos Delta deposition resulted in an wide-spread interval of condensed sedimentation and clay deposition known as the MMU Mid-Miocene Unconformity (MMU; Huuse & Clausen, 2001; Rasmussen, 2004; Thöle et al., 2014).

With the onset of glacial-interglacial transitions in the Late Neogene, eustatic sea level changes increasingly affected the sedimentation with peak sedimentation rates during the glacials and changes in channel-network characteristics (Overeem et al., 2001; Thöle et al., 2014). Consequently, progradational cycles of the delta deposits are separated by erosional unconformities that may be caused by eustatic sea-level falls and by Maximum Flooding Surfaces that may be representing transgressions by eustatic sea-level rises (Thöle et al., 2014). Propagation of the delta continued to the west in the Dutch North Sea in the Early Quaternary moving north while infilling the North Sea Basin and forming up to 1.2 km thick Quaternary sediment successions (Kuhlmann et al., 2004; Ottesen et al., 2014; Lamb et al., 2018). In the German North Sea sector, in contrast, glacial deposits such as sanders and tills, fluvial deposits including peats, lacustrine deposits as well as brackish to marine sediments are found due to the glacial-interglacial transitions and the resulting eustatic sealevel changes in the Quaternary (Ottesen et al., 2014; Lamb et al., 2017, 2018; Coughlan et al., 2018). A thin cover of relatively mobile sands and lag deposits formed in the Holocene, while fine sediments are only found in the Heligoland mud area (Zeiler et al., 2000, 2008).

From a structural perspective, the processes of glaciotectonic deformation and glacial erosion including subglacial meltwater flow are major factors to understand the geological setting. In this context, prominent features are tunnel valleys, which are elongated and overdeepened depressions eroded into the bedrock or unconsolidated sediment (Cofaigh, 1996; van der Vegt et al., 2012). A commonly applicable model for tunnel valley generation is the quasi-steady-state model as described in Huuse & Lykke-Andersen (2000b), van der Vegt et al. (2012) and references therein. According to this model, tunnel valleys are mainly formed during still stand or retreat phases of the ice margin by small meltwater outbursts, which originate from stable meltwater pathways. The quasi-steady-state hypothesis is supported by the genetic link to eskers, the general lack of tills and the upwards-decreasing glacial influence in the infill. Tunnel valley formation by catastrophic

events requires special, local settings to build up large meltwater reservoirs. Additionally, glacial erosion is supposed to play an important role for the formation of broad and shallow valleys. For the southeastern North Sea, the most detailed and recent mapping of tunnel valleys has been performed by Lohrberg et al. (2020) updating the previous mapping of Lutz et al. (2009).

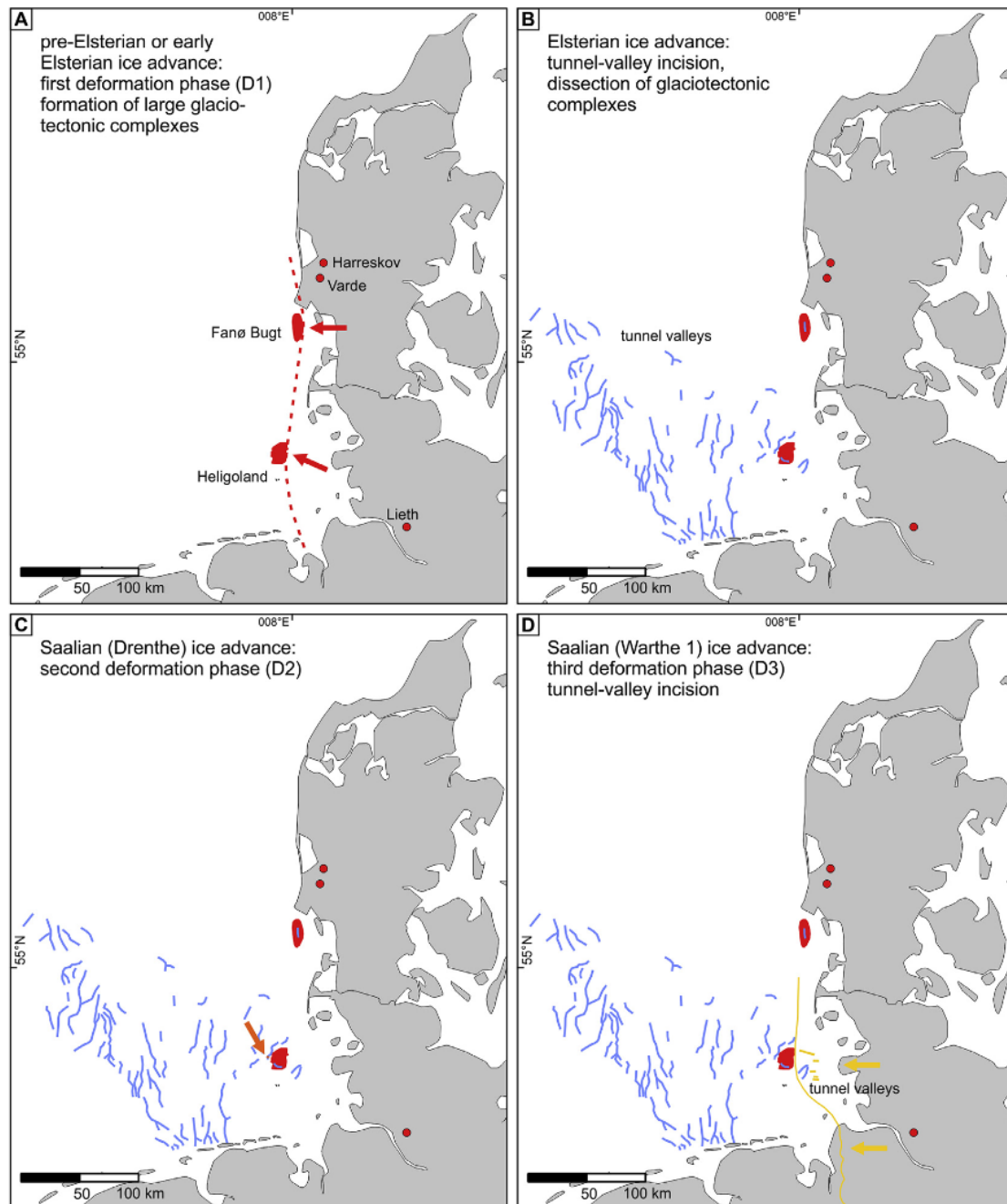


Figure 1-3: Paleogeographic maps taken from (Winsemann et al., 2020) depicting the glacial history of the study area and showing the tunnel valleys in the surrounding of the study area. A) First deformation phase in which a pre- or early Elsterian ice advance towards the West formed the Heligoland and possibly the Fanø Bugt glaciotectionic complex. B) During the Elsterian (MIS 12 or MIS 19) deep tunnel valleys have been incised at the margins of ice advances from the North. C) Second deformation phase during the Saalian Drenthe ice-advance (MIS 6) during which shallow, westward-dipping thrusts formed. D) Third deformation phase during the Saalian late Drenthe or Warthe 1 ice advance during which shallow east-west-trending tunnel valleys formed and during which the glaciotectionic complexes and previously incised tunnel are deformed.

Several generations of tunnel valleys, some of which are displayed in Figure 1-3, have been found and the authors propose a formation of the deep and U-shaped tunnel valleys during the Elsterian glaciation and a formation of the shallower and V-shaped tunnel valleys during the Saalian. The main mechanisms of deformation found in the glacially influenced sediments in the North Sea are gravity spreading causing folds and dislocation structures (Pedersen, 1987) and glacial pushing or bulldozing causing push moraines (Bennett, 2001). Both mechanisms are linked to the ice margin. The depth of the detachment surfaces have been linked to the depth of the paleo-permafrost, especially when structures predating the deformation are preserved, as freezing favours the conservation of those structures (Ehlers, 2022). A large number of glaciotectionic thrust complexes have been identified by Huuse & Lykke-Andersen (2000a) in the eastern Danish North Sea. Thrusts towards the southeast in mostly Neogene sediments above clay layers at the MMU and the base of the Quaternary making up a detachment surface are described by Winsemann (2020). Due to the orientation and as the thrusts are found below subglacial valleys, the deformation is most likely linked to Elsterian or possibly Saalian ice advances (MIS 6-12). Saalian ages are also assumed for the Fanø Bugt Complex shown in Figure 1-3A during a westward ice advance (Larsen & Andersen, 2005; Winsemann et al., 2020). Similarly, Bendixen et al. (2018) propose, that a pre-Elsterian grounded ice sheet most likely during MIS 16 caused thrust deformation at the ice margin in the Central North Sea. Closer to the area of interest of this study, the Heligoland glaciotectionic thrust-fault complex has been investigated by Winsemann et al. (2020) and Lohrberg et al. (2022). Here Neogene sediments above two detachment surfaces are deformed in three deformation phases as shown in Figure 1-3A, C, and D. Due to the presence of overlaying presumed Elsterian to Early Saalian tunnel valleys (MIS 10-12) the deformation most likely happened during pre-Elsterian (MIS 16) to Early Elsterian (MIS 12) ice advances.

1.1.3 Utilization of Seismic Data to Study the Marine Near Surface

A broad range of geophysical methods exists to explore the Earth. Yet, controlled source or active seismics have a special role and importance. Conducting an active seismic experiment – as described, e.g., in Mintrop (1930), Yilmaz (2001), or Dondurur (2018) – in the marine environment, a seismic source is typically towed by a vessel or rarely deployed on the seafloor as shown in Figure 1-4. This seismic source generates body waves into the surrounding medium (see description in “1.1.1 The Marine Near Surface”; Lowest panel in Figure 1-4B). Surface waves travel in the form of Rayleigh Waves (combined longitudinal and vertically polarized shear waves) along air/vacuum-solid interfaces, Scholte Waves (vertically polarized shear waves) along water-solid interfaces, Stoneley Waves (vertically polarized shear waves) along solid-solid interfaces, or Love Waves (horizontally polarized shear waves), which are only observed for low velocity layers above high

velocity layers. As the water is basically inviscid in the seismic frequency range, the oscillation in the water column only takes place in the form of spherically spreading P-Waves and surface waves are rarely observed. Sources at or below the seafloor could also directly introduce S-Waves.

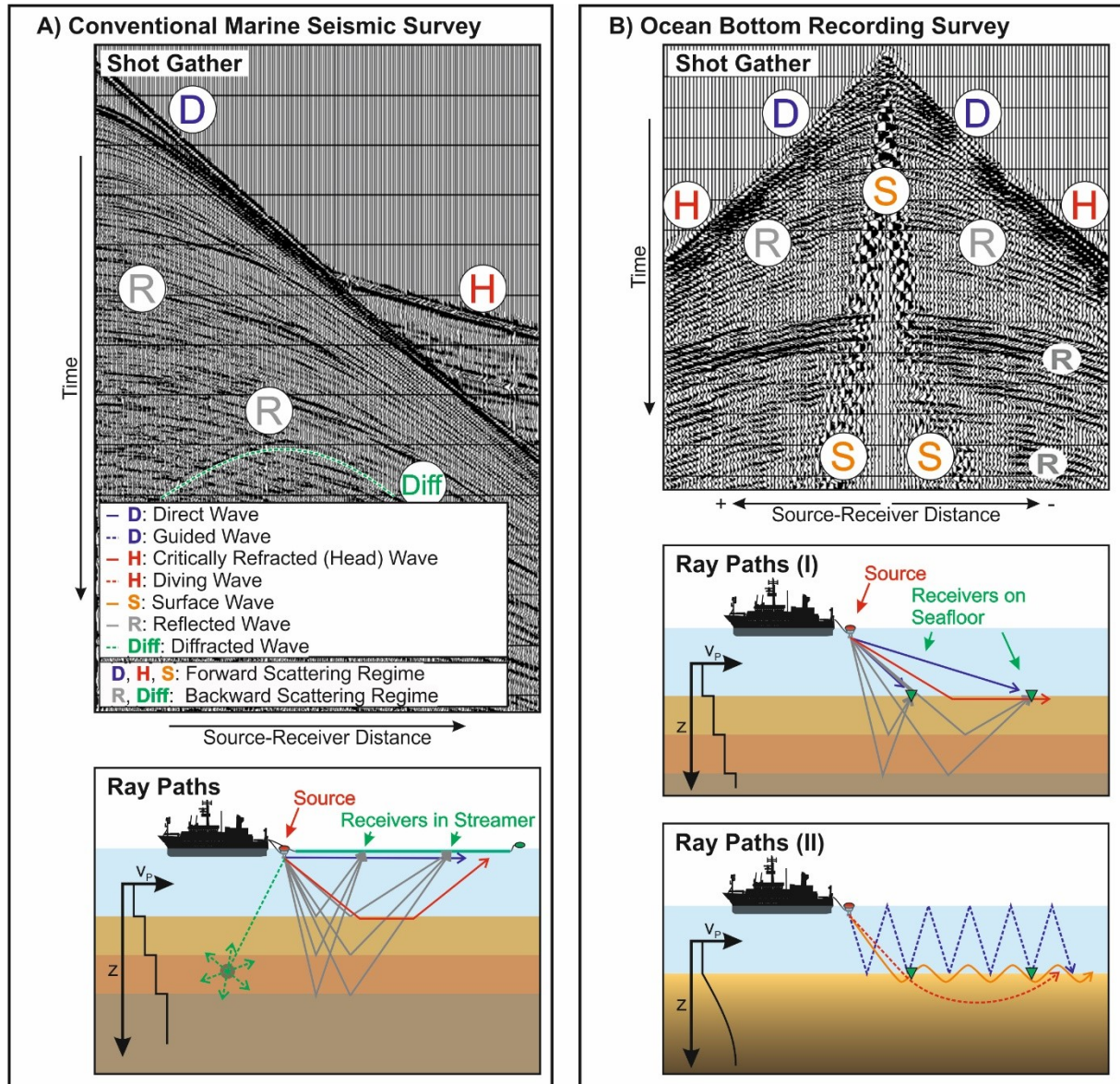


Figure 1-4: Shot gathers and corresponding ray paths with a P-Wave velocity v_p profile increasing stepwise or continuously with depth z A) a conventional marine seismic survey with a hydrophone streamer and a source towed behind a ship and B) an ocean bottom recording survey with receivers deployed on the seafloor and a source towed behind a ship modified after Klein et al. (2005), Dondurur (2018) and Clementi et al. (2022).

As a wave propagates through the water and then through the subseafloor, this wave is transmitted, reflected, refracted, and converted (from a P- to a S-Wave or vice versa) at interfaces of changing elastic properties as shown in Figure 1-5. At small scale heterogeneities, the wave is diffracted (see Figure 1-4A).

The resulting wavefield can be separated into two different regimes, as described by Virieux et al. (2014) and visualized in Figure 1-4. In the forward scattering regime, only small variations of the initial wavefront are caused by transmission, conversion and refraction allowing the wavefront to continue to propagate generally forward. In the backward scattering regime, reflection and diffraction causes a significant change of the propagation direction. Multiscattering occurs when wave is scattered forward or backward at least two times. Examples for multiscattering are multiples, which are events with more than one reflection on the wave path, or ghosts, which originate from sea-surface reflection of the up-going wavefield. Receivers measuring either pressure changes or displacement are also towed by the same or a different vessel or deployed on the seafloor to record the wavefield scattered forward and backward as a time series. For marine reflection seismic applications, the wavefield records are processed to resemble vertical incidence time series of P-Wave reflections, as described in “2.1.3 Seismic Data Processing”. Many of these vertical incidence time series are gathered in 2D or 3D sections and the resulting images are geologically interpreted (Simm & Bacon, 2014). Estimates of v_p can be used to convert the time series to depth to make the interpretations usable for other scientific disciplines or for engineering purposes (Vardy et al., 2017). Without the depth conversion, seismic sections are presented with a vertical time axis on which the transit time of the signal from the source to the receiver is noted as the Two-Way-Traveltime TWT .

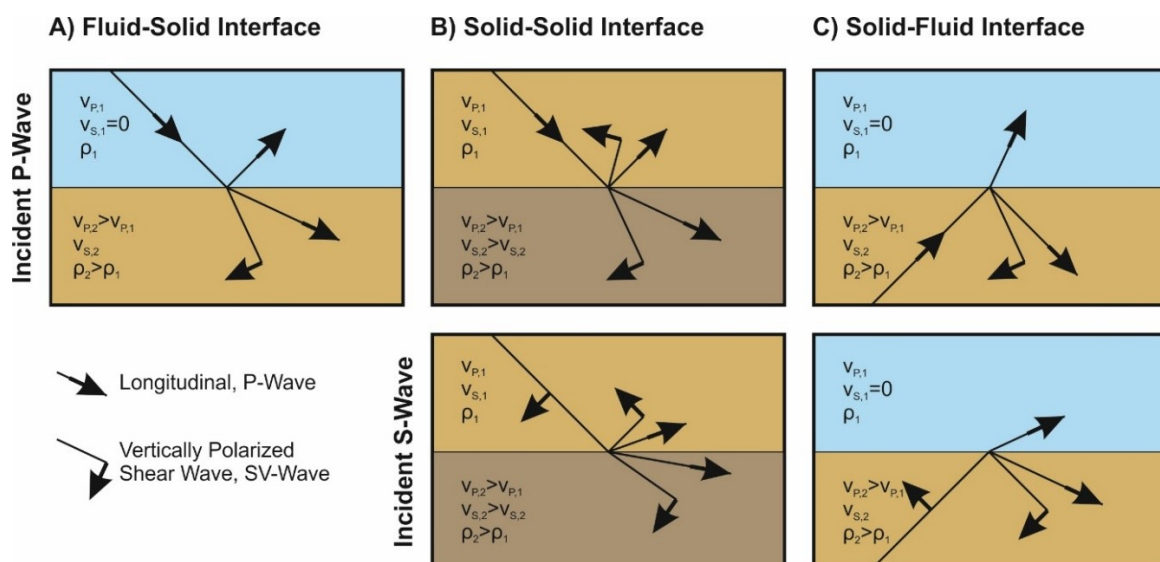


Figure 1-5: Notation of the possible reflection and transmission coefficients of incident P-Waves and S-Waves at interfaces between solid and fluid half-spaces modified after Aki & Richards (2002). As seawater is inviscid for seismic waves, only P-Wave phases occur in the fluid half-space.

The described reflection seismic method bears several advantages compared to other geophysical, geological, or geotechnical exploration methods. Most importantly, the seismic parameters ρ , v_p , and v_s , on which records of seismic data depend, are suitable parameters to characterize the subsurface (Douglas W. Oldenburg & Li, 2005) with a significant variation as shown in Figure 1-2. While the geophysical methods are non-destructive, the subsurface is disturbed, when samples are taken or when geotechnical Cone Penetration Tests (CPT) are performed. As described in Robertson (2009, 2016) and Robertson & Cabal (2015), CPT are a geotechnical standard method, for which metal cones in a size range of 10-15 cm² are pushed into the seafloor while continuously measuring the resistance of the cone, friction along the sleeve of the push rod, penetration pore pressure and occasionally v_s . The CPT measurements are interpreted by means of Soil Behaviour Type (SBT) charts to deduct the type of material encountered and by means of correlations to geotechnical parameters. With CPT, the large stress-strain parameters are directly tested in a very small area, while only small stresses and strains are introduced by seismics. If there are small scaled variations, boreholes and CPT might not yield representative results, while lateral variation can easily be covered by seismics (Henson & Sexton, 1991). Compared to geophysical potential field methods such as magnetics, gravimetry, or geoelectrics, reflection seismic images are generally more intuitively interpreted, as potential field methods are usually analysed by means of anomaly maps or modelling.

In academia, near surface seismic data sets are used, e.g., for studies of the Quaternary geology, site investigations for drilling, lithological studies, or fluid distribution and migration. For the installation of offshore wind energy capacity, a broad range of offshore structures is necessary as listed in Table 1-1. Near surface survey data is used by energy companies for engineering purposes to plan the foundations of these structures (Muskulus & Schafhirt, 2014; Kallehave et al., 2015; Arshad & O’Kelly, 2016; Terente et al., 2016) and for installation risk minimization (Römer-Stange et al., 2022). In Germany the planning procedure has been fixed in a standard (Lesny et al., 2014), which is the most restrictive standard of the European North Sea countries (Fischer et al., 2019). But at least the procedures in the Netherlands (Forsberg et al., 2022) and also industry best-practice recommendation generally resemble this standard (Terente et al., 2016). According to the German standard (Lesny et al., 2014), there is a differentiation between the development and construction phase. In the development phase, firstly a desk study is conducted collecting the available information and data. Then, geophysical data are collected with hydroacoustic, magnetic and seismic methods. During the hydroacoustic surveys covering the whole wind farm area, data are collected with multi-beam echo-sounders to generate maps of the water depth and side-scan sonar to map the surface sediments and surface structures. The major task for magnetic surveys is the

identification of Unexploded Ordnance (UXO) wrecks, cables, or other metallic objects. Seismic investigations are performed to identify the type, spatial extent, and depth below the seafloor of the geological units in the area. Further following the German standard, a preliminary geologic model is generated after the seismic data is interpreted to plan the geotechnical campaign in the development phase. In this campaign, the subsurface is explored either directly by drilling and sampling or indirectly by cone penetration testing or borehole geophysical methods at representative locations and at a minimum of 10% of possible foundation locations during this geotechnical campaign. The samples are further analysed in the laboratory to determine geotechnical parameters and a geotechnical report is written. As a last step of the development phase, the geophysical and geotechnical results are combined in a geological report. In the following construction phase, at least one geotechnical investigation has to be carried out at each plant location of an offshore wind energy plant. An integrated ground model report summarizes then all results for foundation planning.

In general, the investigation depth for offshore wind applications is supposed to be greater than the embedment length of possible foundations (Lesny et al., 2014). The greatest embedment lengths are to be expected with monopile foundations (Lesny & Richwien, 2011), which are also the most commonly used foundation type (Negro et al., 2017). The dimensions of the monopiles reach a length-to-diameter or slenderness ratio of 5-9 with a maximum value of 10 with a reported maximum pile diameter of 10 m (Schmoor & Achmus, 2015; Burd et al., 2017; Negro et al., 2017; BVG, 2019; Naser et al., 2022). Therefore, the maximum embedded depth is expected to be about 100 m. The maximum embedded length reported is 60 m (Negro et al., 2017) and geotechnical wells typically reach 50-70 m (BVG, 2019). Those depth ranges fit to the classical definition of the near surface.

1.2 Quantitative Interpretation

Considering the described usage of seismic data, qualitative imaging and interpretation can be considered the main purpose of reflection seismic data acquisition and processing. But quantification has always been a central topic in geophysics. In seismics, quantification has mainly been achieved by travel time inversion, Amplitude Versus Angle (AVA) analysis, and a range of seismic inversion approaches.

Actually, the first inverse problem in geophysics has been formulated and solved by Herglotz in 1907, in which travel time curves of earthquakes have been used to deduct the vertical velocity structure of the Earth (Ben-Menahem, 1995). Since then, travel time curves representing the kinematic characteristics of the wavefield have been used extensively with direct inversion and tomographic inversion methods to construct velocity models for seismological and exploration seismic applications (Boehm et al., 1996; Woodward et al., 2008; Köhn, 2011).

Due to the use of Automatic Gain Control (AGC) filters, the relative amplitude information was lost in the early days of data acquisition and the amplitude information only started to be interpreted in the late 1960s to find high amplitude or bright spots indicating the presence of gas (Chopra & Marfurt, 2007; Fawad et al., 2020). Afterwards, in the 1980s, the AVA analysis developed, in which the dynamic characteristics of the wavelet in the form of the angle dependent changes of P-Wave amplitudes are used to quantify the v_p , v_s , and ρ contrasts across an interface (Chopra & Castagna, 2014). The theoretical basis of the AVA analysis is the quantification of the reflection and transmission coefficients as they are shown in Figure 1-5. The calculation of those coefficients has been described first by Knott (1899) in terms of energy partitioning and by Zoeppritz (1919) in terms of seismic amplitude. The boundary conditions for the so-called Zoeppritz equations are the continuity of displacement and traction across a welded interface. Thereby, the P-Wave reflectivity r_{PP} is used most often and depends on the incidence angle measured from the vertical θ_1 , the properties of the upper layer $v_{P,1}, v_{S,1}, \rho_1$ and the lower layer $v_{P,2}, v_{S,2}, \rho_2$ in the notation of Dvorkin (2014) in Equation 1-1:

$$r_{PP}(\theta_1) = \left[\left(b \frac{\cos\theta_1}{v_{P,1}} - c \frac{\cos\theta_2}{v_{P,2}} \right) F - \left(a + d \frac{\cos\theta_1}{v_{P,1}} \frac{\cos\Phi_2}{v_{S,2}} \right) Hp^2 \right] \cdot \frac{1}{D}$$

$$p = \frac{\sin\theta_1}{v_{P,1}} = \frac{\sin\theta_2}{v_{P,2}} = \frac{\sin\Phi_1}{v_{S,1}} = \frac{\sin\Phi_2}{v_{S,2}}$$

$$a = \rho_2(1 - 2\sin^2\Phi_2) - \rho_1(1 - 2\sin^2\Phi_1)$$

$$b = \rho_2(1 - 2\sin^2\Phi_2) + 2\rho_1\sin^2\Phi_1$$

$$c = \rho_1(1 - 2\sin^2\Phi_1) + 2\rho_2\sin^2\Phi_2$$

$$d = 2(\rho_2 v_{S,2}^2 - \rho_1 v_{S,1}^2)$$

$$D = EF + GHp^2$$

$$E = b \frac{\cos\theta_1}{v_{P,1}} + c \frac{\cos\theta_2}{v_{P,2}}$$

$$F = b \frac{\cos\Phi_1}{v_{S,1}} + c \frac{\cos\Phi_2}{v_{S,2}}$$

$$G = a - d \frac{\cos\theta_1}{v_{P,1}} \frac{\cos\Phi_2}{v_{S,2}}$$

$$H = a - d \frac{\cos\theta_2}{v_{P,2}} \frac{\cos\Phi_1}{v_{S,1}}$$

Equation 1-1

A range of simplifications and AVA approximations for Equation 1-1 with varying ranges of validity exist (Chopra & Castagna, 2014). Despite the success of travel time inversion and AVA analysis, seismic inversion has become increasingly important.

Generally, seismic inversion describes the process of finding a quantitative subsurface model for which modelled data fits best to observed data (Aki et al., 1977; Bishop et al., 1985; Tarantola, 1986). Similarly, Buland & Omre (2003) define the aim of inversion as the estimation of subsurface parameters based on geophysical measurements and general knowledge. With the rather subjective input of knowledge and selection of a method, seismic inversion is a form of quantitative interpretation, although the success of inversion is quantitatively measurable and justifiable as well as reproducible. The definitions of seismic inversion already hint, that there are three crucial, methodological components to seismic inversion, namely seismic data acquisition, seismic data modelling and optimization to find a best fit model. With this iterative method, unrealistic and wrong subsurface models will be found, if the observed data, optimization strategy and the forward model do not fit the exploration target (Weglein, 2013). In a strict sense, the above given definition only describes model-driven and iterative inversion approaches and excludes direct or analytic and filtering approaches to inversion (Veeken & Silva, 2004; Weglein, 2013). As model-driven inversion has proofed to be beneficial for noisy data (Veeken & Silva, 2004; Provenzano et al., 2017; Vardy, 2015; Yao et al., 2020), only model driven approaches are considered in the following.

1.2.1 Optimization Methods

Inversion methods are differentiated according to the optimization method and the type of solution provided. In the case of deterministic inversion, a single best-guess solution result is determined based on the optimization of a single initial estimate (D. Cooke & Cant, 2010). For linear problems

conjugate gradient type methods are common, while Gauss-Newton, Levenberg-Marquardt, or Occam's inversion are often used for nonlinear problems (Aster et al., 2013a). With probabilistic inversion following a Bayesian approach, a (a posteriori) likelihood distribution of the model parameters is determined based on a measured or guessed initial (a priori) likelihood distribution. Many forward models are run for example with Markow Chain Monte Carlo methods (Buland & Omre, 2003; Aster et al., 2013b). Rather than optimizing the initial distribution, the entire distribution space is sampled and compared to the observed data and more likely solutions based on a quantitative criterion are selected. With stochastic optimization processes such as genetic algorithms (Stoffa & Sen, 1991; Sen & Stoffa, 1992) or simulated annealing (Ma, 2002) the randomly defined initial distribution is optimized. Due to the random initialization, multiple inversion runs are likely to result in a range of solutions, which can be analysed to retrieve an a posteriori likelihood distribution.

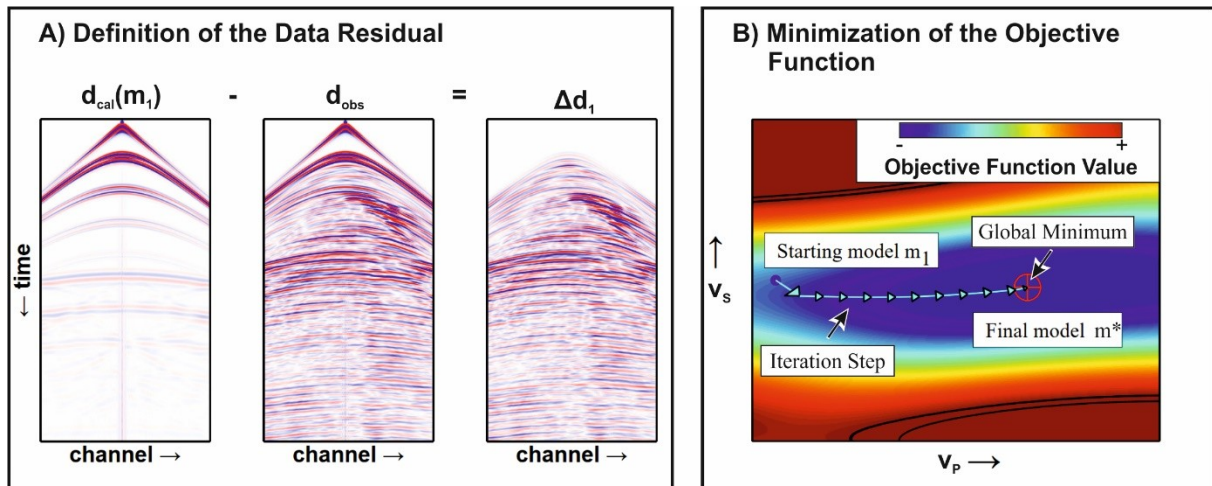


Figure 1-6: Visualization of optimization principles modified after Köhn (2011). A) Definition of the data residual Δd_1 of the initial subsurface model m_1 as the difference between the calculated seismic data $d_{cal}(m_1)$ and the observed seismic data d_{obs} . B) Minimization of the objective function in the parameter space of the P-Wave velocity v_p and S-Wave velocity v_s with gradient descent methods in which every iteration step updates the subsurface model until the final model m^* is reached. Ideally, m^* is equivalent to the global minimum of the objective function.

The aim of seismic inversion can also be described to be the estimation of a subsurface model for which the difference between the calculated seismic data based on the model is minimized in comparison to observed data (Sirgue & Pratt, 2004). Therefore the need arises to quantify the misfit between the observed seismic data d_{obs} and the modelled data $d_{cal}(m_i)$ depending on the input subsurface model m_i of the iteration i by means of the residual $\Delta d_i = d_{cal}(m_i) - d_{obs}$. An illustration of the data residual is given in Figure 1-6A. The initial model $d_{cal}(m_1)$ only contains a low frequency model with the general trend of the subsurface properties and the main reflections.

In Δd_1 , the missing high frequency variation of d_{obs} is visible. It is the aim of the seismic inversion in this case to retrieve this high frequency variation. After a successful inversion, $d_{cal}(m^*) \approx d_{obs}$ should be reached and Δd should be zero or only contain uncorrelated noise. Following Crase et al. (1990) the misfit function to be minimized takes the form of Equation 1-2, of which the L_2 -norm in Equation 1-3 is a special case.

$$S(m_i) = \sum_{TWT=TWT_0}^{TWT_{max}} W \left[\frac{\Delta d_i}{\sigma_i} \right]$$

Equation 1-2

$$W_{L2} \left[\frac{\Delta d_i}{\sigma_i} \right] = \frac{1}{2} \left[\frac{\Delta d_i}{\sigma_i} \right]^2$$

Equation 1-3

Figure 1-6B illustrates how iterations of gradient descent methods lead to a minimization of the objective function. Following the description in Köhn (2011), a new model m_{i+1} is calculated further minimizing S until a minimum or a different stopping criterion is reached such as the number of iteration steps. The model update is determined by Equation 1-4 with the step length μ_i and the search direction δm_i or gradient.

$$m_{i+1} = m_i + \mu_i \delta m_i$$

Equation 1-4

Thereby, the calculation of the search direction depends on the inversion approach. The global minimum of the objective function is the lowest value of the objective function in the entire data space and represents the subsurface model, e.g., described by v_p and v_s , which fits best to d_{obs} and is thus the estimate of the inversion m^* . If m_1 is not close enough to m^* , the described deterministic methods potentially fail to retrieve the true model. Taking into account Figure 1-6B, a wrong initial model would be an initial model which is not connected to m^* with a monotonically decreasing path. If a wrong initial model is used, the optimization will be trapped at a local rather than at a global minimum and the subsurface parameters will be wrongly estimated. Probabilistic and stochastic optimization methods are less likely to be trapped at local minima, as the parameter space is broadly sampled and it is more likely to find a starting model close to the global minimum (Sen & Stoffa, 1992; Stoffa & Sen, 1991; Ma, 2002; Buland & Omre, 2003).

1.2.2 Post-Stack Impedance Inversion

The first milestone of seismic inversion reached first by Lindseth (1972) has been post-stack impedance inversion. Following Lindseth (1972, 1979), Cook & Schneider (1983), or Oldenburg (1983), a seismic trace resembles a time series of a vertically incident wave after stacking, migration and spherical spreading correction (see also “2.1.3 Seismic Data Processing”). In this setting and without attenuation or multiscattering, a seismic trace d can be modelled with a purely acoustic approximation as a convolution of the seismic source signal time series w with the P-wave reflectivity time series r_{PP} as given in Equation 1-5:

$$d = r_{PP} * w$$

Equation 1-5

Equation 1-6 is the vertical incidence equivalent $\theta = 0^\circ$ of the Zoeppritz equation given in Equation 1-1, at time step i of the TWT depending on the P-impedance Z_p - which quantifies the resistance of a system to acoustic flow resulting from acoustic pressure and is determined by the product of ρ and v_p - at this time step and the next time step $i + 1$.

$$r_{PP,i} = \frac{Z_{P,i+1} - Z_{P,i}}{Z_{P,i+1} + Z_{P,i}} = \frac{\rho_{i+1} \cdot v_{P,i+1} - \rho_i \cdot v_{P,i}}{\rho_{i+1} \cdot v_{P,i+1} + \rho_i \cdot v_{P,i}}$$

Equation 1-6

Applying a deconvolution, autoregression, prediction filters or with optimization methods, and a known or estimated w , r_{PP} can be estimated from d (see Equation 1-5) and Z_p can be calculated recursively from Equation 1-6.

The resulting Z_p estimate will not yet resemble the true ground model, as w is band limited and thus the impedance estimate determined from d is also band-limited, which is shown in Figure 1-7. A seismic wavelet only contains a usable signal in a certain, limited frequency range. The missing high frequencies lead to a limited resolution (Cooke and Cant 2010). The missing low frequencies, in contrast, cause the band-limited impedance to have an unknown starting value and wrongly estimated low frequency trend (see the lower panel of Figure 1-7B; Ferguson and Margrave, 1996). Therefore Lindseth (1979) and Ferguson & Margrave (1996) proposed to add a high-cut filtered low frequency trend, e.g., derived from velocity analysis or logs to a low-cut filtered band-limited impedance estimate to restore the low frequency component of the impedance. For this purpose, the relative scaling of a seismic trace also needs to be estimated and corrected.

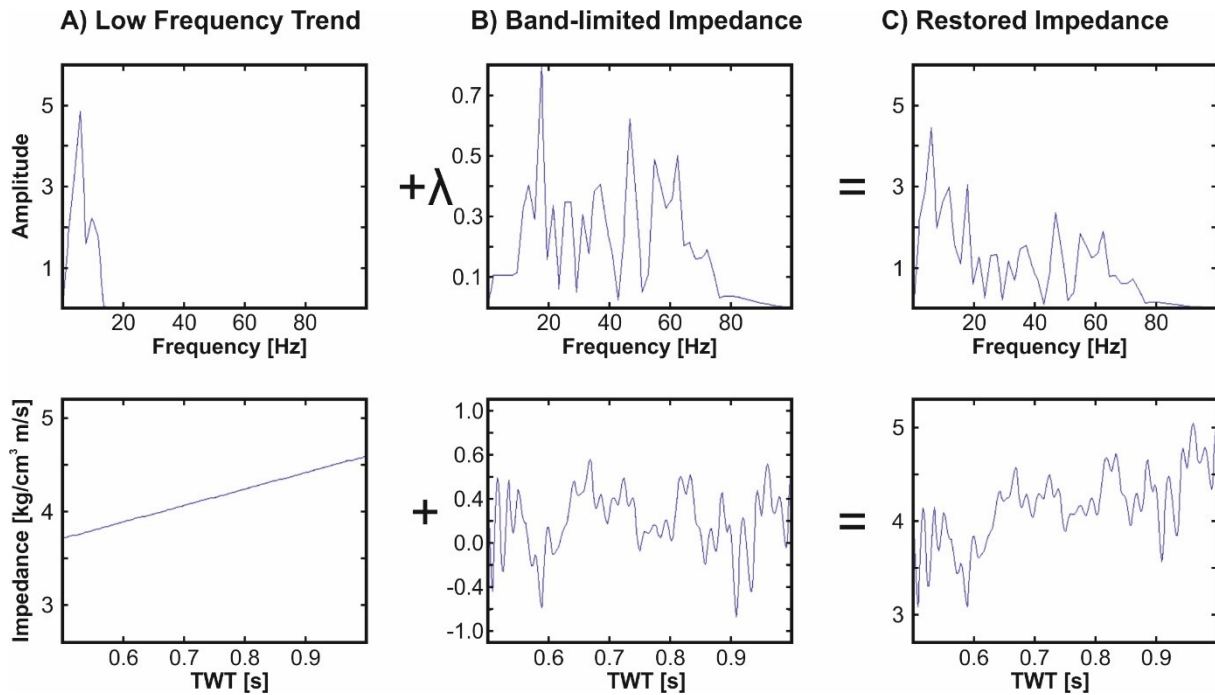


Figure 1-7: Addition of the low frequency trend to the band limited impedance to restore a full bandwidth impedance estimate modified from (Ferguson & Margrave, 1996). A) Spectrum and time series of the low frequency trend, e.g., resulting from velocity analysis or logging data. B) Spectrum and time series of the band-limited impedance. Both the high and low frequencies outside the frequency range of the wavelet are missing and the relative scaling factor λ of the band-limited impedance relative to the low frequency trend are unknown. In the time series the factor is already applied, but due to the band limitation, the impedance resembles a variation around zero. C) Restored impedance in which the low frequency trend has been added to the band-limited impedance. The missing high frequency are not restored leading to a limited resolution.

Although there are a number of constraints for the application of impedance inversion algorithms, impedance sections bear several advantages. Figure 1-8 aims to illustrate, that the full information encoded in a post-stack seismic image can be retained performing impedance inversion, while the details of the image are potentially lost with qualitative interpretation (Vardy, 2015). In contrast to travel time inversion, there is no need to manually, or automatically pick arrival times of seismic events and seismic inversion is not only sensible to v_p or v_s . Seismic inversion is also efficient, as whole seismic traces, gathers or sections are analysed with seismic inversion, while AVA analysis focuses on single events.

Additionally, e.g., the impedance is of direct value for engineering applications, which can even be improved for potential end-users with conversion to geological or geotechnical parameters (Vardy et al., 2017, 2018; Vardy, 2020). Furthermore, subjective biases can be reduced with seismic inversion by improving the data use and automatization (Alcalde & Bond, 2022). Inversion results showing quantitative unit properties, especially after conversion to depth, are also a versatile way to represent seismic results to other professions. The interpretation of reflection seismic sections showing interface properties by untrained personnel can lead to misconceptions due to various

effects caused by seismic velocity, acquisition geometry, data recording and processing (Tucker & Yorston, 1973) or noise (Ismail et al., 2012). Due to these advantages, impedance inversion has been broadly applied in the Oil+Gas Industry (Fawad et al., 2020).

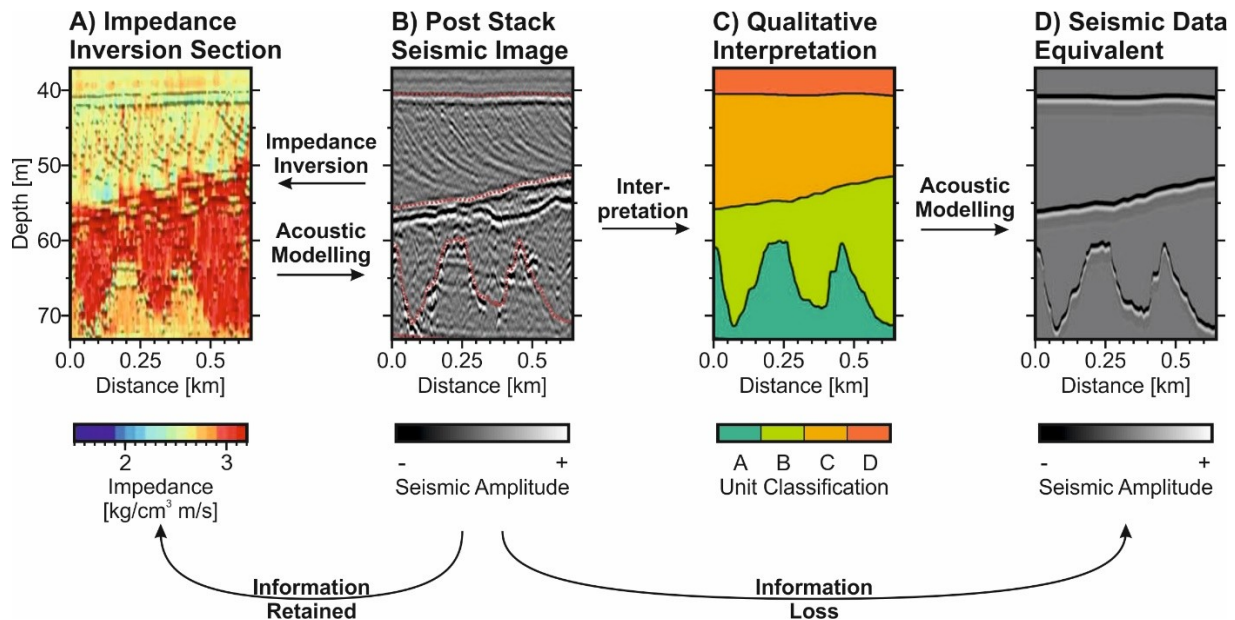


Figure 1-8: Comparison of inversion results with qualitative interpretation for a boomer seismic reflection section from the Walney I wind farm site in the Eastern Irish Sea, taken and modified from Vardy et al. (2018) and Vardy (2020). A) Impedance inversion section retaining the full details of the B) Post-stack seismic image. C) Ground model after geologic interpretation showing four distinctive units whose boundaries are indicated in (A) with red, stippled lines. D) Seismic data equivalent of the four layer model in (C) which resembles considerable information loss compared to the seismic image in (B).

The concept of impedance inversion has been extended to non-vertical incidence angles with the main purpose to emphasize certain contrasts, particularly for fluid detection. Connolly (1999) developed the Elastic Impedance (EI) concept, which was modified by Whitcombe et al. (2002) to the Extended Elastic Impedance (EEI). It can be deduced from Formula 1.1 and more readily from the AVA approximations, that certain lithological and fluid contrasts are more pronounced at certain incidence angles. By creating angle stacks at those incidence angles and invert for EI or EEI, the contrasts are better visible than in Z_P sections. Additionally, correlation to other parameters of interest were determined and exploited (Fawad et al., 2020). Creating EI/EEI for a range of angle gathers, the combined results can be visualized jointly with projection methods.

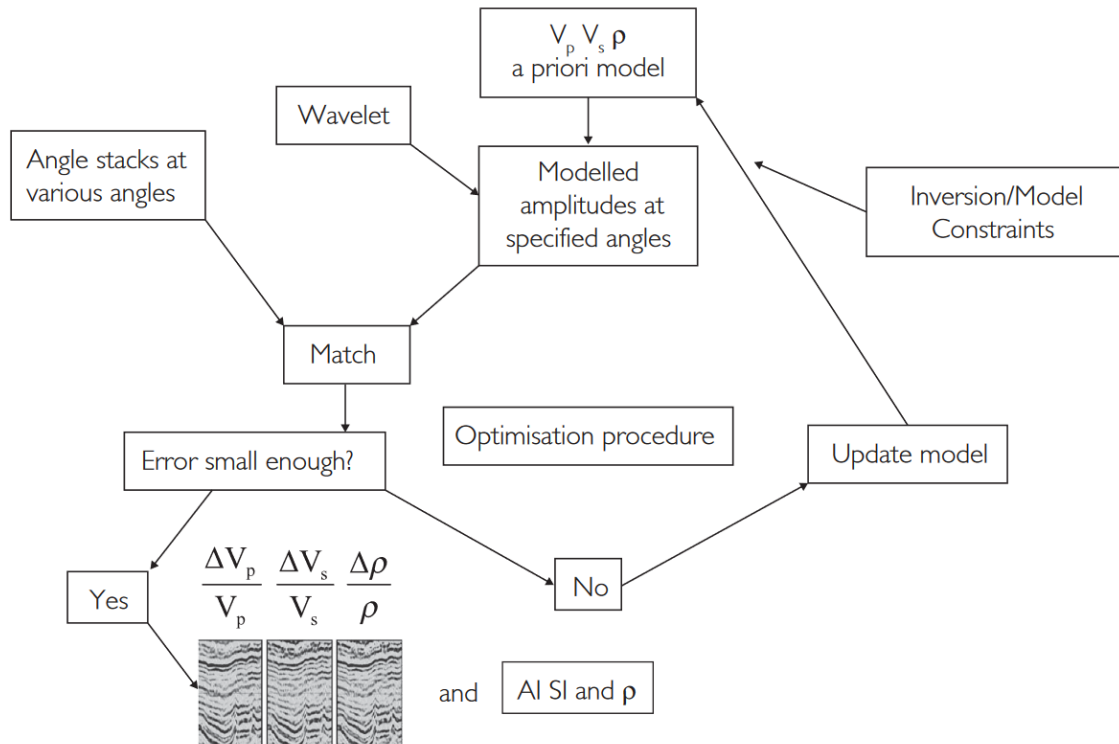


Figure 1-9: Workflow of pre-stack inversion taken from Simm & Bacon (2014), in which angle stacks are modelled and compared to the observed seismic data. Unless the misfit is below a stopping criterion, the model is updated to reduce the misfit. To stabilize the optimization process a number of constraints such as the Gardner relation of constant P-Wave to S-Wave velocity ratio can be introduced.

1.2.3 Pre-Stack Inversion

To avoid multiple runs of EI or EEI to assess AVA properties or the analysis of single events with AVA analysis, algorithms have been developed for pre-stack inversion, also known as pre-stack simultaneous inversion or AVA inversion (Russell, 2014; Simm & Bacon, 2014; Fawad et al., 2020). As shown in Figure 1-9, the optimization procedure is based on the modelling of angle stacks or other gathers, a comparison of those models with the observed gathers and an update of the model to improve the fit between observation and model until satisfactory results are achieved. Thus, the inversion is “simultaneous”, as one inversion result is achieved for all traces used as an input. Following Ma (2002), angle gathers can be modelled with a convolution of an estimated wavelet with calculated reflectivity time series, e.g., using Formula 1.1 or the AVA approximations. The AVA approximations bear the advantage that the inverse problem can be linearized allowing simplifications of the inversion scheme. The first, basic assumption for this approach is, that all traces collected for an inversion run only depend on the vertical variation of the subsurface parameters and the angle of incidence. The processing of the seismic data before the AVA inversion needs to reflect this setting (Veeken & Silva, 2004). Numerous optimization schemes such as stochastic optimization with simulated annealing (Ma, 2002) or probabilistic Bayesian

inversion (Downton et al., 2001; Buland & Omre, 2003; Downton & Lines, 2004; Hampson et al., 2005; Russell, 2014) have been implemented. To stabilize the inversion process, the constraints as indicated in Figure 1-9 are introduced limiting the solutions to certain ranges such as the Gardner relation in Figure 1-2 or fixed v_p/v_s -ratios.

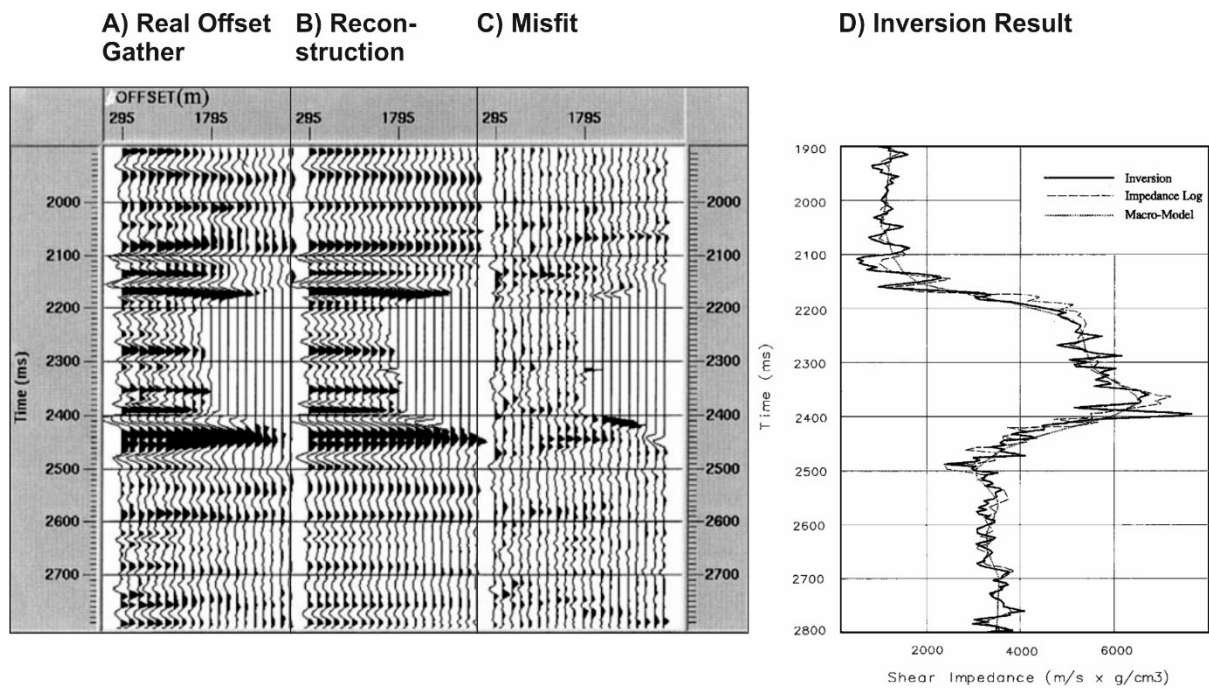


Figure 1-10: Pre-stack inversion result achieved with simulated annealing from a commercial North Sea 3D seismic data set modified after Ma (2002) showing A) the real offset gather of a deep (approximately 2-2.8 km assuming $v_p = 2000$ m/s) seismic section with offsets exceeding 2 km; B) The corresponding reconstruction after the pre-stack inversion; C) The misfit or likewise the difference between (A) and (B); D) the shear impedance ($Z_S = v_s \cdot \rho$) result of the inversion as a black solid line in comparison to the initial model as a grey dotted line and the ground truth from logging data as a grey dashed line.

The development of pre-stack inversion allowed the additional deduction shear properties such as shear impedance $Z_S = v_s \cdot \rho$ derived from seismic data as shown in Figure 1-10 as well as the differentiation of the ρ impact opposed to the v_p impact on Z_p . Although a simulated annealing algorithm allowing for a broad parameter search has been used by Ma (2002) and shown in Figure 1-10 allowing for a wide search in the parameter space, the inversion results follow generally the initial model and the inversion only solves for the small scale variation superimposed on the macro model. This observation is equivalent to the lack of low frequencies for the impedance inversion (see Figure 1-7). Constraints, initial model and the choice of the optimization procedure have significant impact and in benchmark studies only 50% of the contractors were able to produce reliable results (Neepe, 2008).

As mentioned in “1.1.1 The Marine Near Surface”, v_s is less sensitive to fluids in the pore space than v_p . Therefore, the ratio of $\frac{v_p}{v_s} = \frac{Z_P}{Z_S}$ has been broadly used to identify and characterize oil and gas reservoirs. For offshore infrastructure installations, the shear properties are also critical parameters to be estimated. Seismic waves introduce small strain and the small-strain, dynamic shear modulus $G_{max} = \rho v_s^2$ is an important parameter to assess the vulnerability of foundations to dynamic loading such as wind and waves in the case of offshore wind farms (O’Kelly & Arshad, 2016; Fu, 2018). As G_{max} directly depends on v_s , seismic inversion is a versatile tool to estimate this shear property, in particular since sampling can destroy the internal structure of the soil during the probing. Furthermore, a range of correlation of the dynamic properties to large strain, static properties and other construction parameters have been established (Brotons et al., 2016; L’Heureux, 2016; Wichtmann et al., 2017; Fjær, 2019).

1.2.4 Waveform Inversion

Although already envisioned earlier (Lailly, 1984; Tarantola, 1986), a broader application of waveform inversion is the most recent development in terms of quantitative interpretation. As described by Virieux & Operto (2009), the basic idea behind waveform inversion is that physically accurate models are used to simulate the entire content of seismograms and that an subsurface model is found fitting to the observed seismograms with an global search optimization scheme. In the practical application, the computation of the synthetic seismograms is computationally demanding, so local optimization algorithms such as the conjugate-gradient method, quasi-Newton algorithms, or Newton and Gauss-Newton algorithms are used. Therefore, an accurate starting model is of great importance. Fichtner (2011) points out, that there is “full language confusion” regarding the different waveform inversion approaches. For matters of consistency, approaches relying on the forward scattered wavefield as displayed in Figure 1-4 are termed Full Waveform Tomography (FWT), although in the literature phrases such as Early-Arrival Full Waveform Inversion are also common. Contrastingly, methods inverting the backward scattered wavefield are termed Reflection Waveform Inversion (RWI). Only approaches in which both the forward and the backward scattered wavefield are considered are Full Waveform Inversions.

Considering Equation 1-4, it is imperative for, e.g., a gradient optimization scheme to estimate the gradient. As an illustrative description, the gradient quantifies how the model should be changed at every location to fit better to the observed data. To find the gradient, two core principles of seismic exploration – migration and the Born approximation – are harnessed (Mora, 1987, 1989). Simplistically described, migration describes a seismic data processing step, in which observed backscattering events are mapped to their true subsurface location (Bednar, 2005). According to

the Born approximation, those backscattering events are due to small scale changes (heterogeneities) in the smooth background velocity field (Beylkin, 1985). So, when a synthetic seismogram is modelled for inversion as shown in Figure 1-6A, the residuals in comparison to the observed data are due to missing or wrong heterogeneities. With migration, the residuals can be mapped to the subsurface locations, which have to be changed to improve the fit. For FWT and FWI the definition of migration is generalized to backpropagation (Tarantola, 1986), as the forward scattered field is analysed (see Figure 1-4). The gradient is then calculated with the backpropagated residual wavefield, e.g., based on the equations of motion (Köhn, 2011).

The choice of parametrization, modelling algorithms and objective function is of major importance for waveform inversion approaches. For the forward scattered wavefield, the highest sensitivity is for v_p and acoustic modelling assuming constant ρ is justifiable (Sirgue et al., 2010; Virieux & Operto, 2009). For FWI, elasticity, attenuation and potentially anisotropy play a significant role and should be considered (Kugler et al., 2007; Köhn et al., 2012; Kurzmann et al., 2013; Thiel et al., 2019). Due to the shorter offsets, RWI is typically less sensitive to velocity than FWT or FWI. Therefore, it has been shown to be beneficial to separate the velocity update of the model and adopt the calculation of the objective function (Provenzano et al., 2017; Yao et al., 2020). The choice of the objective function can also be adopted to the presence of noise since, e.g., the L_2 norm is more sensitive to noise bursts or irregular data than the Cauchy criterion given in Equation 1-7 (compare Equation 1-2 and see Crase et al., 1990).

$$W_{cauchy} = \frac{1}{2} \ln \left\{ 1 + \left[\frac{\Delta d_i}{\sigma_i} \right]^2 \right\}$$

Equation 1-7

1.3 Motivation and Objectives

Reflection seismic imaging plays a central role in both scientific research and industrial applications. For deep targets and in the Oil+Gas Industry, also seismic inversion has become an important method to improve the knowledge about the subsurface. Contrastingly, seismic inversion seems to be underused in the marine near surface and several research questions need to be answered to establish seismic inversion in the marine near surface.

1.3.1 Open Questions

Currently it is unclear, how marine near surface seismic data should be acquired to be an optimum basis for inversion. It has been generally recognized in the Oil+Gas Industry, that there are special requirements for seismic data sets to be inverted and that even re-acquisitions of available data sets are sometimes necessary to provide a suitable data basis (Virieux & Operto, 2009; Sirgue et al., 2010). The findings for those relatively low resolution surveys focussing on deep targets in hard rocks are not directly transferable to the near surface and available acquisition guidelines do not focus on inversion (Lesny et al., 2014; OGP, 2017; Fischer et al., 2019; ISO 19901-10, 2021). In contrast to other seismic surveys, high-frequency seismic sources with relatively low sound pressure levels are used in the near surface (ISO 19901-10, 2021) and thus the noise levels are high (Danbom, 2005). The working environment is also problematic due to multiscattering masking significant parts of the seismic section (Vardy et al., 2017) and limiting the available bandwidth (Provenzano et al., 2020). With those more high frequent sources, static corrections and exact positioning of the receivers are critical for the preservation of the signal content during processing (Gutowski et al., 2002; Duarte et al., 2017; Reiche et al., 2020). An important aspect to the data acquisition are also possible constraints and limitations to seismic inversion posed by the properties of the unconsolidated near surface sediments. The most important aspects in this context are, that impedance contrasts are typically dominated by density, and especially S-Wave velocities are low (see Figure 1-2). Signal penetration can be low due to attenuation, as the sediments are comprised of unconsolidated sediments predominantly sands in the North Sea (Ehlers et al., 2011; Graham et al., 2011), or clays and tills overlying the chalk bedrock in the Baltic Sea (Björck, 1995; Andrén et al., 2011). Shallow gas being a major cause for attenuation is abundant, too (Tóth et al., 2014; Römer et al., 2017, 2021).

Furthermore, there is a lack of inversion strategies and inversion algorithms for near surface seismic data. To begin with, the low frequency trend estimation or initial model estimation is a critical step (Claerbout, 1986; Jannane et al., 1989). It is generally recognized, that low frequency trends derived from wells can suffer large errors and are spatially sparse (Yuan et al., 2019). So, a low frequency trend estimation for the near surface based on seismic data needs to be developed. In previously published studies (see Vardy et al., 2017 and references therein), the low frequency trend has mainly been added as a linear trend and it is unclear whether an added linear trend is sufficient to restore the full bandwidth. To cope with low signal-to-noise ratios, very stable algorithms are needed, e.g., to determine P-Wave impedance. Although there are promising approaches such as the genetic algorithm by Vardy (2015), none of the algorithms is available or currently reproducible. At this stage it is also not clear whether shear properties can be predicted. On the one hand, sediment

physical models like the Biot-Stoll model (Biot, 1956; Stoll, 1977) are more appropriate than rock physics (see Figure 1-2). As a consequence, empiric relations such as the v_p - ρ relation by Gardner et al. (1974) are not applicable although being used for impedance (Lindseth, 1979) or Amplitude-Versus-Angle (Chopra & Castagna, 2014) inversion methods. On the other hand, the FWI approach for the near surface by Provenzano et al. (2017) is not sensible to shear property changes in the relevant range and does not account for dipping strata. To improve the stability and outcomes, often constraints are included in the inversion workflow. Currently, it is not known which constraints for stabilization are justifiable. Also, it is not clear how a v_s starting model can be derived or how the FWI can be incorporated in an exploration workflow. As shown by Nepp (2008), there can be large differences between inversion results, even for synthetic data. Therefore, it is critical to provide reproducible workflows and to assess or possibly quantify uncertainties.

To further promote the use of seismic imaging and inversion results it is critical to answer the question on how seismic results can be made usable for other professions such as geologists and engineers. The physical properties derived by seismic inversion – such as density, elastic or shear moduli and attenuation – allow an analysis of the lithology, the fluid content and the stress regime (Breitzke, 2006; Vardy et al., 2017; Provenzano et al., 2019). Thus, detailed insights about the fluid distribution, fluid migrations and pathways, compaction trends, (glacio-) tectonics, nature and distribution of glacial sediments can be gained. Seismics can also answer important questions for current and future challenges such as drilling de-risking, foundation planning of offshore wind, geothermal energy exploration, Carbon Capture and Storage or hydrogen storage site monitoring. But for this purpose, seismic results need to be accessible for non-experts and further steps such as depth conversion, data integration and approval by certifying bodies have to be taken.

1.3.2 Scientific Objectives

Following the stated open questions, the manuscript presented in Chapter 3 aims to identify suitable inversion techniques and to identify requirements on data acquisition to invert marine near surface seismic data sets in a depth range of 80-100 m in a North Sea or Baltic Sea setting. For this purpose, sediment properties are analysed, field measurements of near surface seismic sources are collected, and numerical experiments are conducted. On this basis, inversion techniques and data acquisition are discussed. In the context of this thesis the conventional data acquisition with towed sources and receivers are considered.

In Chapter 4 the hypothesis is tested, that a marine near surface seismic data set can be inverted for P-Wave impedance with low uncertainty only based on seismic data and that the inversion

results provide valuable subsurface information for geotechnical and geological application. A test data set from a location of a windfarm area in the German North Sea has been selected as a realistic application scenario. From a methodological point of view, this target required adequate data processing, the accurate estimation of P-Wave velocity, a conversion of this velocity to impedance, attenuation correction and impedance inversion. To make further use of the data, inversion results were converted to depth, correlated to geotechnical parameters and are jointly interpreted.

As the shear properties are an important geotechnical and geological parameter, it is the aim of Chapter 5 to reproduce ground truthing data with the S-Wave velocity predictions by pre-stack inversion. To further improve signal-to-noise ratios, a toolbox to prepare CMP super-gathers for inversion has been developed. Those gathers are used as an input for an inversion scheme with no constraints and a deterministic steepest descent optimization.

The utilization of impedance inversion in a Baltic Sea setting is tested in Chapter 6. The previously developed workflow has been adopted to include ground truthing data for the generation of the low frequency model. In this geological setting, impedance can be assessed as a tool for detailed stratigraphic and structural interpretation in geologically complex areas. Also, the hypothesis of a correlation of impedance with geotechnical parameters is tested in an additional environment.

Belonging to the field of applied geophysics, the objectives of this thesis can be classified by means of the Technology Readiness Levels (TRL) as proposed by Mankins (1995) and adopted for geoscience, e.g., by Armstrong (2015). Marine near surface seismic inversion is at the level of TRL 1-6, as the basic principles are observed and reported (Lindseth, 1972; Lailly, 1984; Tarantola, 1986; Ma, 2002), the technology concept has been formulated (e.g., Provenzano et al., 2017; Vardy, 2015), and the proof of concept has been made with validation and demonstration by synthetic data and in a relevant environment (see Vardy et al., 2017; Provenzano et al., 2019; and references therein). As described above, there are gaps of knowledge, which need to be filled for further application. On the one hand, some of these gaps are aimed to be filled with this thesis. In Chapter 4, it is validated in a relevant environment (TRL 5), whether impedance inversion can be based only on seismic data and the associated uncertainties are quantified. Chapter 5 maps into TRL 3 as a proof of concept for S-Wave velocity estimation. On the other hand, the work conducted belongs to TRL 7 “Technology prototype demonstration in an operational environment” with data acquisition aspects and possible limitations in Chapter 3, and demonstrations of the technology in a North Sea and Baltic Sea setting in Chapter 4 and Chapter 6.

1.3.3 Reference to the SynCore Project

It has been specified as a political aim in Germany, to improve and simplify subsurface investigations for offshore wind energy projects as well as to lower the costs (BMW_i, 2014). For that matter, geotechnical surveys have been identified to pose a significant risk with high costs and with limited availability of geotechnical vessels (BVG, 2019). From a geological perspective, subsurface investigations only relying on geotechnical surveys should also be critically assessed, as lateral changes on small scales might not be identified (Henson & Sexton, 1991). Therefore, working groups at the Fraunhofer Institute for Wind Energy Systems, the Fraunhofer Institute for Industrial Mathematics and the University of Bremen together with the industry partner GuD Consult successfully applied to conduct the research project “SynCore - Synthetic Coring: Deriving Virtual Geotechnical Ground Data from Seismic Measurements and Geostatistical Data”. In this context, the PhD thesis at hand aims to establish seismic inversion methods for the assessment of the physical properties of the marine near surface.

Chapter 2 Material and Methods

2.1 Seismic Data

Seismic data have been acquired in the field and synthetically generated as a data basis for inversion, as described in the following. Processing and interpretation have been conducted with commercial software, while custom inversion algorithms have been developed and programmed for this thesis.

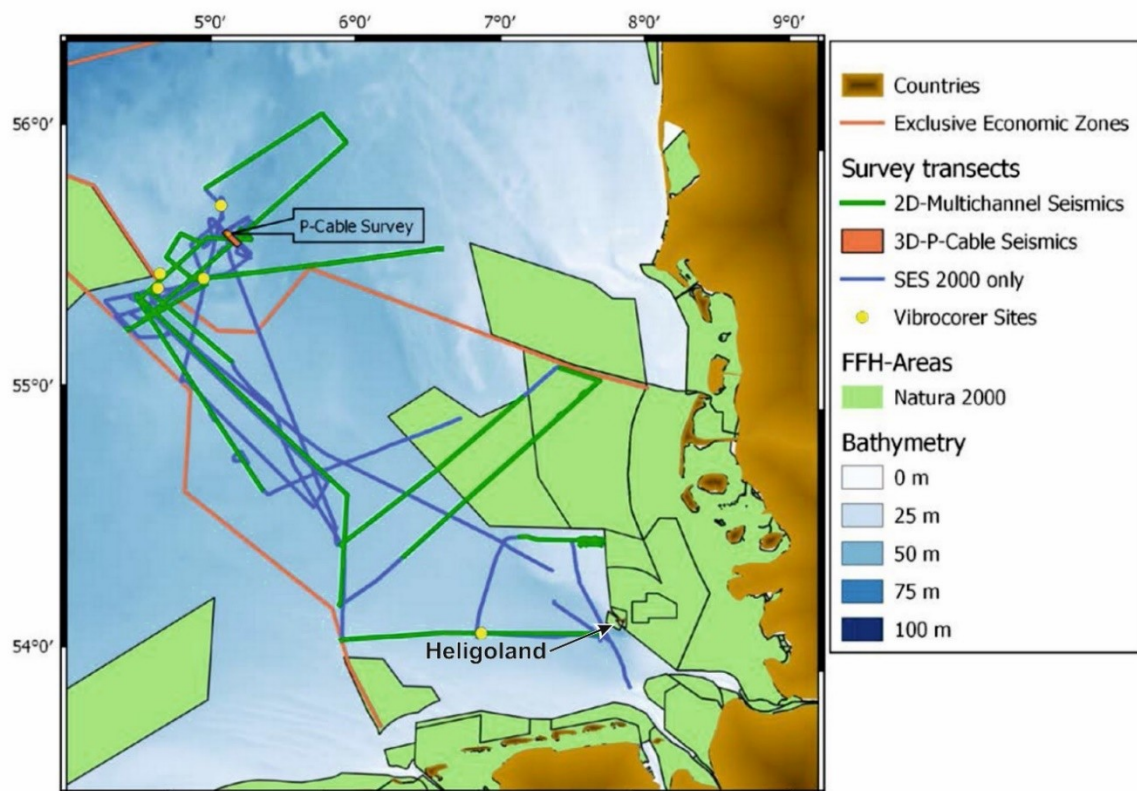


Figure 2-1: Overview map of the data collected during research expedition He569, modified after Keil et al. (2021).

2.1.1 Field Measurements He569-GeoB21-033

During the research expedition He569 (Keil et al., 2021) in the German North Sea, the seismic Profile He569-GeoB21-033 was acquired in February 2021 on R/V Heincke (AWI, 2017) at 22-25 m water depth in the north of the island Heligoland. An overview map and track chart of the cruise is shown in Figure 2-1. Alternate shooting of the Miro-GI airgun and the AADS400 sparker has been performed, the main acquisition settings are given in Table 2-1 and further described below.

Table 2-1: Seismic Data Acquisition Parameters of He569-GeoB21-033.

Device	Parameter	Description
Source	UHR Source	Sercel micro-GI Volume 2 x 0.1 L
	UUHR Source	Applied Acoustics Dura-Spark UHD 400 Sparker (AADS400) 1750 J
	Shot Point Spacing	Approximately 6 m (2.4 s time trigger with approximately 2.5 m/s speed over ground)
Receiver	Type	Analogue Single Hydrophone Streamer
	Channel Spacing	1-4 m, variable
	Tow Depth	0.7 m (Depth keeping with 5 ION DigiBirds)
	Offsets	7-230 m
Recording	Sampling Rate	8 kHz
	Analog to Digital - Conversion	MaMuCS (Dr. Hanno Keil, University of Bremen) 16 bit Texas Instruments AD Converters.
	Recording Length	Sercel micro-GI: 1.7 s AADS400: 0.5 s
Positioning	Type	Differential GPS on the ship
	Processing	Lay-Back
	Accuracy	m to dm-level

The micro-GI airgun is a customized mini-GI airgun (Sercel, 2022) with a total volume of 0.2 l. The airgun source has been operated in harmonic mode in which the two chambers have the same volume of 0.1 L each. The sound signal is produced by a sudden release of pressured air from the first chamber of the gun referred to as the Generator. The oscillation of the released air bubble is suppressed by the release of air from a second chamber referred to as the Injector with a delay of 13 ms. The pressure of the supplied air is regulated and supplied via an umbilical from compressed air tanks, which are filled by a compressor. Solenoid valves, which are triggered electrically via the umbilical by the custom gun control system, control the opening of the chambers. The source is towed on a hanger attached to a buoy. This construction allows for the vertical positioning of the gun in ~ 1.0 m depth.

The second seismic source used was the Applied Acoustics Dura-Spark UHD 400 sparker. The source consists of a towed catamaran with an electrode deck with five rows of 80 tips at 0.2 m depth and a high voltage cable that connects the device via a junction box to the dry-end 3.7/4.0 kV power supply (AAE, 2022). A discharge of the charged capacitors across the tips to the earth on the catamaran frame through the water is initiated with a trigger signal from the custom gun control system. This realization is a negative discharge setup in which the tips are the cathode reducing the oxidation on the tips. The seismic signal is by both the generation and collapse of a bubble generated by a local vaporization of the water forming channels in which gas-phase streamer-like electric discharge (Rutgers & de Jong, 2003; Joshi & Thagard, 2013).

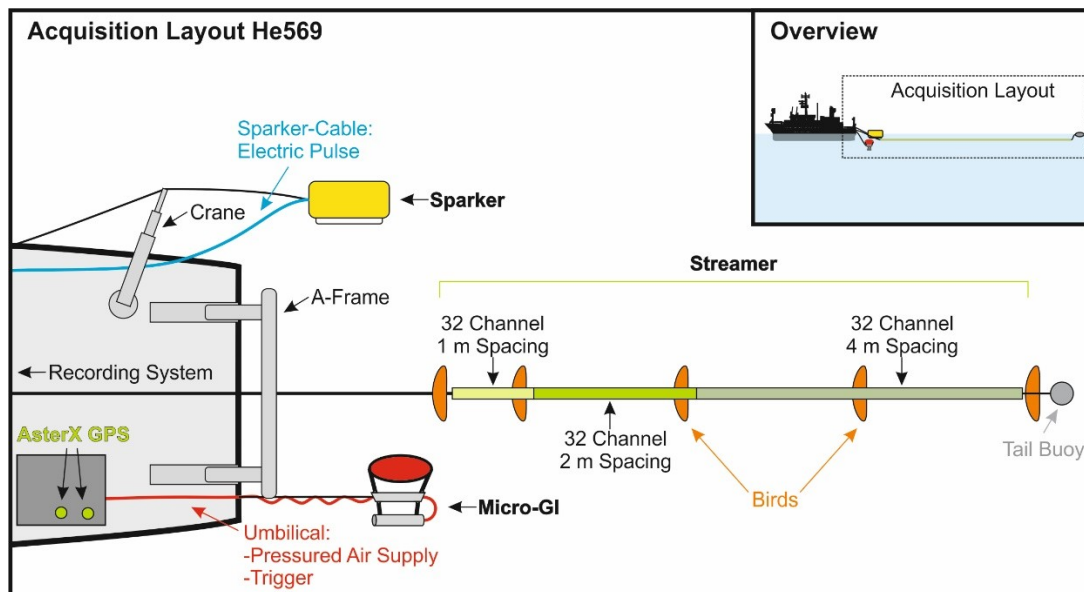


Figure 2-2: Acquisition layout for the Profile He569-GeoB21-033 acquired during the research expedition He569 redrawn after Keil et al. (2021). The main elements of the acquisition system are two seismic sources including a Sercel micro-GI airgun and an Applied Acoustics Dura-Spark UHD 400 sparker, and a 96 channel single hydrophone streamer with variable channel spacing.

As described in further detail in the cruise report by Keil et al. (2021) and shown in Figure 2-2, a 96 channel analogue hydrophone streamer has been towed behind the centre of the ship. The custom design, gel-filled streamer has been manufactured by Teledyne with a single Mini-T2 hydrophone for each channel. Overall, the active sections consist of four sections with variable channel spacing. The channel spacing in the first 32 channel section is 1 m, while the spacing in the second 32 channel section is 2 m. Those two sections are followed by two further, 16 channel sections with a 4 m channel spacing each. To keep the streamer at a depth of 0.7 m, a total number of five ION DigiBird 5011 (birds) depth control units are mounted on the tails of the stretch and the active sections. A deck cable connects the recording system in the laboratory to the 60 m long lead-in and a 10 m long elastic stretch section in front of the active section. As not the entire lead-in has been deployed, an offset range of 7-230 m is reached for the micro-GI records. With the custom recording system MaMuCS, a total number of 96 channels can be recorded at a maximum sample rate of 10 kHz per differentially coupled input channel. This high sample rate is reached with three NI 6052E AD-Converter cards reaching 330 kHz combined with three NI SCXI1102C Multiplexer Boards. Live quality control is enabled with displays of shot gathers and brute stacks. Triggering of the sources and the recording system is controlled with a custom made 16 channel trigger generator. A mobile AsterX RTK GPS-system positioned at the aft of the research vessel close to the towed equipment is the basis for the time synchronization and positioning. The reference datum was set to WGS84 and both time synchronization and records were distributed via ethernet in the laboratory.

2.1.2 Source Strength and Directivity Measurements

Directivity estimates are particularly important as such angle dependent source strength variations potentially mask AVA effects. The directivity of both seismic sources, the micro-GI airgun and the AADS400 sparker, has been investigated during the research expedition AL546 (Spieß et al., 2022) in 2020 and AL566 in 2021 on *R/V Alkor* (Lackschewitz & Heinitz, 2015). The experiments have been conducted with 2 kn speed through the water at water depths >20 m. Both seismic sources were towed ~ 20 m behind the ship. The Reson TC4033-3 hydrophone (S/N 616122) was fixed on a rope, which was connected to a buoy and a depressor with a depth sensor. Adjusting the length of the rope between ship to buoy and buoy to depressor, it was possible to place the hydrophone at selected depths and offsets to the sources. The exact positioning was corrected with the depth measurements at the depressor and first break picks of the seismic record. Digitalization was conducted with a 24 bit Texas Instruments Analog-to-Digital Converter whose recordings were triggered by the gun control unit. Data were stored in SEGY-format with MaMuCS (Dr. Hanno Keil, University of Bremen). At least 30 shots were averaged for each depth-offset position.

For calibrated measurements, the source strength and signal shape of the micro-GI airgun has been investigated during the research expedition AL581 on *R/V Alkor* (Lackschewitz & Heinitz, 2015) in September 2022 in the Baltic Sea at a water depth of about 22 m to 25 m. The micro-GI airgun was towed ~ 20 m behind the ship and a calibrated hydrophone with a linear sensitivity of $4.7 \cdot 10^{-5}$ V/Pa in the frequency range of interest was placed in the near field of the source (Reson TC4033-3, S/N 616122). The hydrophone was digitized with a USB-oscilloscope at 100 kHz with a maximum resolution of 0.02 V. The experiment consisted of four runs in which increasing air pressures supplied to the source from 60 bar to 140 bar were tested. A total of 10 repetitions were executed for each run and mean values for each run are reported here, which were converted to pressure $[p] = 1$ Pa. To characterize the signal, the Peak Sound Pressure Level $[SPL_{peak}] = 1$ dB (re $1 \mu\text{Pa}$) relative to the reference pressure for water $p_0 = 10^{-6}$ Pa was calculated.

The primary, calibrated source characteristics of the Applied Acoustics Dura-Spark UHD 400 Sparker (AADS400) sparker were investigated during a harbour test at the Fischereihafen Bremerhaven (Germany, 53.5165°N 008.5748°E) in March 2022. At the test location, the brackish water is ~ 6 m deep. The AADS400 sparker was deployed via a crane at ~ 5 m distance to the harbour wall. A calibrated hydrophone with a linear sensitivity in the frequency range of interest of $4.2 \cdot 10^{-5}$ V/Pa supplied by Applied Acoustics was mounted with ropes vertically below the centre of the tip array at 1 m distance. The hydrophone was digitized with an USB-oscilloscope at ~ 4.8 MHz with 0.04 V resolution. The experiment included eleven runs in which the different

discharge energies from 375 to 2000 J were tested. A total of 32 repetitions were executed for each run and mean values for each run were converted to pressure. To characterize the signal, the normalized amplitude spectrum was determined and SPL_{peak} was calculated.

2.1.3 Seismic Data Processing

Seismic data processing has been conducted with GLOBE Claritas (initially started with version 7.3.2, later updated to version 2023.1.1) aided by various custom programs. After data import, initial quality control has been conducted on shot and constant offset gathers. As illustrated in Figure 2-3A, a shot gather includes all recorded time series (traces) of a single shot sorted by the offset or channel number representing the position in the streamer. In a constant offset gather as displayed in Figure 2-3B and Figure 2-4A, in contrast, all traces of one particular channel of the whole a seismic line are gathered. In those seismic sort orders, noise, e.g., caused by the ship or the birds and dead channels can be easily identified. During the pre-processing, dead channels and noisy channels have been deleted.

Then, the custom program WinGeoApp (Version 2019.03, Dr. Hanno Keil, University of Bremen) has been used to merge the navigation records to the seismic data and calculate the lay-back geometry. Initial binning with a Common Mid Point spacing of 1.0 m has been performed. Figure 2-3C shows, that after Normal Move Out (NMO) correction, reflection events in CMPs should be flattened. The velocity in the water column can be estimated from the direct wave with a linear move out velocity analysis, NMO velocity analysis or is known from direct measurements, so there is little uncertainty. Therefore, it can be assumed that relative shifts of traces inside a CMP after NMO correction are due to the vertical movement of the streamer in the water column, e.g., due to waves. So, after a first pass of semblance velocity analysis and Normal Move Out (NMO) correction, statics were corrected with the average static correction method (Gutowski et al., 2002). For the further processing, the initial NMO correction has been inverted after the static correction. Comparing Figure 2-4B with C the effect of the static correction with a better focusing of the main reflectors and a reduced, relative noise level can be observed.

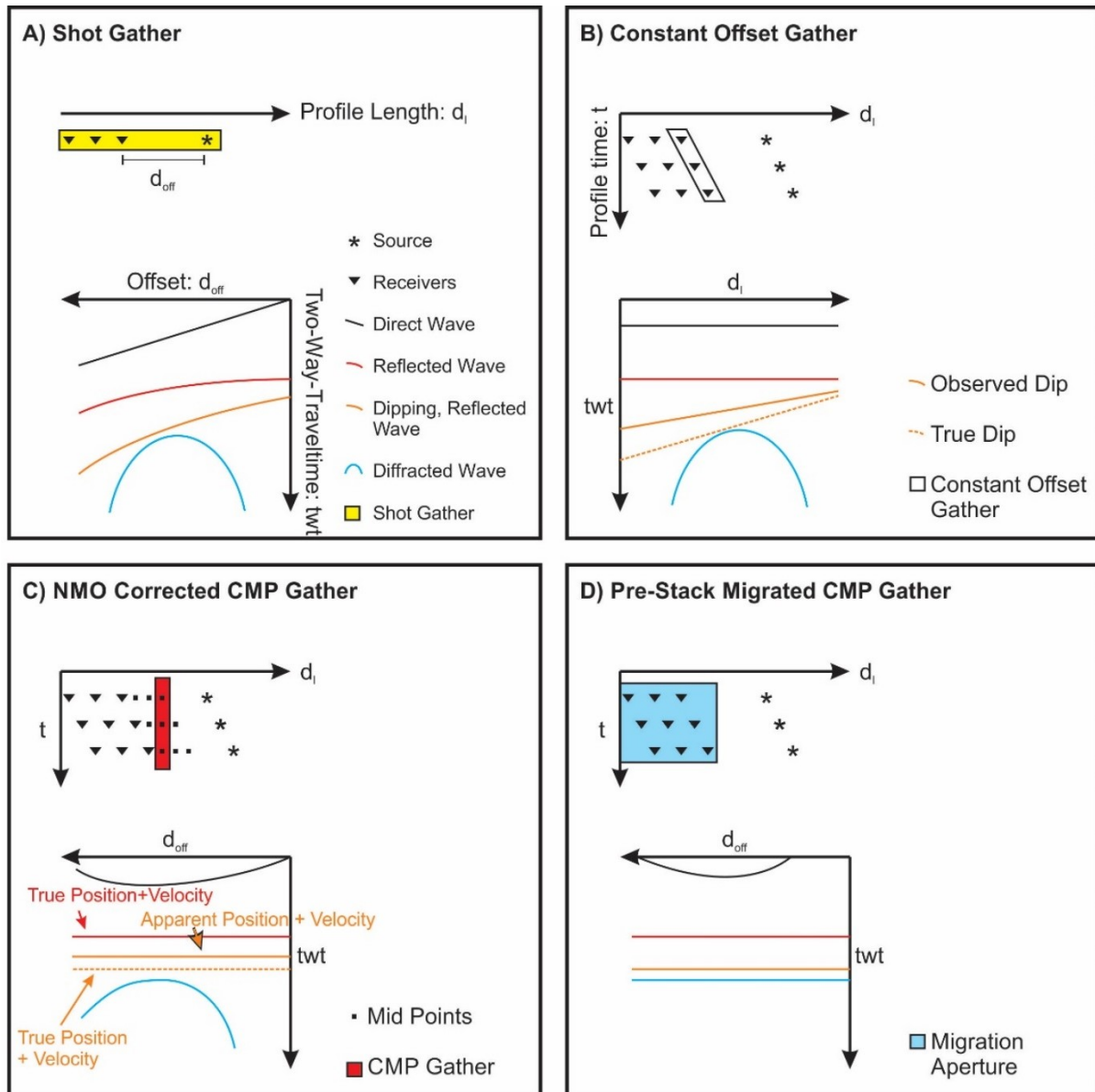


Figure 2-3: Illustration of data spaces to visualize seismic data for processing and quality control purposes and the effect of important processing steps. A) Shot gather in which all channels for one shot of the seismic source sorted by source-receiver distance (offset d_{off}) or by channel number are displayed. Events such as the direct wave, or backscattered waves appear at the uncorrected Two-Way-Traveltime TWT . B) Constant offset gathers display the traces of one channel for a number of consecutive shots along the length of a profile d_i . The seismic events appear at the uncorrected TWT . Dipping reflected and diffractions events appear not at the true position. C) Assuming that reflection originate from the midpoint between source-receiver pairs, all traces whose midpoints falls within a certain section of the profile are collected in Common Mid Point (CMP) gathers. When the Normal Move Out (NMO) is corrected, reflection events from horizontal reflectors appear at the true subsurface position and are flattened using true average velocity. The NMO velocity of dipping events, in contrast, is not equivalent to the average velocity to the reflector and dipping reflectors are not positioned at the true subsurface location by NMO correction. The assumption that the midpoint is the reflection point is violated for dipping reflectors. Stacking describes the summation of all traces inside a CMP to determine the average trace. With post-stack migration, dipping reflectors are moved to their true subsurface position. D) With pre-stack migration, all traces within a certain distance also called aperture around a CMP are gathered and all backscattering events are corrected to their true subsurface position.

As the streamer has been towed shallowly (compare Table 4-1), no ghost notch appears in the frequency range of the source signal. But due to the shallow water depth, the seafloor multiples are problematic. Especially in Figure 2-4B and C, a strong first and second seafloor multiple can be observed. The multiples are superimposed on the reflection image and mask the deeper part of the section. Thus, a multiple model has been generated and subtraction in a first pass as proposed by Wang (2003). Three additional passes of multiple model subtraction based on Monk (1993) are done for the full trace, 25 ms gates and 10 ms gates. After multiple suppression, the imaging below the first seafloor multiple is enhanced as shown in Figure 2-4D and E. The repicking of the velocity after multiple suppression and static corrections further improves the imaging and the suppression of the multiple. The second pass velocity model was also used for spherical divergence and Normal Move Out (NMO) correction before stacking. Furthermore, the data has been re-binned to 10 m CMP spacing. A second pass of velocity analysis was performed. After the processing of the seismic data (Figure 2-4E), the imaging is enhanced and small scale features such as the channel incisions and a second reversed polarity reflector in the deeper section can be differentiated. Due to the large dips, the tunnel valley flanks are poorly imaged and pre-stack migration (see Figure 2-3D) would be necessary for further improvements.

For the later impedance inversion, the CMP gathers were restricted to 0-30° incidence angles before stacking to avoid the influence of Amplitude Versus Angle (AVA) effects. The resulting stack was filtered with a Butterworth bandpass filter with filter flanks of 20-40-900-1800 Hz. For the final imaging, the stacked data has been post-stack migrated with a F-D-migration algorithm using a smoothed interval velocity model determined from the second pass velocity analysis.

A different processing approach was followed to obtain wavelets for the AADS400 and micro-GI extracted from the seafloor reflection. For this purpose, a layback geometry was set and the data has been binned to a CMP grid with a spacing of 6 m equalling approximately the shot point distance. At this stage a debias correction, spherical divergence correction, trace balancing to get an average amplitude of one in a window of 25-50 ms and Butterworth bandpass filtering (Filter flanks: 10-20-900-1800 for the micro-GI airgun and 80-160-2000-3800 for the AADS400 sparker) was applied. A Normal Move Out (NMO) correction based on a first pass, interactive semblance and stacking velocity analysis has been performed with a 70% stretch mute and a 20 ms taper. Statics were corrected with the average static correction method (Gutowski et al., 2002). After static correction, the CMP gathers were stacked with unity normalization. The seafloor was then flattened to 10 ms and an estimate of the wavelet at the seafloor was obtained by stacking 500 CMP stacks after flattening.

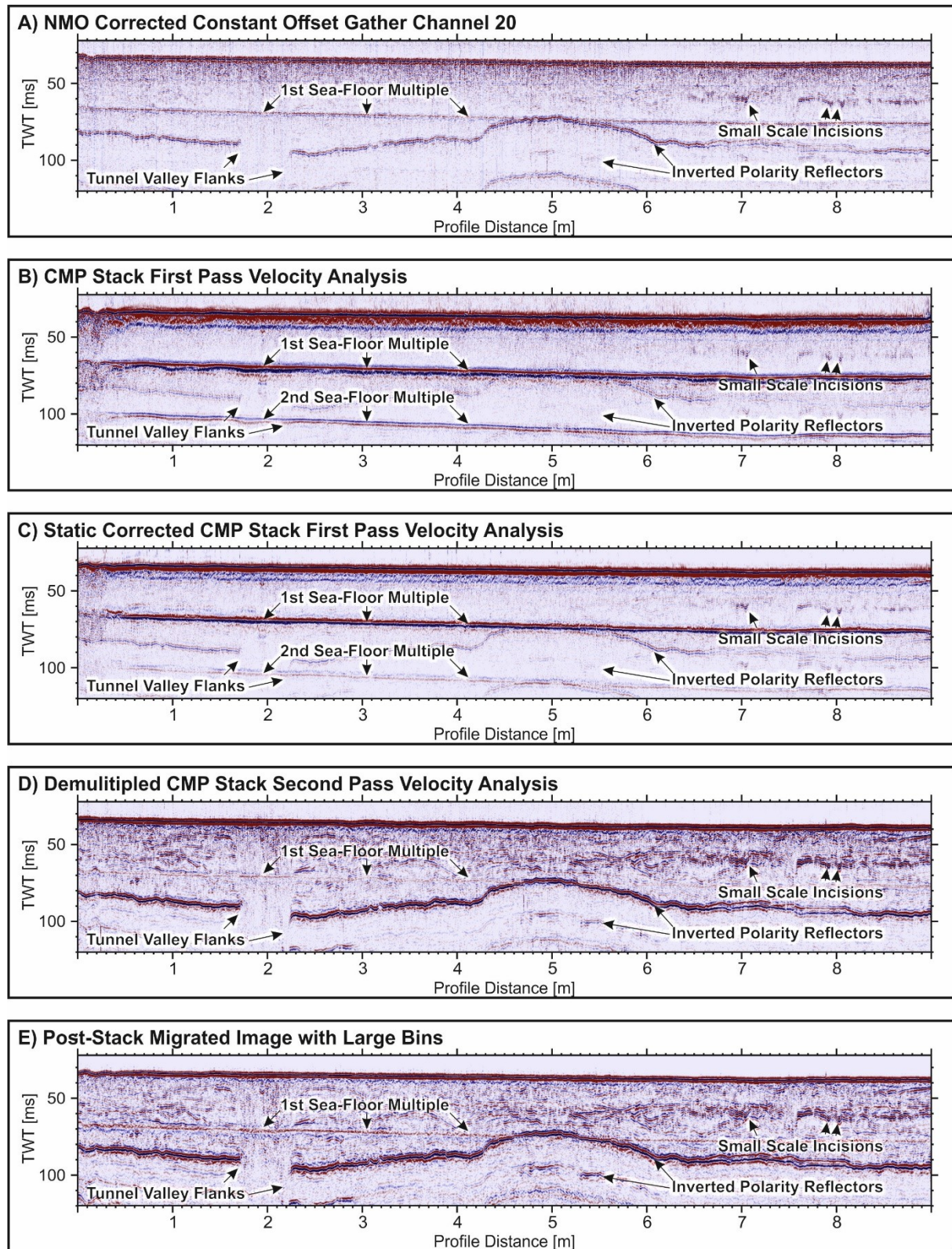


Figure 2-4: Effect of the seismic data processing on the Profile He569-GeoB21-033 in terms of the suppression of the seafloor multiples, the enhancement of the reflections, suppression of noise and correction to the true subsurface position. To allow for a better comparison of the relative amplitudes, an Automatic Gain Control in a 200 ms window has been applied and then the seismic sections are scaled to the same amplitudes. For further details on the principles refer to Figure 2-3 and for further processing details refer to the main text (Section “2.1.3 Seismic Data Processing”). The panels from A-E reflect the enhancement of the seismic image with progress in the processing flow.

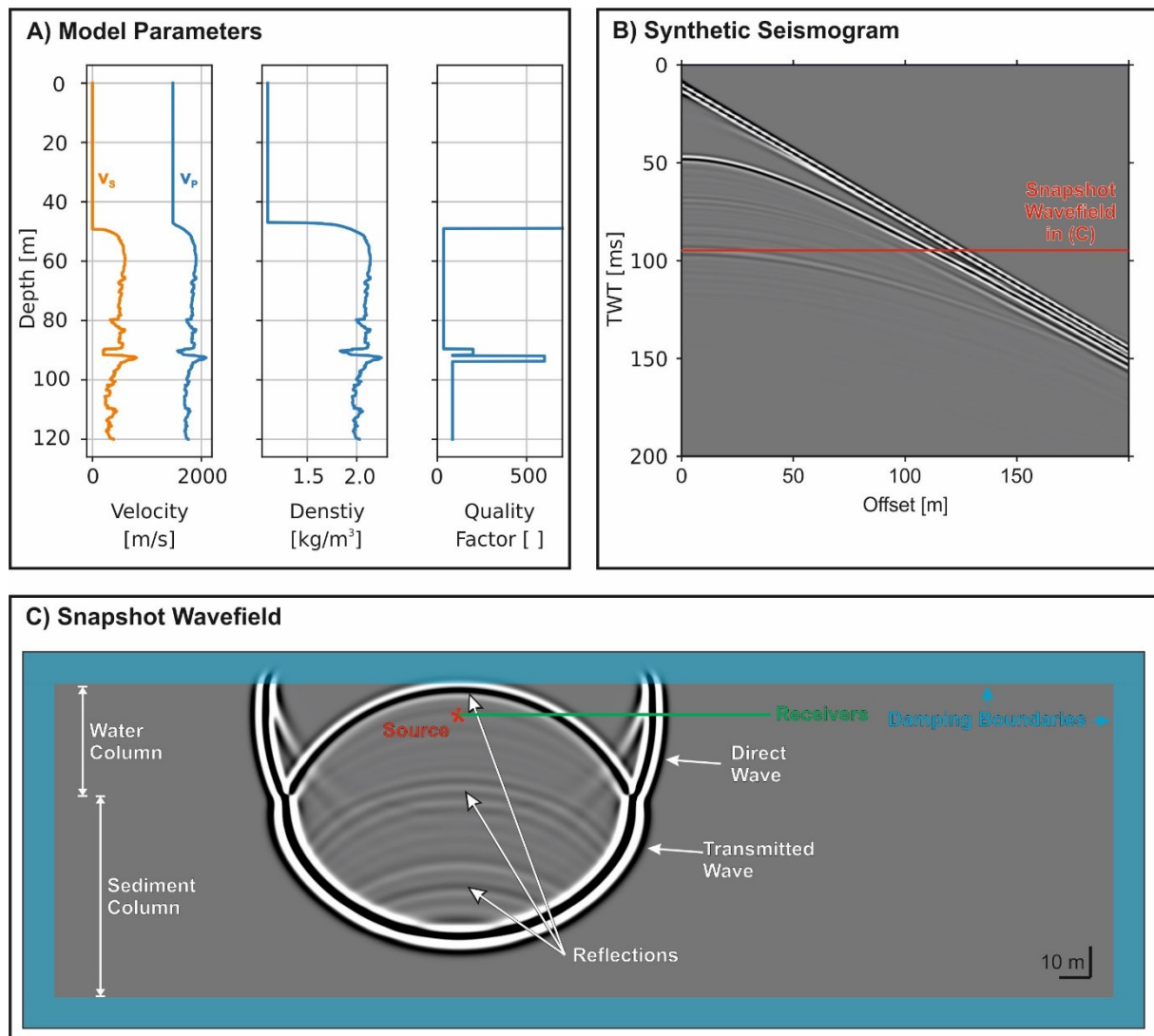


Figure 2-5: Synthetic seismogram generation with SOFI2D for a 250 Hz Ricker wavelet. A) Model parameters for the visco-elastic modelling defined by the P-Wave velocity v_p , the S-Wave velocity v_s , density, and attenuation quality factor Q . B) Synthetic seismogram calculated with the model parameters in (A). C) Annotated snapshot of the wavefield at approximately 95 ms. Damping model boundaries are implemented with a width of about 10 m. Thus, the source and the receivers are placed in a depth of 20 m and the model region is extended beyond the area of interest to avoid model edge artefacts.

2.1.4 Synthetic Seismograms

The 2D finite differences modelling algorithm SOFI2D (<https://git.scc.kit.edu/GPIAG-Software/SOFI2D>) based on Bohlen (2002) has been used to generate synthetic seismograms for the tests of inversion algorithms. Both elastic and viscoelastic models as shown in Figure 2-5 have been run. To be able to run arbitrary model geometries, a script was prepared to supply the input grids of v_p , v_s , ρ , and $Q_p = Q_s$. For the current application horizontal layering is assumed and the properties vary only vertically. The minimum v_s has been fixed to 100 m/s for the modelling. This minimum velocity is the limiting factor for the modelling. For the modelling to be stable, the model resolution had to be set to 0.04 m and 0.01 ms for modelling 250 Hz Ricker wavelets, and 0.025 m

and 0.0045 ms for 750 Hz Ricker wavelets respectively. As shown in Figure 1-2, v_s can be as low as 50-60 m/s. Halving the minimum velocity in the model from 100 m/s to 50 m/s would result in factor eight larger computational demand as both the vertical and horizontal as well as the temporal resolution would need to be two times finer (compare Bohlen, 2002). As shown in Figure 2-5C, the modelling region has been extended to avoid the appearance of edge artefacts in the seismic record. The model boundaries were set to be damping with a damping factor of 3% per grid cell and a width of 10 m.

2.2 Seismic Inversion

In the following, the general principles of seismic inversion methods used are described. Further details on the impedance inversion are found in Chapter 4 and in Chapter 5 for the pre-stack inversion.

2.2.1 Travel Time Curve Inversion

Based on identified reflections, it is the result of travel time curve inversion to provide a blocky interval velocity model of v_p , in this study primarily to derive a low frequency model. Such model is also valuable for processing of the seismic data. This effort is necessary, as it has been found, that, e.g., the conventional Dix formula is not accurate enough (Cameron et al., 2008). Also, a probabilistic or stochastic approach allowing the quantification of uncertainty is highly desirable.

Three different methods to calculate travel time curves have been implemented. As given in Yilmaz (2001) and if the velocity varies only vertically, the conventional second order NMO equation as given in Equation 2-1 can be used to calculate travel time curves. The NMO velocity v_{NMO} can be approximated by the Root-Mean-Square velocity v_{RMS} as given in Equation 2-2.

$$TWT_{NMO} = \sqrt{TWT_0^2 + \frac{off^2}{v_{NMO}^2}}$$

Equation 2-1

$$v_{NMO} \approx v_{RMS} = \sqrt{\frac{\sum_{n=1}^N v_{i,n}^2 \cdot \Delta TWT_n}{\sum_{n=1}^N \Delta TWT_n}}$$

Equation 2-2

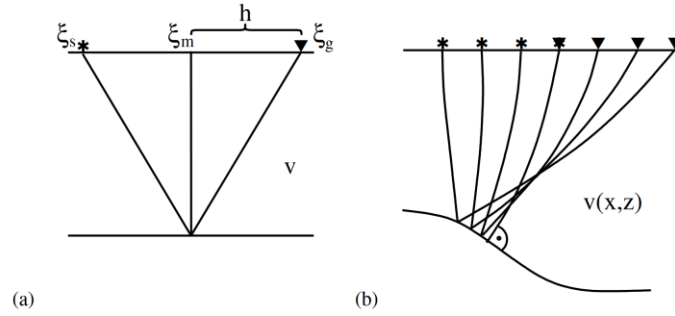


Figure 2-6: Graphic representation of travel time curve calculation methods taken from Duveneck (2004). A) The travel time for a plane reflector depending on the offset $h = \text{off}$ in a homogenous medium with P-Wave velocity v is exactly described by Equation 2-1. B) The travel time curve for a curved, dipping reflector in a smooth laterally inhomogeneous medium with the P-Wave velocity $v(x, z)$ is described by Equation 2-3.

Assuming, that the backscattering response is locally continuous across several traces in the CMP direction, a Common Reflection Surface stack operator can be used to calculate the travel time curves of dipping events (Jäger et al., 2001; Hertweck et al., 2004; Duveneck, 2004). Following the simplification of Barros et al. (2015), the CRS travel time TWT_{CRS} can be determined by Equation 2-3, which depends on both the offset off and the distance h_{md} of the trace midpoint to the CMP position investigated.

$$TWT_{CRS} = \sqrt{(TWT_0 + a \cdot h_{md})^2 + b \cdot h_{md}^2 + c \cdot h_{off}^2}$$

$$h_{off} = \frac{\text{off}}{2}$$

$$a = \frac{2 \sin(\alpha)}{v_0}$$

$$b = \frac{2 \cdot TWT_0 \cdot \cos(\alpha)^2}{v_0 \cdot R_n}$$

$$c = \frac{4}{v_{NMO}^2}$$

Equation 2-3

As a third option, a ray-shooting algorithm has been implemented. This algorithm is based on Margrave & Lamoureux (2019). Similar to Figure 2-6A, a stack of homogenous layers is assumed, and the source and receivers are placed on the surface of the stack. For the computation it is advantage to determine the equivalent one-way raypath as shown in Figure 2-7.

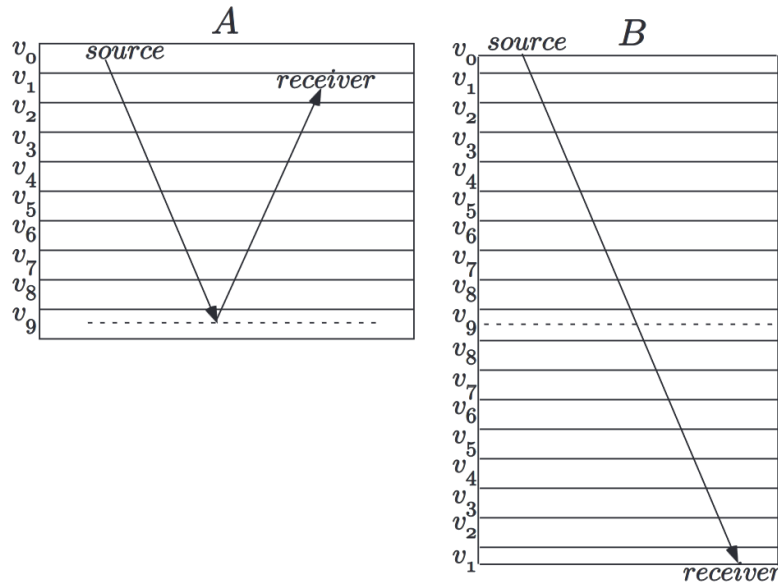


Figure 2-7: Illustration of the equivalent one-way raypath in a stack of laterally homogenous layers for a P-P reflection at the location of the dashed line taken from Margrave & Lamoureux (2019). A) Source-Receiver raypath for a P-P reflection. B) Equivalent one-way raypath to the two-way raypath shown in (A).

As a ray passes through the stack, the ray parameter given in Equation 2-4 remains constant. With known $v_p(z)$ and an initial angle θ_0 , the emergence distance which is equivalent to *off* and the two-way traveltime *TWT* of the equivalent one-way raypath can be determined.

$$p = \frac{\sin\theta_0}{v_{p,0}} = \frac{\sin\theta}{v}$$

Equation 2-4

As the contrasts in v_p and thus the degree of refraction is usually small, the initial angle θ_0 can be approximated with the offset *off*. To find *TWT(off)*, a fan of rays around θ_0 is calculated. Based on this fan, θ_0 is updated until the desired *off* is reached within the desired accuracy.

The input to the velocity model building are picks of travel time curves. The aim of the travel time curve inversion is then to estimate a v_i model based on the picks with a forward modelling as described above. As there are only a few layers are used as an input, the inverse problem is suited for stochastic global optimization schemes. For the travel-time curve inversion, a differential evolution genetic algorithm originally proposed by Storn & Price (1997) and adopted for CRS by Barros et al. (2015) has been implemented as shown in Figure 2-8. At the start of the optimization, a population of N_p individuals of randomly initialized models $v_p(z)$ is initiated. For the initialisation, random velocity and depth values of the layer boundaries are set within expected

limits. Then, the optimization loop starts and begins with the calculation of synthetic travel time curves as discussed above for every individual in the population of models. The L_2 -norm is calculated to compare the synthetic and the picked travel time curves. Based on the error, the individuals are optimized with a differential evolution scheme and a new generation of synthetic travel time curves is calculated. This procedure continues until a stopping criterion is reached. Two possible stopping criteria are implemented. On the one hand, a number of iterations is used. On the other hand the standard deviation of the model population is determined and iteration stops, when the models are within a set limit. The final model is determined from the population of optimized models by determining the mean value of $v_p(z)$ considering the best fitting models.

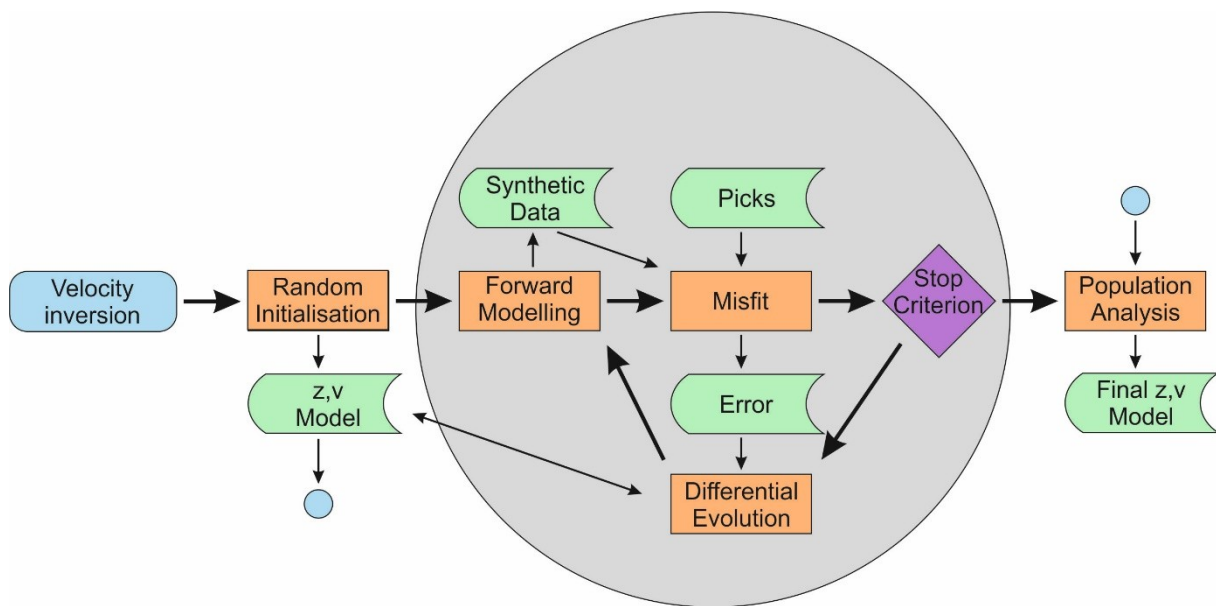


Figure 2-8: Optimization procedure for the travel time curve inversion. As a starting point, a number of random velocity v and depth z models is initiated. Then synthetic travel time curves are calculated for every individual in the population of models and compared to the picked travel time curves. Based on the error, the individuals are optimized with a differential evolution scheme and a new generation of synthetic travel time curves is calculated. This procedure continues until a stopping criterion is reached. The final model is determined from the population of optimized models.

The differential evolution, as described by Storn & Price (1997) and Barros et al. (2015), optimizes the model population with three steps mimicking natural evolution processes: Mutation, crossover, and selection. For the mutation, three different models $m_{G,r_{1-3}}$ of the population of generation G are chosen. The mutated model of the new generation is determined by Equation 2-5 with the constant mutation factor f_m . The mutation is performed for N_p members to make a new population.

$$m_{G+1,mut} = m_{G,r_1} + f_m(m_{G,r_2} - m_{G,r_3})$$

Equation 2-5

In the following crossover, a crossover probability P is calculated for all elements in m_G . Single elements of m_G are then replaced by $m_{G+1,mut}$, if P is smaller than a set threshold value termed crossover probability and the crossover population $m_{G+1,co}$ is determined. In the final selection step, the misfit of m_G is compared to $m_{G+1,co}$ and the new population m_{G+1} is constituted of the individuals with the smaller misfit.

2.2.2 Attenuation

For the attenuation estimation it is assumed, that Q can be estimated from the change of the wavelet with distance or TWT . Due to interferences and noise it is a non-trivial problem to estimate the shape of the wavelet. To reduce the effect of interference, the spectra can be calculated from averaged and normalized (normalization: $\hat{X} = \frac{X}{|X|}$) autocorrelations across a set number of CMPs with time windows at the seafloor A_{SF} and at a horizon A_{refl} , as proposed by Schock et al. (1989). Using this approach, the phase information of the wavelet is lost, which is not supposed to be problematic, as only the frequency content will be used.

To estimate Q it is assumed, that A_{refl} is equivalent to A_{SF} multiplied with a loss function A_{loss} . For the determination of A_{loss} it is a common approximation, that attenuation is independent of the frequency, hence $Q = const$ within homogenous layers and thus the frequency dependent loss due to attenuation can be determined by Equation 2-6 (Bickel & Natarajan, 1985; Yilmaz, 2001; Dondurur, 2018).

$$A_{refl} = A_{SF} \cdot A_{loss}$$

$$A_{loss} = e^{-\pi \cdot f \cdot \Delta TWT / Q_{ave}}$$

Equation 2-6

In Equation 2-6, ΔTWT is the travel time which a wave needs to pass a certain interval and Q_{ave} is the average attenuation in this interval. If this interval is composed of a stack of N homogenous layers, the interval Quality Factor $Q_{i,n}$ relates to Q_{ave} by Equation 2-7 (Y. Wang, 2004).

$$\frac{1}{Q_{ave}} = \frac{1}{TWT} \sum_{n=1}^N \frac{\Delta TWT_i}{Q_{i,n}}$$

Equation 2-7

The final Q -estimation follows the idea of Merouane and Yilmaz (2017), but has been adopted to use the autocorrelations of single seismic events as an input. The core concept of the method is to determine a range of theoretically possible Q_{ave} values and calculate the theoretic spectra $\widehat{A}_{SF} \cdot A_{loss}(Q_{ave})$ of the reflection event for the range of Q_{ave} . The misfit between the theoretic spectra and the observed spectrum is determined by Equation 2-8.

$$L(Q_{ave}) = \sum_{f=f_{min}}^{f_{max}} [\{\widehat{A}_{SF} \cdot A_{loss}(Q_{ave})\} - \widehat{A}_{refl}]^2 / N_f$$

Equation 2-8

The best estimate of Q_{ave} is found at the minimum of this error function and the Probability Density Function (PDF) to determine uncertainties is given by (Sen & Stoffa, 1992; Vardy, 2015):

$$PDF(Q) = \frac{\sum_{q=Q_{min}}^{Q_{max}} L_q}{L(Q)}$$

Equation 2-9

It follows from Equation 2-6, that the gain to correct the attenuation effect $G(TWT)$ can be calculated by Equation 2-10.

$$G(TWT) = \frac{1}{A_{loss}(TWT)} = e^{\pi \cdot f \cdot TWT / Q_{ave}(TWT)}$$

Equation 2-10

For high frequencies, the attenuation, A_{loss} approaches zero and hence G becomes large. If G is large, but there the seismic signal is below the noise, the noise instead of the seismic signal will be boosted. Therefore, it is useful to implement a damping function as given by Aster et al. (2013a) and Provenzano et al. (2020) with a damping constant p_G as given in Equation 2-11.

$$G_{damp}(TWT) = \frac{A_{loss}^2(TWT)}{A_{loss}^2(TWT) + p_G} \cdot \frac{1}{A_{loss}(TWT)}$$

Equation 2-11

The proposed method can be applied both on pre- and post-stack data. If applied to pre-stack data, ΔTWT needs to be corrected to reflect the travel time through the subseafloor. It follows from the geometric relationship assuming straight rays, that corrected ΔTWT can be approximated by Equation 2-12 with the picked time $TWT_{horz}(off)$ and the zero-offset seafloor reflection time $WT_{sf}(off = 0)$.

$$\Delta TWT = TWT_{horz}(off) - \frac{TWT_{horz}(off) \cdot TWT_{sf}(off = 0)}{TWT_{horz}(off = 0)}$$

Equation 2-12

2.2.3 Band-Limited Impedance Inversion

For the Band-Limited Impedance Inversion, an adoption of the inversion scheme by Vardy (2015) has been implemented. The general optimization procedure is shown in Figure 2-9, in which every stacked trace of each CMP is inverted independently. First, a population of N_p reflectivity models is initiated. To achieve a sparse initialisation, a random number vector with numbers in the range [0,1] is generated for every individual. If the random number is smaller than a set limit termed reflector probability, a random reflectivity within the range of expected values is initiated at the specific location of the individual. So, if the time vector spans 100 ms at a sample rate of 4000 Hz, the time and the reflectivity vectors have a length of 400. At a probability of 5%, in average 20 reflectors are initialized at random times and with random reflectivity for every trace.

Then, the optimisation loop starts, which is repeated until a set number of iterations is reached. Inside the optimization loop, synthetic seismic data are calculated for every individual of the population by static convolution. As a measure of the misfit to the observed stacked data, the L_1 norm (see Equation 1-2) is calculated. Similar to the Differential Evolution scheme described in “2.2.1 Travel Time Curve Inversion” optimization by means of selection, crossover, and mutation takes place. The stochastic remainder scheme is employed as a selection method, in which first a new model space is initiated. Then, all better than average models are directly inserted to this model space. The remaining spaces are filled at random. For the crossover operation, random pairs of individuals are chosen. By a set probability, a randomly defined section of the individuals is replaced by the partnered individual. In the mutation operation, a random vector with elements in the range [0,1] is initiated. If the random number is smaller than the set mutation probability, the element in the vector is replaced by a randomly chosen reflectivity. After this optimization, the final model is

determined from the population of optimized models and the impedance is calculated from the reflectivity rearranging Equation 1-6.

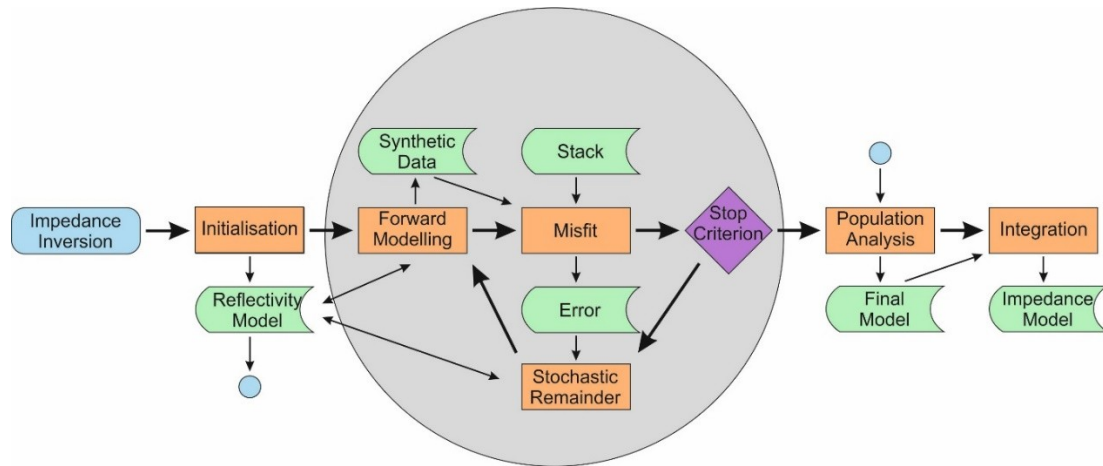


Figure 2-9: Optimization procedure for the impedance inversion. Every stacked trace of each CMP is inverted independently. As a starting point, a number of random reflectivity models is initiated. Then synthetic data is calculated for every individual in the population of models and compared to stacked data. Based on the error, the individuals are optimized with a stochastic remainder scheme. This procedure continues until a stopping criterion is reached. The final model is determined from the population of optimized models and the impedance is calculated from the reflectivity.

2.2.4 Low Frequency Model Merging

After the band-limited impedance inversion, two major problems can occur. On the one hand, the low frequency trend is missing and certain gradients such as the compaction gradient are invisible to the seismic record. On the other hand, the seismic records are usually not calibrated. So, neither the pressure emitted at the source nor the absolute pressure values are necessarily known. The seismic processing is also often not tailored to conserve the absolute amplitudes. To compensate for these problems, the Band-Limited IMPedance inversion (BLIMP) algorithm based on Ferguson & Margrave (1996) and described in greater detail in Lloyd (2013) has been implemented. According to Ferguson & Margrave (1996), the main components of the algorithm are scaling within a selected frequency band and merging of two different inputs in the frequency domain with a low-pass filtering of the low frequency trend and a high-pass filtering on the band-limited impedance. Before the transformation into the frequency domain, the linear trend of the estimated low frequency model and band-limited impedance is subtracted. The detrended results are then transformed to the frequency domain. Analysing the amplitude spectra, a frequency range is to be selected, in which both the low frequency model as well as the band-limited impedance contain usable signal. In this frequency range, the L_2 -norms of both spectra are calculated. The scaling factor is given by the ratio of the norms. To merge the low frequency model with the band-

limited inversion a characteristic frequency within the previously identified overlap region should be defined. After the filtering, the calculated scaler is applied and the inputs are transformed back into the time domain. The impedance with restored low frequency content is the sum of the filtered inputs plus the linear trend of the low frequency model.

In initial implementations filtering artefacts such as ringing and the unproportional enhancement of the frequency band in the overlap region occurred. Thus, the low and high pass filtering had to be adopted. It was found that a filter function has to be used, which does not cause filter artefacts and fulfils the criterion, that the sum of the filters is equal to 1. If the latter criterion was not met, the resulting spectrum would be distorted in the overlap region. A Linkwitz-Riley crossover filter of the second order is constructed by two cascading Butterworth filters of the second order fulfilling both criteria (Linkwitz, 1978) and has thus been implemented.

2.2.5 Pre-Stack Inversion

There are a number of strategies for pre-stack inversion as introduced in section “1.2.3 Pre-Stack Inversion”. In the following, an approach is developed in which the observed data are corrected until only the AVA effect causes the amplitude variation on the gathers. Then, a model is inverted to explain the observed AVA effects with a workflow as given in in Figure 1-9. While a general description is given in the following, further details can be found in Chapter 5.

To prepare the observed data, a CRS travel time curve inversion as shown in “2.2.1 Travel Time Curve Inversion” and an attenuation correction as given in “2.2.2 Attenuation” is conducted. With the determined velocity model, angle stacks are calculated. A near angle stack can be used for impedance inversion as explained in “2.2.3 Band-Limited Impedance Inversion”. Empiric relations as shown in Figure 1-2 are then used to first determine the low frequency impedance trend and then second to define a v_p, v_s, ρ starting model from the final impedance inversion results. The angle stacks are corrected for angle dependent source strength variations (see “Source Strength and Directivity Measurements Source Strength and Directivity Measurements” for details on the measurements) and spherical divergence. For the spherical divergence correction, an offset-

dependent geometrical spreading correction function $g(TWT_0, off)$ as given in Equation 2-13 is multiplied with the trace after projection to zero offset using the approach of Ursin (1990).

$$g(TWT_0, off)^2 = g(TWT_0, off = 0 m)^2 + \left[2 \cdot \left(\frac{v_{RMS}}{v_0} \right)^2 - 1 \right] \cdot off^2 + \frac{1}{TWT_0^2} \cdot \left(\frac{1}{v_0^2} - \frac{1}{v_{RMS}^2} \right) \cdot off^4$$

$$g(TWT_0, off = 0 m) = \frac{TWT_0 \cdot v_{RMS}^2}{v_0}$$

Equation 2-13

Following Sheen et al. (2006) the seismic data is in general determined by Equation 2-15.

$$d = F(m)$$

Equation 2-14

For convolutional modelling, the functional to generate synthetic seismic data is given in Equation 2-15 (Dvorkin et al., 2014) in which the reflectivity can be calculated by the Zoeppritz equation as given in Equation 1-1. Figure 2-10A shows an example of such a convolutional model. The wavelet w needs to be known or estimated from the data. In case of the pre-stack inversion, the convolution needs to be done for every angle of the angle gathers.

$$F(m) = r_{pp}(m) * w$$

Equation 2-15

In case of shallow water data, NMO stretch or likewise the equivalent stretch phenomena caused by CRS or migration are a data processing artefact, which can cause inversion artefacts if it is not considered (Downton, 2005). A non-stationary convolution operator as displayed in Figure 2-10B can be introduced to include the stretch in the forward modelling. As taken from Downton and Lines (2004) and Claerbout (2010) the NMO correction, the inverse NMO correction and convolution with the wavelet can be cast in a matrix multiplication of the reflectivity vector with the matrices N , N^T , and W . Thus, the non-stationary deconvolution operator is given by NWN^T .

Thereby, N^T is the transpose of N , which is the interpolation operator mapping the $TWT(off = 0)$ to the recorded TWT .

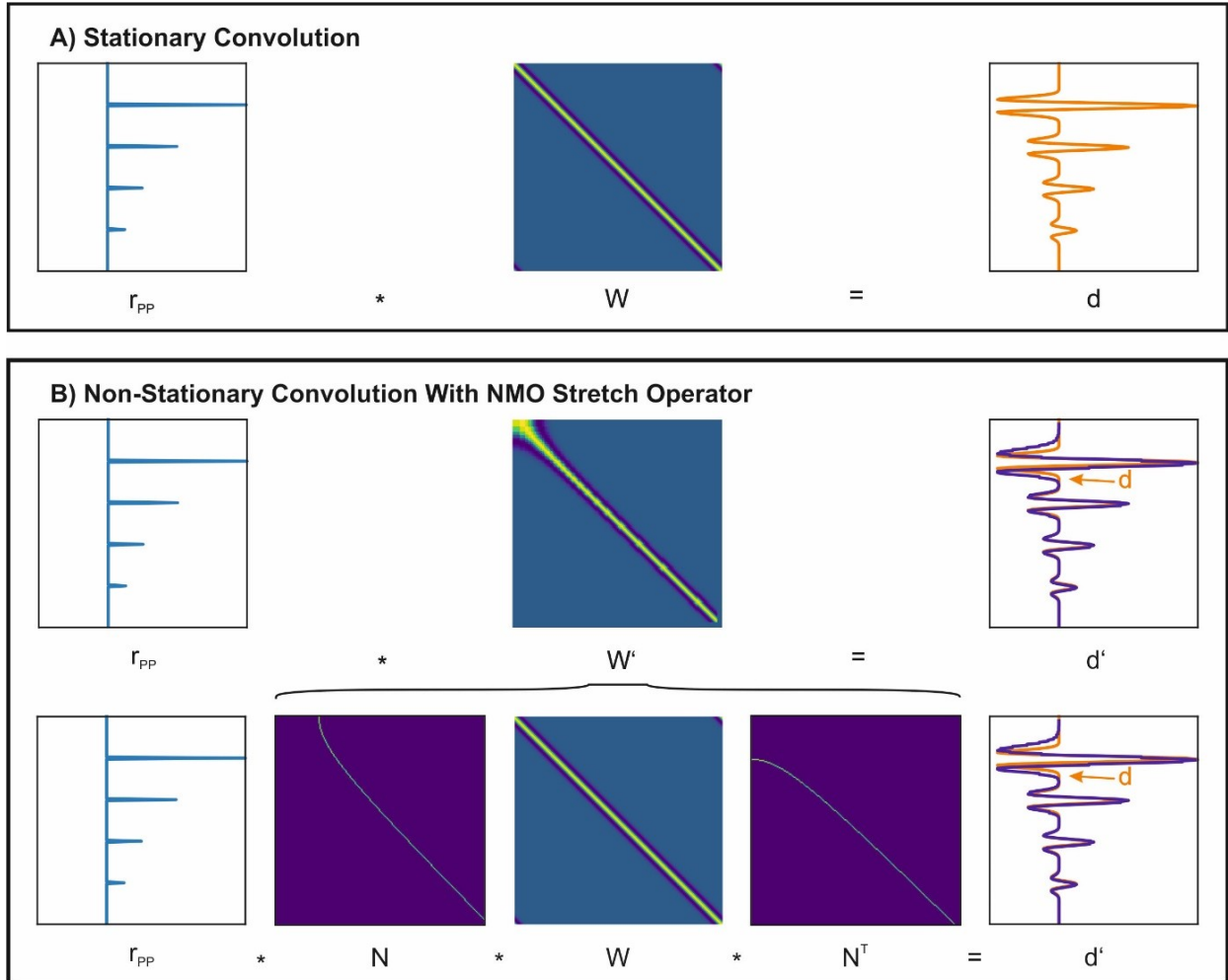


Figure 2-10: Matrix operation representation of a stationary and non-stationary convolution with a NMO stretch operator modified after Downton and Lines (2004) and Claerbout (2010). A) For a stationary convolution, the column vector of the reflectivity r_{PP} with the length of N_{TWT} time samples is multiplied with the convolution matrix of the size N_{TWT} by N_{TWT} to model the seismic trace column vector d of the length N_{TWT} . B) To approximate the seismic trace with the effect of NMO stretch d' , r_{PP} is multiplied with the convolution matrix W' which includes the stretch. The calculation of the matrix W' is based on the NMO interpolation matrix N of the size N_{TWT} by N_{TWT} . This matrix contains all zeros except for the trajectory of the NMO hyperbola being ones. The matrix for the inverse NMO correction is the transpose N^T . The non-stationary convolution matrix is calculated by the matrix multiplication of $N * W * N^T$.

The convolutional forward modelling can then be used in the inversion. Further following Sheen et al. (2006), the inversion model update function as given in Equation 1-4 can be reformulated to Equation 2-16 in which ∇S_d is the gradient of the L_2 norm of the model misfit, see Equation 1-2 and Equation 1-3.

$$m_{n+1} = m_n - \mu \cdot \nabla S_d$$

Equation 2-16

The gradient, according to Operto et al. (2013) is defined by Equation 2-17.

$$\nabla S_d = \left[\frac{\delta d_{cal}}{\delta m} \right]^T \Delta d = \sum_R \sum_{TWT} \frac{\delta d_{cal}}{\delta m} \Delta d$$

Equation 2-17

Using the approach of Provenzano et al. (2017), the gradient can be calculated discretely by a perturbation of each model parameter at all depths as given in Equation 2-18.

$$\nabla S_d(TWT) \approx \sum_R \{ [d(m_{n,p}) - d(m_n)] \cdot \Delta d \}$$

Equation 2-18

With the calculation of the step length as estimated by Equation 2-19 following Köhn (2011) or likewise Kurzmann et al. (2013) the model update can be performed.

$$\mu = p_\mu \frac{\max(m)}{\max[\nabla S_d(m)]}$$

Equation 2-19

Chapter 3 Data Acquisition Requirements and Limitations for Near Surface Reflection Seismic Inversion

Nikolas Römer-Stange¹, Hanno Keil¹, Stefan Wenau², Maximilian Merl¹, Aisgo Oguro², Carlos Ramos Córdoba², Volkhard Spieß¹

¹Department of Geosciences, University of Bremen, Klagenfurter Str. 2-4, D-28359 Bremen, Germany

²Fraunhofer Institute for Wind Energy Systems IWES, Am Fallturm 1, D-28359 Bremen, Germany

Recommended for publication in *Near Surface Geophysics* with major revisions on 2023-08-25. Format and references have been adopted to match the thesis.

Keywords

Attenuation, Data Acquisition, Density, Inversion, Modelling, Near Surface, Reflection, Seismic, Shallow Marine Shallow Subsurface, Site Characterization, Traveltime, Velocity

Abstract

Seismic inversion has the potential to play a key role for the quantitative characterization of marine near surface targets. This technique bears great benefits, but the working environment and the lithologies of interest make both the data acquisition and the inversion a challenge. Accordingly, not all acquired data sets are suitable for inversion, especially as there are no established recommendations for data acquisition tailored for near surface seismic inversion. In this study, the working environment in terms of the sediment properties and the acquisition settings are characterized for North Sea and Baltic Sea settings, and the relevant acquisition factors are identified and analysed as well as assessed in terms of their interrelations to find optimal acquisition parameters. Detailed analyses of two types of near surface seismic sources as well as sediment, source, and receiver models are described. To test the effect of acquisition artefacts and determine suitable receiver set-ups, a travel time inversion algorithm based on a genetic algorithm was developed. Furthermore, the ranges of the Amplitude Versus Angle effect for the identified target lithologies are explored to investigate the potential for shear property estimation. From those analyses, data acquisition recommendations and both implications and limitations for near surface inversion are derived. Source code and primary research data are openly accessible to allow a reproducibility of all results and to allow a transfer of knowledge to other use cases.

3.1 Introduction

Marine reflection seismic data acquisition for imaging and inversion aiming for near surface targets is both a challenging and important task. The near surface is often characterized by highly variable and small-scaled geologic features in the range of decimetres to meters and an important target, as most of the interactions of natural processes and humans with the solid earth are restricted to the first 30 m of the earth's crust (Butler, 2005). Due to those manifold interactions, the near surface is a key element to understand and mitigate climate change effects, e.g., by Carbon Capture and Storage (IPCC, 2022). Also, the uppermost 80-100 m of the marine subsurface have to be investigated for offshore infrastructure constructions such as wind energy turbines (Lesny et al., 2014; Fischer et al., 2019).

Typically, boreholes and cone penetration tests (CPT) are driven into the seafloor to assess the geotechnical properties of the ground as a basis for construction design (Fischer et al., 2019; Pein et al., 2020). This direct probing is a very time-consuming and costly method and lacks information about the 3D variability of the medium required to really understand the subsurface (Henson & Sexton, 1991). Geophysical surveys bear the potential to significantly reduce costs and risks for offshore operations through high-confidence mapping of geologic structures (Carbon Trust, 2020) or, e.g., boulders (Römer-Stange et al., 2022) in 2D profiles or 3D data cubes. Additionally, near surface reflection seismic data can be utilized to directly derive sediment properties by inversion as summarized in Vardy et al. (2017) or synthetic CPTs using geostatistical methods or machine learning (Sauvin et al., 2019; FUGRO, 2020; Pein et al., 2020).

Inversion approaches including seismic tomography can be used to gain quantitative information. The seismic inversion constitutes an optimization processes aiming to find a ground model which fits to the observed seismic data with the least error after the ground model has been transformed to synthetic seismic data by a forward modelling step (Aki et al., 1977; Bishop et al., 1985; Tarantola, 1986).

A range of algorithms is available for the seismic forward modelling, e.g., acoustic models including the parametrization of material density ρ and P-Wave velocity v_p , elastic models extending the parameter range with S-Wave velocity v_s and viscoelastic models further extending the parameter range with attenuation, e.g., quantified by the Quality Factor Q are possible (Bohlen, 2002; Thiel et al., 2019). As an alternative to the described parameters, derivatives of the parameters can be used. Convolutional acoustic models (Vardy, 2015), or

analytical elastic solutions (Fuchs & Müller, 1971; Provenzano et al., 2017) are computationally very effective. Compared to those models, Finite-Difference Models as, e.g., used in Kurzmann et al. (2013) require high computational costs, especially when low v_s and high frequencies are considered, as the grid spacing is defined by the minimum shear wavelength (Bohlen, 2002). As the real spreading of a seismic wave are very complex physical phenomena, all those forward modelling algorithms are a simplification to the reality. To allow for the application of specific seismic inversion algorithms, the raw, recorded seismic data need to be processed to meet the approximations of the forward modelling approach chosen. After sufficient processing of the raw data, the forward modelling can reproduce the recorded and processed seismic data with the correct ground model. Consequently, the choice of the forward modelling defines both the processing necessary before inversion and the parameters, which can be deduced by the inversion and make up the physical model.

Finding a best fit ground model is not a trivial problem. On the one hand, a quantitative measure of model to real data fit needs to be established. The selection of this misfit function, e.g. the L_2 -norm or a correlation factor is critical for the inversion success and, e.g., the sparsity of the solution (Fichtner, 2011). On the other hand, an optimization method in the form of a minimisation of the misfit functions needs to be selected. There are deterministic, probabilistic and stochastic algorithms for the optimization to find the best fit ground model. Deterministic, iterative optimization schemes are generally fast and simple, but prone to converge to local minima of the misfit function (Fichtner, 2011). Stochastic algorithms, in contrast, provide statistically meaningful results by testing a wide parameter range and include uncertainty estimations (Stoffa & Sen, 1991; Vardy, 2015). Depending on the inversion algorithm, starting models for the inversion also might be needed to allow for a successful optimization.

In the following, post-stack inversions, pre-stack inversions and Full Waveform Inversions (FWI) are differentiated. After seismic data processing, every vertical trace of a post-stack reflection seismic image is considered to contain a depth dependent signal and the amplitude and phase of each trace can be inverted to obtain a 1D ground model. Typically, P-Wave impedance Z_p or attenuation are derived by post-stack inversion methods (Oliveira et al., 2009; Vardy, 2015; Vanneste et al., 2015; Cevatoglu et al., 2015). Impedance is generally defined as the ratio of acoustic pressure to volume flow, thus Z_p quantifies the resistance of a system to acoustic flow resulting from acoustic pressure and is determined by the product of ρ and v_p .

Pre-stack inversions are more complex. Gathers of seismic data containing amplitude and phase information at two dimensions, e.g., depth and incidence angle of the seismic wave, are

inverted to obtain a 1D ground model at the position of the gather. Additional information such as v_S can be gained with pre-stack inversion, as the transmission, reflection, refraction and conversion of waves at interfaces depends on the incidence angle and the properties of the layers at the interface (Santoso et al., 1996; Riedel & Theilen, 2001; Sobreira et al., 2010). The relative amplitude changes of reflected P-waves depending in the incidence angle is termed the Amplitude Versus Angle (AVA) effect. Typically, the data have been processed before pre-stack inversion to correct, e.g., spreading, or attenuation phenomena, or acquisition artefacts so that the inversion only solves for the AVA effect.

For FWI, in contrast, the full wavefield is modelled and fitted to the seismic records with no or very little processing applied (Virieux & Operto, 2009). So, FWI relies on the inversion of the kinematic information of seismic data and both amplitude and phase. Similar to pre-stack inversion, ρ , v_P , v_S can be inverted, but higher resolution is gained as all wave phenomena such as diffractions, refractions, or guided waves are included in the inversion (Tarantola, 1986; Fichtner, 2011).

Besides the choice of the inversion algorithm, additional factors limit the number of parameters which can successfully be inverted for in one inversion run. Some parameters in the model have to be deduced by other means or kept constant due to inadequate data acquisition, the ill-posedness of the inversion or interrelations of parameters (Brossier et al., 2009; Virieux & Operto, 2009). Marine seismic data acquisition with towed streamers suffers from the additional limitation that S-waves are not directly recorded and thus some elastic effects will only be visible as an AVA effect (Thiel et al., 2019). Also, seismic data is band limited, i.e., frequencies from 0 Hz to the lower limit of the source spectrum and frequencies higher than source spectrum are missing. For post-stack and pre-stack inversion, the missing low frequencies have to be obtained separately, e.g. by velocity analysis or tomography or by the analysis of boreholes, to obtain absolute values with correct low frequency trends (Claerbout, 1986; Jannane et al., 1989; Mora, 1989) and have to be merged with the inversion results (Ferguson & Margrave, 1996). To make FWI computationally feasible and to avoid the trapping of the inversion at local minima, estimates of the low frequency trend are often used as a starting model for the inversion (see, e.g., Provenzano et al., 2017; Thiel et al., 2019; Tromp, 2020). The low frequency or starting model has a significant impact on the inversion results and needs to be generated carefully.

The near surface seismic data acquisition poses many acquisition challenges, as high resolution in comparison to Oil+Gas Industry surveys is needed, the records tend to contain a lot of

noise and require a significant number of near vertical incident reflection arrivals (Danbom, 2005). Also, the lithologies of interest limit the application of some inversion schemes and signal penetration due to attenuation, as the sediments are in the North Sea predominantly comprised of unconsolidated sands (Ehlers et al., 2011; Graham et al., 2011), or clays and tills overlying the chalk bedrock in the Baltic Sea (Björck, 1995; Andrén et al., 2011). Shallow gas is abundant, too (Tóth et al., 2014; Römer et al., 2017, 2021). For near surface seismics, precise positioning and static correction is necessary (Gutowski et al., 2008; Duarte et al., 2017). To achieve broadband seismic images and thus to obtain optimal resolution, reflections originating from the sea-surface, so-called ghosts, need to be removed from the record by the application of deghosting algorithms (Provenzano et al., 2020), i.e., in connection with slanted streamer towing and stable sources are needed (Monrigal et al., 2017).

Although the requirements for high quality data acquisition are high, the existing guidelines on reflection seismic data acquisition for near surface targets are mostly given in the form of minimum requirements targeted on economic site investigations. For those investigations, seismic data are acquired to gain structural images of the seafloor (Lesny et al., 2014). Commonly, those images are considered to show only qualitative information and require geotechnical ground truthing for ground model building (Cook et al., 2014). Geologic knowledge and thus information for engineering tasks is gained by geologic interpretation. Due to historic reasons, most experience with near surface investigations was gained conducting offshore drilling hazard site surveys in the Oil+Gas Industry focussing on the upper approximately 500 m of the seafloor. Consequently, the acquisition guidelines of this industry sector as given in OGP (2017) are still widely applied and standardized, e.g., in ISO 19901-10 (2021). Following this standard, the seismic reflection methods are differentiated based on their frequency content into High-Resolution (HR, 75-300 Hz), Ultra-High-Resolution (UHR, 250-800 Hz) and Ultra-Ultra-High-Resolution (UUHR, 750-2000 Hz) methods. More recently, recommendations for ground investigations for the offshore wind energy industry were published. In this context, the standard of the German Federal Maritime and Hydrographic Agency (Lesny et al., 2014) became a standard reference, at least in Europe (Fischer et al., 2019).

We identify a lack of optimum recommendations for near surface seismic data acquisition for imaging and especially inversion targeting the uppermost 100 m of the seafloor as required, e.g., for offshore wind applications. The available near surface guidelines are mostly in the form of minimum requirements for industrial surveys for offshore wind farms or the installation of other offshore infrastructures and de-risking of drillings, while optimum

requirements for structural imaging or inversion have not been defined. The established knowledge on low resolution, Oil+Gas Industry seismics and inversion with targets at kilometre range depths is not directly applicable (Vardy, 2015; Duarte et al., 2017; Monrigo et al., 2017). Additionally, relatively few inversion examples from the near surface exist and in general most inversion efforts are focussed on deep targets for the Oil+Gas Industry. Also, the interdependence of the acquisition parameters although a major factor, has not been properly considered.

Therefore, this manuscript thus aims to answer the questions: Which inversion techniques are suitable and which requirements on seismic data acquisition need to be fulfilled to successfully perform inversion on near surface, targeting the uppermost 80-100 m of the subseafloor for soil characterization in a North Sea or Baltic Sea geologic setting? To answer those questions, sediment properties are analysed, field measurements of near surface seismic sources are collected, and numerical experiments are conducted. The results were brought into context with the relevant literature to give a technical discussion on optimal acquisition settings for near surface seismic inversion.

3.2 Material and Methods

As a first step, literature data on sediment properties were collected and compared to modelled properties. This data compilation served three main aims. First, realistic sediment properties were extracted for the synthetic data generation. Second, the resolution of the parameters necessary to gain knowledge from the inversion results was analysed. Finally, the assumptions on which some inversion techniques are based were tested against the sediment properties. Furthermore, field measurements and models of two typical seismic sources are presented to characterize the acquisition set-up and investigate the influence of the sources on the inversion. Then synthetic experiments are conducted to investigate the general acquisition set-up and particularly the receiver set-up necessary to successfully conduct inversion. Furthermore, AVA curves for typical lithology contrasts are analysed to investigate the requirements to invert for shear properties.

Modelling of receiver configurations are documented in the appendix “C.1 Receiver Configuration Modelling”. Those analyses are included to support the discussion, but largely reproduce established knowledge and are thus omitted from the main body.

3.2.1 Sediment Properties

To be able to tailor data acquisition and subsequent inversion to the investigation target, geophysical parameters were brought into relation to the CPT Soil Behaviour Types (SBT) for near surface sediments of the North Sea and Baltic Sea. The descriptions and initial density ρ as well as porosity ϕ ranges are taken from Robertson (2009) and Robertson & Cabal (2015). Those values are complemented with average values of core and logging data of ρ , ϕ as well as P- and S-wave velocity v_p , v_s taken from the BSH Pinta Database (2021) for the German offshore wind farm areas N0307, N0308 and O0103. The velocity estimates for organic soils and clays have been taken from Breitzke (1997), in which the elastic wave propagation in sediment cores has been investigated with ultrasound.

Literature values from Pinson et al. (2008) are added as field measurements of the attenuation Quality-Factor Q , which is assumed to be frequency independent. These measured values are contrasted with modelled data based on the Biot-Stoll model as described in the appendix “C.2 Biot-Stoll Modelling”. Biot-Stoll-modelling allowed for an estimation of frequency dependent attenuation quantified by Q and the characteristic frequency f_Q .

Based on the parameters described above, the characteristic values v_p/v_s ratio, P-Impedance $Z_P = \rho \cdot v_p$ and Poisson's ratio $\nu_{PR} = \frac{(v_p/v_s)^2 - 2}{2(v_p/v_s)^2 - 2}$ are calculated for sediment characterisation.

3.2.2 Source Characteristics

Two examples for typical seismic sources for near surface investigations, a Sercel mini-Generator Injector (GI) airgun with reduced chamber volume and an Applied Acoustics Dura-Spark UHD 400 (AADS400) sparker, are investigated in detail to estimate the influence of sources on the inversion. For this purpose, three experiments have been conducted to measure source characteristics and directivity. A calibrated hydrophone was used to derive the Peak Sound Pressure Level $[SPL_{peak}] = 1 \text{ dB (re } 1 \mu\text{Pa)}$ relative to the reference pressure for water $p_0 = 10^{-6} \text{ Pa}$:

$$SPL_{peak} = 20 \cdot \log_{10} \left(\frac{\max|p|}{p_0} \right)$$

Equation 3-1

Those calibrated pressure data have also been used to determine the normalized amplitude spectra of the wavelets (Python Numpy FFT package). To estimate the directivity of the sources, a hydrophone was positioned at varying incidence angles and depths relative to the sources during a stationary experiment on an offshore survey. The spatial pattern in signal strength and shape as a function of incidence angle is then analysed and modelled. Furthermore, the 2D reflection seismic Profile GeoB21-033 has been collected shooting the two sources in an alternating mode to compare the two sources directly in a realistic setting. Further technical details of the sources, the measurements and analysis are given in “2.1 Seismic Data”. The theoretical basis of the resolution calculations based on the determined source characteristics is given in the appendix “C.2 Biot-Stoll Modelling”.

3.2.3 Traveltime Curve Inversion

To test the potential effects of errors in source delay estimation, offset distribution, and positioning, traveltime curve inversion experiments were conducted (see “2.2.1 Travel Time Curve Inversion” for further details on the experiments). In this context, source delay describes a constant time shift of the recorded seismograms relative to the initiation of the seismic source signal, e.g., due to the mechanism of the signal generation or delays in the synchronisation of the source control.

In this inversion experiment, an acquisition set-up including potential acquisition errors is defined, then synthetic traveltime picks are determined, which are then inverted for interval velocity and depth. For the optimization, a differential evolution global optimization algorithm described in Barros et al. (2015) and the L_2 -norm as a misfit function are used. Initial traveltime calculations for the inversion are done with raytracing based on a ray shooting algorithm described in Margrave & Lamoreux (2019). The synthetic traveltime picks are inverted with a second order NMO equation including a Root Mean Square (RMS) velocity estimate. A dual metric to stop the optimization algorithm including a convergence criterion and a maximum number of generations of 5000 is established. Convergence is defined to be reached when the mean standard deviation of the velocity population is smaller than 5.0 m/s.

The true velocity model for the travel time curve inversion experiments is a model with six layers with stepwise increasing P-wave velocities (Figure 3-1). Source delay artefacts were introduced by shifting the picks of the seismic events from -10.0 ms to +10.0 ms in steps of 1.0 ms. In the second experiment, systematic positioning errors were evaluated adding a constant error from -10 m to +10 m to the offsets in steps of 1.0 m. Thirdly, random errors

for the positioning for individual receivers were implemented by adding a randomly generated number in the range of $-R$ to $+R$ to the offsets and increasing the maximum absolute error R from 0.0 m to 10.0 m in steps of 0.5 m.

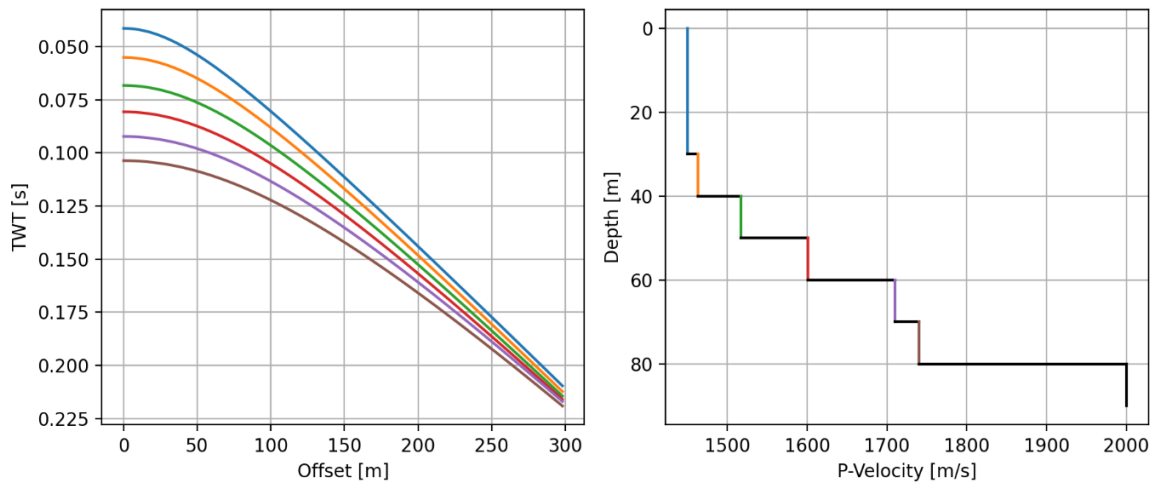


Figure 3-1: Initial model for the traveltime curve inversion experiments. A) Hyperbolic traveltime curves of the Two-Way-Traveltime (TWT) plotted on an offset axis. B) Ground model including six horizontal layers of 10 m thickness of stepwise increasing velocity.

3.2.4 Amplitude Versus Angle (AVA) Curves

Another basis for the analysis of acquisition parameters for inversion is the expected range of AVA curves and the approximation of those curves. For this purpose, mean estimates of v_p , v_s and ρ for each SBT in Table 3-1 are determined. The range of expected curves is then modelled for all possible combinations of SBTs. The modelling of the curves is based on the Python package BRUGES (2015; Agile Geoscience; Bruges 0.5.4 for Python; <https://pypi.org/project/bruges/>). As only upcoming P-Waves are recorded with marine seismic streamers, the absolute amplitude of the upcoming P-wave is analysed. The Zoeppritz equation is used as a reference curve, while the Aki-Richards, the Bortfeld, the Fatti, the Hiltermann and the Shuey approximation as defined in Chopra & Castagna (2014) are compared to this reference. Pearson's Correlation Coefficient and the RMS error are calculated to give a quantitative level of fit.

3.3 Results

The basis for the acquisition optimization is first set with typical sediment properties in the North Sea and Baltic Sea and second with an analysis of seismic source characteristics. This basis then feeds into models of data acquisition and AVA effects to find suitable acquisition parameters.

3.3.1 Typical Sediment Properties in the North Sea and Baltic Sea

Assuming that the SBTs are representative of certain sediment types, geophysical parameters are attributed to those sediment types as shown in Table 3-1. From a sedimentological point of view, the trend from SBT 3 to SBT 7 represents a coarsening of the sediments from clays to sands. For those sediments, as documented in Table 3-1, ρ , v_p and v_s increase, and consequently Z_p and k increase, while ϕ decreases with increasing SBT. While v_p ($1460 \text{ m/s} < v_p < 1800 \text{ m/s}$) increases by $\sim 20\%$, ρ ($1350 \text{ kg/m}^3 < \rho < 2250 \text{ kg/m}^3$) potentially increases by 40-60% and v_s ($60 \text{ m/s} < v_s < 400 \text{ m/s}$) by a factor greater than 600%. Due to the comparatively large v_s increase, the v_p/v_s -ratio drops from 18 to 4, while v_{PR} shows only a minor decrease from 0.50 to 0.47. While little to no attenuation is expected for finer sediments with high $Q > 300$, strong attenuation is to be expected for sands at characteristic frequencies in the range of UHR and UUHR seismics. In the literature (Pinson et al., 2008), Q is assumed to be frequency independent. The Biot-Stoll modelling, in contrast, suggests, that attenuation is frequency dependent with little to no attenuation at low frequencies and minimum Q at the f_c . Also, the velocities of sandy sediments, especially SBT5-7, are dispersive. The velocity ranges in Table 3-1 for the Biot-Stoll modelling give a measure of the velocity dispersion in the frequency range of 50-4000 Hz.

SBT 1 and SBT 2 are the fine end members of the distribution with very low ρ , low v_s , v_p and Z_p , but with high ϕ . Their respective attenuation is low and outside of the frequency range of UHR and UUHR seismics.

The highest Z_p are found for SBT 8 and SBT 9 being the compacted end members. With ϕ being reduced to a minimum of 20% and low permeability, v_p and v_s can be as fast as 2340 m/s and 1000 m/s respectively. Very high Q -values are to be expected.

1 **Table 3-1: Geophysical parameters in comparison to the Cone Penetration Testing (CPT) Soil Behaviour Types (SBT) for the near surface sediments of the North Sea and**
 2 **Baltic Sea derived from (1) Robertson (2009) and Robertson & Cabal (2015); (2) BSH Pinta Database (2021) for N0307, N0308, O0103 or likewise (*) Breitzke (1997); (3)**
 3 **Biot-Stoll Modelling (Hovem et al., 1991; Badiey et al., 1998; Dvorkin et al., 1999; Breitzke, 2006; Carcione & Picotti, 2006); (4) Pinson et al. (2008).**

CPT Soil Behaviour Type		Density ρ [kg/m ³]		Porosity ϕ [%]		Permeability k [m ²]	S-Wave Velocity v_s [m/s]		P-Wave Velocity v_p [m/s]		Attenuation Parameters			Derived Seismic Parameters		
Type (1)	Name (1)	(1)	(2)	(1)	(2)	(3)	(3)	(2)	(3)	(2)	f_c [Hz] (3)	Minimum Q_p (3)	Q_p (4)	v_p/v_s []	Poisson's ratio ν_{PR} []	P-Impedance Z_P [mg/m ³ m/s]
1	Sensitive, fine grained	1300-1450		70-80		7,1E-15	40		1460		14E6	120	>300	33	0,50	1,8-2,0
2	Organic soils - clay	1300-1800	1640	50-80	70	7,1E-15	60	60-70*	1460	1460-1670*	14E6	120	>300	22	0,50	1,8-2.4
3	Clay- silty clay to clay	1350-2150	1720	30-80	60	7,1E-15	80	60-80*	1460	1460-1620*	11E6	60	>300	18	0,50	2,0-3,2
4	Silt mixtures - clayey silt to silty clay	1450-2100	1880-1940	40-70	40-50	2,3E-12	170	230	1490-1500	1660	26E3	50	50	9	0,49	2,2-3,3
5	Sand mixtures silty sand to sandy silt	1450-2200	1860-2050	30-70	30-50	2,3E-11	230-240	210-420	1560-1600	1720-1750	2.0E3	40	30	7	0,49	2,3-3,7
6	Sands - clean sand to silty sand	1500-2250	2020	30-70	40	5,4E-11	320-330	240	1650-1720	1740-1780	630	30	25	5	0,48	2,6-4,1
7	Gravelly sand to dense sand	1750-2250	1970-2030	30-60	30-40	1,0E-10	390-400	200-400	1680-1720	1730-1790	340	30	25-50	4	0,47	3,0-4,1
8	very stiff sand to clayey sand	2100-2300	2250	20-40	30	9,9E-13	1620	560	2740-2750	1920	24E3	600		2	0,26	3,4-6,6
9	Very stiff fine grained	2100-2300	1980	20-40	30-40	1, 5E-17	740	970-1000	2100	2270-2340	1.6E9	11800		3	0,43	4,4-4,8

3.3.2 Source Characteristics

Field measurements including near and far field records as well as models of source characteristics of the micro-GI airgun and the AADS400 sparker are shown and described.

Sercel micro-Generator Injector Airgun

The wavelet of the Sercel micro-GI airgun with a total volume of 0.2 l towed in approximately $d_s = 1.0$ m depth as shown in Figure 3-2 is characterized by a sharp primary pulse, which corresponds to the release of air from the Generator.

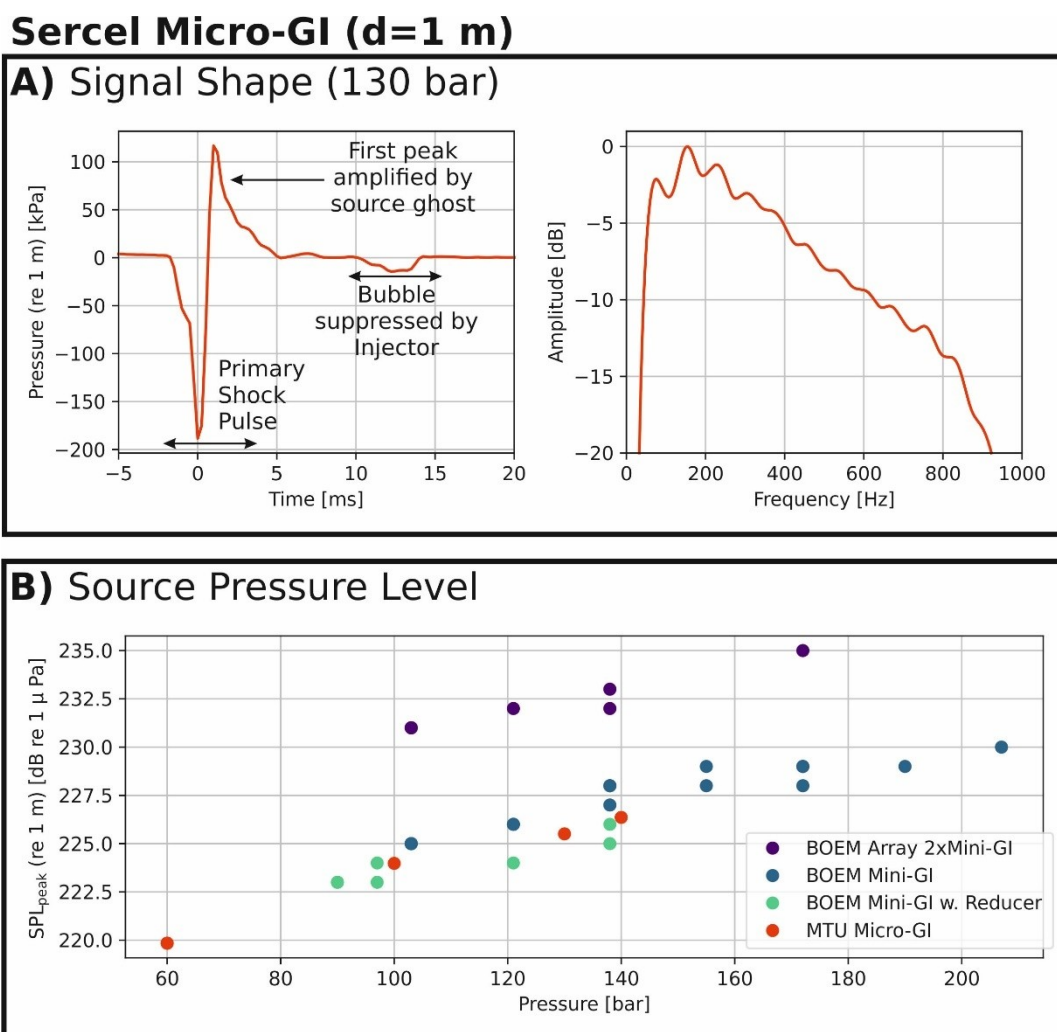


Figure 3-2: Characteristics of a Sercel micro-GI airgun with a volume of 2 x 0.1 L towed in approximately 1.0 m depth in terms of A) the signal shape in the time domain on the left side and normalized frequency spectrum on the right side. B) Peak Sound Pressure Levels (SPL_{peak}) of the Sercel micro-GI and mini-GI airguns depending on the air pressure supplied to the sources. The values for the Mini-GI airgun with 2 x 0.454 L volume, mini-GI airgun with reducers limiting the volume to 2 x 0.227 L and the array of two mini-GI airguns with a total volume of 2x (2x0.454) L are taken from Crocker & Fratantonio (2016) and Crocker et al. The SPL_{peak} of the micro-GI airgun with a volume of 2 x 0.1 L has been measured during the research expedition AL581.

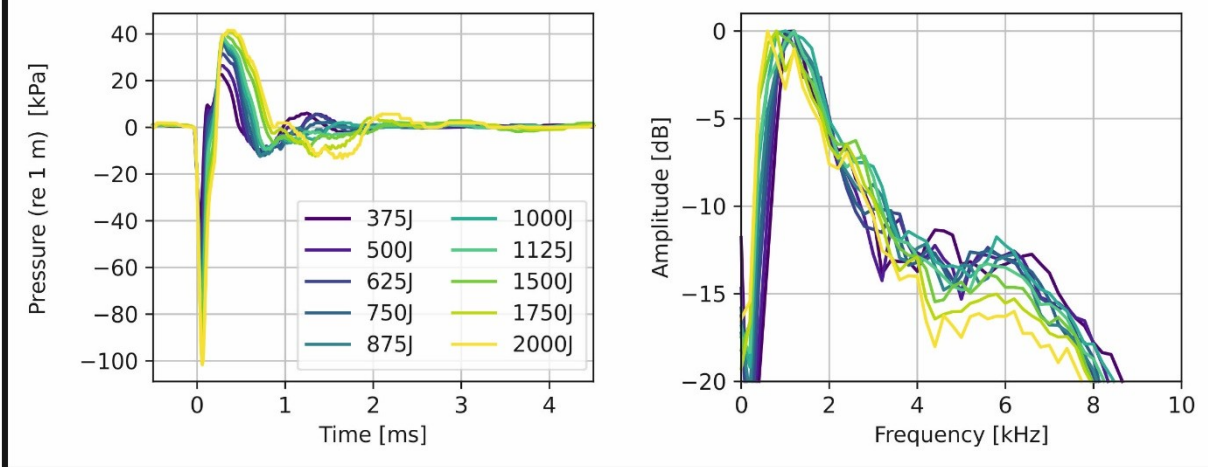
The oscillation of the released air bubble is aimed to be suppressed by the release of the Injector at 13 ms delay. At a towing depth of 1 m, the source ghost is expected at the two-way-traveltime $tw t_{ghost} = \frac{2 \cdot z_s}{v_w} = \frac{2 \text{ m}}{1500 \text{ m/s}} = 1.3 \text{ ms}$. Thus, the expected delay of the source ghost overlaps with the first peak of the primary shock pulse. The raw source spectrum peaks at 155 Hz and spans a bandwidth of 200 Hz ranging from approximately 60-260 Hz at -3 dB (Figure 3-2A). The SPL_{peak} is found to be positively correlated with the pressure supplied. A typical operation of the micro-GI airguns results in $SPL_{peak} = 225.5 \text{ dB (re } 1 \mu\text{Pa)}$ at 130 bar and $SPL_{peak} = 226.4 \text{ dB (re } 1 \mu\text{Pa)}$ at 140 bar with both measurements corrected to a reference distance of 1 m. Following Crocker & Fratantonio (2016), the measurement uncertainty is estimated at $\pm 2 \text{ dB}$. The measured SPL_{peak} shown in Figure 3-2B are in good agreement with the SPL_{peak} of a mini-GI airgun (2x0.454 L volume), a mini-GI airgun with reducers (2 x 0.227 l) and an array of two mini-GI airguns (2x[2x0.454] L) (Crocker & Fratantonio 2016; Crocker et al.,2019). Both mini-GI airguns with reducers and the micro-GI airgun emit $\sim 226 \text{ dB (re } 1 \mu\text{Pa)}$ at 140 bar, while the mini-GI airgun without reducers is $\sim 1 \text{ dB}$ louder. The array of two mini-GI airguns emits $\sim 5.5 \text{ dB}$ more than a single mini-GI airgun, which is less than expected as an increase of 6 dB equals a doubling of energy.

Applied Acoustics Dura-Spark UHD 400 Sparker

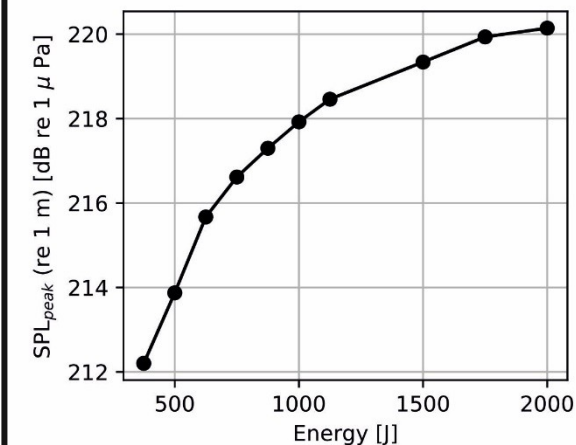
The source characteristics of the AADS400 sparker is found to vary with the supplied electric energy for signal generation. A general amplitude increase as well as an increase of the low frequency content with increasing energy from 375 J to 2000 J is observed (Figure 3-3A). So, the frequency content at the -3 dB limits changes from 900-1550 Hz at 375 J to 420-1380 Hz at 2000 J. The amplitude increase is also reflected in the emitted SPL_{peak} rising strictly monotonically from 212 dB (re 1 μ Pa) to 220 dB (re 1 μ Pa) with a decreasing slope (Figure 3-3B). Tow depth of the source has a direct effect on the signal characteristics (Figure 3-3C). The strongest amplitudes correspond to the primary shock pulse, which can be described as a sequence of a trough and a peak with an amplitude ratio of 3:2. The second pronounced event is the source ghost (Figure 3-3C). In comparison to the primary peak, the source ghost shows only about a half of the initial amplitude. At shallow tow depths, the source ghost overlaps with the peak of the primary shock pulse. After the primary shock pulse and the ghost, more low frequency reverberations occur (Figure 3-3 C).

AA DuraSpark UHD (d=0.2 m)

A) Signal Shape



B) Source Pressure Level



C) Signal Characteristics

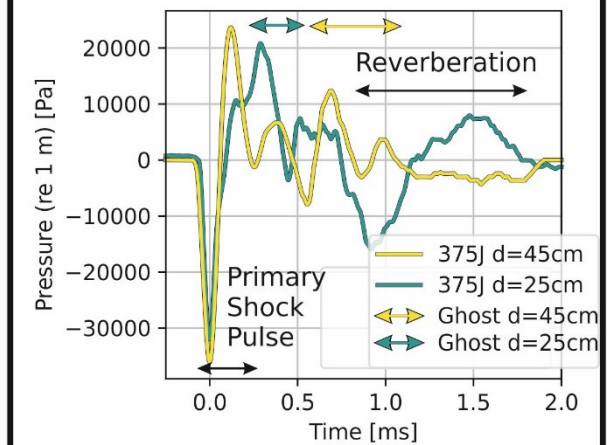


Figure 3-3: Source characteristics of an Applied Acoustics (AA) DuraSpark UHD 400 with the tip banks at 0.2 m depth. A) Signal shape in the time domain on the left and the normalized frequency spectrum on the right depending on the supplied electric energy. B) Peak Sound Pressure Level SPL_{peak} as a function of the supplied electric energy. C) Sparker signals characteristics exemplified for two different depths of the tip banks.

Directivity Measurement

Furthermore, the directivity of the micro-GI airgun and the AADS400 sparker have been investigated (Figure 3-4). In the angle gather of the micro-GI airgun, little to no directivity is observed. Correspondingly, all wavelets are characterized by the same peak frequency and the majority of the traces is also characterized by a similar spectrum. Except for the 40° wavelet, the spectra are basically equal above the -3 dB level. The 40° wavelet shows a comparatively strong high frequency content.

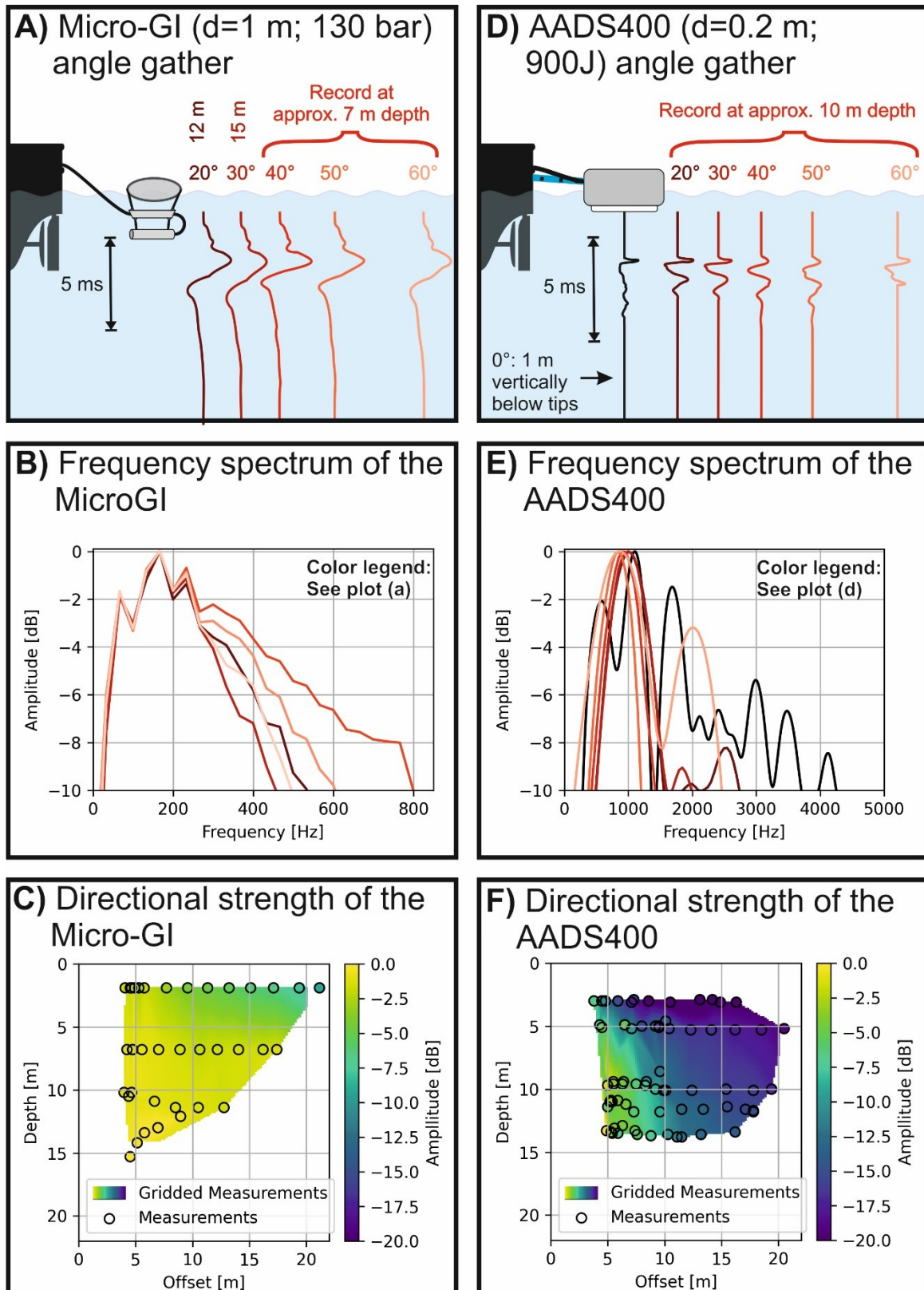


Figure 3-4: Comparison of the directivity of the Sercel micro-GI airgun and the Applied Acoustics Dura-Spark UHD 400 (AADS400). A, D) Schematic drawing of the sources towed behind a vessel (not to scale) including a normalized angle gathers of the emitted wavelets. B, E) Normalized frequency spectra of the wavelets shown above sharing the colour code. C, F) Measurements of the directional strength of the sources corrected for spherical divergence.

The measurements of the directivity of the micro-GI airgun show the amplitude normalized to the maximum value as a function of depth and along-track offset, which is the distance of the source to the hydrophone in towing direction. The micro-GI airgun appears to be only weakly directive with the -3 dB occurring approximately at an incidence angle of 70° as derived from depth and offset of the measurements. In contrast, pronounced wavelet changes are observed in the angle gathers of the AADS400 sparker. In Figure 3-4D, the relative amplitude decrease of the leading wavelet minimum in comparison to the low frequency reverberations with increasing incidence angle is especially noticeable. In the frequency domain, this decrease corresponds to a lower bandwidth and a decreasing high frequency content (Figure 3-4E). The peak frequency drops from approximately 1100 Hz at vertical incidence to approximately 850 Hz at 60° . Overall, the AADS400 sparker appears to be strongly directive exceeding a signal strength decrease of -20 dB at high angles (Figure 3-4F).

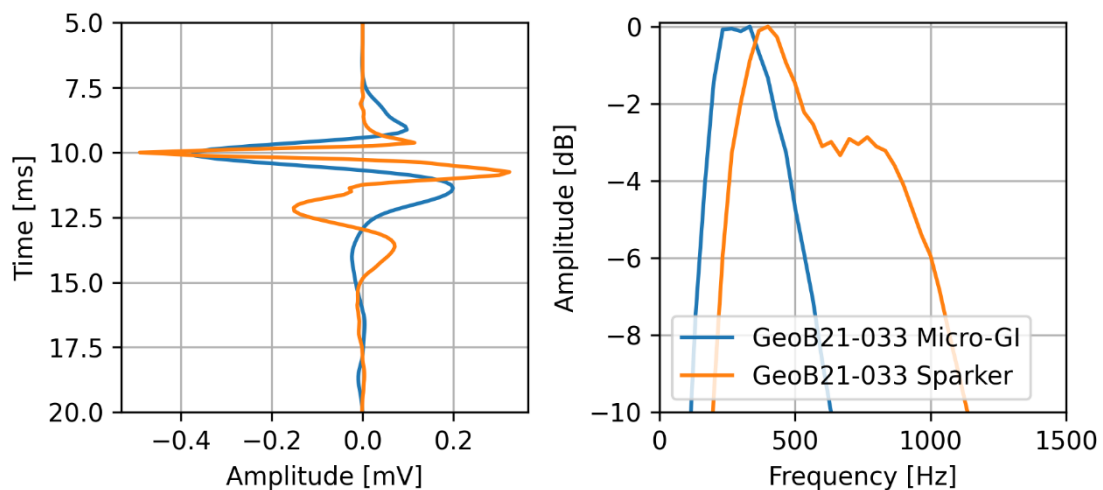


Figure 3-5: Wavelets of the Sercel micro-GI airgun and the Applied Acoustics Dura-Spark UHD 400 sparker extracted of the seafloor reflection of Profile He569-GeoB21-033. A) Time series of the wavelets. B) Normalized frequency spectra.

Field Measurements He569-GeoB21-033

The source signature of the wavelet in a seismic record is of particular interest. The extraction of the wavelet at the seafloor is one possibility to retrieve this signature. Compared to the near field measurements presented before, the seafloor wavelet is a measurement in the far field, includes the effect of the receiver ghost and is affected by processing. The time series of the micro-GI airgun wavelet (Figure 3-5A) is close to the shape of a minimum phase wavelet with $f_c = 330$ Hz and a bandwidth of 280 Hz ranging from 180-460 Hz at -3 dB (Figure 3-5B). Determining the inflection

points (see appendix “C.2 Biot-Stoll Modelling”), a temporal resolution of $T_{res} = 0.9$ ms with $f_d = 400$ Hz is determined. Also, the AADS400 sparker time series resembles a minimum phase wavelet, but the wavelet appears to be longer although the central lobe is less wide. The increased resolution of the main lobe is reflected in the properties of the wavelet with $f_c = 400$ Hz (270-590 Hz at -3 dB), $f_d = 890$ Hz and $T_{res} = 0.38$ ms.

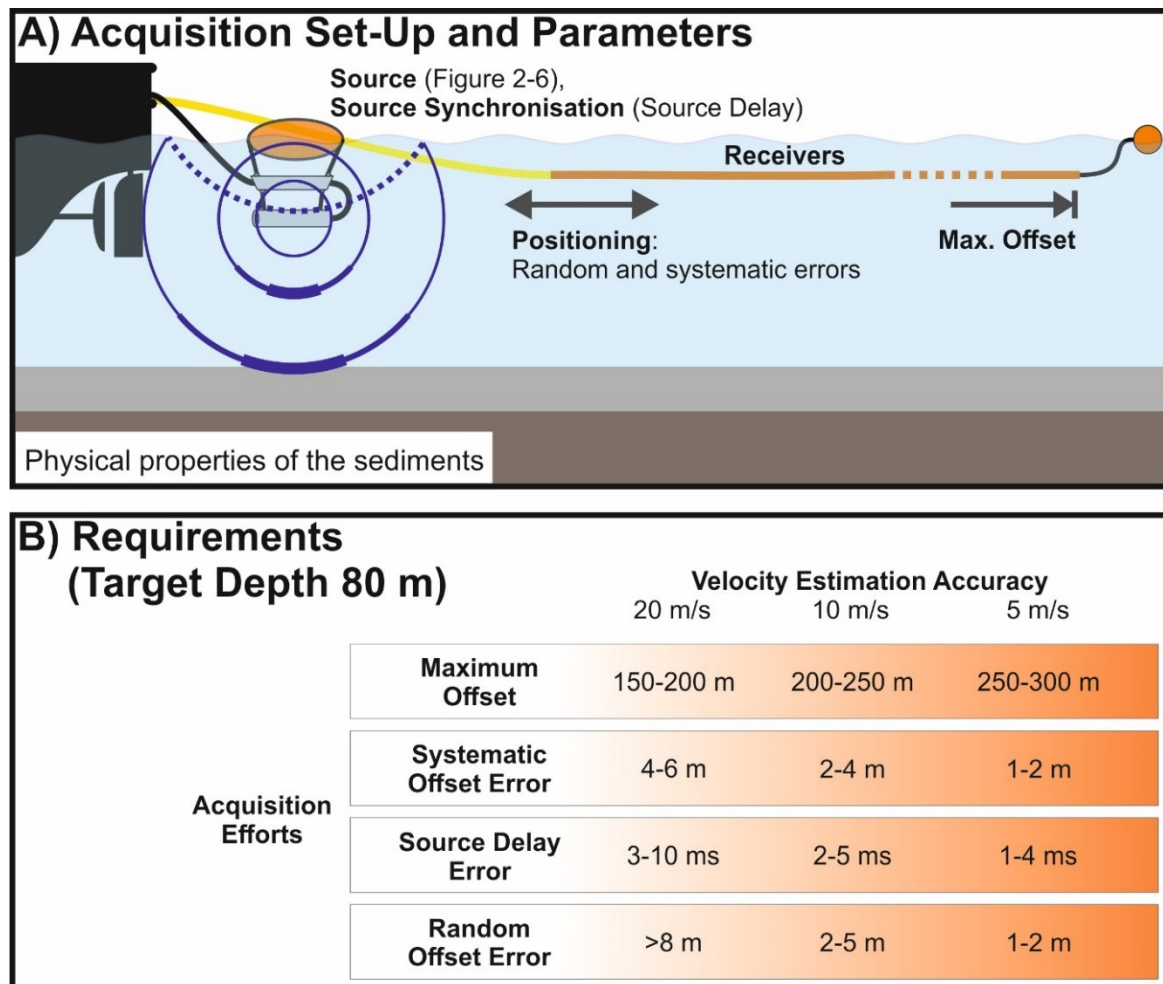


Figure 3-6: Schematic illustration of relevant acquisition parameters for near surface seismic inversion and the impact of the acquisition efforts on the velocity estimation accuracy. A) Acquisition setting for near surface seismics with a seismic source depicted as a micro-GI airgun in this case and a streamer towed behind a vessel. The references in the illustration link to figures in which the parameter is discussed. B) Impact of acquisition parameters and efforts on the traveltime curve inversion accuracy.

3.3.3 Traveltime Curve Inversion

Parameters connected to the reception of the seismic signal generated are in the focus of the numerical experiments described below. Relevant parameters include the maximum offsets available, positioning limitations by random and systematic errors as well as incorrect source delay

correction (Figure 3-6A). It was investigated to which accuracy the true velocity model can be reproduced when a certain error was introduced (see “2.2.1 Travel Time Curve Inversion”). It is then reported, in which error range the envisioned accuracy threshold is crossed. The genetic algorithm used for the inversion generates a population of solutions. The ranges of those populations are reported. In some cases, the accuracy has been found to depend on the modelled reflector depth. In those cases, the maximum errors are reported in Figure 3-6B. For example for a maximum depth of 80 m and a velocity inversion accuracy of 20 m/s, a maximum offset of at least 150 m is necessary (Figure 3-6B). Furthermore, systematic offset errors should not exceed 4-6 m, random offset errors should be <8 m and source delays are required to be corrected to a precision of 2-5 ms. Source delay errors affect shallow layers more dramatically due to their decreasing impact on overall traveltimes for longer raypaths. For better velocity estimation accuracy, the acquisition efforts need to be increased. Accordingly, maximum offsets of 250-300 m are necessary to reach 5 m/s accuracy (Figure 3-6B). Offset errors have to be reduced to <1-2 m and the source delay correction needs to be within 1-4 ms.

3.3.4 Amplitude Versus Angle (AVA) Curves

The expected range of AVA curves is an important basis for the acquisition optimization, as the AVA effect is e.g. used in pre-stack inversion or FWI to determine density or shear properties. Only if the AVA effect is significant and not masked by other effects or acquisition artifacts, more than just impedance can be estimated. In Figure 3-7, the AVA curves based on the Zoeppritz equation of all possible combinations of SBT 3-7 with comparatively low AVA effects are shown. The vertical incidence reflectivity is generally low ($r \ll 1$) with maximum values of 0.11. For these soil types, only minor changes in reflection amplitude up to 10% are observed below incidence angles of $\sim 25^\circ$ (Figure 3-7A). In the range of 25° to 58° the amplitude changes - relative to vertical incidence - by 50%, while the amplitudes change by 100% in the range of $\sim 42^\circ$ to 65° (Figure 3-7A). The critical angles are found in the range of 55° to 80° . In Figure 3-7B it is shown whether simplification to the Zoeppritz equation is defined in the angle ranges of interest and whether they are valid. All simplifications can reproduce the amplitudes at low angles $< 25^\circ$ and are defined at this range (Chopra & Castagna, 2014). It is demonstrated here that only the Aki-Richards simplification shows a very high positive correlation as well as low RMS errors for higher angles. SBT 1-2 and SBT 8-9 are the low and high v_s , v_p , ρ and Z_p endmembers of the SBT classification (Table 3-1). Consequently, these endmembers would show up as anomalies with comparatively strong AVA effects.

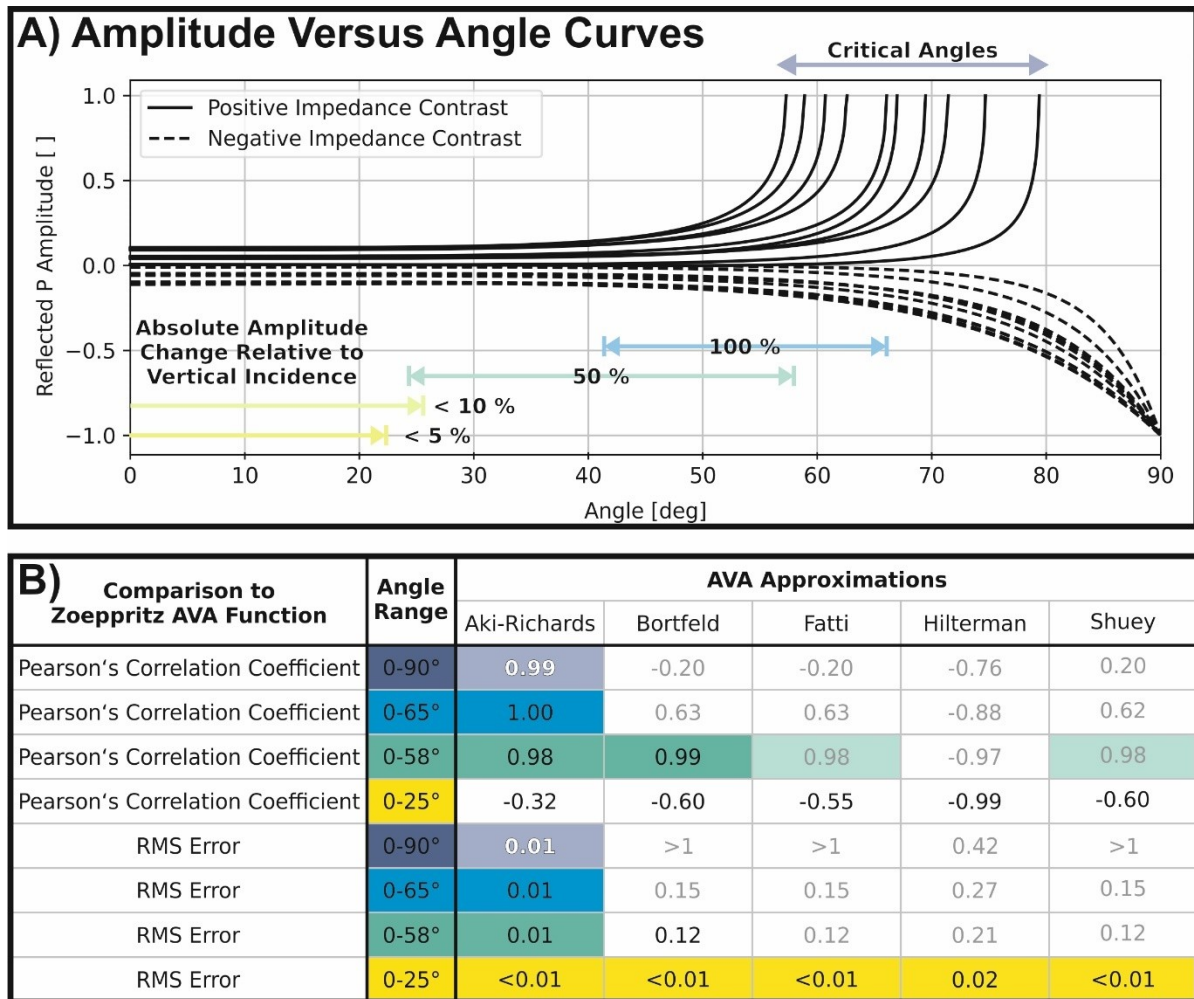


Figure 3-7: Analysis of the range of possible Amplitude Versus Angle (AVA) curves of reflected P-waves. A) Expected range of AVA curves calculated with the Zoeppritz equation for all possible interfaces between sediments of Soil Behaviour Type 3-7 taken from Table 3-1. B) Comparison of AVA simplifications to the Zoeppritz equation using the Pearson's Correlation Coefficient and the Root Mean Square (RMS) error. The simplifications are only valid to a certain maximum incidence angle according to their definition (Chopra & Castagna, 2014). Accordingly, grey numbers in the table indicate, that the simplification is invalid for the incidence angle range in the row of the table according to the literature. The coloured boxes show whether the correlation coefficient and the RMS error indicate to be valid for the soil type tested.

3.4 Discussion

To determine the requirements on data acquisition and inversion techniques for characterization of near surface sediments down to 80-100 m depth, we discuss the results for all relevant parameters introduced above. First, the necessary accuracy and to establish requirements is derived from an analysis of sediment properties. Second, seismic source characteristics are assessed to

determine resolution requirements and the applicability of a source for inversion. Then, the receiver geometry and its set-up and variability are analysed. Finally, conclusions are drawn on the implications for the acquisition and the choice of inversion techniques, and the findings are compared to and contextualized with the relevant literature.

3.4.1 Sedimentological Basis

This study is basically restricted to the range of expected sediment properties in the North Sea and Baltic Sea, and the following discussion of required parameter accuracy for inversion is guided by this regional distribution.

Properties of the Sediments in the North and Baltic Sea

Based on the geologic history of the North Sea and Baltic Sea (e.g., Björck, 1995; Andrén et al., 2011; Ehlers et al., 2011; Graham et al., 2011), we expect the Soil Behaviour Type (SBT) 3-7 to be volumetrically most abundant in the near surface of 80-100 m depth. The lithological equivalent of those SBTs range from clays to dense sands or gravelly sands. The trend of SBT 3-7 represents a general coarsening of the sediment which corresponds to a gradual decrease of porosity ϕ and hence a gradual increase in density ρ and both P-Wave velocity v_p and S-Wave velocity v_s . SBT 1 and 2 are the fine end member of the distribution and represent sensitive or organic clays as, e.g., described in Robertson (2009). Such sediments are found, e.g., in the Holocene Muds in the Baltic Sea or thin layers in the North Sea and are characterized by low ρ , v_p , v_s compared to SBT 3-7. Consequently, a layer of SBT 1 or 2 in the seismic record results in anomalously large negative P-Wave Impedance Z_p contrasts with a strong Amplitude Versus Angle (AVA) effect. Those layers are relatively easily identified in seismic sections due to their anomalous nature. As we set the aim to characterize the whole column of near surface sediments down to 80-100 m, inversion techniques have to be able to differentiate also soils of SBT 3-7 with more subtle parameter changes. Similarly for the case of SBT 8 and 9, compaction and cementation result in high ρ , v_p , v_s and hence high Z_p resulting in anomalously large positive Z_p contrasts in the seismic record.

There is a remarkable trend of strongly increasing v_s with SBT and v_p as well as ρ to be observed in Table 3-1. This trend allows for a prediction of v_s based on v_p as suggested by Lee (2006) and shown in Figure 1-2. It is also shown for fine grained sediments, that v_s can be very small in the range of 40-80 m/s. Consequently, the shear wavelengths for HR to UUHR seismic sources can be at the cm-scale. The grid resolution of Finite-Difference models has always to be smaller than the minimum shear wavelength, the exact value depends on the operators used (Bohlen, 2002). As this requirement also affects the time step for those models, which is chosen small enough to avoid

a seismic wave to travel across two adjacent grid points at the maximum seismic velocity and thus at the scale of 10^{-5} s, Finite-Difference models are computationally very demanding.

Commonly, the attenuation quality factor Q is considered to be frequency independent (see, e.g., Pinson et al., 2008; Vardy et al., 2012). The Biot-Stoll modelling, in contrast, indicates a frequency dependent Q -factor and relevant velocity dispersion for sandy soils. Although the Q -values in Table 3-1 for modelling and literature data are in fair agreement, it is unclear at this stage, what the effect of frequency dependent Q and the velocity dispersion is for the inversion.

Required Parameter Accuracy

The seismic properties v_p , v_s , ρ and Q as well as the derived parameters P to S velocity ratio $\frac{v_p}{v_s}$, Poisson's ratio ν_{PR} and Z_P (Table 3-1) are suitable to differentiate CPT soil types, as those parameters show a distinct variation. In particular, ρ and thus Z_P as well as Q , v_s and $\frac{v_p}{v_s}$ show a larger variation than v_p or ν_{PR} (see Table 3-1). Parameters with a larger variation will be better suited for soil differentiation, if they can be estimated at a sufficient accuracy from seismic data. We estimate the accuracy necessary to differentiate units SBT 3-7 from Table 3-1 as given in Table 3-2.

Table 3-2: Minimum parameter accuracy necessary for inversion to differentiate the expected Soil Behaviour Types (SBT) 3-7 given in Table 3-1. As SBT 1-2 and SBT 8-9 are characterized by comparatively larger contrasts, the accuracy restrictions to differentiate those SBTs are less strict.

Parameter	Minimum Accuracy
Δv_p	20 m/s
Δv_s	10 m/s
ΔQ	5
$\Delta v_p/v_s$	1
$\Delta \nu_{PR}$	0.01
ΔZ_P	0.1 mg/m ³ m/s

Limitations

In this analysis, SBTs are linked to a lithological equivalent and a geophysical parameter range. It is important to highlight in this context that in CPT analyses and in a strict sense a certain SBT gathers all soils responding similarly to the penetration of the cone during testing (Robertson, 2009). The values of the properties of North Sea and Baltic Sea near surface sediments (Table 3-1) are thus not representative for all possible soils of a certain SBT. In fact, the properties in the study

are associated with the recognized SBT classification. The differentiation based on a limited set of seismic properties can also be non-unique, as the ranges are relatively large and overlaps and a general positive covariance of v_p , v_s and ρ as well as a negative covariance to ϕ exists. For those overlaps Q is an important measure, as it seems to be a good grainsize indicator (Pinson et al., 2008). Maybe even more importantly, detailed geologic knowledge about the evolution of a sedimentological basin such as the North Sea and Baltic Sea can help to determine boundary conditions and exclude improbable solutions.

3.4.2 Seismic Source Considerations

Multi-tip sparkers are often used for near surface seismic applications, as they are anticipated to provide high spatial and lateral resolution. The AADS400, for example, has been used for the offshore wind farm site investigations in German territorial waters (BSH, 2021). Also, sparkers are relatively easy to use and almost maintenance free in the case of negative discharge sparkers (Rutgers & de Jong, 2003). Despite those advantages of sparkers, the practicably achievable resolution has previously been not well investigated and the applicability for inversion techniques remained to be evaluated. Therefore, we discuss the resolution of the micro-GI airgun and the AADS400 sparker as well as the advantages and disadvantages for inversion in the following.

Resolution

The selection of the seismic source is a critical decision and inherently linked to the resolution required for a certain study. In Table 3-3, we summarized the resolution ranges for ideal Ricker wavelets and for all source recordings in this study based on Kallweit & Wood (1982) with more details given in the appendix “C.2 Biot-Stoll Modelling”. Based on the frequency ranges and the resolution criterion, vertical resolution in depth D_{res} can be derived for High Resolution (HR) seismic surveys in the range of 10-2 m, for Ultra-High Resolution (UHR) seismic surveys in the range of 3-0.8 m and Ultra-Ultra-High Resolution (UUHR) seismic surveys in the range of 1-0.3 m. For the micro-GI airgun, a temporal resolution $T_{res} = 0.9$ ms which equals D_{res} of 1.3-1.6 m and a lateral resolution after migration equalling the dominant wavelength λ_d of 3-5 m is reached. No difference in T_{res} between the wavelet measured near field in the water column and the one extracted from the seafloor has been found, although the central f_c and predominant frequency f_d changes presumably as a function of the receiver ghost. For the AADS400, the wavelet extracted from the seafloor shows a stronger low frequency content than the near field measurement. This difference could be due to differences of near to far field measurements of the wavelet and the directivity of the sparker. However, also data processing effects, in particular Normal Move Out

(NMO) stretch and residual statics, have an impact on the stacking quality and thus the frequency content of the seafloor wavelet. Assuming that the seafloor wavelet is suitable to realistically estimate resolution, a vertical resolution of about $T_{res} = 0.4$ ms or $D_{res} = 0.6$ m and $\lambda_d = 2$ m can be derived. At this point, we want to stress that ideally T_{res} defined by the inflection points of the central lobe of a wavelet and f_d should be documented for any seismic survey. Those measures do provide information about the resolution of a wavelet while f_c is less relevant.

Table 3-3: Estimation of the vertical resolution in time T_{res} and depth D_{res} and the lateral resolution after migration which is equal to the dominant wavelength λ_d . Estimates are based on Kallweit and Wood (1982) as described in the appendix ‘‘C.2 Biot-Stoll Modelling’’ and given for a lower boundary with a high P-Wave velocity $v_p = 1800$ m/s and an upper boundary with $v_p = 1500$ m/s. Peak f_c and predominant f_d frequencies are reported. The classification of the sources follows ISO 19901-10 (2021) High Resolution (HR, 75-300 Hz), Ultra-High-Resolution (UHR, 250-800 Hz) and Ultra-Ultra-High-Resolution (UUHR, 750-2000 Hz).

Source		Lower Boundary $v_p = 1800$ m/s	Upper Boundary $v_p = 1500$ m/s
HR	General Range Ricker Wavelet	$f_d = 75$ Hz, $\lambda_d = 24$ m $T_{res} = \frac{1}{2.31 \cdot f_p} = 5.8$ ms $D_{res} = 10.4$ m	$f_d = 300$ Hz, $\lambda_d = 5$ m $T_{res} = \frac{1}{2.31 \cdot f_p} = 1.4$ ms $D_{res} = 2.2$ m
		$f_d = 250$ Hz, $\lambda_d = 7.2$ m $T_{res} = \frac{1}{2.31 \cdot f_p} = 1.7$ ms $D_{res} = 3.1$ m	$f_d = 800$ Hz, $\lambda_d = 1.9$ m $T_{res} = \frac{1}{2.31 \cdot f_p} = 0.54$ ms $D_{res} = 0.8$ m
UHR	Micro-GI Airgun Water Column Record (Vertical incidence, 130 bar)	$f_d = 350$ Hz, $f_c = 170$ Hz $T_{res} = 0.88$ ms	
		$\lambda_d = 5.1$ m $D_{res} = 1.6$ m	$\lambda_d = 4.3$ m $D_{res} = 1.3$ m
	Micro-GI Airgun Seafloor Wavelet He569-GeoB21-033 (130 bar)	$f_d = 440$ Hz, $f_c = 330$ Hz $T_{res} = 0.88$ ms	
		$\lambda_d = 4.1$ m $D_{res} = 1.6$ m	$\lambda_d = 3.4$ m $D_{res} = 1.3$ m
	AADS400 Sparker Seafloor Wavelet He569-GeoB21-033 (1750 J)	$f_d = 890$ Hz, $f_c = 400$ Hz $T_{res} = 0.38$ ms	
		$\lambda_d = 2.0$ m $D_{res} = 0.68$ m	$\lambda_d = 1.7$ m $D_{res} = 0.57$ m
UUHR	General Range Ricker Wavelet	$f_d = 750$ Hz, $\lambda_d = 2.4$ m $T_{res} = \frac{1}{2.31 \cdot f_p} = 0.58$ ms $D_{res} = 1.0$ m	$f_d = 2000$ Hz, $\lambda_d = 0.75$ m $T_{res} = \frac{1}{2.31 \cdot f_p} = 0.22$ ms $D_{res} = 0.32$ m
		$f_d = 2600$ Hz, $f_c = 800$ Hz $T_{res} = 0.06$ ms	
	AADS400 Sparker Water Column Record (Near Field, 1750 J)	$\lambda_d = 0.7$ m $D_{res} = 0.11$ m	$\lambda_d = 0.6$ m $D_{res} = 0.09$ m

As the wavelet effect is, e.g., removed by post-stack impedance seismic inversion, the resolution is improved. The question remains to which degree resolution is improved. One possible inversion resolution limit is the Widess' criterion, which is defined as $\lambda_d/8$ (Widess, 1973; Kallweit & Wood, 1982). If two interfaces are closer than the Widess' criterion, only the seismic amplitude changes, but not the phase of the composite reflection event. Consequently, thickness and reflection coefficient changes cannot be differentiated. For impedance inversion it has been shown (Vardy, 2015) that the wavelet effect can be removed to retrieve reflectivity profiles, and, by a following integration, to generate impedance profiles. If the Widess' criterion is not met, wavelet shape does not change and consequently the layers cannot be resolved by inversion. This assumption results in a vertical depth resolution after inversion of about 0.5 m for the micro-GI airgun and 0.25 m for the AADS400 Sparker considering the seafloor wavelet of the sparker or 0.09 m considering the near field measurement of the sparker. Vertical resolution is at an optimum at vertical incidence compared to lower incidence angles (Vermeer, 1999). Consequently, the vertical resolution is supposed to be highest for impedance inversion and lower for inversion techniques relying on lower incidence angles.

As previously introduced (see sections "3.1 Introduction") mainly Quaternary and thus glacially influenced sediments are in the focus of near surface seismic surveys in the North Sea and Baltic Sea. So, a range of landforms and scales needs to be considered. On the one hand, subglacial landforms such as drumlins, moraines, eskers and tills need are found with dimensions of few meters to tens or hundreds of meter height and few meter to several kilometre lateral extent (Menzies et al., 2018). Kames at the ice edges are typically characterized by dimensions of few meters to few tens of meters height and 50-300 m diameter (Ehlers, 2022). Ice marginal valleys are mega-scale structures such as the Elbe Paleo Valley with 210 km length and 40 km width (Özmaral et al., 2022). Tunnel valleys, which are elongated and overdeepened depressions eroded into the bedrock or unconsolidated sediment (Cofaigh, 1996; van der Vegt et al., 2012), are also very prominent features reaching several hundred meter to kilometres in width. Sander deposits formed in outwash plains and gravel terraces are extensive deposits forming the landscape at regional scale (Ehlers, 2022). Units in glaciolacustrine environments are typically characterized by decimetre to meter scale thickness but laterally widespread (Fitzsimons & Howarth, 2018). Glaciofluvial sediments can be both vertically and laterally small. Coughlan et al. (2018) report layer thicknesses of about 2 m for glaciofluvial layers. Individual units in marine or glaciomarine sediments are typically thin (sub-meter scale) but widespread, while (glacio-)marine sediment packages can reach extensive thicknesses (Jaeger & Koppes, 2016; Menzies et al., 2018). Based on this compilation of the scales and the resolution determined, we are convinced, that UHR seismic images and inversion

results are sufficient to resolve the relevant landforms as well as most internal structures. UUHR images and inversions have the potential to resolve internal structures to a higher degree. This assessment is supported by studies like Andresen et al. (2022), which show the seismic morphologies and landscapes of the Dogger Bank.

It is our understanding of the foundation design for offshore wind sites, that soil properties are determined for units at a scale of meters to tens of meters to determine geotechnical design profiles (BSH, 2021; Forsberg et al., 2022). The main components to be considered are the distributed lateral load and the vertical shear along the whole pile soil interface and the horizontal force and moment at the pile base (Burd et al., 2017). We conclude therefore, that the minimum requirement for seismic inversion methods is to resolve parameters for individual seismic units and detect anomalies such as weak layers. Their detection is important to avoid that piles end in a weak layer and basal slip is thus less likely. Therefore, we conclude that the micro-GI airgun is able to resolve the landforms of interest. By inversion, mean properties of the units could be inverted which can then feed into the foundation design.

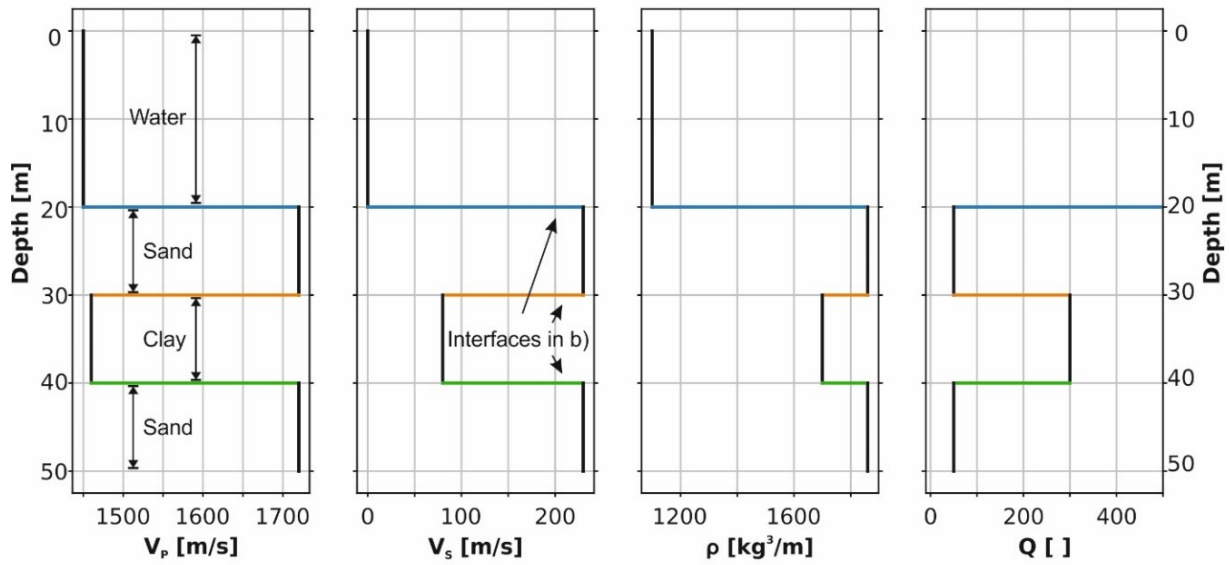
The AADS400 sparker is characterized by a higher resolution. However, we have been able to demonstrate, that the practically achievable resolution of the AADS400 is smaller than indicated by the near field records of the sparker. As results from the wavelet extracted from a real seismic record and listed in Table 3-3, the AADS400 is rather a UHR than a UUHR source, although the resolution is by a factor of two better than the Micro-GI airgun.

Source Directivity and Strength

For the micro-GI airgun, the directivity of the source is almost unidirectional compared to the AADS400 (see Figure 3-8 and section “Directivity Measurement”). So, wavelet changes can be ignored simplifying the forward modelling. The AADS400, in contrast, is a highly directive source with a 3 dB beamwidth of 8-9°. In Figure 3-7, we demonstrated that a doubling of the amplitude by AVA effects can be expected the earliest at an incidence angle of 40°. So, the amplitude effect of the sparker directivity is at least a factor 4 stronger than the AVA effect.

Due to the towing design in a catamaran-like rigid frame with double flotations, sparkers tend to pitch and roll in wavy conditions. Consequently, seismic surveys with sparkers are typically very restricted in terms of the weather and swell conditions. For inversion, a roll and pitch control of a AADS400 sparker will be necessary to correctly compensate for amplitude variations due to the strong angle dependence of emitted amplitudes. A pitch angle of a AADS400 sparker by 8° changes the received amplitudes by a factor of two causing artifacts in the inversion.

A) Ground Model



B) Amplitude Effect

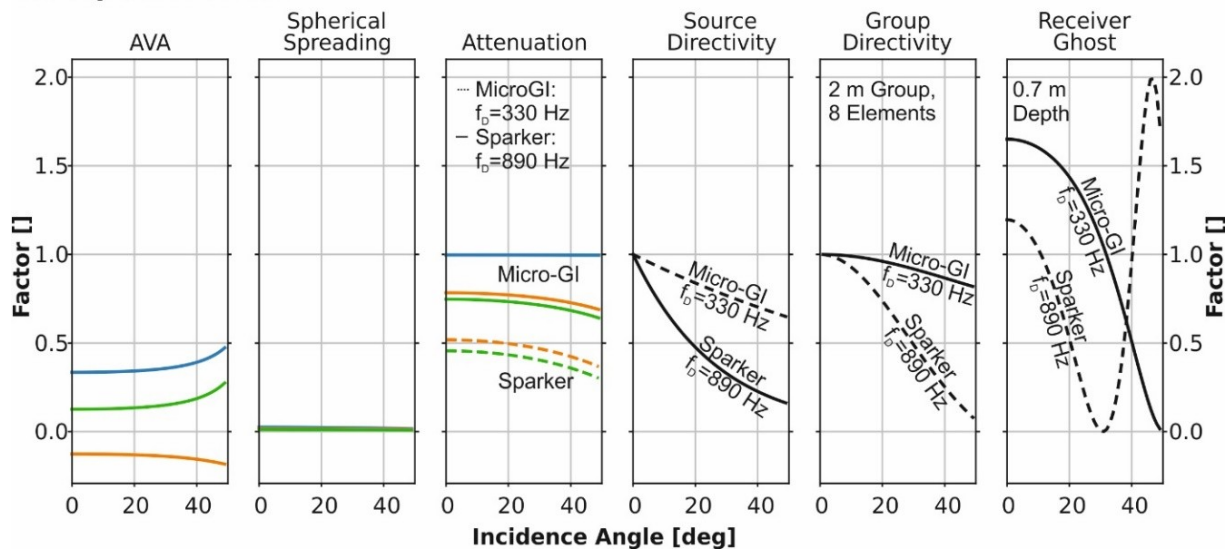


Figure 3-8: Comparison of wave spreading and acquisition effects on the seismic amplitude. A) The ground model for this example includes two sand bodies of 10 m thickness separated by a 10 m thick clay layer at 20 m water depth. Three interfaces (water-sand: blue; sand-clay: orange; clay-sand: green) are investigated. The sediment properties in terms of P-Wave velocity v_p , S-Wave velocity v_s , density ρ , and attenuation quality factor Q are taken from Table 3-1. B) Comparison of the different effects on the seismic amplitude. The Amplitude Versus Angle (AVA) effect can be used to deduce shear properties. This effect is masked by a range of acquisition and wave spreading effects, e.g., the geometric spreading of the seismic wave, which is modelled by spherical spreading here. For the attenuation it is assumed, that Q is constant for the frequency range of interest. Nevertheless, the attenuation effect is depending on the source signal, so a sparker source is attenuated twice as much compared to the micro-GI. The directivity functions of the sources are generated from the measurements shown in Figure 3-4. The use of receiver groups and the receiver ghost introduce additional effects.

As demonstrated in Appendix C.4 (“C.4 Sparker Directivity Modelling”), the directivity of a sparker can be approximated by a convolutional model. The received wavelet forms by a superposition of the wavelets emitted at each tip and the corresponding source ghosts. Although the directivity

pattern emitted by the AADS400 is unfavourable for some inversion applications, the directivity pattern could be optimized for applications by a rearrangement of the sparker tips, but this design is not available on the market. In general, the along track dimension should be small. By turning e.g. the sparker by 90° would already decrease the directivity and increase the amplitude at higher angles.

For near surface applications, SNR generally is a problem as UHR and UUHR sources emit typically 30-40 dB lower source levels (Figure 3-2, Figure 3-3) than reservoir scale surveys (Vardy et al., 2015). The micro-GI airgun is at least 6 dB stronger – equalling a factor 4 for the amplitudes - than the AADS400 sparker resulting in better SNR, which is also beneficial for inversion. As shown in Figure 3-8, the amplitude of the AADS400 is reduced by about 20 dB equalling a factor 100 at incidence angles of 60°. The micro-GI airgun amplitudes are reduced by 3 dB at 70°. Consequently, the stacking power of the micro-GI airgun is manifold larger than the AADS400 sparker.

Implications for Acquisition and Processing

The seismic data processing that is necessary for inversion workflows depends on the inversion technique used. For post-stack impedance inversion, the seismic signal is often considered to represent normal incidence, specular reflections without multiples and a stationary wavelet. Consequently processing including static correction, migration, demultiple, spreading correction and attenuation correction have to be considered, while internal multiples are expected to pose little additional efforts due to small reflection coefficients (Vardy, 2015), if the gas saturation is low.

If the sea-state induced vertical displacement is larger than λ_d , imaging and inversion results suffer from the static effects (Marsset et al., 1998; Missiaen, 2005). As λ_d of the AADS400 sparker is half as big as the λ_d of the micro-GI airgun, static corrections are more important for the AADS400 sparker records.

Additionally, the removal of multiples proves to be difficult for UUHR seismic data, therefore inversion efforts have often been limited to depth intervals above the first seafloor multiple (see Vardy, 2015). A range of explanations exist to argue, that demultiple processing steps are hard to apply to AADS400 sparker data. In section “Applied Acoustics Dura-Spark UHD 400 Sparker” we showed that the wavelet shape also depends on the incidence angle. The incidence angle of the multiple and the direct reflection at one CMP are different. Predictive deconvolution and multiple modelling techniques rely on the prediction of the multiple by the direct reflection. With the wavelet changing with incidence angle, the multiple cannot accurately be predicted by the direct

reflection. For the adaptive subtraction, vertical shifts need to be smaller than λ_d to match model and data. Similar to the static correction, this requirement makes static correction for sparkers harder than for airgun data.

For both UHR and UUHR sources, an exact consideration of source delays and the directivity is necessary in order to obtain seismic data suitable for inversion. Therefore, we recommend the use of a near-field hydrophone for source delay and temporal stability control.

3.4.3 Receiver Set-Up

Based on the acquisition models presented, we conclude, that offset range, receiver configuration and towing depth are relevant factors to optimize data acquisition for inversion. Further technical details on receiver groups and the effect of the receiver ghost are given in appendix “C.1 Receiver Configuration Modelling”. At this point it is important to state, that the usage of receiver groups instead of single hydrophones introduces a strong directivity and a filtering effect as shown in Figure 3-8. Therefore, single hydrophones or groups with a very small lateral extent are to be preferred for near surface seismic studies. To avoid spatial aliasing and achieve high fold and thus good Signal-To-Noise ratios, close spacing of hydrophones at a range of 0.5-4 m for UHR to UUHR sources is beneficial.

Post-Stack Impedance Inversion Set-Up

In the literature, reflectivity (Chotiros, 1994; Bull et al., 1998; Cevatoglu et al., 2015) and impedance (Panda et al., 1994; Sternlicht & de Moustier, 2003; Guo et al., 2006; Zhang & Digby, 2013; Vardy, 2015) are often derived from normal incidence data, but it is seldom specified to which extent seismic data can be considered to be normally incident. True normal incidence data can hardly be acquired as the receivers cannot be collocated with the source out of practical reasons and to avoid tow noise. As AVA effects are negligible for incidence angles $<25^\circ$ (Figure 3-7), data recorded at smaller incidence angles can be considered as normal incidence. Additionally, we consider the NMO stretch, which is smaller than 30% for angles $<30^\circ$ (Yilmaz, 1991), to be negligible.

Normal incidence data are also required for Q-estimation. Up to date, attenuation is typically quantified with vertical incidence data (Schock et al., 1989; Panda et al., 1994; Stevenson et al., 2002; Pinson et al., 2008; Morgan et al., 2012; Cevatoglu et al., 2015), although the longer wave trajectories of non-normal incident data leading to more pronounced attenuation (see Figure 3-8) could be beneficial for attenuation estimation. So, large fold multichannel data with incidence angles up to 25° are ideal for post-stack impedance inversion and attenuation estimation. Consequently, we would recommend a 150 m long streamer with single hydrophones at close

spacing, e.g. 1-2 m, for post-stack impedance inversion targeted on the near surface down to 150 m below the water surface.

Velocity Inversion Set-Up

Maximum incidence angles at the range of 50-60° equalling offsets at the range of three times the target depth have been found to be necessary for velocity estimation with traveltime curve inversion (Figure 3-6). This more elaborate velocity estimation technique is necessary, as Dix type conversions are imprecise. The measurement error of Dix conversions is very sensitive to the picking of velocity and event times especially for closely spaced reflectors (Geldart & Sheriff, 2004). For FWI approaches a maximum offset approximately equal to the target depth has been found to be sufficient for high fidelity P-wave velocity modelling (Provenzano et al., 2019, 2018). There are other, alternative methods, which require more acquisition efforts. E.g., in the Baltic Sea, Scholte Wave inversion with 30-40 m penetration in 15-20 m water depth has been done on ocean bottom recordings with 0.4-1.0 km offset (Bohlen et al., 2004; Kugler et al., 2007). According to Boiero et al. (2013), Guided Waves and Scholte Waves, which can be excited with low frequency sources (1-100 Hz), can be recorded using long offsets of tens of kilometres with towed streamers and ocean bottom seismic sensors, and thus allow to derive velocity information of the first hundreds of meters below the seafloor in approximately 100 m depth. Even though these acquisition efforts are relatively high, vintage data acquired for deep targets can be reprocessed for near surface targets (Clementi et al., 2022).

Especially systematic offset errors are problematic for velocity inversion. According to Figure 3-6B, systematic offset errors have to be smaller than 2-4 m to achieve sufficient accuracy for interval velocity estimations with the travel time inversion algorithm. Random errors at the same range are also observed to pose a problem, but sufficiently large fold and, e.g., residual static correction are expected to reduce the impact of random errors.

Inversion for Shear Properties

It is a critical yet complex discussion to evaluate which amplitude change by the AVA effect is significant and thus large enough to be used for shear property estimation, e.g., with pre-stack inversion. Although this discussion is too complex to be treated fully here, we can point out some limits with our analysis. Considering the shape of the AVA curves in Figure 3-7, we want to highlight, that there is only a negligible AVA effect for incidence angles <20-25°. So, there is no benefit of AVA or FWI inversions compared to pure impedance inversion for this angle range. Provenzano et al. (2017) state, that angles >40° are necessary for their FWI study. Taking into

consideration the ranges of relative amplitude change of the AVA curves for SBT3-7 (Figure 3-7), this limitation for FWI coincides with the range in which the amplitudes double relative to the normal incidence amplitude. To reach this AVA effect, we are suggesting, that angles at least up to 50°, ideally 65°, should be acquired for pre-stack inversion. Thus, the offset range should cover at least 2.5 times the investigation depth. E.g., a 300 m long streamer would be needed to investigate a sediment column of 100 m in 20 m water depth.

3.4.4 Implications for the Choice of Inversion Techniques

Generally stable inversion algorithms (Vardy, 2015; Vardy et al., 2015) have been shown to perform well for $\text{SNR} \geq 5$. As uncertainties associated with limited offset and Dix-conversion are high, alternatives are needed such as stochastic inversions like the genetic algorithm used in this study or the methods described in Provenzano et al. (2017, 2018, 2019). Having a range of inversion algorithms available, the most stable, noise insensitive and thus robust algorithm should be preferred. Based on the results presented and the discussion above, the following implications for the low frequency trend and the inversion techniques are deduced.

Low Frequency Trend

Due to the band limitation of seismic studies, the low frequencies, e.g., for post-stack impedance estimations need to be obtained separately (Claerbout, 1986; Jannane et al., 1989; Mora, 1989). As the low frequency content of the Micro-GI airgun can be as low as at least 60 Hz (see section “Sercel micro-Generator Injector Airgun”), the requirements for the low frequency model, e.g., by an interval velocity analysis are less strict compared to the requirements for the AADS400 sparker with a lower limit of 420 Hz (see section “Applied Acoustics Dura-Spark UHD 400 Sparker”). For post-stack impedance inversion, there should be an overlap of the low frequency trend and the inversion result to scale the band-limited seismic inversion and retrieve full bandwidth inversion results (Ferguson & Margrave, 1996). Using the micro-GI airgun, the gap between the low frequencies in velocity described in Claerbout (1986) and Jannane et al. (1989) can be bridged then the interval velocity analysis reaches a frequency content of 100 Hz.

For FWI, using gradient methods for optimization, the starting model has to match the measured data within less than half a period (Fichtner, 2011). Considering Table 3-3, the fit has to be at the range of 0.5 ms for the Micro-GI airgun and 0.03-0.1 ms for the AADS400 sparker. Those values indicate that the building of a starting model is a major challenge for FWI.

Attenuation Estimation

Despite the disadvantages shown above, UUHR sources such as sparkers like the AADS400 sparker are more practicable than UHR/HR such as the Micro-GI airgun for attenuation estimation or necessary for higher resolution. E.g., the AADS400 sparker shows both a broader bandwidth and a considerably stronger high frequency content than the Micro-GI airgun in Figure 3-5. The Q -estimation especially requires broad bandwidths and high frequencies (J. Wang & Stewart, 2015). The Q effect on sparker data can also be a disadvantage. Attenuation correction of non-stationary convolution needs to be applied for impedance inversion if the wavelet shape changes significantly with depth. In most case studies for attenuation estimation chirps have been employed (Schock et al., 1989; Panda et al., 1994; Stevenson et al., 2002; Pinson et al., 2008; Robb et al., 2006; Vardy et al., 2012; Cevatoglu et al., 2015), while air guns are used relatively seldom (Lei & Morgan, 2015; Morgan et al., 2014; Morgan et al., 2012). Chirps are UUHR sources and suitable for Q estimation as those sources emit a frequency modulated pulse over a specified range of frequencies. Attenuation is an important seismic parameter and thus the use of sparkers for attenuation inversion a relevant acquisition scenario.

Requirements for Shear Property Inversion

When considering pre-stack inversion methods to deduct shear properties, geometric spreading, attenuation, source directivity and ghost effects are much stronger than AVA effects (see Figure 3-7 and Figure 3-8). Noise contamination is another issue, which can mask any AVA effect.

For pre-stack inversion, corrections need to be applied before the inversion, which are critical to restore the AVA effect, e.g. for source and receiver characteristics (Riedel & Theilen, 2001; Provenzano et al., 2017). For the micro-GI airgun and the AADS400 sparker, amplitude correction curves are now made available (Figure 3-4) In the case of highly directive sources such as sparkers, also the angle dependency of the wavelet shape needs to be considered. It remains to be tested, whether angle stacks are a viable option to improve pre-stack inversions. Eventually, amplitude variations due to the pitch and roll of the directive AADS400 sparker could be smoothed by angle stacks. If possible, we consider it to be beneficial to calibrate the corrections with core data or well logs.

In the case of FWI, all effects can be included in the forward modelling part of the inversion. This option dramatically reduces processing requirements. The inversion will run on relatively raw shot or Common-Mid-Point gathers. E.g. in Provenzano et al. (2017) the variable streamer depth is included in the modelling of the seismograms making it unnecessary to correct the receiver ghost.

However, such methods require thorough quality control and will be problematic if the computational time increases too much or covariances of input parameters result in non-unique solutions. Broad source bandwidths and strong low frequency contents have also been found to be beneficial for FWI (Panda et al., 1994; Ker et al., 2013; Provenzano et al., 2019).

The least processing effort will be necessary for Machine Learning (ML) algorithms as, e.g. exemplified in Sauvin et al. (2019). It is our understanding that ML can run on raw gathers, which should extend to at least 50° incidence angles to include significant AVA effects (see Figure 3-7). Despite the advantage of ML to require little processing, there are also drawbacks to be mentioned. An inversion based on ML will require extensive training data, which is often not available. If specific ground types are not included in the training data, they will not be accurately inverted for. Also, there is the risk of overtraining.

In general, the forward modelling for the pre-stack inversion and FWI needs to be carefully chosen. As shown in Figure 3-7, only the Aki-Richards equation has been found to be an applicable simplification to the Zoeppritz equation-based inversion in the near surface. The other simplifications to the Zoeppritz equation are tailored for the Oil+Gas Industry and the underlying simplifications are not applicable to the near surface. The Zoeppritz equation considers a planar wavefront (Chopra & Castagna, 2014) while more realistic spherical wavefronts and the effect of attenuation are not considered. So, in order to apply modelling based on the Zoeppritz equation, attenuation and spherical spreading have to be corrected. Provenzano et al. (2017) use an analytic solution for modelling, which requires the assumption that there is only vertical heterogeneity. This requirement will not be applicable to all geological settings. It has been found previously by Thiel et al. (2019) in the context of FWI and comparing acoustic with elastic models, that two different forward models can lead to significant amplitude differences. If the wrong model is chosen, the field data cannot be matched, or the inversion results are systematically erroneous. Consequently, it is vital to validate inversion methods, clearly state limitations and adopt the processing prior to the inversion to the method used.

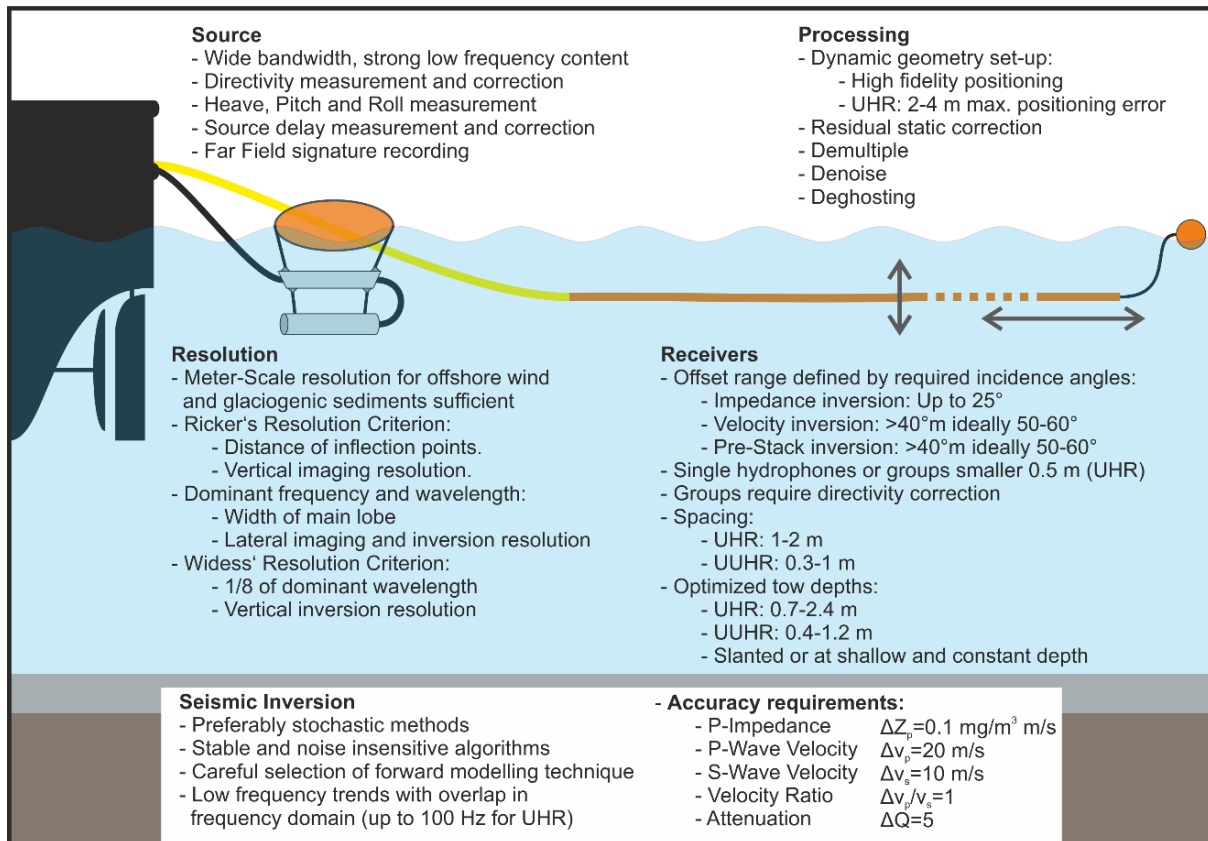


Figure 3-9: Summary of the requirements and boundary conditions for near surface reflection seismic inversion for target depths of up to 80-100 m. The classification of the sources follows ISO 19901-10 (2021) High Resolution (HR, 75-300 Hz), Ultra-High-Resolution (UHR, 250-800 Hz) and Ultra-Ultra-High-Resolution (UUHR, 750-2000 Hz)

3.5 Conclusion

Combining all presented results, we can set limits on requirements and boundary conditions to characterize near surface sediments in a North Sea or Baltic Sea setting down to 80-100 m depth as summarized in Figure 3-9. Inversion techniques providing impedance (resolution/accuracy $\Delta Z_p \leq 0.1 \text{ mg/m}^3 \text{ m/s}$), attenuation ($\Delta Q \leq 5$), P-Wave velocity ($\Delta v_p \leq 20 \text{ m/s}$), S-Wave velocity ($\Delta v_s \leq 10 \text{ m/s}$) and P- to S- Wave velocity ratio ($\Delta \frac{v_p}{v_s} \leq 1$) estimates are most suitable to quantitatively characterize the near surface. Machine Learning techniques would be promising approaches reducing the processing efforts, if extensive ground truthing becomes available. Despite higher efforts, other inversion techniques allow a broader application range and potentially enhance the imaging and the systematic understanding.

Ultra-High Resolution seismic sources such as the Sercel micro-GI airgun are especially suitable for inversion. With such sources the resolution gap to low frequency trends can be more easily

bridged, they are characterized by a high Signal-to-Noise-Ratio and the processing in terms of demultiple and static correction has been shown to be feasible. Advantages of Ultra-Ultra-High Resolution sources such as the Applied Acoustics Dura-Spark UHD 400 in terms of resolution and attenuation estimation are opposed with the strong directivity in terms of signal strength and signal shape. Consequently, this sparker will only be applicable for inversion, if the directivity is corrected, which includes the measurement of the heave, pitch and roll of the device. Also, there are higher requirements for the receivers in terms of spacing and tow depth, for the estimation of the low frequency trend, the statics and the demultiple. The practically achievable resolution of the sparker has been found to be significantly lower than implied by near field measurements. So, source signature recordings should be routinely conducted in the far field.

We propose the use of single hydrophone streamers with lengths exceeding three times the target depth and high-fidelity positioning. High fold data with small incidence angles to a maximum of 25° are considered ideal for post-stack impedance inversion. Incidence angles $>40^\circ$ and ideally up to $50-60^\circ$ provide a sound basis to invert for interval velocities, to record Amplitude Versus Angle effects and thus to invert for shear properties. Especially systematic offset errors are problematic for inversion and should be kept as small as possible with maximum offset errors of 2-4 m for micro-GI airgun data.

When data of sufficient quality has been acquired, it is our recommendation to first invert for post-stack impedance. On the one hand, impedance can be readily used with empiric relations to predict marine sediment types and properties (Panda et al., 1994; Vardy et al., 2015; J. Wang & Stewart, 2015). On the other hand, we consider impedance to be a good basis for the communication with other disciplines such as geotechnics or geology. Additionally, the impedance inversion results can be used as starting models for further pre-stack inversion or Full Waveform Inversion. As the shear properties are of particular interest, pre-stack inversion should aim for v_s or v_p/v_s . As simple approaches tend to be stable, we recommend to first work on Amplitude Versus Angle inversion methods and develop into more complex inversions when required. In terms of technical advancements, ocean bottom recordings are a good perspective to possibly capture S-Waves. We are convinced that also the imaging will be greatly improved, if the data acquisition is optimized for inversion purposes, as the target illumination is extended, velocities, e.g., for stacking and migration are improved and the wavelet is better controlled.

Chapter 4 From Interface to Unit Characterisation: Stochastic Near Surface Seismic Impedance Inversion in the German North Sea

Nikolas Römer-Stange¹, Natasha Morales², Hanno Keil¹, Norman Ettrich³, Sigrid Wilhelm⁴, Stefan Wenau², Aisgo Oguro², Maximilian Merl¹, Carlos Ramos Córdova², Lennart Siemann², Taisiya Pein², Patrick Arnold⁴, Volkhard Spieß¹

¹Department of Geosciences, University of Bremen, Klagenfurter Str. 2-4, D-28359 Bremen, Germany

²Fraunhofer Institute for Wind Energy Systems IWES, Am Fallturm 1, D-28359 Bremen, Germany

³Fraunhofer Institute for Industrial Mathematics ITWM, Fraunhofer-Platz 1, D-67663 Kaiserslautern, Germany

⁴GuD Geotechnik und Dynamik Consult GmbH, Darwinstr. 13, D-10589 Berlin, Germany

Submitted to Geophysical Journal International on 2023-08-23. Format and references have been adopted to match the thesis.

Keywords

Near Surface, Ultra-High Resolution Reflection Seismics, Waveform inversion, Machine learning, Acoustic properties

Abstract

Remote and quantitative characterization of the physical properties of marine sediments in the near surface plays a vital role for the geoscientific research and industrial applications such as the site characterization for offshore wind farms or for the planning and monitoring of Carbon Capture and Storage sites. Quantitative unit properties can be generated with seismic inversion, but for most inversion approaches additional information from direct measurements such as borehole logs or Cone Penetration Tests is needed. Those direct measurements sample the subsurface with a very small footprint, are often not broadly available in the early phases of projects and more expensive in comparison to seismic investigations. Where inversion results are available, the uncertainties have often been poorly constrained. Therefore, there is the need to implement stochastic inversion approaches based on seismic data only, also quantifying uncertainty. To apply seismic inversion for this purpose, the main remaining challenges have been identified to be the tailoring of the data acquisition, data processing, the establishment of inversion methods and the coupling with soil mechanical parameters. To demonstrate near surface seismic inversion, impedance inversion algorithms have been implemented and applied to a seismic profile in the North Sea crossing an offshore wind park area. The algorithms cover attenuation estimation, low frequency trend estimation by interval velocity estimation and density transformation, band limited impedance inversion, merging of low frequency trend and band limited impedance as well as depth conversion. The generated absolute impedance profile recovers sediment properties, correlates well to the Cone Penetration Test measurements in the area and allows for the quantitative interpretation of geologically complex areas reducing interpretation biases. The Soil Behaviour Type along the 2D seismic profile has been classified successfully based on the impedance inversion. Thus, these seismic inversion results improve the extraction of important sediment properties for engineering purposes from an indirect data source and therefore enhance the knowledge transfer in interdisciplinary studies, e.g., between geoscientists and foundation engineers.

4.1 Introduction

The non-destructive and effective measurement of subsurface properties is a key motivation for marine geophysics. Especially because of the global energy transition, there is an increased need for marine near surface characterisation for offshore wind energy, Carbon Capture and Storage developments and associated offshore infrastructure such as cables, pipelines and platforms. In this context, seismic inversion can fill an important information gap (Figure 4-1) and reduce costs. A very dense grid of one-dimensional information as delivered by coring or Cone Penetration Testing (CPT) is needed to resolve small scale geologic features such as channels or dipping strata without spatial aliasing and to achieve high correlation between adjacent boreholes.

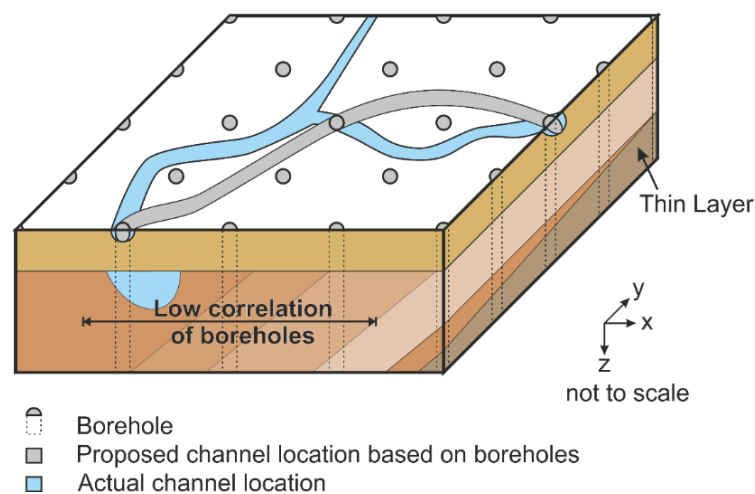


Figure 4-1: Sketch of the possible discrepancy of the interpretation based on one-dimensional information to actual, complex and small scale features, modified and extended from Henson and Sexton (1991). If dipping or folded strata or small-scale features such as channels are encountered in the subsurface, adjacent boreholes will show low correlation.

Conducting a CPT, large stresses and strains are introduced into the seafloor. The recorded soil behaviour is a measure of the static moduli and can be empirically related to geotechnical parameters (Ramsey, 2002; Mayne, 2014) and dynamic moduli of sediments (Wichtmann et al., 2017). Small stresses and strains are introduced shooting a seismic survey and those small stresses and strains directly relate to the dynamic moduli defining the compressional wave velocity v_p and shear wave velocity v_s . Reflection seismic images directly reveal the interfaces between geological units and thus the structure of those units as well as the properties of the interfaces. In addition to the structure, the unit properties rather than the interface properties are of interest, as seismic unit properties can be directly linked to geological and geotechnical parameters. Of those unit properties, the compressional impedance $Z_p = \rho \cdot v_p$ with the density ρ is amongst the most important properties in reflection seismics. Therefore, the determination of Z_p is a primary target

for the quantitative characterization of the subseafloor. Z_p sections derived from a reflection seismic data set show unit properties, which can be linked to geological and geotechnical parameters (Buiting & Bacon, 1999; Bacon et al., 2003). Consequently, Z_p sections can significantly improve the geologic interpretation and form the link from qualitative seismic interpretation to a quantitative understanding of the subseafloor geology.

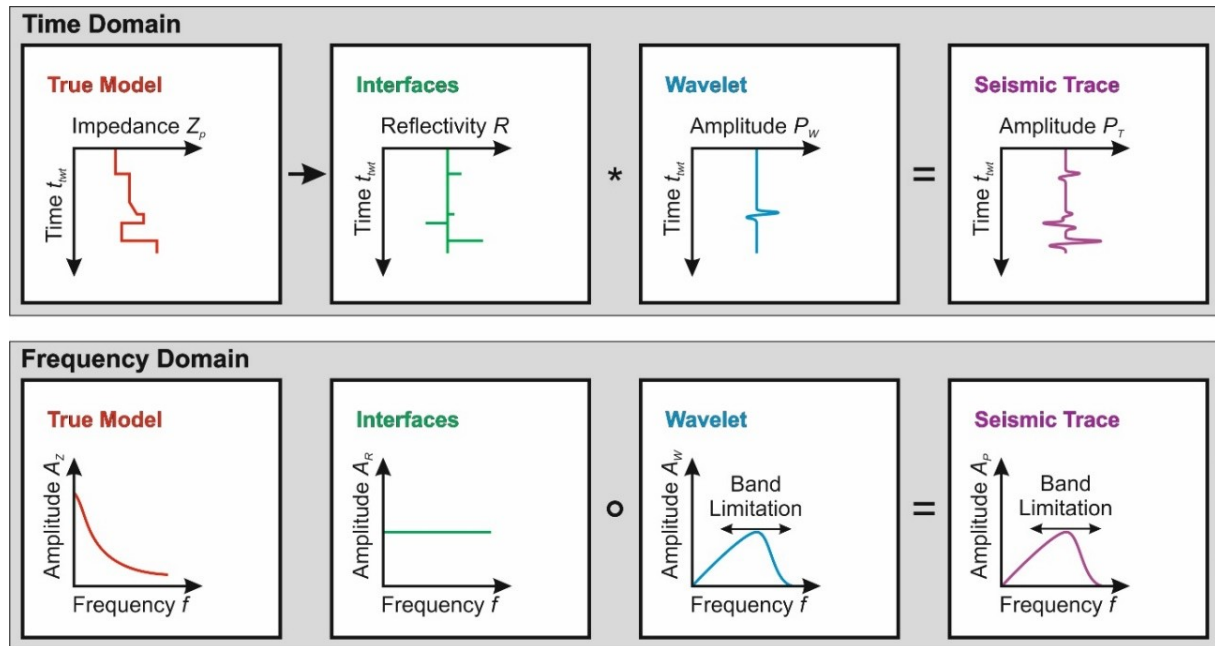


Figure 4-2: Time domain (top row) and frequency domain (bottom row) representation of the convolutional model of a seismic trace. In a vertical incidence scenario without attenuation and geometric spreading, impedance contrasts define the reflectivity of interfaces, and a seismic trace can be modelled by the convolution of the reflection time series with the time series of the wavelet. In the frequency domain, this convolution is represented by the multiplication of the spectra.

The determination process to obtain Z_p from a seismic record is termed impedance inversion and describes the optimization process to find a Z_p model, which reproduces a recorded seismic data set by forward modelling (Aki et al., 1977; Bishop et al., 1985; Tarantola, 1986). In a vertical incidence scenario and considering only primary reflections without geometric spreading and attenuation, the convolutional model can be used to generate synthetic seismic data. In this described case, a seismic trace can be considered to result from the convolution of the reflectivity R with the source wavelet as shown in Figure 4-2. In this context, the subsurface property measuring the resistance to particle motion of a medium is quantified with Z_p . Thus, interfaces of changing Z_p define R , as the system is required to conserve both continuity of pressure and flow (Aki & Richards, 2002). The convolution in the time domain is represented by a multiplication of the R spectrum with the band-limited wavelet spectrum resulting in a band-limited seismic trace.

Band limitation describes that the very low and high frequencies are absent in the spectra of the wavelet and the seismic record. Due to the band-limitation, both the low frequency trend and the very high-frequency variation cannot be resolved by seismic inversion (Claerbout, 1986; Jannane et al., 1989). So, an appropriate seismic source needs to be selected based on the bandwidth to resolve the necessary level of detail. The low frequency trend, in contrast, needs to be derived from additional data such as borehole logs or CPT data. Furthermore, seismic methods, such as velocity analysis or tomography, can also be used for low frequency trend determination as those methods quantify the average compressional velocity in units or layers, which is termed compressional interval velocity $v_{p,int}$. Starting with Lindseth (1979) and growing to be more important with the availability of high quality and 3D data sets (Buiting & Bacon, 1999; Bacon et al., 2003; Oliveira et al., 2009), impedance inversion has been established as a standard tool in the Oil+Gas Industry. In contrast, there are to our knowledge less than ten case studies for near surface applications, which is also due to a limited interest in the near surface of the industry in the past (Vardy et al., 2017). Recently, impedance inversion results for the development of ground models for the offshore wind industry gained more interest. Z_p has been shown as the most important basis for the determination of synthetically generated CPT records with machine learning methods to construct integrated ground models (Sauvin et al., 2018, 2019; Forsberg et al., 2022; O'Neill et al., 2023). One of the most promising approaches for impedance inversion in the near surface is the use of stable and robust genetic algorithms for acoustic impedance inversion introduced by Vardy (2015), which is based on a convolution for the forward modelling. The employed nonlinear optimization bears advantages for seismic data inversion, as there is no need for a starting model and trapping at local minima is avoided (Sen & Stoffa, 1992). Commonly, the missing low frequency trends are considered in the form of linear trends derived from borehole or CPT data.

Attenuation needs to be negligible or corrected to allow the application of acoustic impedance inversion algorithms (Vardy, 2015). If the attenuation has a significant effect, impedance changes are increasingly underestimated with depth and the spectrum shifts to lower frequencies, i.e., high frequencies are attenuated, and seismic amplitudes are reduced. Therefore, processing steps such as zero-phase conversion without prior attenuation correction as employed by O'Neill et al. (2023) can be insufficient and leads to artefacts and inaccurate inversion results. The Seismic Quality Factor Q can be used to quantify the anelastic attenuation and to correct the effect by inverse filtering (Y. Wang, 2008). Thereby, Q is inversely proportional to the energy loss per cycle. High frequencies cycle more often in the same period of time and are thus more affected. Pinson et al. (2008) show, that especially sands to coarse silts are characterized by strong attenuation with $25 < Q < 75$, while sediments finer than medium silts or rocks can reach $Q > 250$. The estimation of

Q will be associated with great uncertainties and with significant differences between different methods (Jannsen et al., 1985; Nemtsov, 2019). In general, spectrum and wavelet modelling methods have been found to be superior, e.g., if noise is present, as compared to spectral ratio methods, where interference is a major problem (Jannsen et al., 1985; Merouane & Yilmaz, 2017; Pinson et al., 2008). Trace autocorrelation functions can be used to reduce the negative impact of interference (Schock et al., 1989).

The inversion of marine near surface seismic data is a challenge. It is problematic to apply established inversion techniques, as unconsolidated sediments rather than hard rocks are of interest in the near surface. Sediment physical models like the Biot-Stoll model (Biot, 1956; Stoll, 1977) are applicable rather than rock physics. As a consequence, empiric relations such as the v_p - ρ relation by Gardner et al. (1974) are not applicable although being at the core of some impedance (Lindseth, 1979) or Amplitude-Versus-Angle (Chopra & Castagna, 2014) inversion methods. As previously introduced, unconsolidated and especially coarse sediments are also strongly attenuating the seismic signal. Also, High Resolution to Ultra-Ultra High Resolution (ISO 19901-10, 2021) sources are used in near-surface seismic studies, causing a gap between high frequency seismic data and commonly available low frequency trends (Claerbout, 1986; Jannane et al., 1989). From the previously published studies it is not clear, whether the full bandwidth has been restored with the addition of the low frequency trend (see Vardy et al., 2017 and references therein). Additionally, static corrections and exact positioning of the receivers are critical for the preservation of the high frequency signal content during processing (Gutowski et al., 2002; Reiche et al., 2020). Additionally, noise levels of near surface seismic surveys are high due to the working environment (Danbom, 2005) and the use of high-frequency seismic sources with relatively low sound pressure levels. The working environment is also problematic due to the usually shallow water depths causing multiple reflections that mask significant parts of the seismic section. Inversions are thus usually limited to the depth above the multiple (Vardy et al., 2017), which reduces their usefulness for, e.g., foundation planning for offshore wind. From a project development perspective, it is also not ideal, that inversion results are often only available at late stages when well data have been integrated as a low frequency trend. Furthermore, it is generally recognized, that well driven low frequency trends can suffer large errors and are spatially sparse (Yuan et al., 2019).

Generally, it is the aim of this study to quantitatively estimate subsurface parameters to improve the interpretation of marine seismic reflection data sets recorded at shallow water depths and convey seismic results to other disciplines such as geology or engineering. The data presented to showcase the potential of seismic impedance inversion has been collected in the framework of a project with industry partners at the location of a windfarm area. We establish an open source and

fully stochastic workflow and investigate uncertainties for the approximation of seismic and geotechnical parameters based only on seismic data for a depth interval extending below the first multiple reflections (~ 80 m below seafloor). Data acquisition and processing before inversion reflects this setting. The low frequency trend is derived from $v_{p,int}$ resulting from the inversion of picked travel time curves. For the calculation of the low frequency trend of Z_p based on v_p , sediment physical models are fitted to unconsolidated sediments. A Q estimation method is developed, and a time-varying amplitude correction based on a Q model is performed to correct the effect of anelastic attenuation. High frequency Z_p is determined with a genetic algorithm. The merging of high and low frequency inversion results incorporates the reconstruction of the full bandwidth and includes a scaling of the high frequency impedance inversion. The results are converted to depth with an optimization of $v_{p,int}$. After depth conversion, the results are correlated to geotechnical parameters and a joint interpretation is performed with CPT measurements.

4.2 Geological Setting

The study area is located in the German North Sea in the north of the island Heligoland in a glaciotectonically influenced area. As confidential CPT data are shown in this study, the exact location of the CPTs cannot be disclosed. As shown in Winsemann et al. (2020) and Lohrberg et al. (2020, 2022), the thrust-fault complex of the Heligoland Glaciotectonic Complex presumably forms a Hill-Hole Pair caused by an ice advance during the pre-Elsterian (MIS16) or Elsterian (MIS 12). Neogene sediments above two detachment surfaces have been deformed and the tops of the complex have been eroded. Tunnel valleys of supposedly Elsterian (MIS12) or Early Saalian (MIS10) age are also incising into the glaciotectonic complex.

Considering the general framework of Cenozoic sedimentation in this area as described in Thöle et al. (2014), the Mid-Miocene Unconformity (MMU) marking the onset of the Eridanos fluvio-deltaic deposits is to be expected at 450-500 ms two-way travelttime corresponding to ~ 400 -500 m depth (also compare Winsemann et al., 2020). The pre-Quaternary sediments above the MMU have been supplied by the Eridanos fluvio-deltaic system and the Fennoscandian Shield (Overeem et al., 2001; Anell et al., 2012; Thöle et al., 2014) and supposedly are Miocene to Pliocene delta deposits due to the location in the depositional environment. In the Quaternary, glacial deposits such as sanders and tills, fluvial deposits including peats, lacustrine deposits as well as brackish to marine

sediments have been deposited during various glacial and interglacial periods (Ottesen et al., 2014; Lamb et al., 2017, 2018; Coughlan et al., 2018). A thin cover of relatively mobile sands and lag deposits formed in the Holocene, while fine sediments are only found in the Heligoland mud area (Zeiler et al., 2000, 2008).

4.3 Material and Methods

A workflow for impedance inversion as a basis for quantitative ground models has been developed which is shown in Figure 4-3. This workflow is described in detail in the following sections and summarized to the following main points. The seismic data forming the basis of this study was acquired with a set-up optimized for inversion. A stochastic traveltime curve inversion was employed to derive $v_{p,int}$ at a high spatial and temporal resolution. Empiric relations were utilized to determine Z_p as a low frequency trend from $v_{p,int}$. Furthermore, a post-stack migrated image was generated, Q has been estimated and a time varying amplitude correction has been applied based on a Q model. Then, the stochastic inversion scheme based on Vardy (2015) was used to derive high frequent Z_p from the corrected seismic image. Merging of the low and high frequency inversion with a crossover filter (Ferguson & Margrave, 1996) after scaling resulted in an absolute Z_p estimate. Finally, all available results were combined for an interpretation. Four CPTs and two cored boreholes adjacent to the seismic line are analysed for the ground truthing of the inversion results and for depth conversion.

While the seismic data processing has been based on commercial software, the inversion has been implemented in PYTHON and is available via GitHub (<https://github.com/roestanik/ImpedanceInversion>) under a CC BY-NC 4.0 license.

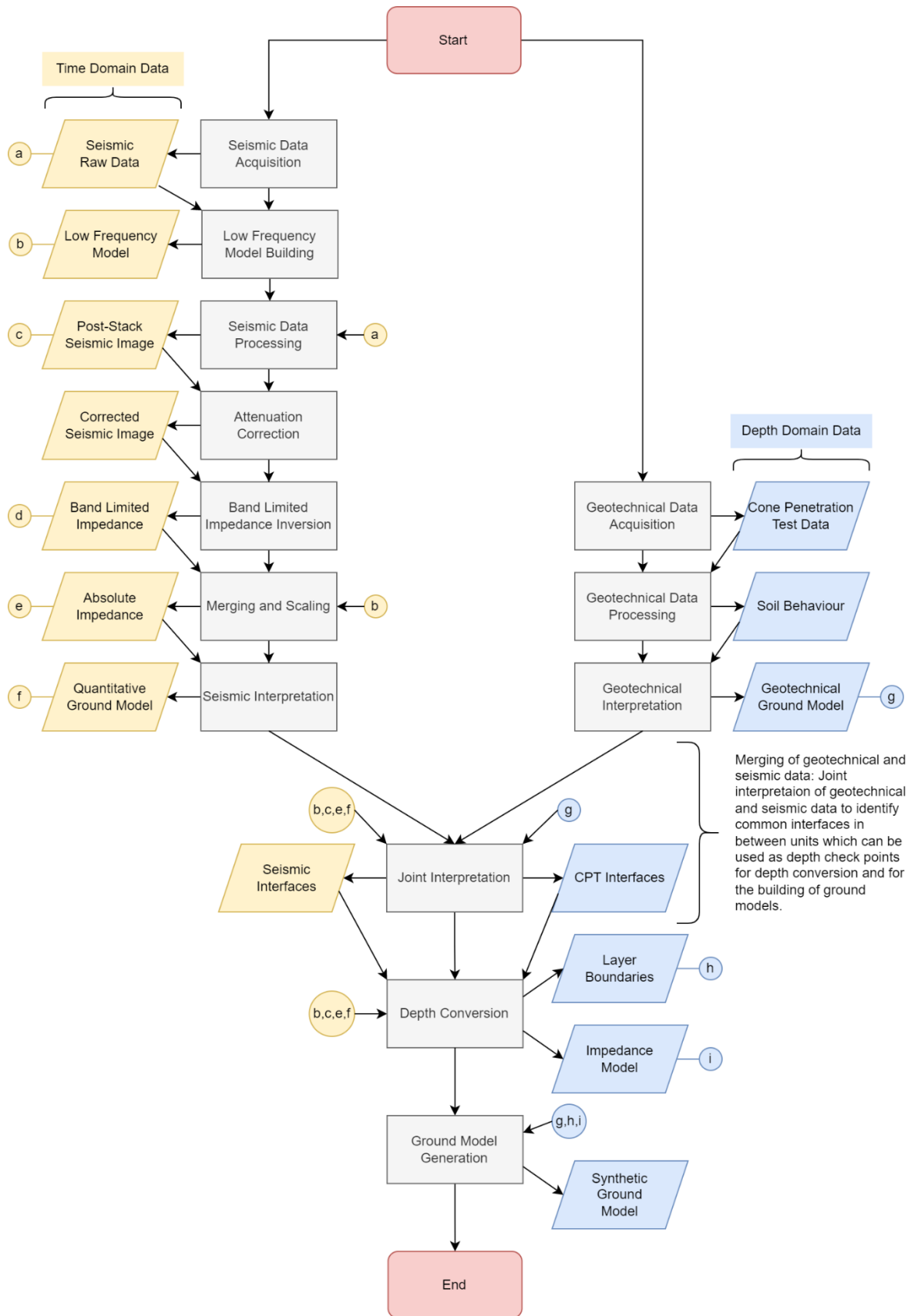


Figure 4-3: Methodological flow chart to derive quantitative ground models with near surface seismic inversion and Cone Penetration Test (CPT) data. Seismic data is acquired, processed, and inverted as time series data, while CPTs are recorded in depth. After CPT and seismic results are brought together in a joint interpretation step, the seismic results can be converted to depth. The depth converted results can further be used for the generation of ground models.

4.3.1 Seismic Data Acquisition and Standard Processing

The research Cruise He569 (<https://www.mtu.uni-bremen.de/2021-he569.html>) in the German North Sea, on which the seismic Profile He569-GeoB21-033 has been acquired, took place in February 2021 on R/V Heincke (AWI, 2017). According to the norm ISO 19901-10 (2021), the data has been acquired as an Ultra High Resolution (UHR) data set, of which the main acquisition settings are given in Table 4-1.

Table 4-1: Seismic Data Acquisition Parameters of He569-GeoB21-033.

Device	Parameter	Description
Source	Type	Sercel micro-GI (Volume 2 x 0.1 L)
	Source Pressure Level	226.4 dB (re 1 μ Pa) at 1 m distance 140 bar air pressure supplied to gun
	Tow Depth	1 m
	Central Frequency	330 Hz (Seafloor Wavelet, after processing)
	Dominant Frequency	440 Hz (Seafloor Wavelet, after processing)
	Shot Point Spacing	Approximately 6 m (2.4 s time trigger with approximately 2.5 m/s speed over ground)
Receiver	Type	Analog Single Hydrophone Streamer
	Channel Spacing	1-4 m, variable
	Tow Depth	0.7 m (Depth keeping with 4 ION DigiBirds)
	Offsets	7-230 m
Recording	Sampling Rate	4 kHz (resampled from 8 kHz)
	Analog to Digital -Conversion	MaMuCS (Dr. Hanno Keil, University of Bremen) 16 bit Texas Instruments AD Converters.
	Recording Length	0.220 s (cut from 2.2 s)
Positioning	Type	Differential GPS on the ship
	Processing	Lay-Back
	Accuracy	m to dm-level

The most important elements of the seismic data processing flow are the static correction, multiple suppression as well as Normal Move Out (NMO) correction, Common Mid Point (CMP) stacking and post-stack migration. Seismic data processing has been conducted with GLOBE Claritas (V7.3.2) aided by various custom programs. The processing sequence starts with the set-up of the lay-back geometry, binning with a CMP spacing of 1.0 m, further pre-processing including static correction and a first pass of semblance velocity analysis. Statics were corrected with the average static correction method (Gutowski et al., 2002). The following multiple model generation and first pass subtraction is based on Wang (2003). Three additional passes of multiple model subtraction based on Monk (1993) are done for the full trace, 25 ms gates and 10 ms gates. After multiple suppression, the data has been re-binned to 10 m CMP spacing. A second pass of velocity analysis was performed. This velocity model was used for spherical divergence and Normal Move Out

(NMO) correction before stacking. To avoid the influence of Amplitude Versus Angle (AVA) effects, the gathers were restricted to 0-30° incidence angles before stacking. The stack was filtered with a Butterworth bandpass filter with filter flanks of 20-40-900-1800 Hz. For the final imaging, the stacked data have been post-stack migrated with a F-D-migration algorithm using a smoothed interval velocity model determined from the second pass velocity analysis.

4.3.2 Low Frequency Model by Traveltime Curve Inversion and Density Estimation

A low frequency Z_p model has been built by interval velocity inversion and ρ estimation to calculate Z_p . First, manually picked travel time curves have been inverted for $v_{p,int}$. As it was not possible to get reliable results from automatic velocity analysis or picking algorithms, four strong and continuous horizons were identified in a stacked seismic section. Those horizons were then picked manually in constant offset sections. For quality control, the picks were checked in CMP sort order. As shown in Figure 4-4, maximum offsets of about 120-140 m were reached for the seafloor and the deepest reflectors. Due to overlaps with other events, those large offsets were not reached for shallower horizons. Traveltime curve inversion for interval velocities has then been conducted on every CMP resulting in a horizontal resolution of 10 m by means of a genetic algorithm with differential evolution (Barros et al., 2015) and a second order NMO equation.

For this purpose, the picked traveltime curves have been interpolated to a regular offset spacing of 5 m in a range of 10-140 m without extrapolation. For every CMP, a total number of 300 runs of the inversion are conducted with the interpolated picks. The inversion results appear to be normally distributed and are thus a normal distribution is assumed. The estimates for $v_{p,int}$ and depth estimate for each layer, as shown in Figure 4-4, result from the median value of the 300 inversion runs, while the uncertainty is determined by the standard error of the mean. An example of such an inversion result for one CMP is given in Figure 4-4. In every run of the inversion, a population of 500 random layer models with velocities ranging from 1400 m/s to 2100 m/s to a maximum depth of 120 m has been initialized. The mechanisms of selection, crossover and mutation mimicking natural evolution processes, which are described in Barros et al. (2015) for this implementation, have then been executed until a stopping criterion is met to optimize the models. Thereby, a mean standard deviation of 2 m/s of the $v_{p,int}$ populations in the layers or a maximum number of 200 generations are used as stopping criteria. The forward modelling is based on a Root Mean Square velocity $v_{p,RMS}$ estimate and a second order NMO-equation.

The Z_p model is then generated by the multiplication of the inverted interval velocities with empirically derived densities. This empiric relation for the velocity to density transformation is adopted from Raymer et al. (1980).

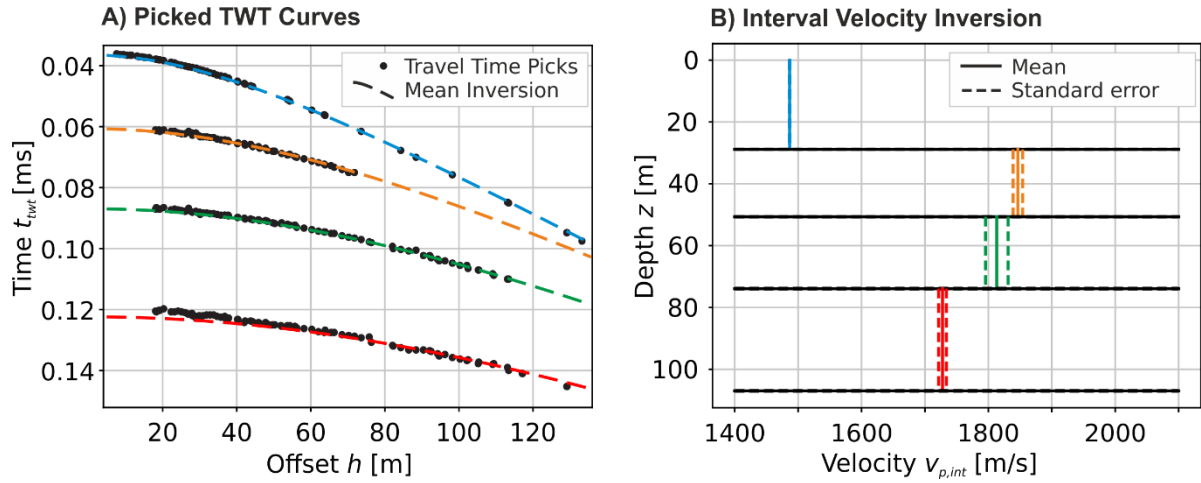


Figure 4-4: A) Traveltime curves of four reflection events and B) corresponding inversion results for CMP 492 of the Profile He569-GeoB21-033 which is adjacent to the location of CPT 3. The uncertainty is quantified by the standard error of the mean (dashed lines in B).

4.3.3 Attenuation Estimation and Correction

A stable approach was developed to estimate and then correct the effect of attenuation quantified by Q on stacked data. First of all, the average quality factor Q_{ave} from the seafloor reflector to selected horizons is estimated. Then, Q_{ave} is inverted for the interval quality factor Q_{int} of the units in between the horizons. This Q_{int} estimate is then used for the Q model building and amplitude gain correction calculation.

For the Q_{ave} estimation, the spectrum modelling algorithm of Merouane & Yilmaz (2017) has been adopted for horizons. The basic idea of the method is that the frequency spectrum at a horizon will be equal to the frequency spectrum at the seafloor multiplied with an attenuation function for the Q_{ave} value at the horizon. The frequency dependent attenuation function A_{loss} for a frequency f independent, constant Q_{ave} is determined by:

$$A_{loss} = e^{-\pi \cdot f \cdot \Delta t_{twt} / Q_{ave}}$$

Equation 4-1

depending on the difference of the two-way traveltime Δt_{twt} between the reflector and the reference horizon, i.e., the seafloor reflector (as described in Jannsen et al., 1985; Pinson et al., 2008; Merouane & Yilmaz, 2017; Nemtsov, 2019). To reduce the effect of interference, the spectra are calculated from averaged and normalized (normalization: $\hat{X} = \frac{X}{|X|}$) autocorrelations across a set number of CMPs with time windows at the seafloor A_{SF} and at the horizon A_{refl} (Schock et al., 1989). To estimate the Q_{ave} value from those spectra, a range of possible Q_{ave} values is defined, and the misfit error $L(Q_{ave})$ is calculated in a selected frequency range $f_{min} \leq f \leq f_{max}$ with N_f frequency samples by:

$$L(Q_{ave}) = \sum_{f=f_{min}}^{f_{max}} [\{\widehat{A}_{SF} \cdot A_{loss}(Q_{ave})\} - \widehat{A}_{refl}]^2 / N_f$$

Equation 4-2

The best estimate of Q_{ave} is found at the minimum of this error function and the Probability Density Function (PDF) to determine uncertainties is given by (Sen & Stoffa, 1992; Vardy, 2015):

$$PDF(Q) = \frac{\sum_{q=Q_{min}}^{Q_{max}} L_q}{L(Q)}$$

Equation 4-3

With the method described above, Q_{ave} from a reference reflector, i.e., the seafloor reflector and to a specified reflector are determined. The Q_{ave} of N layers relate to Q_{int} depending on the layer thickness Δt and over all thickness $T = \sum \Delta t$ (Y. Wang, 2004):

$$\frac{1}{Q_{ave}} = \frac{1}{T} \sum_{i=1}^n \frac{\Delta t_i}{Q_{int,i}}$$

Equation 4-4

Corresponding to Equation 4-1, the attenuation effect can be reduced to an amplitude gain correction G depending on the central frequency f_c of the wavelet and the two-way traveltime t_{twt} , if $Q_{ave}(t_{twt})$ as a function of t_{twt} is available:

$$G(t_{twt}) = e^{\pi \cdot f_c \cdot t_{twt} / Q_{ave}(t_{twt})}$$

Equation 4-5

The model $Q_{ave}(t_{twt})$ can be calculated with Equation 4-4 with the estimated Q_{int} and background values of negligible attenuation in the water column $Q_{int} = 5000$. As the Q_{int} below the last horizon is unknown, this Q_{int} is set to the value of the last known layer. Therefore, the lowermost horizon for Q estimation should be lower than the investigation range.

4.3.4 Band Limited Impedance Inversion

An acoustic impedance inversion algorithm for Z_p based on the genetic algorithm described in Vardy (2015) has been implemented. As shown in Figure 4-5, this inversion algorithm optimizes a reflectivity model to match the seismic data. Integrating the reflectivity, the unscaled and bandlimited Z_p can be calculated. Here, a migrated seismic image with employed Q correction in the form of a gain correction is the data basis for the inversion. Z_p is derived by integrating the reflectivity model and using Z_p of water as a starting value. As the true scaling of the wavelet in relation to the recorded data is not known, the resulting Z_p is both bandlimited and unscaled.

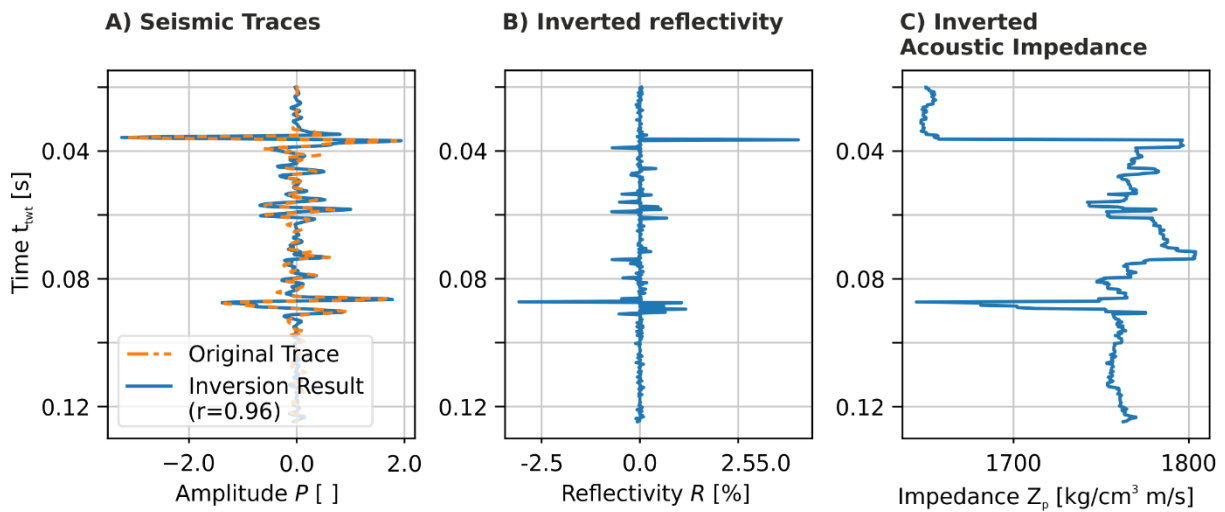


Figure 4-5: Exemplary bandlimited impedance inversion of CMP492 adjacent to CPT 3. A) Comparison of the seismic amplitudes of the original trace and the inversion result with a correlation coefficient (Pearson's R) of 0.96. For the example shown here, the attenuation has not been corrected. The results of the inversion are the (B) inverted reflectivity and the (C) bandlimited inverted acoustic impedance.

In general, inversion starts with the initialisation of the reflectivity models of a set number of individuals of the first generation. Each individual has the length and sampling of the time vector and is assigned a reflectivity in a range defined by the minimum and maximum Z_p to be expected, which is given in Table 4-2 with the remaining parameters for the inversion.

Table 4-2: Parametrisation of the genetic algorithm for impedance inversion. For the uncertainty estimate 1000 repetitions with the given parameters were executed.

Parameter	Value
Number of individuals in each generation	2000
Number of generations	1000
Crossover Probability	0.6
Mutation Probability	0.0015
Probability to be a reflector for initialisation	0.05
Reflectivity Range for initialisation	-58% to 58 %
Number of models for final result	100

To achieve a sparse solution, each sample is also assigned a random number in the range [0,1]. All reflectivity samples are set to zero whose random number is lower than a defined probability to be a reflector. So, if the time vector spans 100 ms at a sample rate of 4000 Hz, the time and the reflectivity vectors have a length of 400. At a probability of 5%, in average 20 reflectors are initialized at random times and with random reflectivity at every trace. Then, the optimization starts and is performed for a set number of iterations, which is the number of generations. In every iteration, first of all, seismograms are generated with the current model. The forward modelling is based on the convolution of a statistical seafloor wavelet with reflectivity models. Then the processes of selection, crossover and mutation are conducted. In the implemented stochastic remainder selection, better than average models are automatically carried forward, while the remaining population is filled up randomly from the whole population. So, some worse than average models are willingly lost. Those selected models are paired up randomly and a new population is generated by piecing together the models of each pair at a random location in the crossover operation. During the mutation, additional and random reflection events are added to the new models. Those new models are the starting point for the next generation. Performing the optimization for a set number of generations, the mean of a set number of the best fitting models is then determined to be the final result. Z_p is calculated recursively from the reflectivity model with a set starting value. Repeating the whole inversion process multiple times, a range of models fitting to the observed seismogram is generated. Analysing the statistical distribution of this range of models, the most probable model and the model uncertainty is determined. The most probable model is the mean of the models and the uncertainty is equal to the standard error of the mean.

In the current implementation and on workstation computers, one CMP is inverted in about one minute. As the code is parallelized, the inversion of a whole seismic section is rather fast. In our case with 60 cores, 60 CMPs were inverted in one minute. So, compared to other processes in a

typical near surface processing scheme, e.g., the modelling and subtraction of the multiple, the inversion is quite fast and scalable.

4.3.5 Scaling and Merging of the Band Limited Impedance with the Low Frequency Model

To compensate the various limitations of the seismic data set and estimate absolute, properly scaled Z_p , an algorithm for Band-Limited IMPedance inversion (BLIMP) based on Ferguson & Margrave (1996) has been implemented. As a first step, the linear trend of the estimated low frequency model and the high frequency Z_p inversion is subtracted. The detrended results are transformed to the frequency domain. A scaling factor is determined for the high frequency Z_p by the ratio of the L_2 -norms in the frequency range from 50-150 Hz. To merge the estimates and gain full bandwidth, a Linkwitz-Riley crossover filter with a characteristic frequency of 10 Hz for the unsmoothed and 40 Hz for the smoothed inversion results are defined. The high frequency Z_p is high-pass filtered, while the low frequency model is low-pass filtered and subsequently transformed back to the time domain. Finally, the scaled absolute Z_p is the sum of the filtered high and low frequency estimates and the linear low frequency trend.

4.3.6 Absolute Impedance Uncertainty Estimation

A stochastic analysis is performed to estimate the uncertainty of the final, scaled absolute Z_p . This uncertainty results from the combined uncertainties in the inversion flow (see Figure 4-3) which are described by their PDFs. A workflow of Z_p estimation and low frequency trend addition is implemented, in which the PDFs of the $v_{p,int}$ and the Q estimation as well as the transformation uncertainty $v_{p,int}-\rho$ are used as input parameters. Performing the workflow multiple times for a single CMP, the PDF and thus the uncertainty of the absolute Z_p can be estimated. The parameters of the inversion are given in Table 4-2.

4.3.7 Cone Penetration Testing

The in-situ testing data used to develop the geotechnical ground model for the joint interpretation was acquired in August 2015 during a geotechnical site investigation campaign onboard the commercial vessel M/V Bucentaur. The dataset consists of four downhole CPTs located along and less than 100 m away from seismic Profile He569-GeoB21-033 with varying total depths ranging between 45 and 60 m below seafloor (mbsf). They were acquired at relatively shallow water depths between 23.0 and 24.8 m relative to the Lowest Astronomical Tide (LAT). At two of the locations, additional sediment coring was performed within a lateral interval of approximately 5 m from the

original CPT site. A summary of the encountered water depth, total penetration of each borehole and its linear distance to the seismic line is provided in Table 4-3.

Table 4-3: General acquisition information from the used in-situ testing CPT and borehole sampling data. The water depth is referred to the echosounder depth reduced to the Lowest Astronomical Tide (LAT). The distance to profile was measured in a straight line, orthogonal to the location of the seismic Profile He569-GeoB21-033.

Name	Data type	Water Depth [m LAT]	Penetration [m]	Distance to Profile [m]
CPT 1	CPT	24.8	45.32	20.46
CPT 2	CPT	24.2	59.81	56.40
CPT 2*	Sampling borehole	24.2	45.60	51.66
CPT 3	CPT	23.4	49.85	81.38
CPT 4	CPT	23.0	60.37	10.06
CPT 4*	Sampling borehole	23.0	60.7	14.88

The data acquisition was done using WIP/WINSON downhole tools in conjunction with rotary drilling using bentonite-water mixture as the drilling fluid. Before the drill string went into the seabed, a SEACLAM frame was placed on the seafloor. On the sampling boreholes CPT 2* and CPT 4*, 53 to 72 mm-diameter and approximately 1 m long individual core sections were collected on a liner, described, photographed, and sampled onboard for laboratory measurements according to the procedure described by the norm ISO 14688-1/2 (2017) and ISO 14688-2 (2017). Core catchers were used in non-cohesive (i.e., sandy) intervals to ensure maximum core recovery. The downhole CPT were conducted in agreement with the norm ISO 22476-1 (2022). During logging operations, a WINSON tool operated with a hydraulic-electric umbilical was used, together with a 10 cm² Piezocone (F5) and a 5 cm² cone (F8). This setting provided real-time readings of the probe at a 0.02 m sampling interval from three measured parameters: cone tip resistance qc , sleeve friction fs and pore pressure u_2 .

The raw CPT curves were then processed to remove acquisition artefacts and other anomalous values. The incoming acquired data were first imported and assessed using the geotechnical software CPeT-IT. A depth correction was carried out using the given inclinometer data. Then, outliers and push footprints were corrected, as shown in Figure 4-6.

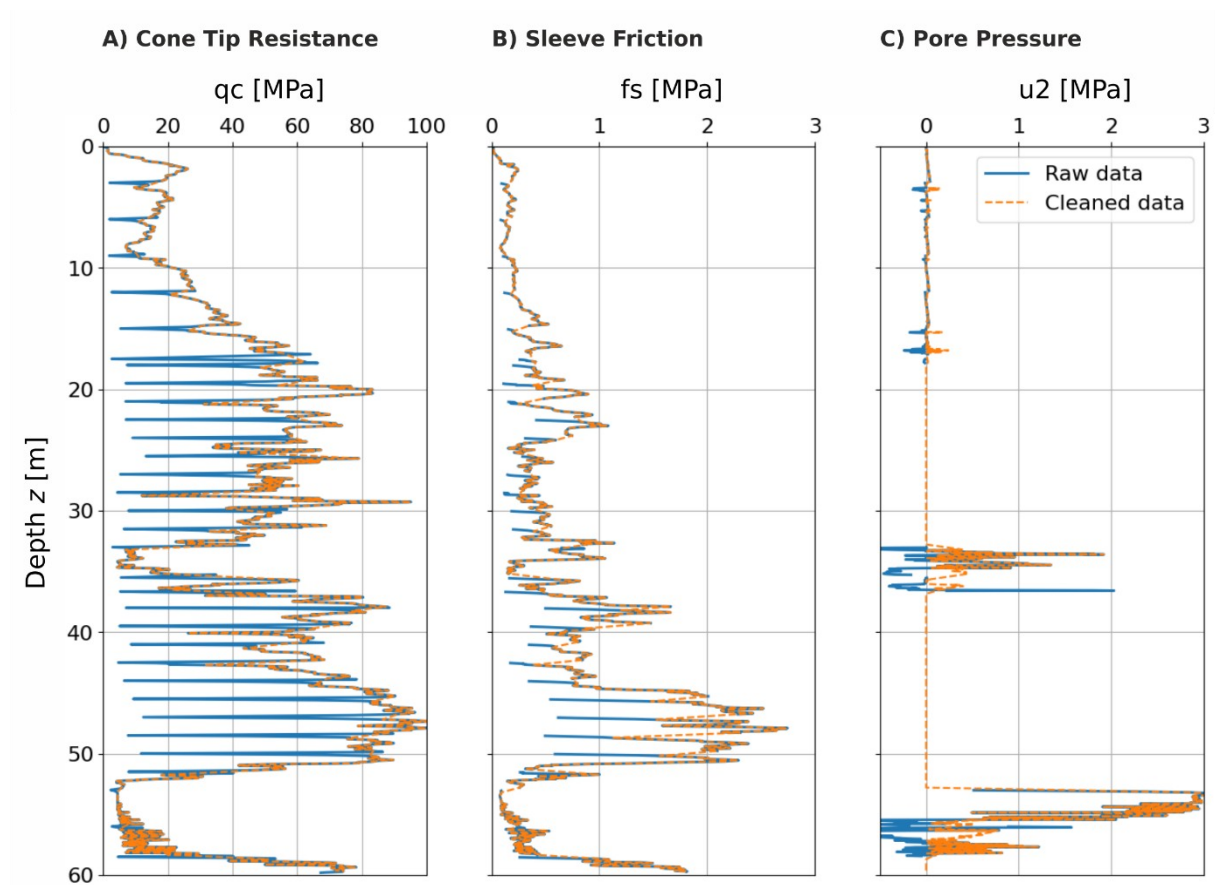


Figure 4-6: Example of the raw CPT data cleaning process. Measured cone resistance (q_c), sleeve friction (f_s) and pore pressure (u_2) from CPT 2. The blue curves show the raw values, and the dashed orange line indicates de cleaned curves.

Based on the standards and recommendations published by Lunne (2002) and Robertson (2016) for quantitative CPT interpretation, the first ten data points at the beginning of every push were removed as well as data with no associated sleeve friction, to avoid contaminating future estimations. After correcting the logs, additional geotechnical parameters derived from the three initial measurements were calculated after the relationships established by Robertson (2016). These estimated values included corrected cone resistance qt , normalized cone resistance Qtn , Friction ratio Fr , normalized Soil Behaviour Type $SBTn$, relative density Dr , shear wave velocity v_s and elastic moduli. The exported processed logs were converted into LAS for their integration with the seismic data. Particularly the $SBTn$ values were used for further integration into the geotechnical ground model and subsequent joint data interpretation together with the quantitative model obtained from the seismic interpretation stage, especially in the CPT locations without an associated sampling borehole.

4.3.8 Depth Conversion

A depth conversion step is implemented to reduce the misfit between ground truthing data and seismic results such as layer depths and the Z_p model. Additionally, uncertainties for unit depths and thicknesses can be estimated at this step.

For this purpose, the $v_{p,int}$ model is scaled with a constant factor for each unit to match known unit boundaries from the CPTs. If one layer does not have ground truth, this unit will be scaled with the next layer. Units without depth fix points are attributed with a 2% $v_{p,int}$ error with a linear taper towards fixed horizons. The 2% error is selected as this error fits to the maximum uncertainty of 25 m/s for the $v_{p,int}$ estimate. A range of possible factors is tested to estimate the best fit. The Root Mean Square Error is calculated as a measure of fitness. The variable z_j for the depth at the base of layer j is the sum of the thicknesses of all layers above determined from the layer thickness in time ΔT and $v_{p,int}$:

$$z_j = \sum_{i=1}^j \left(\frac{\Delta T_i}{2} \cdot v_{p,int,i} \right)$$

Equation 4-6

The uncertainty of the depth estimate is constituted, as a maximum error approximation, by the error of the fit of the known ground truthing points quantified by the standard deviation, the seismic resolution and possible $v_{p,RMS}$ errors for intervals without fix points. For the inversion results, the theoretical resolution limit given by the Widess' criterion, which is defined as $\lambda_d/8$ (Widess, 1973; Kallweit & Wood, 1982) is used. This limit applies as thickness and reflection coefficient changes below this limit cannot be differentiated. The composite reflection event shape of two interfaces, which are closer than the Widess' criterion, does not change.

4.4 Results

In the reflection seismic image four units with a relatively indistinct internal structure have been identified as shown in Figure 4-7. The Horizon H2 with a reverse polarity compared to the seafloor reflection forming a dome like structure at about $t_{twt} = 75-100$ ms and a 110 ms deep and about 600 m wide incision in the eastern part of the profile are the most prominent features. Building a low frequency model from $v_{p,int}$ and estimating Q on selected horizons, the absolute Z_p and the

uncertainty are quantified. In the Z_p estimate, two low Z_p layers – one of them correlating to H2 – as well as some low Z_p anomalies are observed. The background Z_p and Q values correspond to sandy deposits. The CPT measurements and the borehole information generally show sandy deposits with a dominant clay and peat layer in 33-50 m depth below the seafloor with a thickness of 6 m maximum. In the western section of the profile, a 1-2 m thin clay layer is found 15-20 m above this dominant clay and peat layer. Coarser sediments including gravels are found in between the clay layers. Bringing together the CPT and seismic interpretation, fix points for depth conversion are determined. The determined interval velocities are scaled to match the calculated depths from the seismic results to the CPT fix points. The seismics are then converted to depth and uncertainties are estimated.

4.4.1 Reflection Seismic Image

Four main units have been identified based on a seismic facies classification and the reflection terminations. The lowermost Unit U1 is characterized by a parallel to subparallel internal reflector configuration with generally horizontal to slightly wavy and weak reflectors, as shown in Figure 4-7. This unit is bound by the Horizon H1 at the top in depths of $twt \approx 160-190$ ms, which is an unconformity defined by downlaps of the overlying strata. The reflection strength of H1 diminishes towards the east. So, H1 is barely traceable in the eastern half of the profile where it forms a slight bulge. The overlying Unit U2 with the greatest apparent thickness of about $\Delta twt = 80$ ms shows parallel internal reflectors with laterally strongly variable amplitudes. Those internal reflectors are parallel to H2 which is the upper bound of U2 and the most prominent reflector in the seismic section. Two peg-leg multiples of H2 are visible in the section with distances of once and twice the t_{twt} to the seafloor (SF in Figure 4-7: 33-37 ms). Horizon H1.1 in Figure 4-7 is the strongest internal reflector of the unit at a distance $\Delta twt = 20$ ms to H2. Horizons H2 and H1.1 show a reverse polarity compared to SF and form a dome-like structure at the centre of the section with a relative elevation of about 20 ms and a width of about 2 km. A 110 ms deep and about 600 m wide incision in the eastern part of the profile centred at the 7 km mark cuts both H2 and H1.1 forming steep erosional flanks.

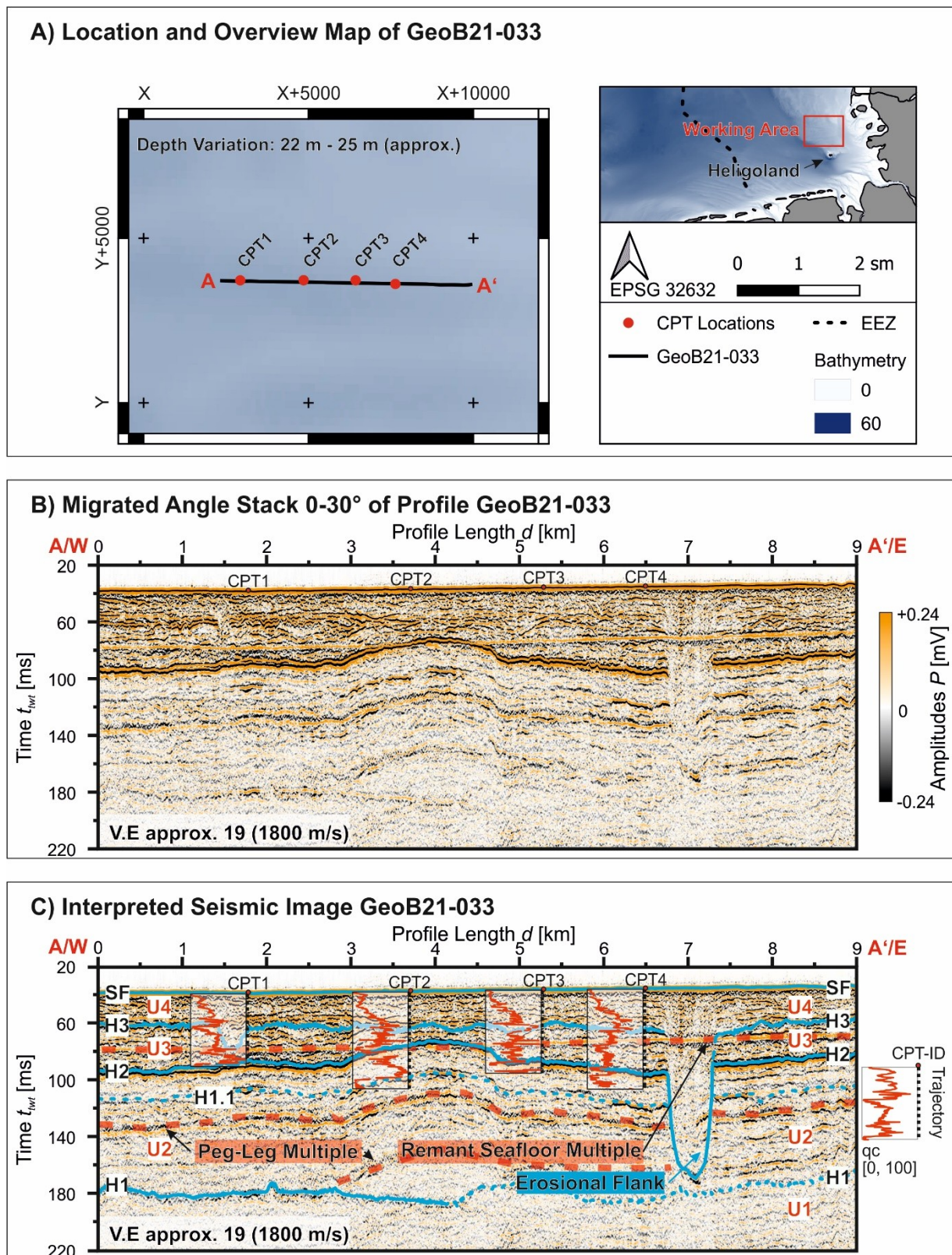


Figure 4-7: Reflection seismic image He569-GeoB21-033 and the corresponding interpretation. A) Location map of the profile in the German North Sea in the north of the island Heligoland. The profile is approximately west-east oriented and 9.0 km long. B) Seismic image in the form of a migrated angle stack with an angle range of 0-30°, which is the basis for the inversion. C) Interpreted seismic image with four main Units U1-U4, which are bounded by the seafloor (SF) at about 40 ms and the Horizons H1-H3. Horizons H2 and H3 show a prominent, U-shaped erosional feature around profile distance 7 km. Remnants of the seafloor multiple are visible around 80 ms, while a peg-leg multiple following H2 at 40 ms distance is observed between 110-140 ms. The tip resistance q_t of the Cone Penetration Test (CPT) is overlain on the seismic image using a brute processing velocity model for the time-depth conversion.

The internal structure of Unit U3 above H2 is predominantly chaotic to hummocky in the upper half of the unit. Unconformity H3 forms the upper bound of the unit and is defined by toplaps and erosional truncations at channel-like incisions. The base of the deep incision cutting H1.1 and H2 mentioned above seems to coincide with H3. Although the multiple suppression reduced the strength of the primary seafloor multiple, some remnants of the multiple are visible at $t_{twt} = 66-76$ ms.

The uppermost Unit U4 in between H3 and SF is characterized by a hummocky to lenticular internal structure with plenty channel like incisions with widths ranging from approximately 500 m to several tens of meters. The amplitudes are generally laterally very variable, but greatest close to H3. So, the Unconformity H3 is also marked by an amplitude decrease.

4.4.2 Low Frequency Model

To derive densities and thus Z_p from the $v_{p,int}$ estimates, the empiric relation described by Raymer et al. (1980) has been fitted to near surface sediments. The parameters given in Table 4-4 are optimized to match the properties of near surface sediments taken from McCann & McCann (1969), Shumway (1960), Hamilton (1970, 1972), Breitzke (2000), Stevenson et al. (2002), Robb et al. (2006) and the BSH Pinta Data Base (2021) for the wind farms N0307, N0308 and O0103. From Breitzke (2000), the cores PS2567-2 from the Meteor Rise characterised by opal rich and calcareous sediments and GeoB2821-1 from the Rio Grande Rise consisting of carbonates were excluded.

Table 4-4: Parameters for the empiric velocity-density relation by Raymer et al. (1980). The parameters were manually optimized to fit to the properties of near surface sediments taken from McCann & McCann (1969), Shumway (1960), Hamilton (1970, 1972), Breitzke (2000), Stevenson et al. (2002), Robb et al. (2006) and the BSH Pinta Data Base (2021) for the wind farms N0307, N0308 and O0103.

Porosity Limit Continuous Rock Matrix: ϕ_R	37%
Porosity Limit Suspension: ϕ_S	53%
P-Velocity Matrix: $v_{p,M}$	3100 m/s
P-Velocity Fluid: $v_{p,F}$	1550 m/s
Density Matrix: ρ_M	2750 kg/m ³
Density Fluid: ρ_F	1000 kg/m ³

As shown in Figure 4-8, the empiric relation is defined at velocities greater than 1480 m/s. The standard deviation of the difference of the measured ρ and the estimated ρ is 54 kg/m³. Considering a maximum $v_{p,int}$ estimation error of 25 m/s, the transformation uncertainty error by the $v_{p,int}$ uncertainty at the region of the steepest slope of the transformation curve is

$\rho(v_p = 1505 \text{ m/s}) - \rho(v_p = 1480 \text{ m/s}) = (1714 - 1533) \text{ kg/m}^3 = 181 \text{ kg/m}^3$. Considering all uncertainties, the maximum error of Z_p is supposed to be at the range of $25 \text{ m/s} \cdot (181 \text{ kg/m}^3 + 54 \text{ kg/m}^3) = 5875 \text{ kg/m}^3 \text{ m/s} \approx 0.006 \text{ kg/cm}^3 \text{ m/s}$. Assuming a minimum Z_p of $2 \text{ kg/cm}^3 \text{ m/s}$, e.g., representative for clays, to get an estimation of the maximum relative error, the total transformation error sums up to a maximum relative error of 0.3 %.

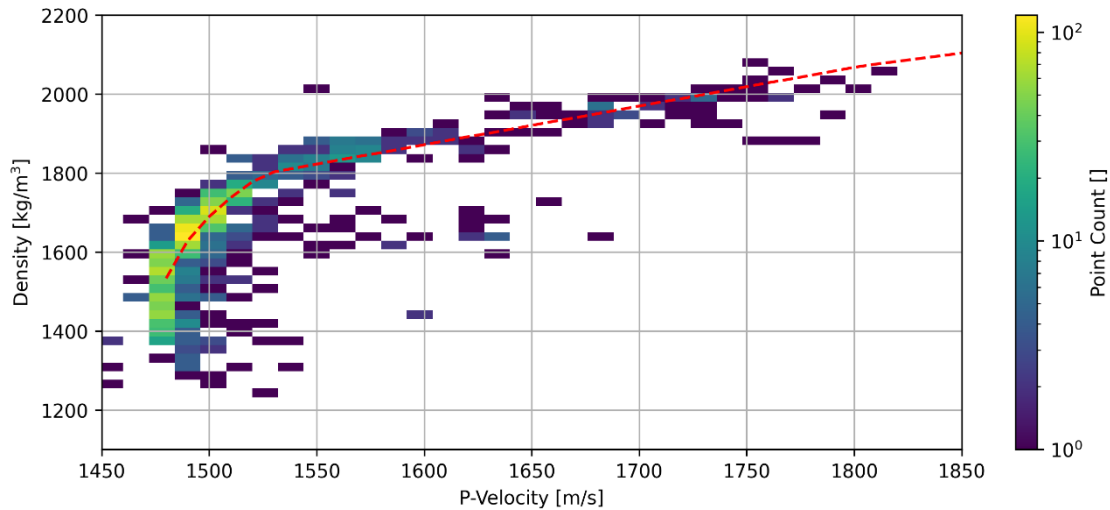


Figure 4-8: Cross-plot of the sediment density and P-Wave Velocity taken from McCann & McCann (1969), Shumway (1960), Hamilton (1970, 1972), Breitzke et al. (2000), Stevenson et al. (2002), Robb et al. (2006) and the BSH Pinta Data Base (2021) for the wind parks N0307, N0308 and O0103 with an overlay of the empiric density to P-Wave velocity relationship by Raymer et al. (1980) whose parameters are given in Table 4-4 .

The four horizons used for the $v_{p,int}$ estimation match approximately H1, H1.1, H2, H3 and SF. Thus, the low frequency model extends to depths of approximately $twt \approx 160\text{-}190 \text{ ms}$ and forms a laterally variable five-layer model. The highest interval velocities and thus Z_p are found in U3 and U4. To build the low frequency model shown in Figure 4-9, $v_{p,int}$ estimates with an uncertainty larger than 25 m/s for U1 and 10 m/s for U2-U4 were rejected for data cleaning purposes to restrict the model to valid and accurate estimates. The resulting interval velocities there then smoothed with a running median filter of 11 CMPs and converted to Z_p as described above. The resulting Z_p are typical for silty to clean to gravelly sands.

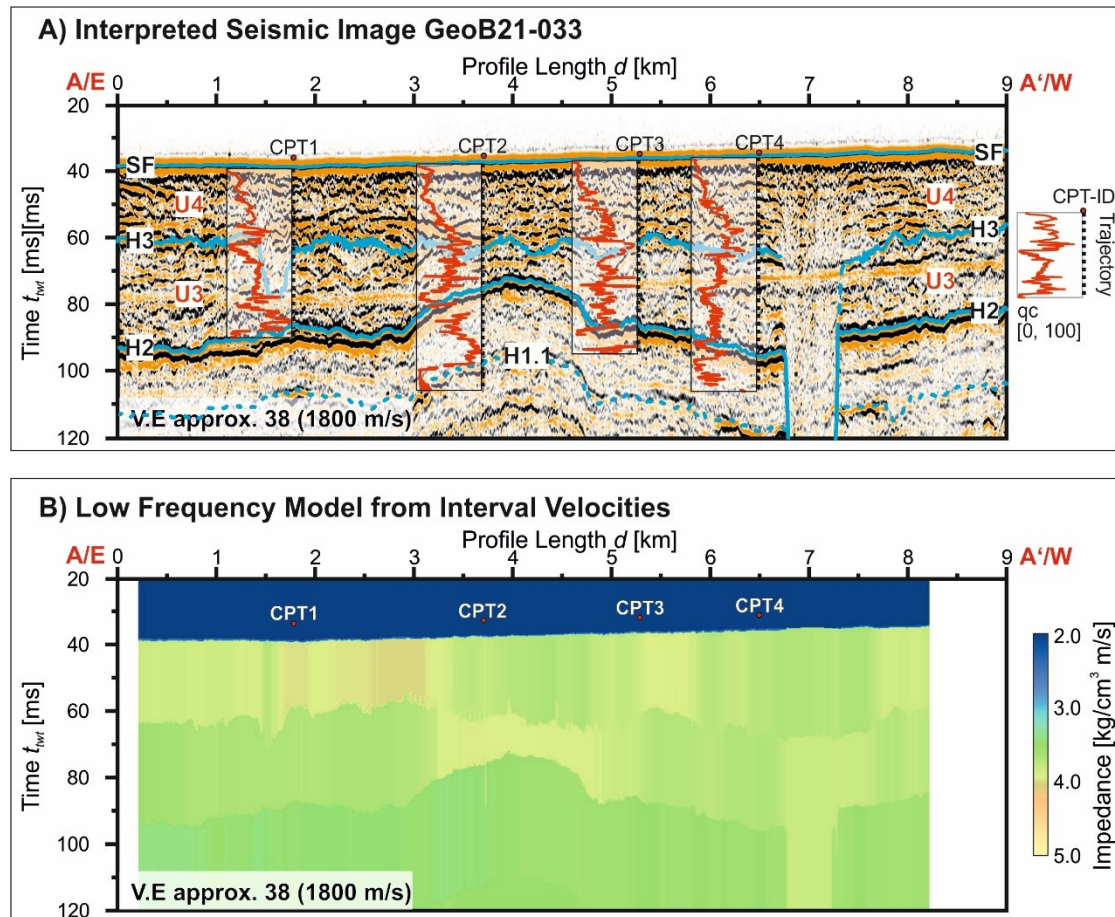


Figure 4-9: Low frequency model derived from the travel time curve inversion. A) Upper part of the interpreted seismic image of He569-GeoB21-033 matching to Figure 4-7. The tip resistance q_c of the Cone Penetration Test (CPT) measurements is overlain using a brute processing velocity model for the time-depth conversion. B) Low frequency impedance model derived from the interval velocity estimation and impedance transformation. The impedances shown are typical for sandy deposits. Highest impedances are found in U3 and U2.

4.4.3 Attenuation Model

The spectra of averaged autocorrelations at selected horizons have been used to determine Q_{ave} and subsequently Q_{int} . Figure 4-10 shows an example of this approach. At the location of CPT 3, the normalized spectra at the previously described Horizons H2 and H1 are determined and significantly shifted towards lower frequencies compared to the seafloor reflection. Additionally, the theoretic spectra changes for a realistic range of Q_{ave} values were modelled. Based on the fit of the modelled spectra to the determined spectrum, PDFs for the Q_{ave} estimation are calculated. Those PDFs show relatively broad peaks but indicate strong attenuation in the upper Units U3+U4 at the range of $Q_{ave} = 30-40$ and lower attenuation for U2 at about $Q_{ave} = 90$. The PDFs are then used as an input parameter for the Q_{int} estimation. In Figure 4-10C, the uncertainty limits indicate the 68.3% confidence intervals. Compared to the Q_{ave} estimation, the Q_{int} shows even broader uncertainty intervals, although there is evidence for strong attenuation in the upper units and lower attenuation in the lower unit.

In Figure 4-10A and B the analysis of Horizon H3 is also included. For the spectra it is observed that the shift towards lower frequencies is relatively small compared to the seafloor spectrum. Consequently, the peak of the PDF for H3 is lower and broader compared to H2 and H1 leading to larger uncertainties. In a first attempt, H3 has also been included in the Q_{int} estimation. In this analysis, it has been found that the uncertainties are exceptionally high, especially at locations where U3 is thin. Due to those large uncertainties, H3 has been excluded from the Q estimation. U3 and U4 are treated as one unit in the Q_{int} model.

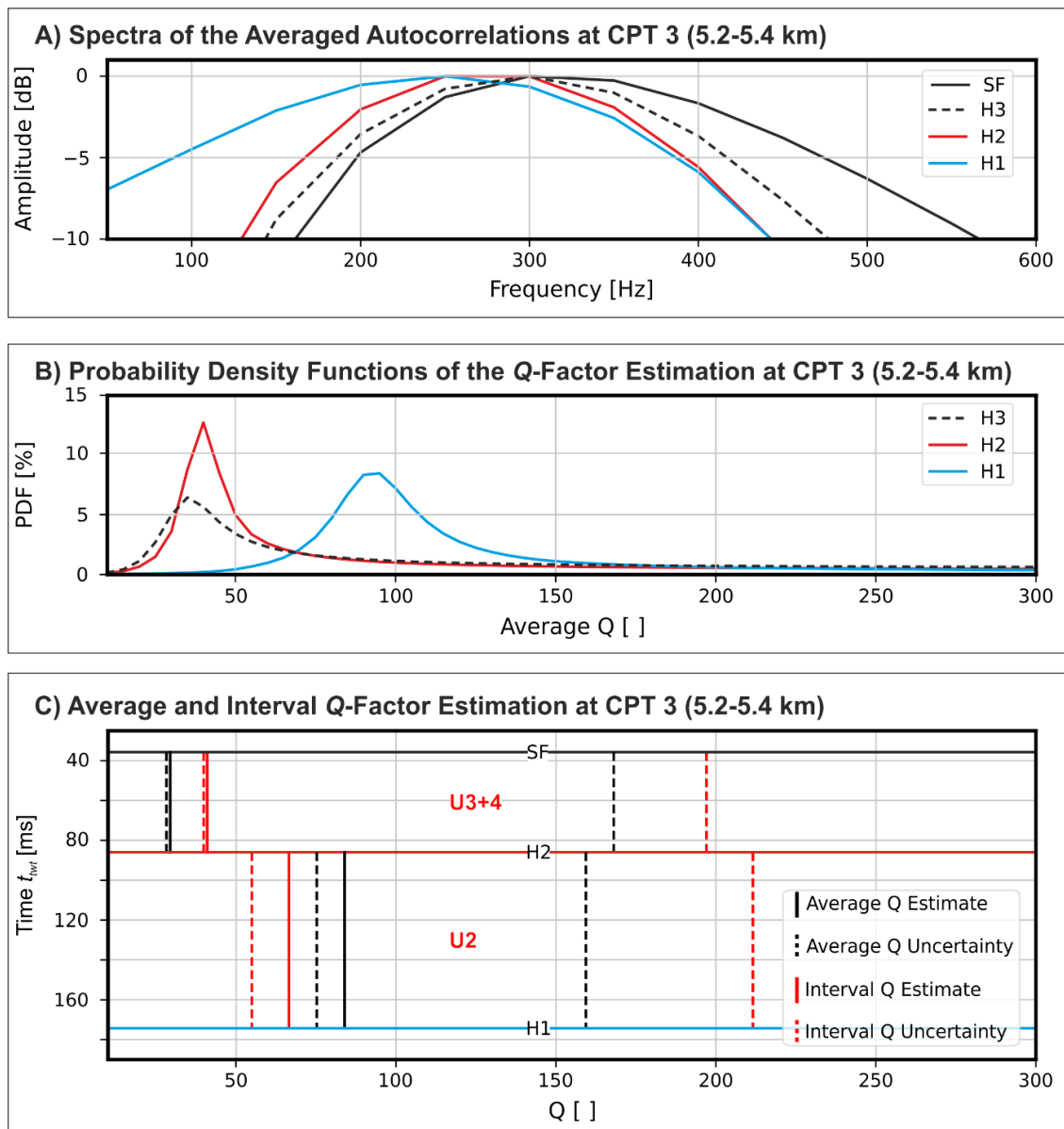


Figure 4-10: Attenuation Quality Factor Q estimation at CPT 3 for an averaged section of 0.2 km from profile length 5.2-5.4 km (CMP 480-500 with a spacing of 10 m). A) Normalized frequency spectra of the averaged autocorrelations showing a clear shift to lower frequencies for the Horizons H2 and H1 compared to the seafloor reflection. B) Probability Density Function (PDF) of the average Q -Factor estimation indicating values around 40 for H2 and 95 for H1. C) Average and interval Q estimates with an uncertainty estimation (68.3% confidence intervals). Low Q values corresponding to high attenuation are observed for the Unit U4 and U3 between SF and H2. Moderately high Q values are observed for U2 between H2 and H1. The range of errors, especially for the upper limit of the uncertainty is larger than the mean value.

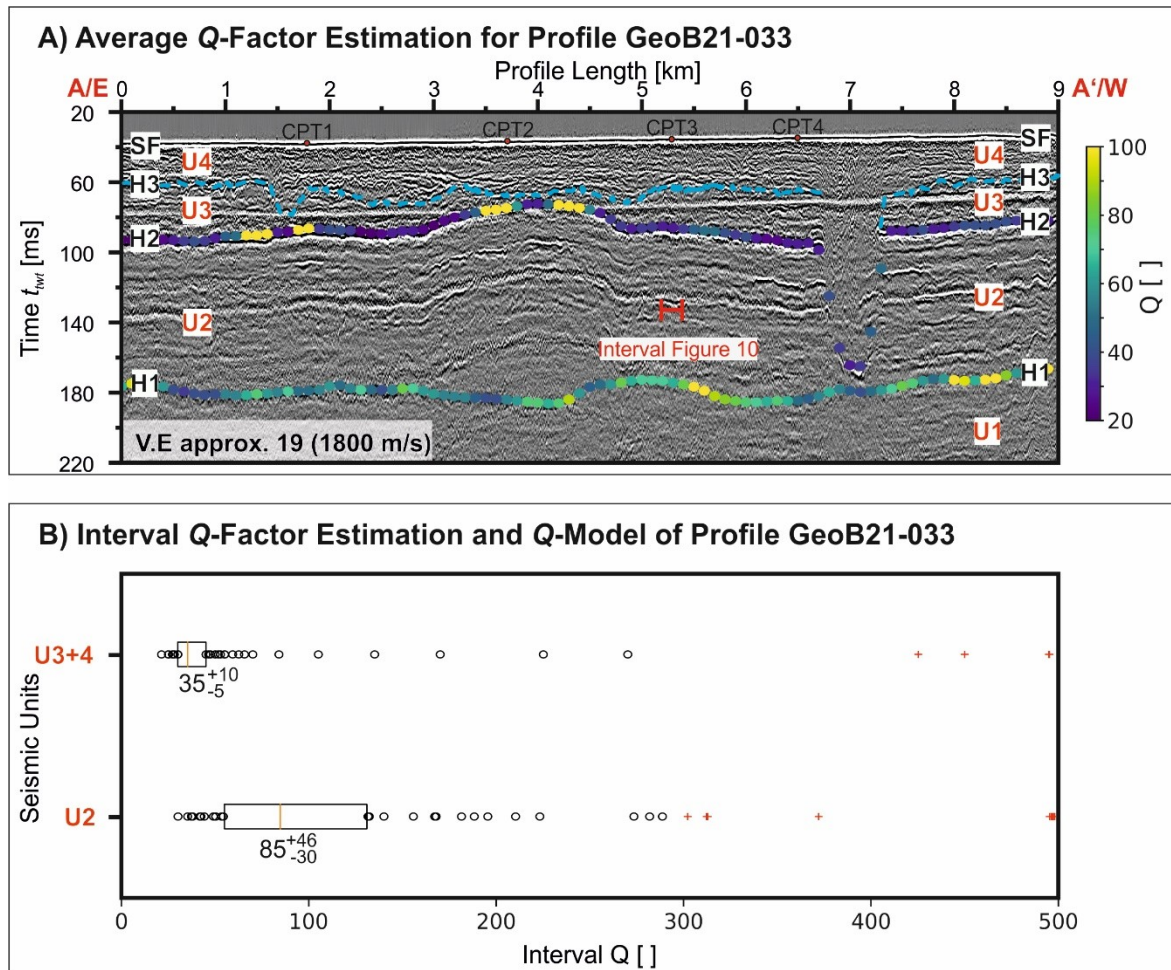


Figure 4-11: Average and interval attenuation Quality Factor Q estimation for the Profile He569-GeoB21-033, see Figure 4-7 for a location map and uninterpreted seismic image. A) Average Q -values at the Horizons H2 and H1. H3 is indicated by a stiped line as this horizon has not been included for the attenuation estimation. The autocorrelations of 20 CMPs in intervals of 10 CMPs have been averaged to determine the average Q . B) Boxplots of the interval Q estimates for the Units U2 and U3+4 inverted from the average Q values in (A). Assuming that the Q -values in the units are constant, those boxplots can be used to determine the layer properties and to build an attenuation model. Interval Q -values above 300 are excluded from the boxplots and plotted as red crosses, as such high Q -values are outside the range of possible values.

The Q analysis is executed for the whole profile on the two horizons selected as shown in Figure 4-11. It is observed that H2 is generally characterized by strong attenuation in the range of approximately $30 < Q_{ave} < 45$. As H2 is the first horizon analysed, Q_{ave} at this horizon is equal to Q_{int} of U3 and U4. There are two exceptions close to CPT 1 and CPT 2, where low attenuation is reported for H2. Those locations coincide with small thicknesses of U3. Generally higher Q_{ave} and thus lower attenuation is observed for H1, an average estimate of $Q_{int} = 85^{+46}_{-30}$ is found for U2. The lateral variation of Q_{int} is smaller than the uncertainty of the Q_{int} estimate of one CMP (compare Figure 4-10 and Figure 4-11) indicating negligible lateral variation. With the given uncertainty ranges and small lateral variation, the layer properties can be inferred from the boxplot and used for Q_{int} model building.

4.4.4 Impedance Uncertainty Estimation and Impedance Inversion Results

Combining Q correction, Z_p inversion as well as the scaling and merging with the low frequency model into a stochastic framework, the uncertainty of the absolute Z_p estimation is calculated. The PDFs of the Q and $v_{p,int}$ estimation and the ρ transformation uncertainty shown in Figure 4-11 are used as input parameters. Conducting 1000 repetitions, the seismic trace is amplitude corrected with the determined Q_{int} model and inverted. Although the uncertainty of the Q_{int} model is large, the scattering of the seismic amplitudes is relatively narrow and no trend, e.g., of increasing uncertainty with t_{twt} is observed. In contrast, the band limited impedance inversion result clearly shows increasing uncertainty with increasing t_{twt} . After scaling and merging of the band limited Z_p with the low frequency trend, uncertainty is greatly reduced. Merging at $f_c = 40$ Hz, the uncertainty is approximately reduced to the level of uncertainty of the low frequency trend of about 5%. This relative error is determined by the mean of the standard deviation divided by mean value. A lower merging frequency such as $f_c = 10$ Hz results in a greater relative contribution of the band limited Z_p to the absolute Z_p estimate and thus greater uncertainties of about 9%.

Conducting only one inversion run, the Z_p estimate for the whole profile is given in Figure 4-13 with a merging frequency of $f_c = 10$ Hz. In Unit U4, a strong trend of increasing Z_p from about $2.5 \text{ kg/cm}^3 \text{ m/s}$ at the top of the unit to $4 \text{ kg/cm}^3 \text{ m/s}$ at the base is observed. In the western part of the profile, several spots with lower Z_p around $2.5\text{-}3 \text{ kg/cm}^3 \text{ m/s}$ of about 0.1 km width and few milli-seconds depth can be observed at H3 at the base of U4. In U3, Z_p shows a less distinct trend varying around $3.5\text{-}4.2 \text{ kg/cm}^3 \text{ m/s}$. Highest Z_p are found above the dome-like structure in the central part of the profile. Beneath H2 at the top of U2, the lowest Z_p values of about $2.5 \text{ kg/cm}^3 \text{ m/s}$ are found. Mostly, those low Z_p are restricted to a thin layer of about $3\text{-}5 \text{ ms}$ thickness with a sharp step to the background value. At some locations throughout the profile, the increase from the low Z_p towards the background value is more gradual. Another layer of low Z_p is found at Horizon H1.1. Apart from those thin layers, U2 is characterized by lower Z_p at around $3.5 \text{ kg/cm}^3 \text{ m/s}$ with relatively little variation compared to U3.

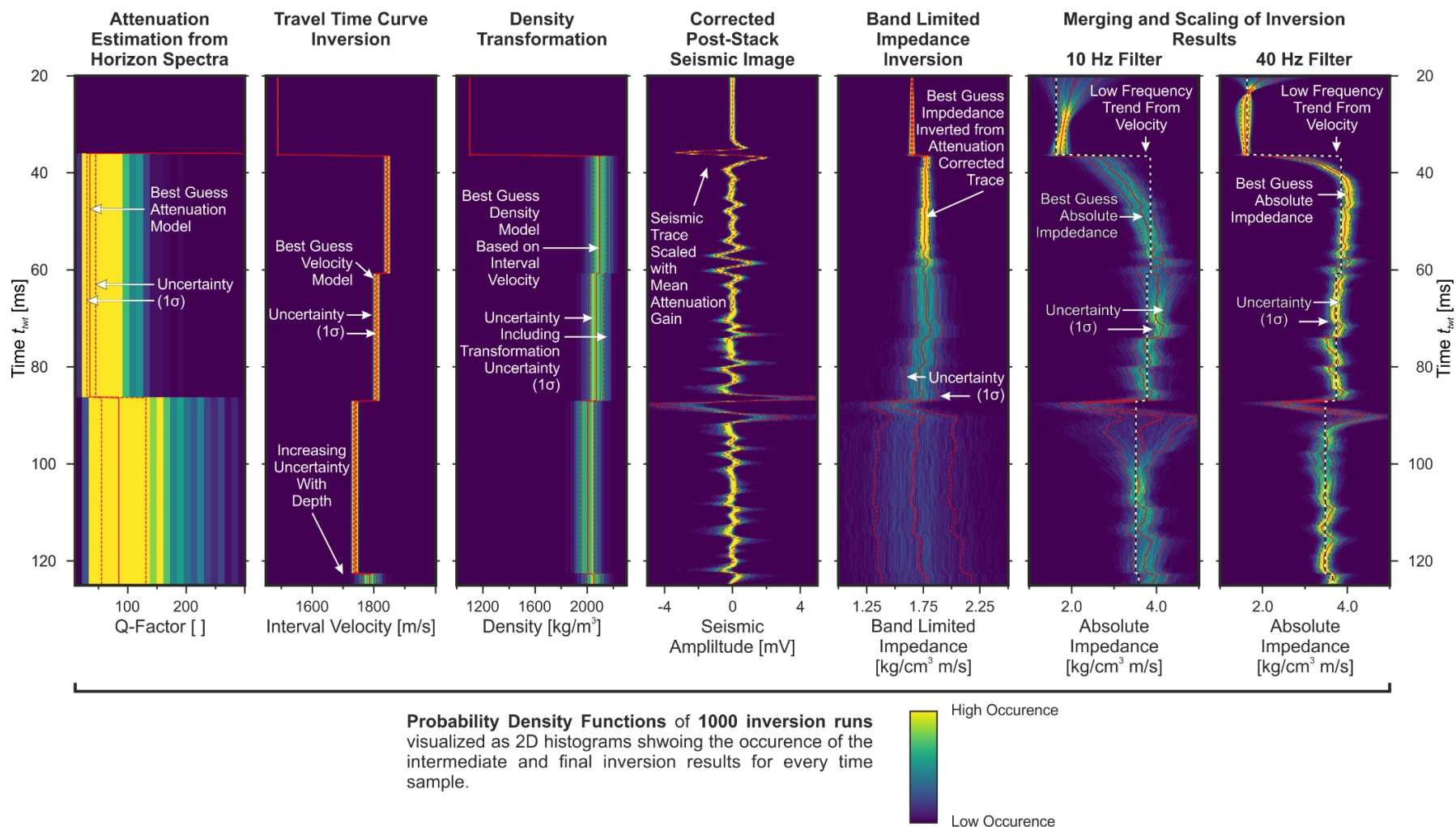


Figure 4-12: Uncertainty estimation of the absolute impedance based on 1000 repetitive inversion runs of the inversion work flow (Figure 4-3) at CPT 3 (CMP 492) using probability density functions of the attenuation Quality Factor Q and the interval velocity as input. The density is derived from the interval velocity based on the transformation curve shown in Figure 4-8. The Q -Factor is used to scale the post-stack seismic trace before the bandlimited impedance inversion. The probability density function of the seismic amplitude shows the occurrence of the modelled seismic traces after inversion. The band limited impedance is not properly scaled, the low frequency trend is wrongly estimated and there is a strongly increasing uncertainty with depth. After the merging and scaling of the inversion results, an absolute impedance estimation is reached.

4.4.5 Cone Penetration Testing

The four CPT measurements and two associated boreholes located along seismic Profile He569-GeoB21-033 show a 60 m thick sequence of fine to coarse sand deposits intercalated by laterally variable fine-grained layers composed mainly of peat and clay, with a thickness ranging between 1 and 6 m. From top to bottom, the encountered sequence begins with U4 (Figure 4-13), a poorly sorted fine to medium sand with a coarsening downwards trend, according to the core descriptions from the sampling boreholes. This interval is characterized by increasing qt values, ranging between 10 and 60 MPa for all four CPT measurements, which agree with the observed downhole grain size variation. Additionally, $SBTn$ values of 6 and 7 were calculated for this interval, implying that this unit overall behaves as a clean - silty sand varying to a gravelly - dense sand towards its base.

Underlying this deposit, a 1-2 m thick clay layer was found at 15-20 mbsf. This fine-grained interval was only present in the sampling borehole CPT 2* and it is associated with a marked decrease in qt values, from 60 to 5-10 MPa, coupled with an increase in Fr and n_2 , indicative of fine-grained and non-cohesive materials. This is supported by a calculated $SBTn$ ranging between 3 and 4 and consistent with a combination between clay – silty clay and silt mixtures.

Since these observations could only be made in the westernmost CPT locations (CPT 1 and CPT2), it is thought that the described layer is discontinuous, pinching out towards the east and constrained to the western section of the profile, where e.g., the variation in the qt curve is more apparent (Figure 4-13).

Below the local soft layer, the sequence continues with U3 (Figure 4-13), a 15-20 m thick, middle to coarse sand with gravel intervals towards the middle of the sequence that was described in both sampling boreholes. This interval is characterized by increasing qt values, that reach a maximum of 90 MPa at approximately 25 mbsf in the centre of the profile (CPT 3) and then decrease slightly towards the base of the unit. This results in higher $SBTn$ values ranging from 6 to 8 throughout this interval, that suggest the presence of either coarser or more compacted/stiff sands throughout the profile.

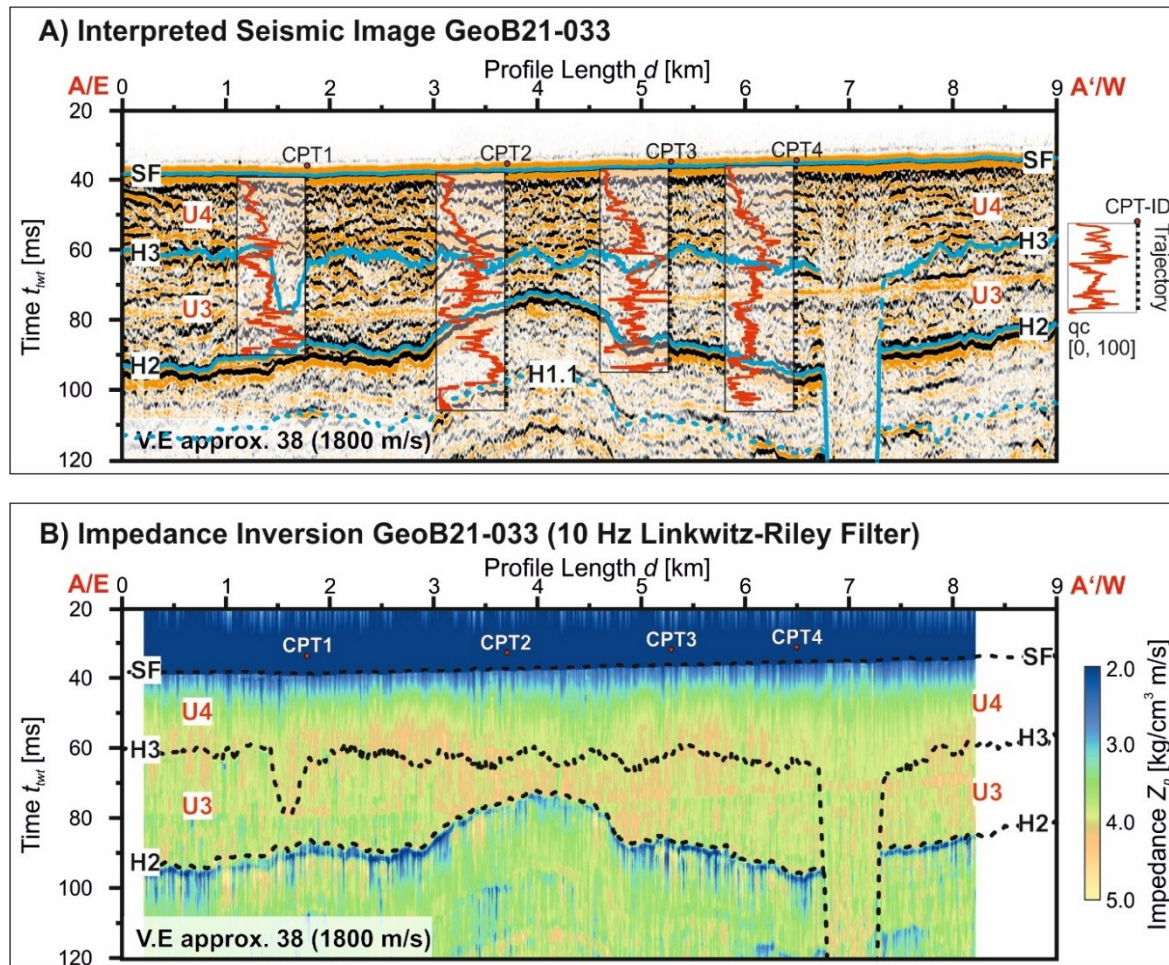


Figure 4-13: Time domain inversion results for the profile He569-GeoB21-033. A) Interpreted seismic image as shown in Figure 4-7. The tip resistance qt of the Cone Penetration Test (CPT) measurements is overlain using a brute processing velocity model for the time-depth conversion. B) Impedance inversion result in which the band limited impedance has been merged with the low frequency trend with a 10 Hz Linkwitz-Riley Filter.

A 3 to 6 m thick peat and organic rich clay layer with wood fragments is described between 33-50 mbsf in both sampling boreholes. There is a strong relationship between the appearance of this fine-gained interval and a certain CPT signature marked by a sudden decrease in qt curve coupled with an increase in Fr ($> 5\%$ up to 8-10 %) and $u2$ values (up to 2 MPa) that oftentimes is accompanied by a discontinuity on $u2$ curve. The calculated $SBTn$ value 3 suggests that the interval is present in all four CPT and is indicative of a clay – silty clay material behaviour. The overall unit thickness, composition, low Z_p , and its distinctive CPT signature made it possible to trace this layer through the Profile He569-GeoB21-033, which is marked by Horizon H2 (Figure 4-13).

Below this dominant clay layer there is a 20 m thick middle to coarse sand deposit, characterized by a considerable increase in qt , ranging between 80-90 MPa. The resulting $SBTn$ values of 6 and 8 are consistent with an overall sand material behaviour, which varies to very stiff around 55 m,

which may have given some problems to retrieve cores since there is no sampling borehole description available for this interval in CPT 2*. At the base of the entire encountered sequence, from 58 m downwards, a last 2 m clay layer could only be described in CPT 2*. This is supported by a noticeable drop in the qt curve towards the bottom of the CPT 2 measurement below the higher values from the overlying stiffer unit that is shown in Figure 4-13, where the Horizon H1.1 could be traced throughout Profile He569-GeoB21-033.

4.4.6 Depth Conversion

The low Z_p layer below Horizon H2 and the thick, dominant clay layer in the boreholes as well as the CPTs are correlated and constitute the basis for depth conversion. In Table 4-5, the calibration points for the depth conversion are given as well as the reference horizons. It is assumed that the CPT measurements start at the seafloor. The upper boundary of the clay layer is then used as fix points of the CPTs. This boundary is identified by the steepest descent of qt . Similarly, the upper boundary of the low Z_p layer below H2, identified by the steepest descent of Z_p , is used as fix points of the inversion results. With the seafloor and the Horizon H2 considered fixed, interval velocities of U4 and U3 are scaled by a factor of 0.93 to obtain an optimum match between CPT depths and seismic depths. The standard deviation of the misfit is 0.5 m.

Table 4-5: Calibration points for depth conversion. The thick, dominant clay layer at the Cone Penetration Test locations and the low impedance layer below Horizon H2 are correlated for depth conversion.

Profile Distance (CMP Number)	CPT Depth (CPT Name)	Depth after fit (TWT)	Reference Horizon (Horizon of Travel Time Tomography)
1.78 km (842)	42 m (CPT 1)	41.5 m (87 ms)	H2 (V3 of travel time tomography)
3.7 km (650)	33 m (CPT 2)	33.9 m (76 ms)	H2 (V3 of travel time tomography)
5.28 km (492)	43 m (CPT 3)	43.4 m (86 ms)	H2 (V3 of travel time tomography)
6.5 km (370)	50 m (CPT 4)	50.7 m (96 ms)	H2 (V3 of travel time tomography)

After the scaling of the interval velocities, the corrected $v_{p,RMS}$ are calculated and the seismic image, the impedance inversion results as well as the horizon picks, which are shown in Figure 4-14, are converted to depth. The uncertainties associated with the depth conversion are determined by the sum of the standard deviation of the misfit, the resolution limit given by the Widess' criterion and a possible $v_{p,RMS}$ error for intervals without depth fix points of 2%. Therefore, the depth uncertainty of the fixed Horizons SF and H2 is at the range of 1 m, while the uncertainty for the unfixed horizons increases with increasing distance to the fixed horizons. As H3 is close to the fixed horizons, the uncertainty remains small with a mean uncertainty of 2.8 m (maximum 3.3 m), while the maximum uncertainty of H1 reaches 7.4 m.

Without the depth conversion and assuming an $v_{p,int}$ error of 2%, the depth uncertainty of the horizons increases with depth to maximum values of 1.6 m for SF to 6.4 m for H3 or H2 and 7.0 m for H1.

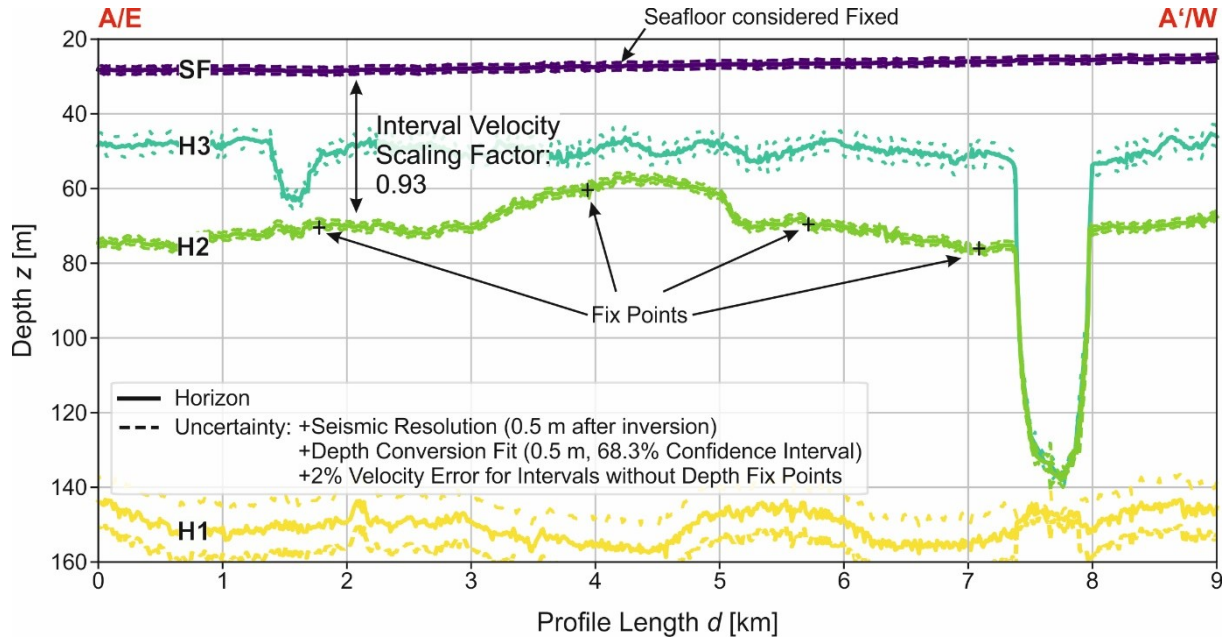


Figure 4-14: Horizon depths and depth uncertainty estimate. For the depth conversion the fix points listed in Table 4-5 are used. The uncertainty of the depth estimate is determined by the seismic resolution, the depth conversion fit and an estimated velocity error for intervals without depth fix points. The maximum uncertainty of the interval velocity estimate is 25 m/s (see “Low Frequency Model by Traveltime Curve Inversion and Density Estimation”) and thus a maximum error of 2% is assumed.

After depth conversion, CPT measurements and Z_p can be directly compared as shown in Figure 4-15. Merging at $f_c = 10$ Hz results in a moderately high correlation coefficient (Person’s R) $r = 0.69$ of Z_p and qt at the location of CPT 3. In general, Z_p shows a smoother curve progression than qt . Apart from this high frequency variation of qt , the first 20 m below the seafloor are characterised by both an increasing Z_p and qt . In between 50-70 m depth, a general match of local maxima is observed. The low Z_p layer at 70 m depth matches to a distinct and broad local minimum of qt .

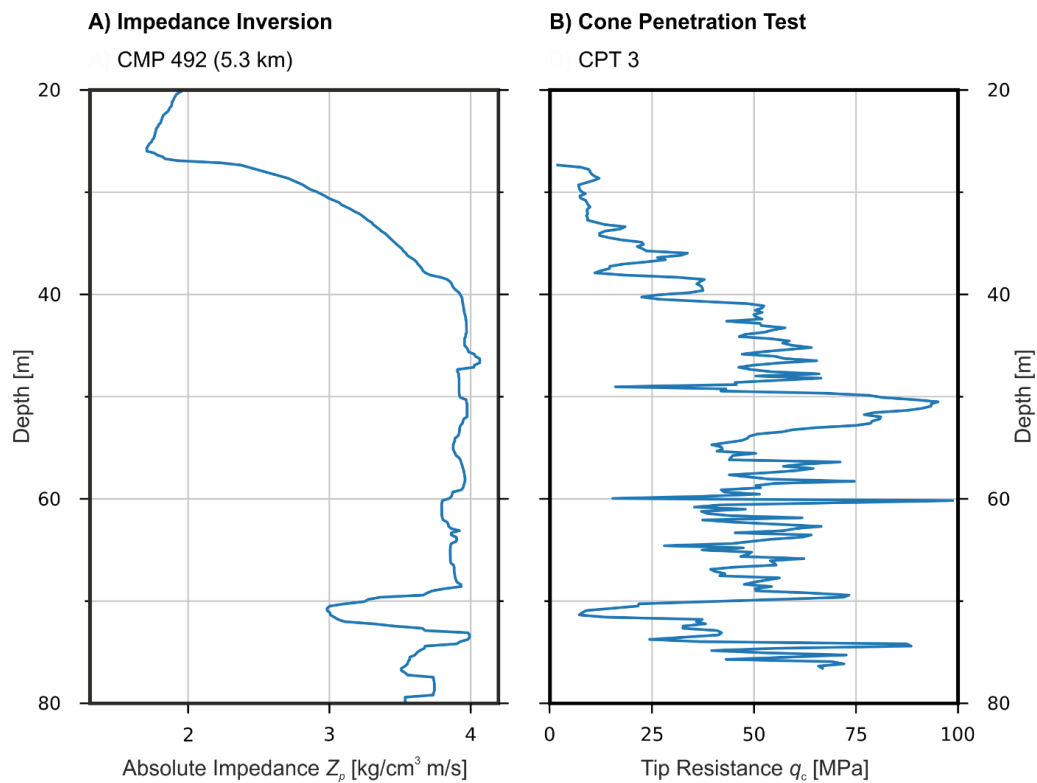


Figure 4-15: Comparison of (A) the absolute impedance Z_p estimation and (B) the tip resistance q_t of the Cone Penetration Testing for location CPT 3. The band limited impedance has been merged with the low frequency trend at a characteristic frequency $f_c = 10$ Hz. Although there is more high frequent variation observed on q_t , the general pattern match with a moderately high correlation of 0.69 (Pearson's correlation coefficient). Especially the low impedance layer below 70 m matches very well to low tip resistance.

4.5 Discussion

4.5.1 Limitations and Uncertainties

The presented methodology shows some general limitations and sources of uncertainty that have to be included in an evaluation of the results. To begin with, the low frequency model has been found to have a great influence on the Z_p estimation, e.g., defining the final Z_p uncertainty. This observation is explained by the functionality of the BLIMP algorithm (see “Band Limited Impedance Inversion”), in which the absolute Z_p values are fixed with the low frequency trend and the small-scale variation is superimposed with the band limited Z_p inversion results. Therefore, the uncertainties of the band limited Z_p estimation are high with a relative error of up to 30% (Figure 4-12). These large errors are explained by the missing low frequency trend in the reflection seismic data due to the band limitation as illustrated in Figure 4-2. Incorporating the low frequency trend into the impedance inversion, the uncertainties of the absolute Z_p estimation are reduced to 9% with a characteristic frequency of 40 Hz and to 5% with 10 Hz. Accordingly, the relative contribution of the low frequency trend increases with increasing characteristic frequency.

Some systematic errors cannot be eliminated, as the inversion results in this study have been based only on information derived from the seismic data and CPT data have only been used for depth conversion. This limited data basis is typical for site investigation studies for offshore infrastructure construction or pre-site drilling surveys (Lesny et al., 2014; Fischer et al., 2019), as seismic surveys are typically conducted before other methods are used. The absence of direct and specific ground truthing, e.g., with borehole logging measurements, is of course problematic for the inversion. Here, the low frequency Z_p model is derived from $v_{p,int}$ estimates determined from picked travel time curves. This procedure is prone to systematic errors caused by, e.g., errors in the acquisition geometry or in the employed transformations.

Although the low frequency model has been generated with the highest possible resolution, a frequency notch in the inversion results cannot be completely excluded, which eventually cannot be corrected with seismic data only. Claerbout (1986) and Jannane et al. (1989) show and argue in the case of low resolution seismic data, that a frequency gap exists between the information derived by velocities reaching 2 Hz and reflectivity information starting at 10 Hz. Considering the data shown here, those limits are different for near surface seismics, especially as other sources and a different receiver set-ups are used. The layer spacing of the low frequency trend shown in Figure 4-9 is on average 20-30 ms and as small as 10 ms. Following Claerbout (2010) this layer spacing results in a low frequency trend reaching 50-100 Hz. Compared to other sources used for near surface seismic studies (Vardy et al., 2017), the employed micro-GI gun (see Table 4-1) has a strong low frequency content and the low cut frequency used is at 40 Hz. In the BLIMP algorithm (see “Band Limited Impedance Inversion”) a frequency range of 50-150 Hz was used for the scaling of the band limited Z_p to the low frequency model, as an overlap of the frequency spectra was observed in this range. Therefore, we argue, that there is only a slight to negligible frequency gap between the low frequency trend used here and the band limited Z_p . This statement is supported by the high correlation (Pearson’s correlation coefficient ~ 0.7 , see Figure 4-15) between qt and the absolute Z_p estimation. Nevertheless, the patterns and especially the smearing of low Z_p anomalies in Figure 4-13 indicate a possible notch in the reconstructed frequency spectra presumably below 40 Hz. At a characteristic frequency of 40 Hz for the merging Linkwitz-Riley Filter smooth Z_p is found (see Figure 4-16). Using those smooth Z_p for correlation with the qt of the CPT correlation coefficients are significantly lower. This leads to the conclusion that some low frequency information may not be recovered.

Although there are high uncertainties associated with the Q_{int} estimation, the Q_{ave} are more robust and the uncertainties do not propagate into the Z_p results but limit the interpretability of

attenuation measures. As already highlighted in Figure 4-10 and Figure 4-11, the Q_{int} estimation is subjected to high uncertainties with relative errors of Q exceeding 100%. Comparing with Forsberg et al. (2022), no lower uncertainty can be reached with other methods. This large uncertainty is problematic for the subsurface characterisation, as Q is a valuable parameter to characterize near surface sediments (Pinson et al., 2008; Vardy et al., 2012). With the statistical analysis of the unit properties calculating the median attenuation for units in the seismic section, the uncertainty can be reduced as shown in Figure 4-11B. Although the lateral resolution is lost, this averaged Q estimate can be used for unit characterisation.

Furthermore, it has to be highlighted at this point, that the gain function calculated from the Q estimation is simplistic, as a time-variant but frequency independent gain function is determined. Some trials have been executed to test this simplification. Including the Q estimation with a frequency dependent gain function into the Z_p estimation slowed down the inversion by several orders of magnitude and resulted in estimates of $Q > 300$. This observation indicates that the wavelet changes by attenuation for the micro-GI are small and the simplistic gain function is sufficient.

Generally, the choice of the wavelet for inversion is critical. For the algorithm employed, phase information of the wavelet is necessary. The estimation of the zero phase wavelet from a smoothed spectrum as conducted in O'Neill (2023) is not sufficient. Using the true phase of the wavelet for the inversion makes a zero-phase conversion of the stacked or migrated data prior to inversion unnecessary and possibly avoids artefacts.

Even though there are some remnants of multiples imprinted on the inversion results, those multiples have been suppressed well enough to obtain good inversion results. Both the processing and the impedance inversion is tailored to suppress multiples. Most importantly, a multiple model has been generated and subtracted from the data. The following NMO correction, stacking and migration further reduce the multiple energy. Consequently, the seafloor and pegleg multiples in Figure 4-7 are weak in comparison to the main seismic events at the interpreted horizons and the internal reflectors in the units. The event shape of the multiples is also different compared to the wavelet due to the subtraction and the de-stacking. Therefore, multiples are further suppressed in the following impedance inversion (Figure 4-13). Figure 4-15 also shows no strong indication of the multiple changing Z_p , as the patterns of qt and Z_p match.

4.5.2 Seismic Interpretation

As previously introduced (also compare Buiting & Bacon, 1999; Bacon et al., 2003), the depth converted Z_p section showing unit properties can significantly improve the interpretation of the interface image of a reflection seismic section. The impedance section constitutes a new framing of the seismic data, providing the interpreter with additional information about the subsurface and thus reducing existing biases, e.g. the framing bias, in seismic interpretation (Alcalde & Bond, 2022). Typically, seismic amplitude images are scaled to emphasize small amplitudes, while large amplitudes are clipped (Figure 16A). Therefore, small amplitudes such as the internal structures in U3 and U4 seem to indicate major changes in the lithology. The Z_p section, in contrast, makes clear that no major impedance changes are found in these units (Figure 16B). Additionally, lateral changes of reflection strength are partially masked due to the clipping of large amplitudes. In Figure 4-13, a lateral change in the impedance of Unit U3 is clearly visible, while such a change cannot be observed in the seismic image. Another example, but with a different implication, is the clay layer below Horizon H1.1. Especially in the standard reflection seismic image before attenuation correction (Figure 4-7), the amplitudes at Horizon H1.1 are apparently weaker than the internal reflectors in U4 and U3. The impedance inversion in Figure 4-13 shows that in fact there is a significant low impedance layer found at this horizon, which is also supported by the ground truthing data. Thus, inversion results are a useful tool to quality check geologic interpretations and to incorporate quantitative interpretation.

Taking into consideration the reflection seismic image, the impedance inversion results as well as the geotechnical measurements, a joint geologic interpretation of the seismic section and the generation of a first SBT ground model is facilitated. From a structural perspective, the channel like incision at 7 km at Horizon H3 is the most prominent feature.

Considering the shape of the incision shown in Figure 4-16 and the seismo-stratigraphy of the Heligoland Glaciotectonic Complex (Lutz et al., 2009; Lohrberg et al., 2020, 2022; Winsemann et al., 2020), this incision most likely resembles a tunnel valley of supposedly Elsterian (MIS12) or Early Saalian (MIS10) age. This tunnel valley cuts the Horizons H2 and H1.1 and the low Z_p layers at these horizons. The Z_p of these layers are in the range of 2-3 kg/cm³ m/s indicating organic soils to clays or silt mixtures. Based on this result and in connection with the CPTs, those low Z_p layers are interpreted as continuous clay and peat layers. In Figure 4-17, a classification of *SBT* based on the impedance is shown based on limits taken from Chapter 3 which are built on the sediment properties data sets listed in “Low Frequency Model”. The clay and peat layers are

attributed to SBT 2-3 resembling organic soils or clays, which fits to the CPT classification. The thickness of the more prominent clay and peat layer at H2 varies from about 1 m to a maximum of 3 m at CPT 1. Without the inversion, the thickness could not be estimated, as the dominant wavelength in the target depth $\lambda_d = \frac{v_{int}}{f_d} = \frac{1800 \text{ m/s}}{440 \text{ Hz}} = 4 \text{ m}$ is greater than the thickness.

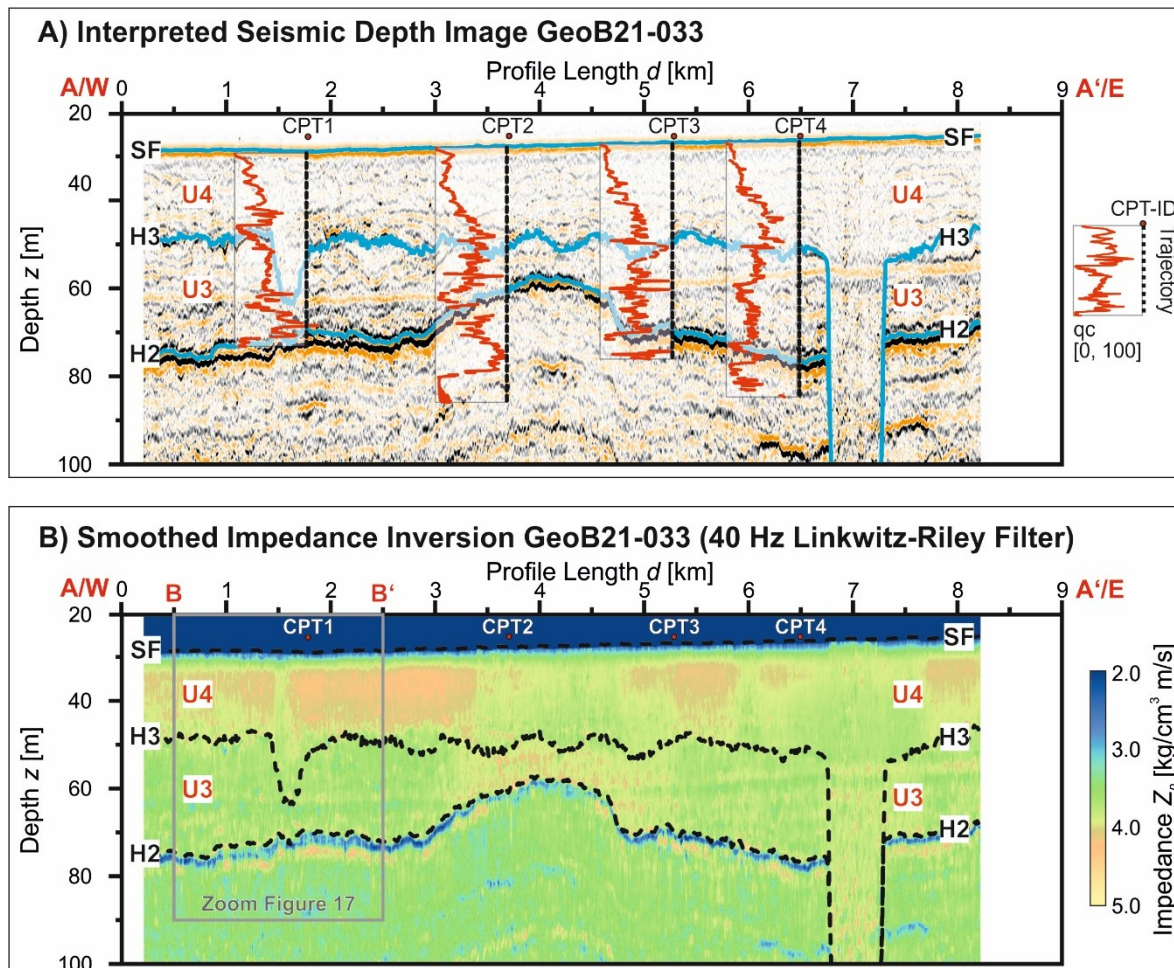


Figure 4-16: Depth converted seismic image and inversion result. A) Interpreted seismic image corrected for attenuation and converted to depth, see Figure 4-7 for location map and seismic time image. The tip resistance q_c of the Cone Penetration Test (CPT) measurements is overlain. B) Smoothed impedance inversion section generated with a 40 Hz Linkwitz-Riley Filter to merge the band limited impedance with the low frequency trend. Small scale impedance anomalies are more easily interpreted in this smoother impedance section, while the impedances rise more steeply directly below the seafloor compared to Figure 4-13.

Beneath the clay layer at Horizon H2, there is a layer of 2 m thickness with high Z_p exceeding $4 \text{ kg/cm}^3 \text{ m/s}$ indicating gravelly or stiff sands (SBT 7-9, see Figure 4-17). Those high impedance values fit to the generally high q_c below the clay and peat layer at H2 and the CPT classification. As reported in “Cone Penetration Testing”, there were coring problems in this interval, which are assumed to be due to the stiffness of the material.

In U3 and U4 the general appearance of the CPT classification can be reproduced by the impedance *SBT* classification shown in Figure 4-17. In U4 *SBT* of 6-7 are deduced from the CPT and the seismic data. In U3 the *SBT*'s are slightly lower around values of 6. In Unit U4 and the unsmoothed Z_p section, a consolidation trend is observed, which is also found in *qt*. At the seafloor, some Z_p anomalies with thicknesses of ~ 1 m are observed in Figure 4-17B. Those anomalies correspond to channels sediment echosounder data which have been formed during the Last Glacial Maximum (compare, e.g., Coughlan et al., 2018). The thin Holocene cover of mobile sands typical for the North Sea is not imaged due to insufficient resolution of the data and appears to be 1-2 m thick in the sediment echosounder data.

The low *SBT*'s of 3-4 at H3 of CPT 1 do not show a direct equivalent in the seismic results. But especially in the western part of the section, several small-scale low Z_p anomalies are observed at H3 (Figure 4-17B, C with annotations in Figure 4-17A). Those anomalies form channel-like incisions and the low Z_p indicate fine grained sediments which is reflected in the *SBT* classifications and core descriptions (CPT 2 and CPT 2*). As Coughlan et al. (2018) describe several glaciofluvial units in the Elsterian, Saalian and Weichselian, those incisions are interpreted as fluvial incisions with associated clays or peats. These fluvial incisions can develop at sea level low stands during the glaciations, when the area was not covered by ice or water. It has to be noted in this context, that CPT 1 does not directly lie on the seismic line but has been drilled in ~ 20 m distance (see Table 4-3). The mismatch of the CPT and the seismic data may be due to the spatially highly variable nature of the fluvial incisions and changes in material composition over distances of few tens of meters. This highlights the limitations of 1D CPT measurements in gaining an understanding of complex geological settings and the need for high quality geophysical data, especially in combination with reliable impedance models.

The Z_p section also allows for a refinement of picked horizons. To begin with, the resolution is improved by the inversion and the effect of the wavelet is removed. Especially for the location of Horizon H3 there is a rather big margin of subjective interpretation, as the internal reflector configuration of U4 and U3 in Figure 4-17A is rather chaotic. For this unconformity, there is no clear phase to follow for the picking in the seismic amplitude section (Figure 4-17A). In the Z_p section (Figure 4-17B), in contrast, the change from higher to lower Z_p from U4 to U3 and the base of the low Z_p river channels can be used to guide the picks and improve the interpretation. E.g., the eastern flank of the incision at CPT 1 should be moved to shallower depths.

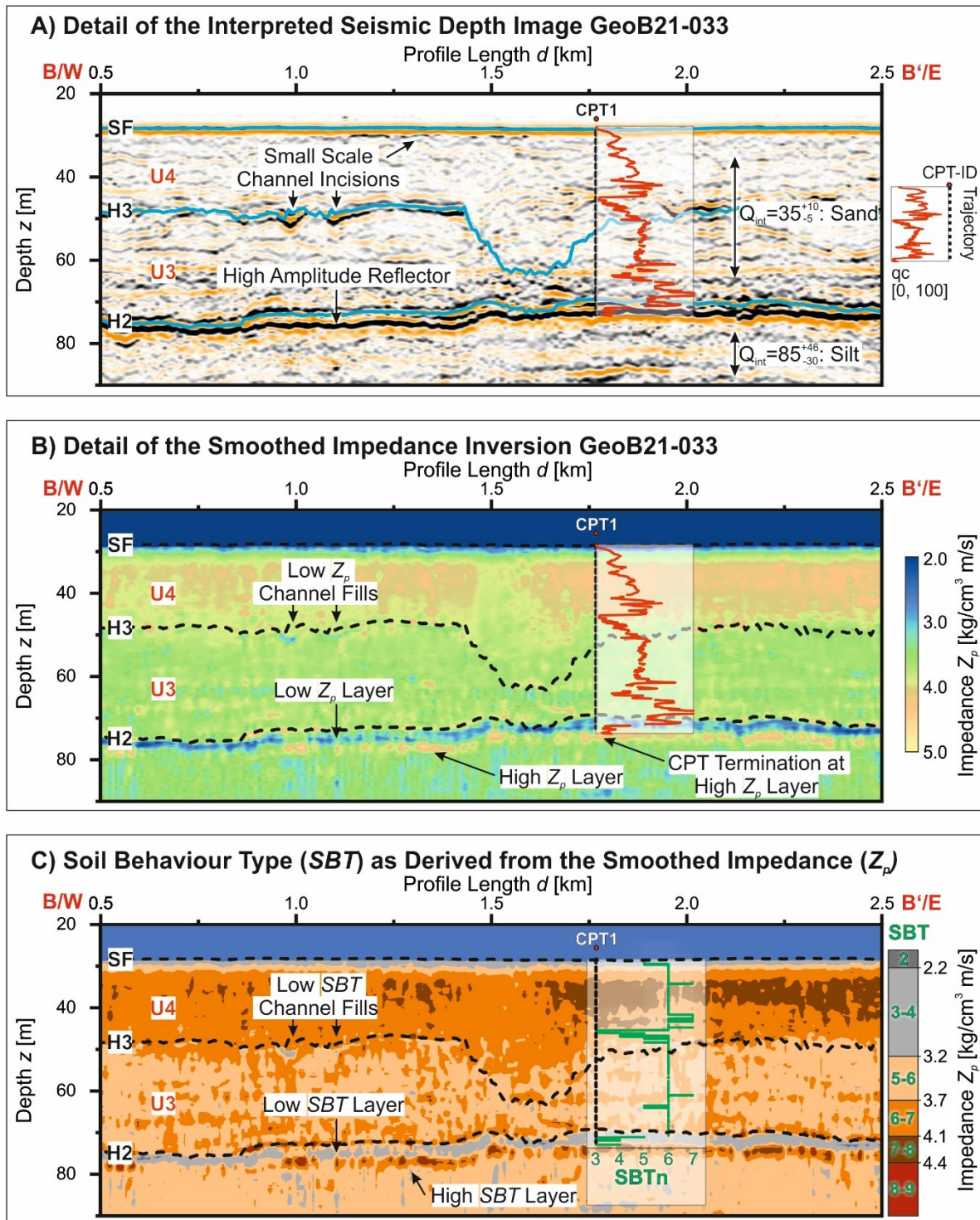


Figure 4-17: Detail of the seismic image and the inversion results. The tip resistance q_c and the normalized Soil Behaviour Type SBT_n of the Cone Penetration Test at location 1 (CPT 1) are overlain. A) Interpreted seismic image corrected for attenuation and converted to depth, see Figure 4-16 for full scale image and location overview. The determined attenuation quality factor Q with the corresponding lithological interpretation is shown for the units on the right side of the plot. Important features such as small scale channel incisions and the peat and clay layer are highlighted. B) Smooth impedance inversion result in which the band limited impedance has been merged with the low frequency trend with a 40 Hz Linkwitz-Riley Filter. C) Classification of SBT based on the impedance shown based on limits taken from Chapter 3 which are built on the sediment properties data sets listed in “4.2 Low Frequency Model” and shown in the legend. Overall a very good match of the CPT SBT_n and the SBT from the impedance can be reached. The small SBT_n at H3 of CPT 1 does not have a direct equivalent in the seismics. But there generally are channel incisions with low SBT observed at H3 and the CPT is located at 20 m distance to the seismic line.

4.5.3 Utilization of Inversion Results for Other Disciplines

Generating seismic unit properties in the depth domain bears great potential for the further presentation, knowledge transfer and utilization of seismic data. Typically, unit properties such as grain size, porosity, density or strength properties such as the static and dynamic moduli are investigated by geologists and engineers, e.g., to design the foundations of offshore wind turbine (Burd et al., 2017; Lombardi et al., 2017). Although seismic properties such as Z_p are fundamentally different to geotechnical or geological properties, these seismic properties provide useful quantitative information. In general, small stresses and strains are introduced by seismic methods and thus only the dynamic moduli can be analysed, while large stresses and strains and thus the static moduli are investigated, e.g. with CPTs. To some concerns, e.g. for cyclic loading, the dynamic moduli are even more informative than static moduli (O’Kelly & Arshad, 2016). Additionally, seismic investigations being non-destructive bear the potential to assess undisturbed sediment properties. This is valuable as the sampling disturbs the sediment fabric, especially in sandy sediments, and laboratory measurements are unlikely to reproduce the in-situ properties (Kiyota et al., 2019).

Since the dynamic and static moduli have been shown to correlate for rocks (Brotons et al., 2016; Fjær, 2019) and unconsolidated sediments (Wichtmann et al., 2017), measurements of the dynamic moduli can be used to deduce static moduli. This correlation also explains why Z_p has successfully been used with machine learning approaches to predict CPT measurements (Sauvin et al., 2018, 2019; Forsberg et al., 2022; O’Neill et al., 2023). Those studies showed that using the impedance results helps to improve the prediction and the definition of uncertainties using the seismic data as guided information for the prediction. By adding more quantitative information and improving prediction one could reduce the amount of necessary ground truth data and therefore reduce cost and risk for offshore wind turbine installation. There is now a movement in the industry (Forsberg et al., 2022; Pein et al., 2020) to certify without having a ground truth information at every wind turbine location as currently specified in the standards (Lesny et al., 2014). Quantifying uncertainties and improving the knowledge of the soil conditions will also reduce cost in pile installation by improved pile design and installation planning (Charles et al., 2022; Kallehave et al., 2015; Muskulus & Schafhirt, 2014)

As Z_p is a unit property, such a depth converted data set can be more easily presented to professionals, which are not educated as seismic interpreters (Ismail et al., 2012). We are convinced, that transformations from Z_p to commonly accepted parameters such as *SBT* (Figure 4-17) will further facilitate the knowledge transfer. In contrast, the interpretation of interface representations

of seismic images, especially if presented in the time domain, can easily lead to misconception due to various effects caused by seismic velocity, acquisition geometry, data recording and processing (Tucker & Yorston, 1973) or noise (Ismail et al., 2012). So, seismic inversion results are a good basis to convey seismic information to other professions.

The probabilistic framework of the inversion presented here is meant to build confidence for the interpretation. As discussed above, some uncertainties prevail and are inherently linked to the seismic method as well as the inversion. In the case of the attenuation estimation, the uncertainty of Q as shown in Figure 4-10 and Figure 4-11 seems too high to deduce subsurface properties from this measure, although some indications can be concluded. The strongest attenuation with the lowest Q is found where the Unit U3 is thickest (Figure 4-11). This fits to the reported coarse sediments consisting of clean to gravelly sands (Pinson et al., 2008). Given the spread of v_p , ρ and hence Z_p (Figure 4-8), the uncertainty of the absolute impedance estimation in the range of 5-9% is sufficient to differentiate sediments. This conclusion can also be drawn from Figure 4-17, showing the large variation of Z_p in the inverted section in the range of 2-5 kg/cm³ m/s and the strong contrast between interpreted seismic units. Differences between U3 and U4 in seismic impedance are clearly extracted while conventional seismic interpretation does not yield a clear differentiation between the two units. The variations within the sandy Unit U3 are at the scale of the uncertainty of the impedance inversion and thus on the edge of resolution. Therefore, we conclude that quantifying uncertainties and clearly communicating capabilities and limitations of the inversion in a probabilistic framework is a dependable basis to build trust for quantitative interpretation and improve cross-disciplinary communication.

4.6 Conclusion

In this study we demonstrate - for the first time - a comprehensive, stochastic workflow for seismic impedance inversion and near surface, ultra-high resolution studies, which is only based on seismic data. Both the seismic data acquisition and processing have been optimized for this purpose. The five main components of the inversion workflow are 1) attenuation estimation and correction, 2) low frequency model building with interval velocity estimation and density transformation, 3) band limited impedance inversion with a genetic algorithm, 4) merging of the low frequency trend and the band limited impedance via a crossover filter as well as 5) depth conversion. The single steps are implemented as probabilistic inversions and are combined in a fully stochastic framework to allow for uncertainty estimation. While the relative uncertainty of about 50% of the Quality Factor

Q as an attenuation measure is high for quantitative interpretation, a relative uncertainty of 5-9% has been reached for the absolute impedance and a detailed, quantitative interpretation is conducted. We can demonstrate in this study, that the inclusion of impedance inversion results into a seismic interpretation workflow mitigates interpretation biases and reduces uncertainties. Presenting seismic data in the form of unit properties also allows for a better knowledge transfer in interdisciplinary studies. For example, a classification into the normalized Soil Behaviour Types was possible based on the impedance estimates. Although there are methodological limitations remaining, the Cone Penetration Test data and the absolute impedance show a good correlation. Especially, the Soil Behaviour Type estimation matches the CPT classification. The main proportion of the sediment column has successfully been identified to be sandy with coarser intervals. Details of the geologic succession such as a widespread clay or peat layer, a deeper very stiff layer posing problems for drilling, as well as small-scale patchy clay layers have been identified based on seismic measurements only. The overall very good match of the inversion results to CPT ground truthing, indicates that our results and methodology can be utilized for further purposes such as the prediction of other geotechnical parameters and the creation of synthetic CPTs.

As the methods presented are stable and comparatively fast, the approaches can be extended to various use cases including 3D inversion. Typically, the offset range of near surface seismic 3D data sets is relatively limited (Duarte et al., 2017; Monrigal et al., 2017; Lebedeva-Ivanova et al., 2018). Also for 2D seismic lines and especially for scientific data, the offset range can be relatively restricted to short offsets (Preine et al., 2020). As migrated near angle stacks are sufficient as an input for impedance inversion, those data sets are a good basis for inversion. Due to the limited offset range the low frequency trend needs to be derived from other sources than interval velocity estimation from reflection travel time curves. In those cases, diffraction imaging (Preine et al., 2020) or ocean bottom recordings (Kugler et al., 2007) with head waves for velocity estimation (Telford et al., 2004) or borehole measurements could serve as a data basis.

The impedance inversion is also a good data basis for further analyses. On the one hand, an impedance model and derivatives of it can serve as starting models for Full Waveform Inversion (FWI) or Amplitude Versus Angle inversion. Especially for FWI such an accurate starting model is highly relevant, as this model has to match to the data within half a wavelength (Fichtner, 2011). On the other hand and as introduced in “Utilization of Inversion Results for Other Disciplines”, data products such as synthetically derived CPT measurements for the planning of offshore wind turbine foundations can be derived from an impedance model, e.g., by co-interpolation/simulation or machine learning (Sauvin et al., 2018, 2019; Forsberg et al., 2022).

Chapter 5 Pre-Stack Inversion on Near Surface Reflection Seismic Data

Nikolas Römer-Stange¹, Natasha Morales², Norman Ettrich³, Hanno Keil¹, Volkhard Spieß¹

¹Department of Geosciences, University of Bremen, Klagenfurter Str. 2-4, D-28359 Bremen, Germany

²Fraunhofer Institute for Wind Energy Systems IWES, Am Fallturm 1, D-28359 Bremen, Germany

³Fraunhofer Institute for Industrial Mathematics ITWM, Fraunhofer-Platz 1, D-67663 Kaiserslautern, Germany

In preparation for Near Surface Geophysics. Format and references have been adopted to match the thesis.

Keywords

Near Surface, Ultra-High Resolution Reflection Seismics, Waveform Inversion, Elastic Properties

Abstract

The quantitative estimation of shear properties is an important aim for seismic investigations in the marine near surface for geologic and engineering purposes. Possibilities to reach this aim include elastic or viscoelastic pre-stack inversion and waveform inversion. But in most cases, high resolution P-Wave reflection seismic data sets with a limited offset range and sparsely distributed ground truthing data are available as a data basis. For this data basis, no applicable and reproducible pre-stack inversion workflow with a processing toolbox fitting the requirements of the pre-stack inversion is available. Published 1D reflection inversion schemes are inaccurate when dipping reflectors occur and those schemes are characterised by a lateral resolution in the range of 10s of meters. To derive a shear property estimation only based on P-Wave reflection seismic data, it is tested, whether the initial model for a developed, unconstrained pre-stack inversion can be generated with impedance inversion. Therefore, a toolbox to conduct Common Reflection Surface travel time curve inversion, angle stacking, impedance inversion, attenuation correction and initial model generation with fitted empiric relations is implemented. The pre-stack inversion is then conducted with a steepest descent optimization scheme and a convolutional forward model based on unconstrained Zoeppritz P-Wave reflection coefficients. In comparison to available Cone Penetration Test ground truth data, the inversion scheme successfully predicted S-Wave velocities, although the sensitivity for low S-Wave velocities is limited. A sensitivity analysis with synthetic test data indicates that the low sensitivity for low S-Waves is a general problem of P-Wave reflection data inversion.

5.1 Introduction

Efficient non-destructive exploration of the viscoelastic properties of the subsurface is a key target of applied geophysical methods in general and for marine near surface reflection seismics in particular. Seismic images and quantitative properties derived from seismic inversion yield the basis to answer fundamental geologic (Tromp, 2020) and applied research questions, e.g., regarding natural resource exploration (Sirgue et al., 2010; Seong & Park, 2001; Chopra & Castagna, 2014), hazard monitoring such as slope stability (Vardy et al., 2012; Provenzano et al., 2018, 2019) or drilling de-risking (Sayers et al., 2020), offshore infrastructure installations such as offshore wind foundations (Provenzano et al., 2017; Forsberg et al., 2022) or harbours (Masoli et al., 2020) and location selection as well as monitoring of Carbon Capture and Storage sites (Cevatoglu et al., 2015).

A range of seismic inversion methods has been developed to deduce quantitative subsurface properties, ranging from tomography (Boehm et al., 1996; Woodward et al., 2008; Köhn, 2011) over post-stack impedance inversion (Lindseth, 1972, 1979), Amplitude Versus Angle analysis (AVA analysis; Chopra & Marfurt, 2007; Chopra & Castagna, 2014; Fawad et al., 2020) and pre-stack inversion (Ma, 2002; Russell, 2014; Simm & Bacon, 2014; Fawad et al., 2020) to waveform inversion (Lailly, 1984; Tarantola, 1986; Virieux & Operto, 2009). Most case studies have been conducted with low-frequency sources below 200 Hz (Dondurur, 2018) in the context of hydrocarbon exploration focussing on deep targets (Virieux & Operto, 2009; Chopra & Castagna, 2014; Tromp, 2020). Typically, unconsolidated sediments are found in the near surface and the physical properties of those sediments are distinctly different to lithified sediments and rocks with high P-Wave to S-Wave velocity ratios v_P/v_S , thus Poisson's ratio $\nu_{PR} = \frac{(v_P/v_S)^2 - 2}{2(v_P/v_S)^2 - 2}$ close to 0.5, and density ρ dominated compressional impedance $Z_P = v_P \cdot \rho$ contrasts (Shumway, 1960; McCann & McCann, 1969; Hamilton, 1970; Breitzke, 2006; Table 3-1 in Chapter 3). For near surface studies, Ultra-High to Ultra-Ultra-High Resolution sources are commonly used with a frequency range of 300-2000 Hz (ISO 19901-10, 2021). Sediment properties, the acquisition set-up and high frequencies limit the application possibilities of inversion algorithms and thus there are comparatively few inversion case studies for near surface seismics (see Vardy et al., 2017; and references therein). So, shear properties are inverted from reflection seismic data with towed streamers and towed hydrophones with AVA inversion by Riedel & Theilen (2001), Riedel et al. (2003) and Aleardi & Tognarelli (2016) as well as with waveform inversion by Provenzano et al. (2016, 2017, 2018). When the angle range is relatively restricted, the contribution of v_P and ρ on

Z_P can not be differentiated due to a strong coupling of the parameters (Tarantola, 1986; Virieux & Operto, 2009; Provenzano et al., 2017, 2018).

The methods applied for those shear property studies are not generally applicable and not reproducible, as the algorithms are not made available. The AVA inversions have been limited to the seafloor reflection (Riedel & Theilen, 2001; Riedel et al., 2003; Aleardi & Tognarelli, 2016) ignoring the deeper sub-surface. In case of the waveform inversion, the forward modelling has been restricted to the laterally homogenous case using the reflectivity method to reduce the computational demands and the Poisson's ratio had been chosen for the parametrization (Provenzano et al., 2016, 2017, 2018). Thus, dipping strata or lateral inhomogeneities introduce inversion artefacts. Also, the Poisson's ratio is not a sensible parameter for the lithologies of interest (see Table 3-1 in Chapter 3). Except for Provenzano et al. (2018) in which the starting model is derived from Normal Move Out (NMO) velocity analysis, it is also not clear how the low frequency models can be derived for absent ground truthing.

In the following study, the hypothesis is tested, whether it is possible to develop an inversion scheme, which provides S-Wave velocity estimates and which is only based on reflection seismic data, is insensitive to noise and accounts for dipping strata. For this purpose, a pre-stack inversion is implemented acting on angle gathers with a steepest descent optimization and a toolbox to prepare Common Mid Point (CMP) super-gathers for inversion. The processing includes Common Reflection Surface (CRS) velocity analysis and stacking in angle gathers, geometric spreading correction, attenuation estimation and correction as well as impedance inversion. Empiric relations for unconsolidated sediments are used to convert the interval velocity and impedance estimates to the low frequency impedance model and the pre-stack inversion starting model. To conduct a feasibility study, the scheme is tested on one super gather of seismic data from a windfarm area in the North Sea and compared to Cone Penetration Test (CPT) data as ground truthing.

5.2 Material and Methods

The implementation of the pre-stack inversion and the processing of the data to meet the prerequisites for the inversion are described in in the following.

5.2.1 Steepest Descent Pre-Stack Inversion

It is the general aim of the seismic inversion to determine the optimum model \mathbf{m}^* , which reproduces the observed seismic data d_{obs} by forward modelling of synthetic data $d_{cal} = F(\mathbf{m})$ with the least-squares misfit S_d as given in Equation 5-1 (Sheen et al., 2006).

$$S_d(\mathbf{m}) = \frac{1}{2} \|\Delta d\|^2$$

$$\Delta d = d_{cal}(\mathbf{m}) - d_{obs} = F(\mathbf{m}) - d_{obs}$$

Equation 5-1

To reach this optimum with the steepest descent optimization method, a model \mathbf{m}_n is incrementally updated in the negative direction of the gradient of the misfit function ∇S_d multiplied by a step length μ to \mathbf{m}_{n+1} until \mathbf{m}^* or an approximation of this optimum is reached, as given in Equation 5-2 (Virieux & Operto, 2009).

$$\mathbf{m}_{n+1} = \mathbf{m}_n - \mu \cdot \nabla S_d$$

Equation 5-2

Therefore, it is necessary to determine μ and ∇S_d for the inversion. As given in Köhn (2011) or likewise Kurzmann et al. (2013), μ of a certain model parameter is the scaling factor of the maximum of the gradient and the maximum of the actual model multiplied by the step length factor p_μ , which was chosen to be 0.1%.

$$\mu = p_\mu \frac{\max(\mathbf{m})}{\max[\nabla S_d(\mathbf{m})]}$$

Equation 5-3

For the calculation of ∇S_d as given in Equation 5-4, the partial derivatives of the wavefield in respect to the model parameter $\frac{\delta d_{cal}}{\delta m}$ are multiplied with the data residual Δd (Equation 5-1) and summed (Operto et al., 2013).

$$\nabla S_d = \sum_R \sum_{TWT} \frac{\delta d_{cal}}{\delta m} \Delta d$$

Equation 5-4

Using the approach of Provenzano et al. (2017), $\frac{\delta d_{cal}}{\delta m}$ can be explicitly calculated by a perturbation of each model parameter $m_{n,p}$ at all depths and thus the gradient of the misfit vector at a particular time step is given by Equation 5-5. The perturbation was set to 10% of the model parameter.

$$\nabla S_d(TWT) \approx \sum_R \{[d(m_{n,p}) - d(m_n)] \cdot \Delta d\}$$

Equation 5-5

The remaining prerequisite for the pre-stack inversion is the functional $d_{cal} = F(m)$ to determine the synthetic data. The convolution of the PP reflection coefficient r_{pp} with the wavelet w described by Equation 5-6 can be used as this functional. For a non-stationary convolution, Equation 5-6 can be replaced by a matrix multiplication of $r_{pp}(m)$ with a convolution matrix W . Although several approximations exist, the Zoeppritz equation, e.g., given by Dvorkin et al. (2014) can be used to calculate $r_{pp}(m)$ for a given incidence angle and with the parameters v_p , v_s , and ρ .

$$F(m) = r_{pp}(m) * w$$

Equation 5-6

As the individual contributions of v_p and ρ on Z_p are indistinguishable at steep angles, (Tarantola, 1986; Virieux & Operto, 2009; Provenzano et al., 2017, 2018), it can be beneficial to use the inverted v_p , v_s , and ρ model to determine derived parameters such as Z_p and $Z_s = \rho \cdot v_s$ for further analysis. Putting the steps described above into a workflow, the following process needs to be executed for a pre-stack inversion:

1. Initialize starting model m_0 with v_p , v_s , and ρ .
2. Optimization loop for N_i iterations:
 - a. Calculate synthetic angle gathers with stationary or non-stationary convolution (Equation 5-6).
 - b. Determine residual (Equation 5-1).
 - c. Calculate the explicit gradient of the misfit function (Equation 5-5) by perturbation of the model parameters.
 - d. Determine step length (Equation 5-3)
 - e. Update the model (Equation 5-2)
3. Smoothing of optimized model and calculation of derived parameters.

5.2.2 Common Reflection Surface Stacking Velocity Analysis and Angle Stacks

To account for dipping layers and make the inversion more robust, the travel time curve inversion with a differential evolution genetic algorithm developed for Chapter 3 and Chapter 4 (see also “2.2.1 Travel Time Curve Inversion”) has been modified. A Common Reflection Surface (CRS)

Two-Way-Traveltime TWT_{CRS} function given in Equation 5-7 is used to calculate the travel time curves across neighbouring CMPs depending on the offset off and the midpoint distance to the central midpoint h_{md} .

$$TWT_{CRS} = \sqrt{(TWT_0 + a \cdot h_{md})^2 + b \cdot h_{md}^2 + c \cdot h_{off}^2}$$

$$h_{off} = \frac{off}{2}$$

$$a = \frac{2\sin(\alpha)}{v_0}$$

$$b = \frac{2 \cdot TWT_0 \cdot \cos(\alpha)^2}{v_0 \cdot R_n}$$

$$c = \frac{4}{v_{NMO}^2}$$

Equation 5-7

The P-Wave interval velocity $v_{P,i}$ model is determined based on the assumption, that the NMO velocity v_{NMO} is equal to the Root Mean Square velocity v_{RMS} , which is determined by Equation 5-8.

$$v_{NMO} \approx v_{RMS} = \sqrt{\frac{\sum_{n=1}^N v_{i,n}^2 \cdot \Delta TWT_n}{\sum_{n=1}^N \Delta TWT_n}}$$

Equation 5-8

For the stacking in the angle gathers, the CRS parameters of the horizons are interpolated to the full TWT range, the CRS traveltimes are calculated according to Equation 5-7 and the move out of the seismic data is corrected. As the data are corrected to normal incidence, the incidence angle is determined by $\theta = \arccos(TWT/TWT_{CRS})$ and angle mutes are determined before stack. The full set of parameters is given in Table A-13 and Table A-14 (see appendix ‘‘C.5 Pre-Stack Inversion Parameters’’).

5.2.3 Attenuation Estimation and Correction

To estimate and correct the effect of inelastic attenuation, the general approach shown in Chapter 4 (see ‘‘4.3.3 Attenuation Estimation and Correction’’) has been followed. So, the quality factor Q is determined from the spectra of the autocorrelations at the seafloor and at a horizon. To allow the

extension of the method to non-normal incident waves, the calculation of the traveltime difference ΔTWT between the seafloor TWT_{SF} and the horizon TWT_{horz} has to be corrected to account for the full traveltime of the wave through the water. Equation 5-9 be used to calculate the corrected ΔTWT and is deduced from the geometric relationships assuming straight rays.

$$\Delta TWT = TWT_{horz}(off) - \frac{TWT_{horz}(off) \cdot TWT_{sf}(off = 0)}{TWT_{horz}(off = 0)}$$

Equation 5-9

To mitigate the boosting of high frequent noise, a damped gain factor G_{damp} - derived from Equation 2-10 or Equation 4-5 and as given in Equation 5-10 - is introduced with a damping scheme proposed by Aster et al. (2013a) and Provenzano et al. (2020). In this equation, the gain damping factor p_G can be adjusted to the noise level, while $A_{loss}(f)$ quantifies the attenuation loss (Equation 4-1).

$$G_{damp}(f) = \frac{A_{loss}^2(f)}{A_{loss}^2(f) + p_G} \cdot \frac{1}{A_{loss}(f)}$$

Equation 5-10

5.2.4 Impedance Inversion

A genetic algorithm has been used for impedance inversion together with the BLIMP algorithm to merge the low frequency trend as described in Chapter 4. As given in in

Table A-15 containing all inversion parameters, the impedance inversion has been repeated 100 times for statistical averaging to produce reliable results.

5.2.5 Empiric Relations for Low Frequency Model Building

To derive ρ and thus $Z_p = \rho \cdot v_{p,i}$ from the $v_{p,i}$ estimates, the empiric relation described by Raymer et al. (1980) has been fitted for near surface sediments. The parameters given in Table A-16 are optimized to match the properties of near surface sediments taken from McCann & McCann (1969), Shumway (1960), Hamilton (1970, 1972), Breitzke (2000), Stevenson et al. (2002), Robb et al. (2006) and the BSH Pinta Data Base (2021) for the wind farms N0307, N0308 and O0103. From Breitzke (2000), the Core PS2567-2 from the Meteor Rise characterised by opal rich and calcareous sediments and Core GeoB2821-1 from Rio Grande Rise consisting of carbonates were excluded.

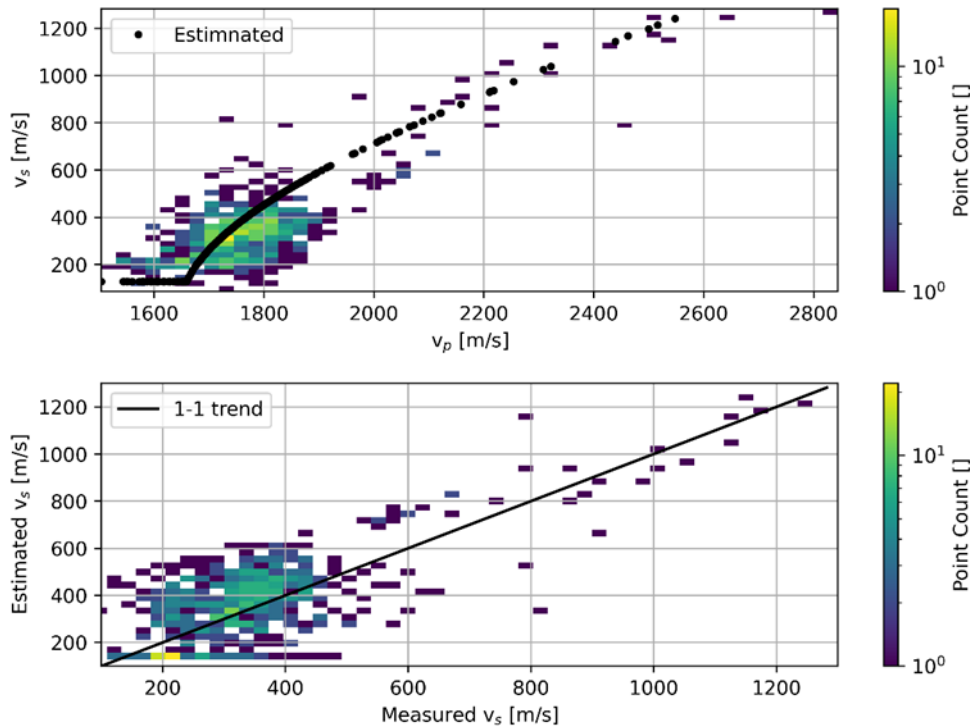


Figure 5-1: S-Wave velocity prediction based on P-Wave velocities as suggested by Lee (2006) for the BSH Pinta Data Base (2021) PS-Logging data of the wind farm sites N0307, N0308 and O0103.

For the low frequency model of the pre-stack inversion, the above given Raymer relation is used to estimate v_p and ρ from Z_p . For the estimation of v_s the approach by Lee (2006) is followed with the parameters given in Table A-17. As shown in Figure 5-1, the mean trend can be reproduced for North and Baltic Sea PS logging data.

5.2.6 Seismic Data

CMPs 487 to 497 of Profile He569-GeoB21-033 as described in Chapter 4 (see Section “4.3.1 Seismic Data Acquisition and Standard Processing” for further details) are considered for the inversion and displayed in Figure 5-2. An Ultra-High Resolution seismic source (ISO 19901-10, 2021) has been used in water depths of 22-25 m with an offset range of 7-230 m. With a CMP distance of 10 m, this super gather spans 100 m. For the velocity analysis and the angle stacks, the distance to the central midpoint CMP492 has been limited to 20 m. Prior to the inversion statics were corrected with the average static correction method (Gutowski et al., 2002) and four strong reflection events were manually picked. Offset dependent spherical divergence has been corrected with a second pass NMO velocity model. The wavelet for the inversion has been extracted from the seafloor reflection.

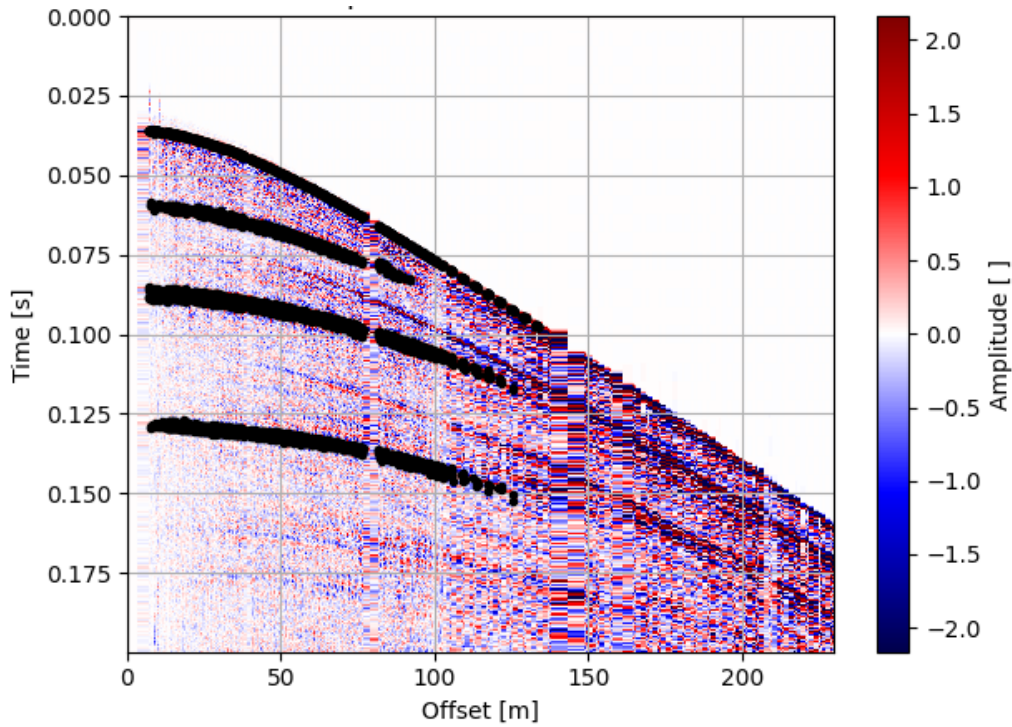


Figure 5-2: Super gather around CMP 492 of the Profile He569-GeoB21-033. Four strong and consistent reflection events have been picked and the picks are superimposed as black dots. Spherical divergence correction has been applied.

5.2.7 Cone Penetration Test Data

The in-situ testing data used for ground truthing for inversion includes a downhole CPT profile with a total penetration depth of 49.85 mbsf located 81.38 m away from CMP 492 of the seismic line He569-GeoB21-033. After assessing and cleaning the incoming raw cone tip resistance qt , sleeve friction fs and pore pressure u_2 data, S-Wave velocity v_s values were calculated using the geotechnical software *CPeT-IT* (GeoLogismiki). This estimation was based on the empirical correlations described by Robertson (2009), where v_s is associated with the CPT cone resistance qt using the soil behaviour type index I_c as shown in Equation 5-11:

$$v_s = [\alpha_{vs}(qt - \sigma_v)/P_a]^{0.5} \text{ in (m/s)}$$

Equation 5-11

where $\alpha_{vs} = 10^{0.55 \cdot I_c + 1.68}$ is the shear-wave velocity cone factor in $(\text{m/s})^2$, $I_c = \left[(3.47 - \log(Qtn))^2 + (\log(Fr) + 1.22)^2 \right]^{0.5}$ is the soil behaviour type index, qt is the corrected cone resistance, and σ_v is the total vertical stress and P_a is the atmospheric pressure.

5.3 Results

As a first step, the full processing flow is applied to a super-gather at CMP 492 on Profile He569-GeoB21-033 adjacent to a CPT borehole. Secondly, impedance inversion is conducted on a near vertical angle stack. Using the fitted empiric relations, the low frequency trend of the impedance derived from the interval velocity estimate is added and an initial model for the pre-stack inversion is generated. With this initial model synthetic trials of the pre-stack inversion are performed to test the algorithm. The synthetic model is then perturbed for a sensitivity analysis of the inversion parameters. Finally, the pre-stack inversion is applied to angle stacks of CMP492.

5.3.1 Data Processing and Post-Stack Impedance Inversion

A high fidelity $v_{p,i}$ model has been determined with the travel-time curve inversion as shown in Table 5-1. In this table, the median values of the multiple inversion runs are reported as the best-guess value and the errors are quantified by the standard deviation. The relative error of $v_{p,i}$ is generally below 1% and the $v_{p,i}$ are typical for clean to silty sands and gravelly sands in the unit above P2 (compare Table 3-1). The dip angles are generally low reaching a maximum of 2.5° . The observed Q -Factor in the range of 40 is also typical for sandy sediments. Higher Q -Factors indicating less attenuation as derived for the lower horizons are commonly found in more fine-grained sediments. As shown in Figure A-18 in the appendix, the Probability Density Functions of the Q estimation are broad and thus associated with high uncertainty.

Table 5-1: Estimates from velocity and attenuation estimation.

Horizon	P-Wave Interval Velocity [m/s]	Depth [m]	Dip Angle	Average Attenuation Factor Q
SF (Water Column)	1469.1 ± 0.6	26.2 ± 0.1	-0.6	
P1	1727 ± 8	47 ± 0.2	-0.6	40
P2	1789 ± 6	72 ± 0.1	-2.5	88
P3	1731 ± 7	108 ± 0.2	-1.9	193

An angle stack in the range of 10 - 30° (see Figure 5-3A) has been determined as a basis for the impedance inversion. For this purpose, the CRS parameters determined are interpolated and used to flatten the input data. Geometric spreading and attenuation are corrected. This stack is then inverted for the band-limited impedance. The result is scaled and merged with the low frequency trend determined from the $v_{p,i}$ model after conversion to Z_p with the empiric Raymer relation. The resulting absolute impedance estimate with restored low frequency trend is given in Figure 5-3B. Below the seafloor, first a gradient zone is observed, and the impedance rises gradually from

2800 kg/cm³ m/s at 35 ms to about 3600 kg/cm³ m/s at 55 ms. At 56 ms, 60 ms and 87 ms, two lesser steps and a larger negative impedance step occur correlating to high amplitude events in the stack.

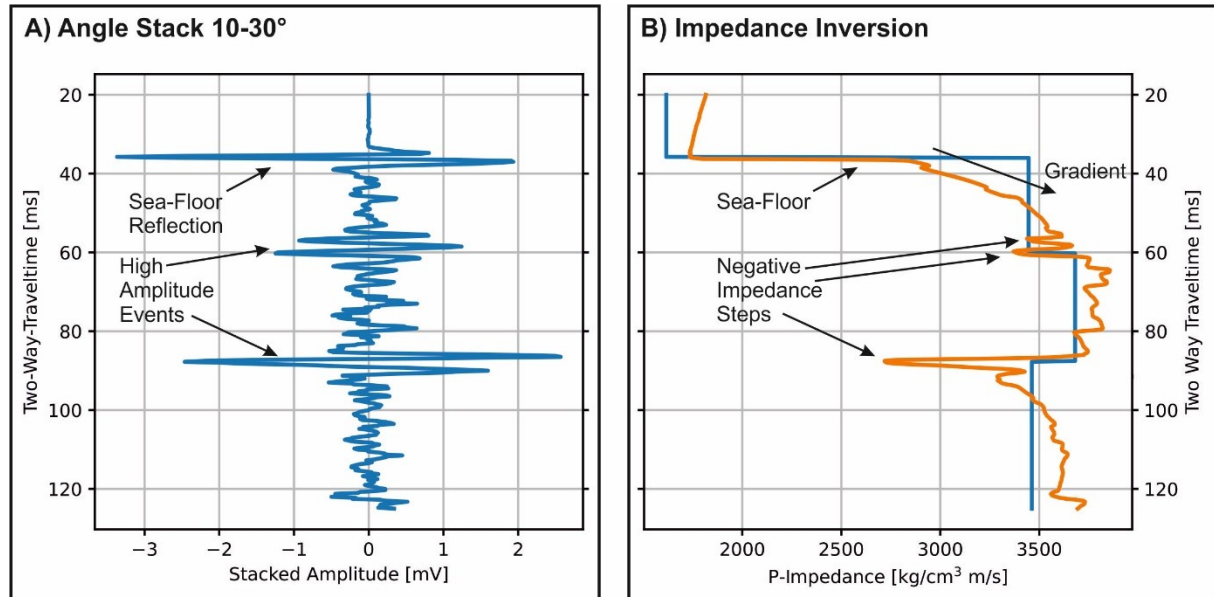


Figure 5-3: Impedance inversion to generate a starting model for the pre-stack inversion. A) Angle stack in the range 10-30° showing a pronounced seafloor reflection and two events with a higher amplitude. B) Low frequency impedance model (blue line) and impedance inversion result (orange line). Below the seafloor a gradient zone followed by two negative impedance steps is observed. A further and pronounced negative impedance step is found at 90 ms.

5.3.2 Synthetic Pre-Stack Inversion Tests

The impedance inversion result is further used to derive the initial model for the inversion and for synthetic pre-stack inversion tests. Firstly, the Raymer et al. (1980) relation (see “5.2.5 Empiric Relations for Low Frequency Model Building” and Table A-16) is employed to derive v_P and ρ from Z_P . Then, an v_S estimate is based on v_P by the Lee (2006) relation (see “5.2.5 Empiric Relations for Low Frequency Model Building” and Table A-17). For the synthetic test of the pre-stack inversion, those parameters are the true model and with this true model angle gathers are modelled as shown in Figure 5-4A. The initial model for the pre-stack inversion for both the synthetic test and the application to real data is a smoothed version of the model using a 6.25 ms long running median filter. The initial model and the generated angle gathers are shown in Figure 5-4B. The small-scale variations such as the two low impedance layers between 65-75 ms disappeared due to the smoothing and the angle stacks show generally lower amplitudes. The pre-stack inversion is then run for 375 iterations and the results are presented by means of shear impedance $Z_S = v_S \cdot \rho$ and compressional impedance $Z_P = v_P \cdot \rho$. The inverted model closely

resembles the true model (compare Figure 5-4A and C) and the small-scale variations are restored. Nevertheless, it is observed that the local Z_S minima are overestimated, the inverted model does not converge to the low values of the true model. Regarding the optimization progress, the L_2 -norm decreases to about 2% of the initial value after 60 iterations (Figure 5-4D) and then the further L_2 -norm decrease seems to flatten. After about 200 iterations, a slight saw-tooth pattern of the norm develops, and the slope is further declining. In the appendix “C.7 Synthetic Pre-Stack Inversion Test after 60 Iterations”, the results of the pre-stack inversion after 60 iterations are additionally shown. While the observed Z_P fit is similar to Figure 5-4C, no change of the Z_S model in comparison to the initial model is observed. Thus, the optimization of v_S occurs after the first 60 iterations. In the beginning, mainly the Z_P model has been optimized.

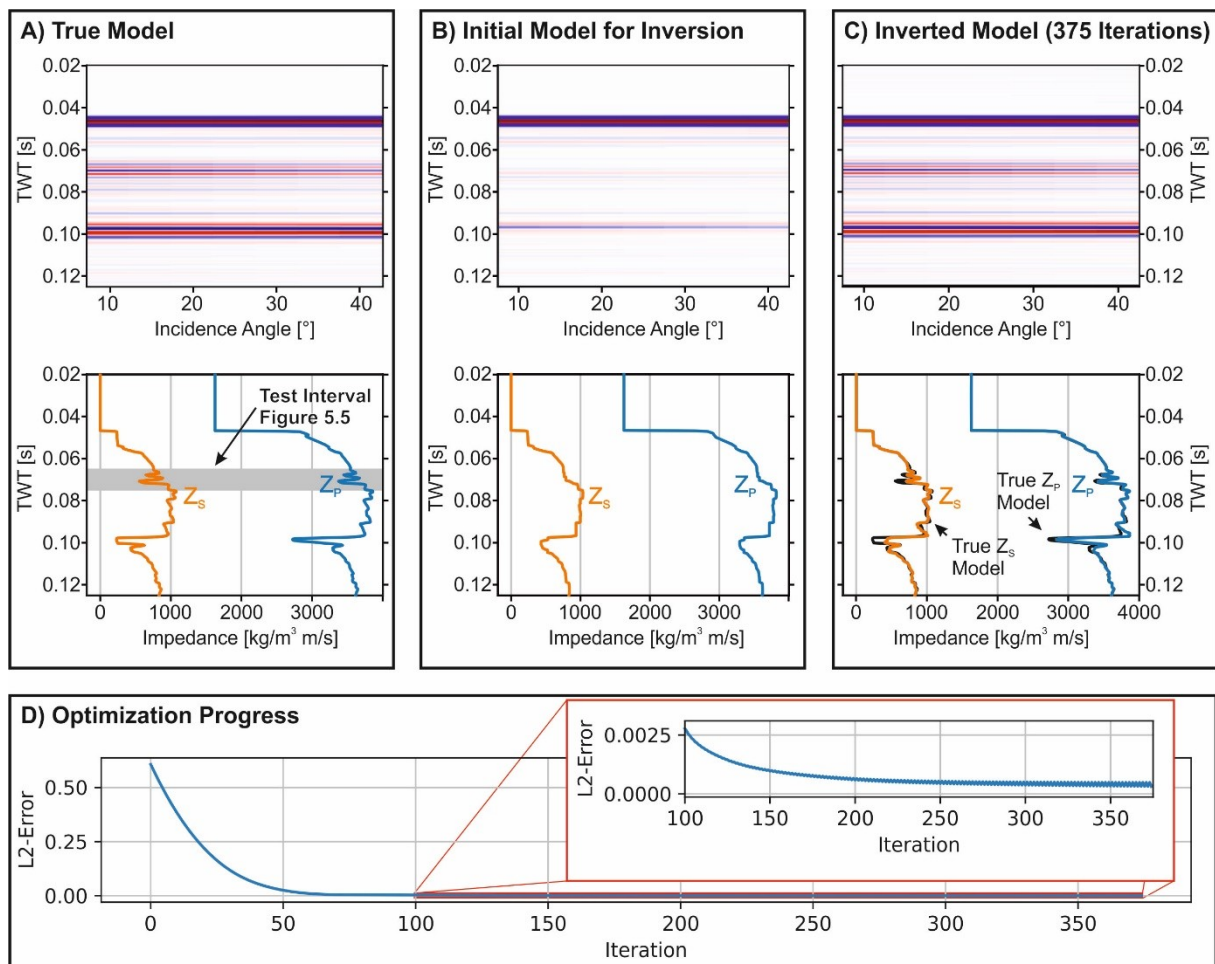


Figure 5-4: Pre-stack inversion on synthetic data. The upper panels of (A)-(D) show angle stacks in the range 10° - 40° in 5° steps which are scaled to the same amplitude, while the lower panels of (A)-(D) show the corresponding compressional impedance Z_P as well as the shear impedance Z_S models. **A)** True model of the synthetic test. The time interval which is used for the sensitivity analysis shown in Figure 5-5 is indicated by a grey bar. **B)** Initial Model for the inversion, which is the true model in (A) filtered with a 6.25 ms long running median filter. **C)** Inverted model after 375 iterations. The true impedances are underlying the inverted impedances and are displayed as black lines. **D)** Optimization progress showing the decreasing L_2 -norm with increasing number of iterations. The subordinate plot shows a zoom on the iterations 100-375.

To test the sensitivity of the model parameters, the lower impedance minimum in the time interval 65-75 ms (see grey bar in Figure 5-4A) has been subjected to changes and the difference to the true model is analysed. For the test of a certain parameter, the remaining parameters were fixed to the true model and the free parameter has been modified to a constant value in a 2 ms window at the location of the lower impedance minimum. Figure 5-5 shows the change of the parameters as well as the development of the L_2 -norm comparing the angle stack of the true model with the perturbed model. For v_p and ρ (see Figure 5-5A and C), the norms are in the same order of magnitude and rise steeply for both higher and lower values than the true model. In Figure 5-5C depicting the v_s changes, the L_2 -norm is one order of magnitude lower and rises steeply for velocities higher than the true model. Velocities lower than the true model result in a comparatively low increase of the norm.

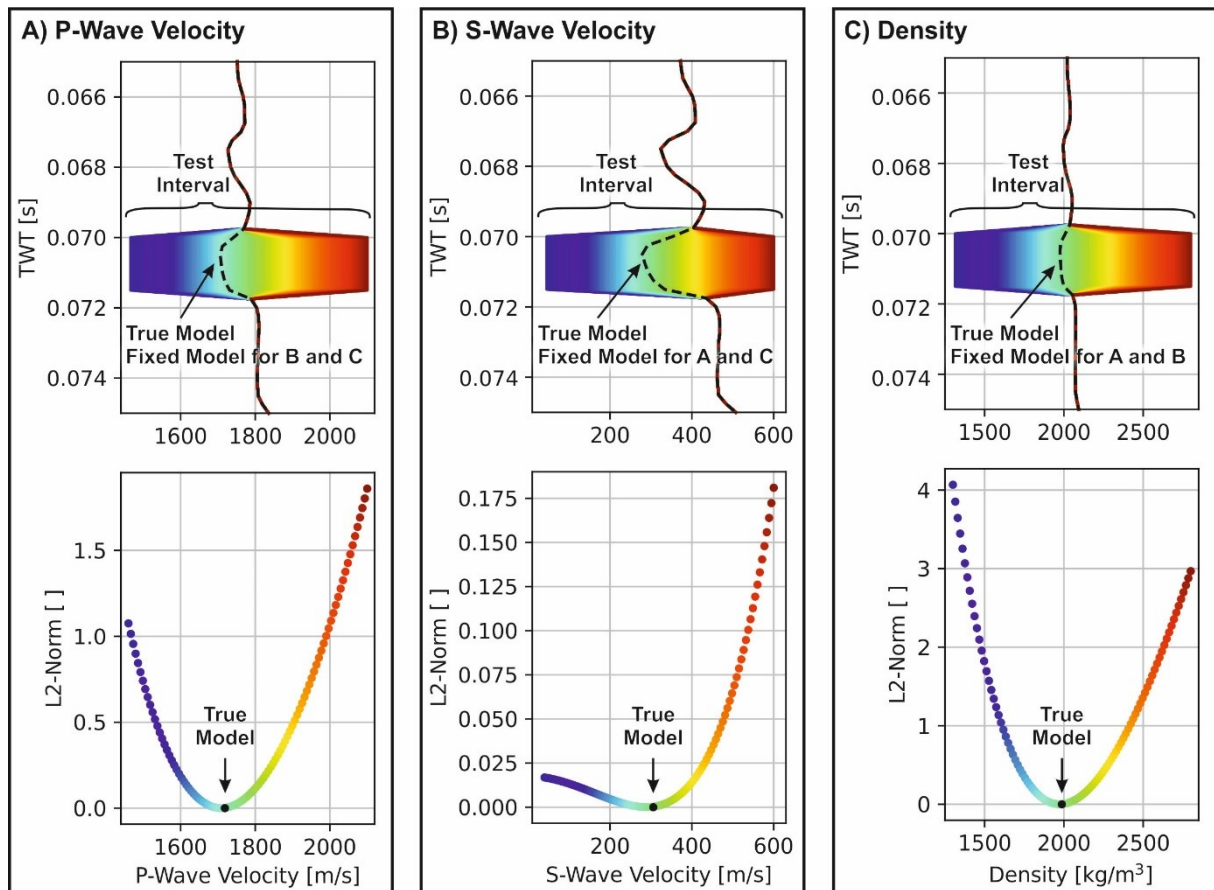


Figure 5-5: Sensitivity analysis of the pre-stack inversion regarding the model parameters P-Wave velocity, S-Wave velocity, and density relative to the true model of the synthetic inversion test (Figure 5-4). To test the impact of the change of a single parameter, the remaining parameters are fixed to the true model and the parameters in a 2 ms interval were changed as shown in the upper panels. The change of the L_2 -norm in respect to the true model is displayed in the lower panels. A) P-Wave velocity sensitivity showing a steep L_2 -norm increase for both higher and lower velocities. B) S-Wave velocity sensitivity showing a steep L_2 -norm increase for higher velocities. C) Density sensitivity showing a steep L_2 -norm increase for both higher and lower densities.

5.3.3 Pre-Stack Inversion of CMP 492 (He569-GeoB21-033)

Using the tested parameters of the synthetic pre-stack inversion test, observed angle gathers of the super-gather at CMP 492 on Profile He569-GeoB21-033 are inverted with 375 iterations. As previously introduced (see “5.3.2 Synthetic Pre-Stack Inversion Tests”), the initial model is derived from the impedance inversion result with empiric relations (“5.3.1 Data Processing and Post-Stack Impedance Inversion”) and has been smoothed with a 6.25 ms long running median filter. As the true scaling of the convolutional model to the observation is not known, an additional scaling step has been performed. For this purpose, the angle gathers of the initial model have been created with an unscaled wavelet. Then the L_2 -norms of the observation and initial model angle gathers are determined and a scale factor for the wavelet being the ratio of the determined norms is calculated. Then the inversion is performed with the scaled wavelet as shown in Figure 5-6. After the inversion, the results are depicted by means of Z_S and Z_P which have been smoothed with a 0.75 ms long running median filter. Comparing Figure 5-6B and Figure 5-6C, the emergence of small-scale variations on the inverted model is observed. Those variations are overall in good agreement with the unfiltered impedance derived models (black lines in the lower panel of Figure 5-6C), although the pre-stack inversion result seems to be more dynamic.

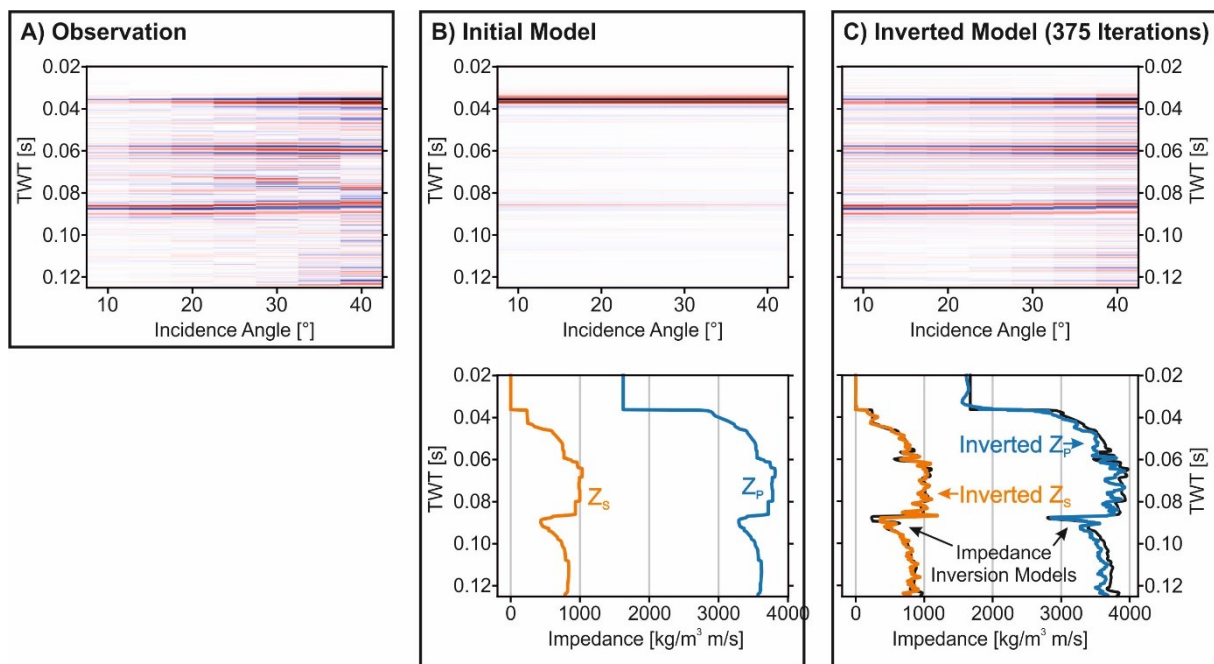


Figure 5-6: Pre-stack inversion of the angle stack at CMP 492 of Profile He569-GeoB21-033. In (A) and the upper panels of (B) and (C) angle stacks scaled to the same amplitude are displayed, while the lower panels in (B) and (C) show the corresponding shear impedance Z_S and compressional impedance Z_P models. A) Observed angle stacks. B) Initial model derived from the post-stack impedance inversion (equivalent to Figure 5-4B). C) Inverted model after 375 iterations. The impedance models after pre-stack inversion generally resemble the post-stack impedance based estimates, although more dynamic variation is observed on the pre-stack inversion results.

Comparing the pre-stack inversion results with the CPT derived estimates, a general agreement is observed as shown in Figure 5-7. For this purpose, the pre-stack inversion result has been converted to depth with the $v_{p,i}$ estimates by the travel time curve inversion. As introduced in Chapter 4, the CPT Soil Behaviour Type (SBT) - ranging from 1 for sensitive soil, over 3 for clay, 6 for clean sand to 9 for stiff material - can be approximated based on Z_p . As displayed in Figure 5-7A, the inversion indicates SBT values of about 4 in the first 9 mbsf, where a SBT of 6 is estimated with the CPT. Beneath 9 mbsf and down to 45 mbsf, both the inversion and the CPT predict SBT in the range of 6-7, although the CPT indicates SBT up to 9 in thin intervals. Below 45 mbsf, there is a CPT data gap corresponding to a continuous clay layer in the area (compare Chapter 4), which is identified by the inversion with low SBT of 4. Below the data gap, high SBT of 8 are predicted by the CPT, while the inversion results in a SBT of 6. The crossplot of the two v_s estimations in Figure 5-7B shows that both predictions follow the same trend and scatter around the 1:1 relation. One group of outliers is found, which corresponds to high v_s CPT estimates below the dominant clay layer. Considering the detailed run of the curves in Figure 5-7A, the CPT estimates appear to show more high frequency variations. At the position of the remnant of the multiple after multiple suppression, no significant variation in v_s or SBT is observed.

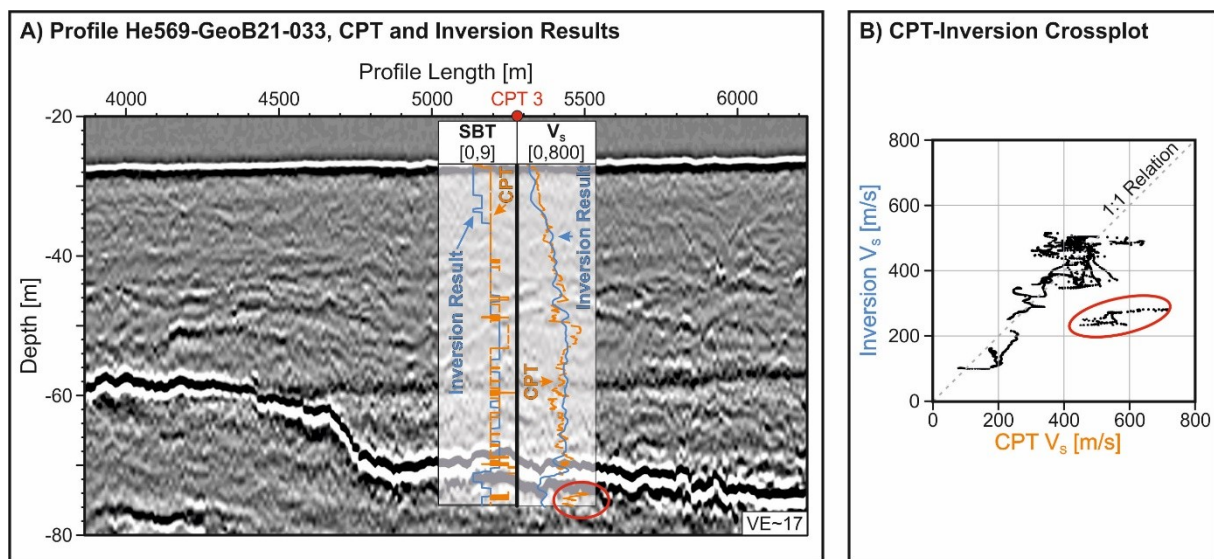


Figure 5-7: Comparison of the Cone Penetration Testing (CPT) and pre-stack inversion results in respect to the Soil Behaviour Type (SBT) and S-Wave velocity v_s . At about 60 m depth, the remnant of the multiple after the multiple suppression is to be observed. A) Section of the attenuation corrected, and depth converted Profile He569-GeoB21-033 taken from Chapter 4 with an overlay of the inversion and CPT result at the well location. B) Crossplot of v_s derived by the CPT measurements and the pre-stack inversion. The outliers marked with a red oval correspond to the high v_s values of the CPT measurements at the bottom of the well in (A), which are also marked with a red oval.

5.4 Discussion

The comparison of the pre-stack inversion results with CPT derived ν_s suggests, that the estimation of shear properties only based on reflection seismic data is feasible, although there are limitations regarding the sensitivity towards low ν_s values and the resolution of the inversion results.

In the example given, the vertical resolution of the CPT measurements is 0.02 m. Taking the estimates of Chapter 3, the vertical resolution for seismic imaging, ignoring potential attenuation effects, is approximately 1.3-1.6 m (compare Table 3-3). Although the pre-stack inversion enhances the vertical resolution, the CPT measurements reveal a one to two orders of magnitude higher vertical resolution. This difference in vertical resolution explains the scattering of ν_s around the 1:1 relation observed in Figure 5-7B. Additionally, the difference in lateral resolution can play a role. As reported in Lesny et al. (2014), multiple CPT measurements can be necessary at one location to estimate representative soil parameters if the seafloor is inhomogeneous. This requirement is also due to the fact, that the cone of a CPT probe intrudes typically through an area of 10-15 cm² (Lunne et al., 2002; Robertson & Cabal, 2015) and due to this small size single measurements might not be representative due to local inhomogeneities. The lateral resolution of the seismic trace, in contrast, is ideally at the scale of the dominant wavelength after migration or equivalent to the Fresnel zone before migration (Yilmaz, 2001). For the seismic source used and without migration, the lateral resolution in this study is in the range of 6 m at the seafloor and 14 m at $TWT=0.125$ ms. Performing pre-stack migration, the resolution in this study could be enhanced to the scale of the wavelength of 3-5 m. As a comparison, due to the 1D modelling approach chosen in the waveform inversion study by Provenzano et al. (2017), the lateral resolution in their study is equal to the imaging aperture of 70 m, although the vertical resolution is at a decametric scale as a result of the higher source frequencies used. To increase the lateral resolution in waveform modelling approaches in general, 2D or 3D modelling would be necessary, which in turn would dramatically increase the computational demands. As a first approximation, the best possible resolution of full waveform inversion is at the scale of the wavelength (Fichtner, 2011) and thus at the same scale as a migrated image. So, with pre-stack inversion a higher lateral resolution compared to 1D waveform inversion can be achieved, although both the lateral and vertical resolution of this seismic study are by an order of magnitude lower than CPT measurements. This difference in resolution can also be an advantage if average unit properties rather than localized and highly scattering measurements are of interest.

Taking into account the sensitivity analysis conducted, the inverted shear properties are characterized by high uncertainties for low v_S values and an upper boundary estimate can be provided for low v_S values. As described in “5.2.1 Steepest Descent Pre-Stack Inversion”, the optimization of the model during an inversion depends on the misfit of the amplitudes quantified here by the L_2 -norm. As shown in Figure 5-5B, the amplitude effect of v_S is significantly smaller than the effect of v_P and ρ . Therefore, the model is first optimized in respect to v_P and ρ . So, Figure 5-4 and Figure A-19 show for the synthetic test that after approximately 60 iterations the Z_P -model is closely resembling the true model, while the Z_S model did not change significantly from the initial model. After 375 iterations, also the Z_S model resembles the initial model, although the relative decay of the misfit after 60 iterations is comparatively small and although the local minima of the inversion model are not reaching the lowest values of the true model local minima (Figure 5-4C). However, the local maxima are well resolved. This observation is also explained by Figure 5-5B. The L_2 -norm rises significantly less distinctly for low v_S values compared to high v_S values. Therefore, model updates towards low v_S values are small or might not be resolved due to noise. This finding is in agreement to the observation of low sensitivity for Poisson’s Ratios ν_{PR} close to 0.5 by Provenzano et al. (2017), as high ν_{PR} correspond to low v_S . Due to an expected range $0.47 < \nu_{PR} < 0.5$ (compare Table 3-1), the parametrization by means of ν_{PR} is rather insensitive to the subseafloor types of interest. Similarly, it is observed in the uncertainty estimation of Amplitude Versus Angle inversion conducted by Riedel et al. (2003) that the probability distributions of v_S are broad and skewed towards low v_S values. Based on those sensitivities it can be generalized, that seismic inversion based on reflected P-Wave amplitudes is associated with high uncertainties for low v_S values. If the initial model is updated towards lower v_S values by the inversion, the model is likely to be an upper boundary estimate of v_S in this interval.

Additionally, the local dip of reflectors can be taken into account with the proposed pre-stack inversion workflow. Performing 1D waveform inversion, only horizontal reflectors are accurately modelled (Provenzano et al., 2016, 2017, 2018). Especially if the v_P estimate is to derive the initial model, this can lead to artefacts, as the velocity of dipping reflectors is wrongly estimated. On the other hand, the contribution of v_P and ρ to Z_P can be decoupled in case of the waveform inversion, but is coupled in the pre-stack inversion for pre-critical angles (Riedel et al., 2003).

Several assumptions are made conducting the proposed pre-stack inversion. First, only primary P-Wave reflections are modelled. Due to the acquisition geometry with limited offsets and towed hydrophones, the forward scattered wavefield or S-Waves are not recorded (compare Yao et al., 2020). Diffractions can be recorded but those events are suppressed by the generation of angle

stacks. Secondly, multiscattering in the form of ghosts or multiples needs to be corrected. As shown in Figure 5-7, there are remnants of the seafloor multiple after multiple suppression (see Chapter 4 and “2.1.3 Seismic Data Processing” for processing details). Those remnants do not seem to cause artefacts in the inversion. Provenzano et al. (2020) propose a method to correct ghost reflections in the frequency domain based on the occurrence of the ghost notches. Due to the acquisition set-up used, no ghost notch is apparent in the data used here and the ghost was not attenuated. As an alternative to the attenuation of the ghost, ghost reflections can also be included in the forward modelling as done by Provenzano et al. (2017) for waveform inversion. For the pre-stack inversion, ghosts can be included in the modelling by a non-stationary convolution. Similarly, attenuation effects or processing artefacts such as stretch can be implemented by a non-stationary convolution. In this study attenuation has been corrected before inversion. Performing data correction before pre-stack inversion has the advantage, that the resulting angle gathers can be quality controlled and that the processing employed is also beneficial for the imaging. On the other hand, the inclusion of, e.g., multiples and ghosts into the modelling is physically more accurate and can also help to improve inversion results (Espin et al., 2022). Furthermore, the reflections need to be flattened by the CRS moveout correction and, e.g., static errors might introduce artefacts. Finally, the general properties of the sediments need to follow the empiric relations. Small scale variations are solved by the inversion, but an initial model needs to be accurate for the inversion to succeed (Virieux & Operto, 2009; Fichtner, 2011). As the initial model in this study depends on two empiric relations, the properties of the subseafloor need to follow those properties for accurate inversion results. Since the general trend of CPT and inversion estimates are matching, the empiric relations are applicable here. The pre-stack inversion itself is unconstrained and therefore, the inversion workflow can be adopted to account for available ground truth data or alternative methods for the generation of the initial model.

5.5 Conclusion

Synthetic tests including a sensitivity analysis as well as the inversion of an angle gather of shallow marine near surface and Ultra-High Resolution reflection seismic data acquired in the North Sea showed that shear properties can be estimated with an elastic pre-stack inversion scheme exclusively based on seismic data. The inversion results fit to Cone Penetration Test data used as a ground truth data, although the sensitivity towards low S-Wave velocities is limited. With a lateral resolution of 6 m close to the seafloor and 14 m at a depth of about 70 mbsf, this inversion scheme provides better resolution than 1D reflection waveform inversion methods. Several assumptions

and prerequisites have to be met to apply the pre-stack inversion. For this purpose, the developed toolbox allows for Common Reflection Surface travel time curve inversion, angle stacking, and attenuation estimation and correction. Two empiric relations are fitted to unconsolidated sediments to allow the generation of the initial model for the elastic pre-stack inversion, which is defined by impedance inversion.

The developed inversion scheme is conceptually simpler than waveform inversion methods. Therefore, this inversion is computationally less demanding, and the simple construction of the inversion algorithm also allows for better quality control of the input data. Including pre-stack migration in the processing flow and non-stationary convolution in the forward modelling of the inversion algorithm, some further improvements can be achieved. The low sensitivity for low S-Wave velocities is assessed to be a general problem of the inversion of P-Wave reflection data. Different and new data acquisition methods for shallow marine near surface seismics are required for more accurate shear property estimations.

Chapter 6 Post-Stack Acoustic Impedance as a Reliable Indicator of Variation in Lithologic and Geotechnical Properties in Southern Arkona Basin – Assessment of Two Near-Surface Impedance Inversion Approaches Using Stationary Wavelets

Opeyemi Ogunleye¹, Guillaume Sauvin², Nikolas Römer-Stange¹, Maarten Vanneste², Volkhard Spieß¹

¹Department of Geosciences, University of Bremen, Klagenfurter Str. 2-4, D-28359 Bremen, Germany

²Norwegian Geotechnical Institute, Sandakerveien 140, 0484 Oslo, Norway

In preparation for Near Surface Geophysics. Format and references have been adopted to match the thesis.

Keywords

Near-Surface, Seismic, Inversion, Cone-Penetration-Test, Site Characterisation

Abstract

Subsurface investigations in structurally and lithologically complex areas could be incomplete and biased, if seismic data was insufficiently incorporated and not used to the full capacity. However, seismic inversion is not yet routinely applied for wind farm development, although impedance has been identified as a predictor of spatial changes in lithology and geotechnical parameters. To facilitate a more widespread application, there is the need for more case studies especially in the Baltic Sea, the evaluation of the predictive potential of acoustic impedance, and the evaluation of different inversion approaches. We performed near-surface post-stack seismic inversion on seismic data sets collected in the Arkona Basin in the southern Baltic Sea and (1) correlated the absolute acoustic impedance with geological ground truths at borehole locations; (2) showed how acoustic impedance vary with the measured cone resistance and sleeve friction; and (3) assessed two approaches of acoustic impedance inversion. The dataset presented comprises of 2D seismic lines (total length 35 km, central frequency ~ 350 Hz, vertical resolution ~ 1.1 m), sediment descriptions from four boreholes, and Cone Penetration Test (CPT) data from one location. This study reveals the absolute acoustic impedance as a significant seismic tool to resolve stratigraphic and structural complexity in a geological succession. The simultaneous variation of acoustic impedance with measured cone resistance and sleeve friction across lithologic boundaries and the statistical correlation of the predicted impedance and measured CPT parameters indicate that acoustic impedance derived from UHR seismic reflection data has the potential to serve as a predictor of cone resistance and sleeve friction in the southern Arkona Basin. The two seismic inversion approaches used are based on stationary wavelets, and they produce absolute acoustic impedance anomalies which correlate well with ground truths.

6.1 Introduction

The acoustic impedance Z_P is a key seismic unit property which can also be estimated from laboratory measurements, core logging, or borehole geophysical logs of primary velocity v_P and shear wave velocity v_S , where density ρ is known or could be estimated by empirical relationships (Gardner et al., 1974; Raymer et al., 1980). Seismic inversion techniques have been developed for analysing elastic properties of formations by transforming seismic records related to reflection coefficients at interfaces to unit-based quantitative geophysical properties such as Z_P (Avseth et al., 2005). Full and partial stacks of seismic reflection data can be inverted to generate Z_P estimates. Simultaneous inversion of partial stacks or pre-stack data can yield multiple layer properties including Z_P and shear impedance Z_S , v_P/v_S -ratio, and ρ . This sort of inversion is based on the Amplitude Versus Angle effect (AVA effect; Zoeppritz, 1919), which can be approximated by, e.g., the Fatti et al. (1994) or Aki & Richards (2002) equation. In our study, however, we carried out seismic inversion of full stacks. In this case, only post-stack acoustic impedance has been generated, which is expected to show formation heterogeneities (Filippova et al., 2011). Using Ultra-High Resolution (UHR, ISO 19901-10, 2021) seismic reflection data acquired in northern Norway, Vardy (2015) showed that empirical relationships exist between Z_P and sediment properties including v_P , ρ , mean grain size and porosity. Moreover, through impedance inversion and modelling coupled with geological and geotechnical data, Vanneste et al. (2015) developed a method to derive geotechnical properties from seismic data in a coastal area affected by shallow landslides in northern Norway. Thus, it is imperative for geologic characterization and windfarm development in the Baltic Sea to evaluate the use of Z_P as a tool for (1) distinguishing and mapping near-surface lithologic units and their internal property boundaries in the southern Arkona Basin; and (2) predicting geotechnical data in the area. In this current study, we employ and improve on the seismo-stratigraphic and structural framework interpreted in Ogunleye et al. (in prep., 2024a) in our study area. We present UHR 2D seismic reflection profiles, sediment descriptions, and CPT profiles in the southern Arkona Basin. In the study area (see Figure 6-1), our objectives are to: (1) demonstrate the applicability of acoustic impedance as an attribute for resolving geological complexity; (2) qualitatively and quantitatively correlate acoustic impedance with measured cone resistance and sleeve friction; and (3) assess the acoustic impedance sections generated by two near-surface post-stack inversion methods, and suggest improvements that could be made in the inversion approaches. This research shows that Z_P is a viable tool for detailed stratigraphic and structural interpretation of geological formations in the southern Arkona Basin. It further points to the usefulness of this quantitative physical property as an attribute for CPT data prediction.

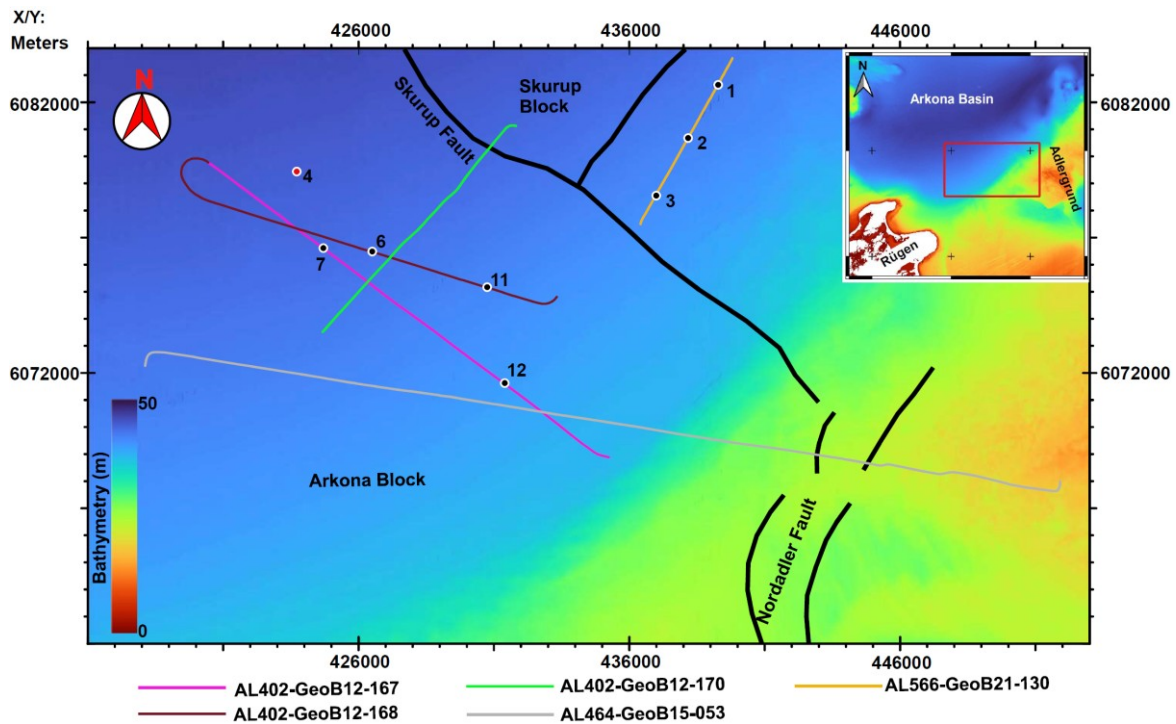


Figure 6-1: Map of the study area (red outline in inset) in the southern Arkona Basin showing the 2D seismic reflection profiles that were inverted in this study and sites with sediment descriptions, velocity logs and Cone Penetration Test (CPT) data. The sites are shown as dots (black dots represent sites located on the inverted seismic profiles; red dot indicates an additional site utilized in Ogunleye et al., in prep., 2024a and 2024b). The name of each site is the number shown in the figure (numbers follow the order introduced in Ogunleye et al., in prep., 2024a) followed by BH/CPT at the locations with CPT data; Site 1 has no CPT data, so its name is 1 BH. 1 BH and 2, 3, 4, 6 and 11 BH/CPT have velocity logs which were utilized in Ogunleye et al., in prep., 2024b for estimating median physical properties of geological units. Pre-Quaternary faults of the Tornquist Zone are depicted (Obst et al., 2017). EMODnet Bathymetry Consortium (2020) is the basis of the water depth values. Map coordinates are in UTM 33N (Modified from Ogunleye et al., in prep., 2024a).

6.2 Geological Setting

The Arkona Basin in the southern Baltic Sea is characterized by a maximum water depth of 48 m and is bordered to the north by the Swedish coast, west by the Krieger's Flak and Plantagenetgrund, south by the Pomeranian Bight, and east by the Bornholm Island (Obst et al., 2017). Pre-Quaternary bedrock chalk in the basin was deposited in the Cretaceous (Winterhalter et al., 1981). During Pleistocene glaciations, subglacial valleys were incised into this bedrock in the southern Arkona Basin (Obst et al., 2017). On the top of the till-dominated valley fills and Cretaceous chalk in the study area, Weichselian glaciers deposited a widespread un-channelized till unit within which a layer of glaciolacustrine clay is sandwiched and the basal section of which is characterized by a localized glaciofluvial cobbly interval in the central part of our study area Ogunleye et al. (in prep., 2024a). Similarly, Weichselian glacial tills have been reported as overlying Cretaceous chalk in the central Arkona Basin (Mathys et al., 2005). Post-glacial sediments, which vary from clay through silt to sand (Moros et al., 2002; Kortekaas et al., 2007) cap the stratigraphic succession.

6.3 Material and Methods

6.3.1 Seismic Data

The five 2D Multi-Channel Seismic (MCS) reflection profiles inverted for Z_P in this study (see Figure 6-1 for location) were acquired in 2012 (AL402-GeoB12), 2015 (AL464-GeoB15) and 2021 (AL566-GeoB21). Only Profiles AL402-GeoB12-167 and AL402-GeoB12-168 (combined length of 35 km) are presented. Other profiles were used to ensure that picked horizons were consistent with already-established seismo-stratigraphic framework (Ogunleye et al., in prep., 2024a) in the study area. The central frequency of the seismic data is ~ 350 Hz with a vertical resolution of ~ 1.1 m (calculated as a quarter of a wavelength with a velocity of 1500 m/s). The MCS data were processed, tied to lithologic logs, and qualitatively interpreted during the work documented in Ogunleye et al. (in prep., 2024a).

Lithologic descriptions and CPT data were provided for our study (see Figure 6-1). The CPT data consist of cone resistance, sleeve friction and pore pressure measurements. In this paper, sediment descriptions from 4 sites (i.e. 6, 7, 11 and 12 BH/CPT) and CPT data from Site 12 BH/CPT are presented as representatives. Lithologic logs at 6 and 11 BH/CPT were tied to the seismic data by using the average velocity of intervals deduced from primary wave velocity logs at the respective locations. Sites 7 and 12 BH/CPT were tied to the seismic data by using the velocity profiles of 6 and 11 BH/CPT, respectively.

6.3.2 Post-Stack Impedance Inversion

The 2D full stacks of seismic data processed for the near-surface intervals were inverted for Z_P using stationary wavelets in two approaches. The inversion products were then correlated with sediment descriptions and CPT data at various sites. Geological boundaries, which were initially interpreted as horizons from seismic amplitude sections, were refined using Z_P sections, and intra-unit boundaries that became newly apparent on the Z_P sections were picked. The two near-surface impedance inversion procedures are described below.

Impedance Inversion with Velocity-Guided Background Trend (Velocity-Guided Approach)

For the purpose of UHR seismic reflection data inversion, we developed a post-stack acoustic impedance inversion algorithm based on the methodology proposed by Vardy (2015). This algorithm integrates a convolutional forward model with a genetic optimization approach to derive Z_P at each trace location.

In this inversion scheme, which is termed velocity-guided approach in this study, the algorithm initiates an initially random set of impedance models within a user-defined Z_P range. This range is based on the minimum and maximum Z_P values for each seismic unit as calculated from P-S logs in Ogunleye et al. (in prep., 2024b). The range is varying with depth and guided by the v_P -model. Subsequently, the algorithm calculates a corresponding set of synthetic traces by convolving the models with a theoretical source waveform (zero phase wavelet). The fitness of each Z_P model within the family is evaluated by quantifying the residual between the synthetic traces and the actual field seismic traces. The generation of new models employs the Stochastic Remainder technique, wherein models with superior fitness are retained along with a random selection of those with lower fitness. These new models are then paired to facilitate crossovers and mutations, simulating the principles of natural selection. A new set of associated synthetic traces is generated. The process of natural selection is controlled by user-specified cross-over and mutation probabilities, which govern the likelihood of paired samples undergoing exchange (crossing over) or a specific sample being substituted with another randomly determined value (mutation). This iterative procedure continues until one of the specified termination conditions is met: Reaching the maximum number of generations, achieving a field trace data residual below a user-defined threshold, or attaining a stable gradient in the residual evolution from generation to generation.

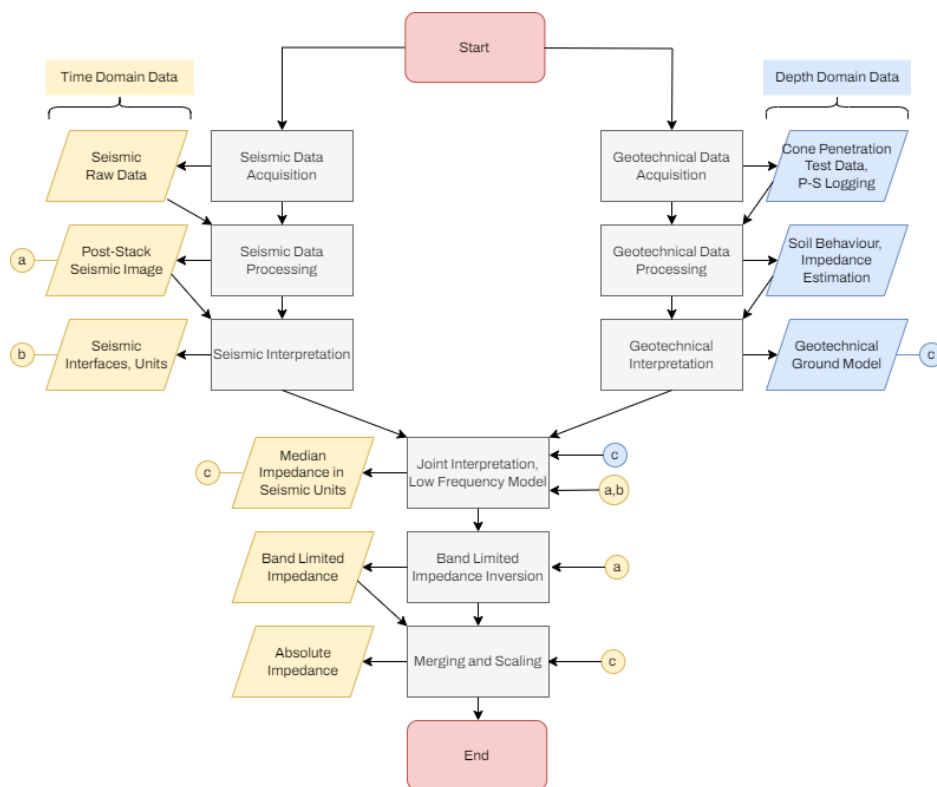


Figure 6-2: Workflow of the band-limited acoustic impedance inversion approach in which a band-limited impedance result is merged with a layer cake low-frequency Z_P model.

Impedance Inversion with Layer Cake Low-Frequency Model (Band-Limited Approach)

A band-limited Z_p section has been generated based on post-stack seismic data and merged with a low-frequency model to generate an absolute impedance estimate (see Figure 6-2 for the workflow), which is termed band-limited approach in the following. As a first step for the low-frequency model generation, unit boundaries were identified in a joint interpretation of the seismic and geotechnical data, as well as the available core descriptions. Those boundaries were used to develop a layer cake model, which was flooded with median Z_p values estimated from P-S logs (Ogunleye et al., in prep., 2024b; see Figure 6-1 for the locations of the velocity logs).

Secondly, band-limited impedance was determined based on the post-stack seismic image with a genetic algorithm as described in Vardy (2015). In this global search and stochastic algorithm (Sen & Stoffa, 1992), forward modelling was performed with a convolution of randomly initialized reflectivity models with a wavelet. The band-limited Z_p is consecutively determined from the reflectivity. For this approach, the wavelet was extracted from the post-stack seismic image by stacking the tapered seafloor reflection along the profile. Further details of the reproducible implementation are described in Chapter 4 and the parameters are given in Table 6-1.

Finally, and to merge the band-limited impedance inversion results with the low-frequency model and thus generate an Z_p estimate, the BLIMP algorithm described in Ferguson and Margrave (1996) was extended and applied. In this method, the band-limited impedance was merged with the low-frequency model in the frequency domain with a Linkwitz-Riley crossover filter (Linkwitz, 1978), after scaling the band-limited Z_p . Using this procedure, the wavelet and post-stack seismic image did not need calibration.

Table 6-1: Impedance inversion parameters for genetic algorithm and merging of band limited impedance with low-frequency model in a layer cake approach.

Band Limited Impedance Inversion Parameters for Genetic Algorithm	
Number of individuals in each generation	1000
Number of generations for optimization	500
Cross-over probability	60%
Mutation probability	0.15%
Probability of a time sample to be a reflector for initialisation	2%
Number of individuals to determine final result	100
Low Frequency Model Merging Parameters	
Low pass frequency for scaling	180 Hz
High pass frequency for scaling	60 Hz
Characteristic frequency for merging	25 Hz

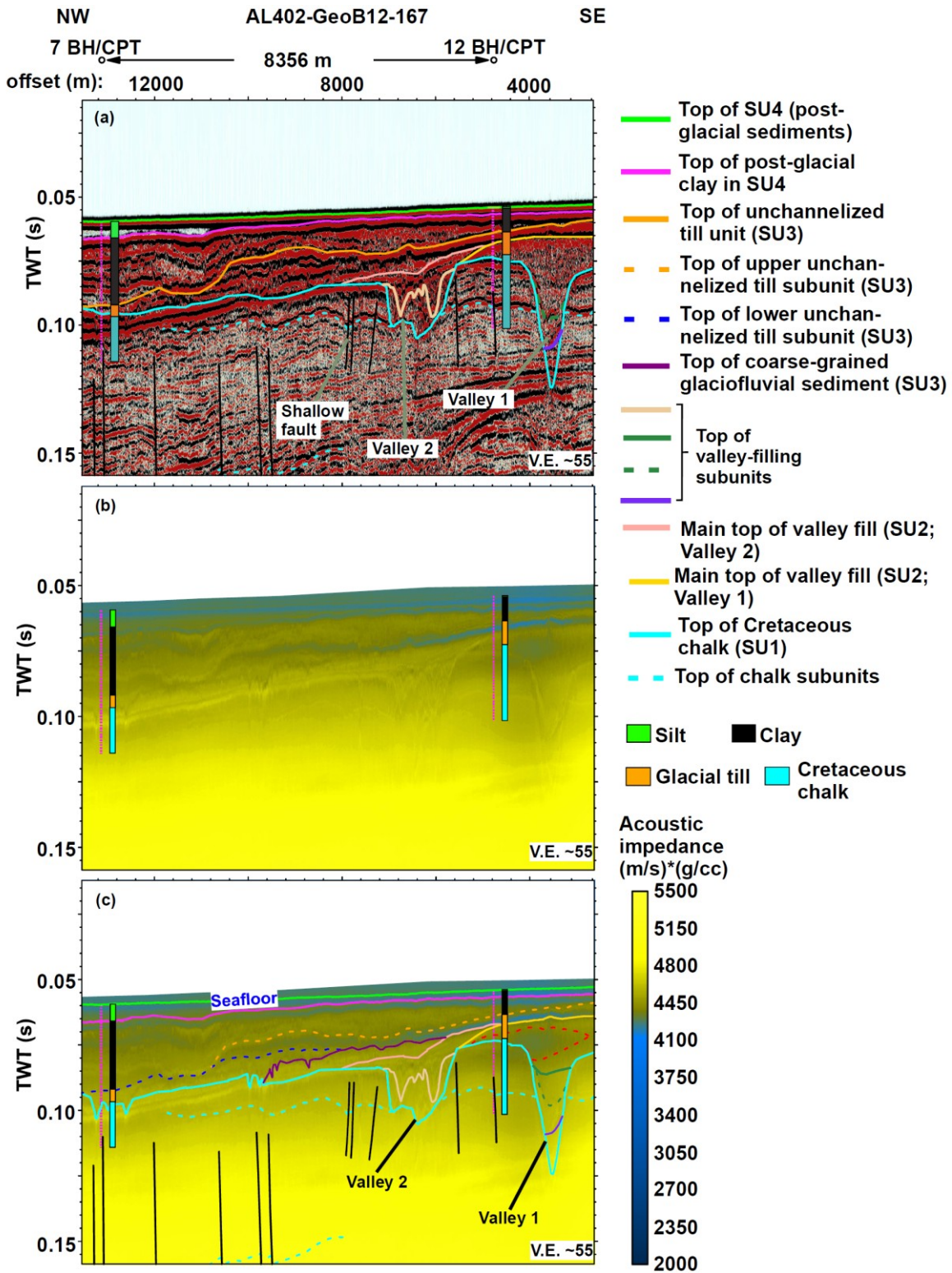


Figure 6-3: 2D seismic Profile AL402-GeoB12-167 tied to the lithologic logs at Sites 7 and 12 BH/CPT (see Figure 6-1 for location): a) Interpreted seismic amplitude section showing the major near-surface seismic units and their lithologic characterization in our study area based on the work presented in Ogunleye et al. (in prep., 2024a); b) Un-interpreted absolute acoustic impedance section of the profile generated with the velocity-guided inversion approach; c) Interpreted version of the impedance section in (b) which has been correlated with sediment descriptions. Notice how impedance anomalies indicate the lateral extent and vertical stacking of stratigraphic units. Two Pleistocene valleys are depicted as cutting into the Cretaceous chalk. Stippled red lines delineate a lenticular zone with relatively low impedance values in a valley fill. TWT = Two-Way Travel-time; SU = Seismic Unit (vertical exaggeration was calculated based on a velocity of 2000 m/s)

6.4 Results

Four main near-surface seismic units (SU1-4) occur in our study area (Figure 6-3a). The horizons produced from seismic amplitude data during the work presented in Ogunleye et al. (in prep., 2024a) were overlaid on the Z_P sections generated with the velocity-guided approach. Besides, in the band-limited approach, new horizons, which were used to build the stratigraphic framework of the low-frequency model, were superimposed on the inversion product. In both approaches, these horizons were re-picked on the impedance sections by following the configuration of corresponding geophysical interfaces across which there was a Z_P contrast and picking intra-unit boundaries where there were distinct zones of anomalous Z_P values within a unit. The succession of geophysical anomalies bounded by these refined horizons is presented in the following sections 6.5.1 and 6.5.2.

6.4.1 Lithology-Related Anomalies on the Absolute Acoustic Impedance Sections Derived from an Inversion of Full Stacks Using the Velocity-Guided Approach

Post-stack inversion of the seismic Profile AL402-GeoB12-168 using the velocity-guided approach yielded the highest values of Z_P in the Cretaceous chalk interval. Lineaments occur on the Z_P section within a zone of bedrock described as fissured chalk at Site 11 BH/CPT (Figure 6-4). Within the tunnel valleys incised into the bedrock chalk in places, multiple valley-filling subunits exist and are separated by curved surfaces across which there is a Z_P contrast (Figure 6-3c). In the uppermost subunit of Valley 1 shown Figure 6-3b and shown Figure 6-3c, a lenticular low Z_P anomaly is defined.

A layer of glaciofluvial rock fragments overlying the Cretaceous chalk at Site 11 BH/CPT ties with anomalously low Z_P (Figure 6-4). The anomaly extends laterally and tapers to the NW and SE, lying on top of the valley fill in places (Figure 6-3b, c and Figure 6-4b, c). Higher up in the stratigraphic sequence, variations in the geophysical attribute show an Z_P anomaly associated with the lower till subunit in SU3 at 11 BH/CPT, and this anomaly extends to and beyond Site 6 BH/CPT, a location where it correlates with the only till unit observed in the borehole (Figure 6-4). Based on the distribution of Z_P values, a subtle boundary could be delineated within the lower till subunit, further separating the till subunit into lower and upper compartments. This boundary terminates on the top of the glaciofluvial rock fragments in the inter-borehole area (Figure 6-4). Furthermore, the top of the lower till subunit shows an undulating and irregular interface across which there is a marked Z_P contrast with the overlying lithologic unit.

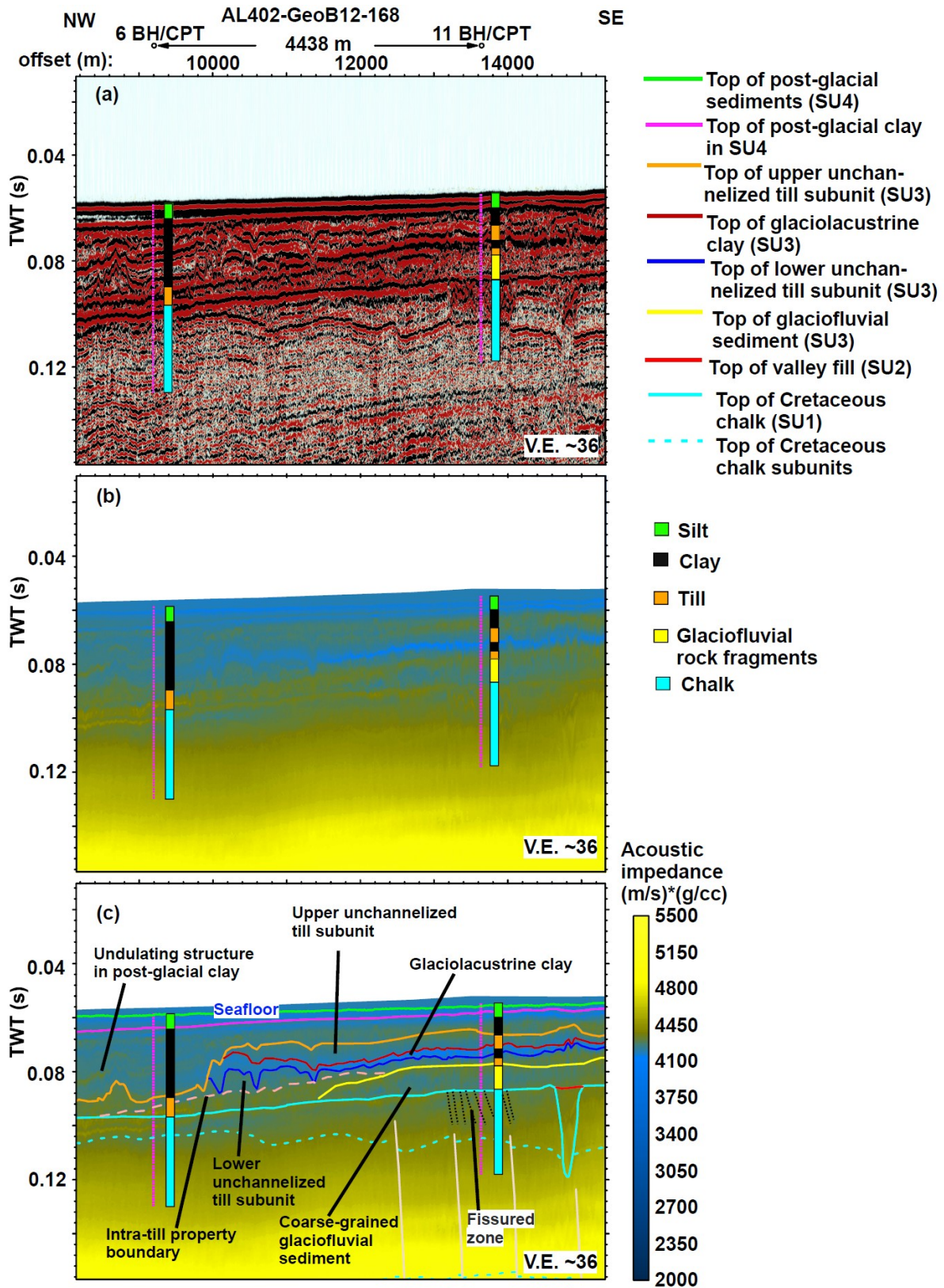


Figure 6-4: 2D seismic Profile AL402-GeoB12-168 tied to the lithologic logs at Sites 6 and 11 BH/CPT (see Figure 6-1 for location): a) Un-interpreted seismic amplitude section along the profile; b) Un-interpreted absolute acoustic impedance section generated from data shown in (a) with the velocity-guided inversion approach; c) Interpreted version of the impedance section in (b) showing the spatial distribution of lithologic units, an intra-till property boundary, and the structural features of geological intervals. TWT = Two-Way Travel-time; SU = Seismic Unit (vertical exaggeration was calculated based on a velocity of 2000 m/s).

Along Profile AL402-GeoB12-168, this top is draped by a blanket of distinctively low Z_P which corresponds to the glaciolacustrine clay at 11 BH/CPT (Figure 6-4) and thickens in the northwestern direction, only to taper out abruptly without being penetrated at 6 BH/CPT. Succeeding the clay unit is the upper subunit of un-channelized till encountered at 11 BH/CPT, which not only exhibits relatively higher Z_P than the clay, but also defines an anomaly that morphologically thins out to the NW without extending to Site 6 BH/CPT (Figure 6-4). Z_P section along Profile AL402-GeoB12-167 reveals that the anomalies of the lower and upper un-channelized till subunits are vertically stacked directly on top of each other where the glaciolacustrine clay does not exist, with the interface between them exhibiting a distinct Z_P contrast (Figure 6-3b, c). Horizon interpretation along the interfaces of Z_P contrasts indicates that in SU3 the tills encountered at 7 and 12 BH/CPT coincide with the Z_P anomalies of the lower and upper till subunits, respectively (Figure 6-3b, c).

Within the post-glacial sediments at Sites 6 and 7 BH/CPT, a thick layer of clay underlying a silt unit was penetrated (Figure 6-3 and Figure 6-4). The lithologic boundary between these units corresponds to a distinct interface between two successive intervals with different Z_P on the velocity-guided impedance sections; the relatively higher impedance values characteristically occur in the underlying layer of clay (Figure 6-3b, c). The undulating structures in the post-glacial clay unit are also preserved on the Z_P sections (Figure 6-3 and Figure 6-4).

6.4.2 Post-Stack Absolute Acoustic Impedance Predicted with the Band-Limited Approach - Comparison with the Velocity-Guided Inversion

On the band-limited impedance section of Profile AL402-GeoB12-167, the Cretaceous chalk and post-glacial sediments have the highest and lowest mean Z_P , respectively, in the near-surface geological interval (Table 6-2). The spatial position and geometry of geophysical boundaries are markedly similar in both the band-limited and velocity-guided impedance sections along the profile (Figure 6-3c and Figure 6-5c). However, the range of Z_P predicted with the two approaches for most seismic units and subunits differs (Table 6-2). For each seismic unit and subunit along the seismic profile, the range of predicted Z_P is wider in the band-limited inversion product than the velocity-guided impedance section (Figure 6-3, Figure 6-5, Table 6-2). Using the statistical estimates derived for each seismic unit from velocity logs as the ground truth in our study area, the range of impedance predicted with the band-limited approach is more comparable to the ground truth than that of the velocity-guided approach does (Table 6-2).

Table 6-2: Measured and predicted statistical estimates of acoustic impedance Z_P for each seismic unit. The ground truth (measured) values are based on a compilation of velocity logs as shown in chapter 4, while the velocity-guided and band-limited values are based on the impedance predicted in each seismic unit along the entire section of Profile AL402-GeoB12-167. The velocity-guided and band-limited values for each seismic unit are calculated by summing the products of mean impedance and sample size at each trace location and dividing this sum by the total number of samples for all the locations. The unit of the statistical measures is (m/s)*(g/cc). The estimated mean values are grand means. Min. = Minimum Value; Max. = Maximum Value; SU = Seismic Unit

Source of estimate	Measure of statistics	Seismo-stratigraphic unit				
		SU4 (post-glacial sediment)	SU3		SU2 (valley fill)	SU1 (chalk)
			Till	Glaciofluvial sediment		
Ground truth	Min.	2670	3647	4039	3204	3942
	Max.	4794	6243	5472	5430	5648
	Mean	3622	4304	4674	4298	4790
Velocity-Guided inversion	Min.	4162	4146	4318	4220	4288
	Max.	4581	4690	4683	4830	5227
	Mean	4362	4413	4492	4484	4758
Band-Limited inversion	Min.	874	2609	2843	2989	2505
	Max.	5771	5974	5782	6006	6483
	Mean	3711	4411	4338	4374	4855

Within the Cretaceous chalk interval, the velocity-guided inversion approach applied to the Profile AL402-GeoB12-167 predicted a grand mean that was very close to the ground truth (Table 6-2). Along the profile, the band-limited approach produced reliable Z_P in both the chalk and post-glacial sediments on the basis of the grand means estimated for the lithologic units. Furthermore, it is evident that the Z_P predicted for the post-glacial sediments with the velocity-guided approach are too low in comparison to the ground truth (Table 6-2). On one hand, along the Profile AL402-GeoB12-167, the band-limited seismic inversion approach produced a lesser grand mean Z_P than the velocity-guided approach within the Seismic Unit SU2, glaciofluvial section of SU3 and post-glacial interval (Table 6-2). On the other hand, a comparison of the band-limited impedance section with its velocity-guided counterpart along the seismic profile appears to indicate that there is no significant difference in the mean Z_P predicted for the till sections of Seismic Unit SU3 (Table 6-2). While the Seismic Unit SU2 on the band-limited Z_P section exhibits a lesser grand mean Z_P relative to the SU3 till, the reverse is the case in the velocity-guided impedance section (Table 6-2).

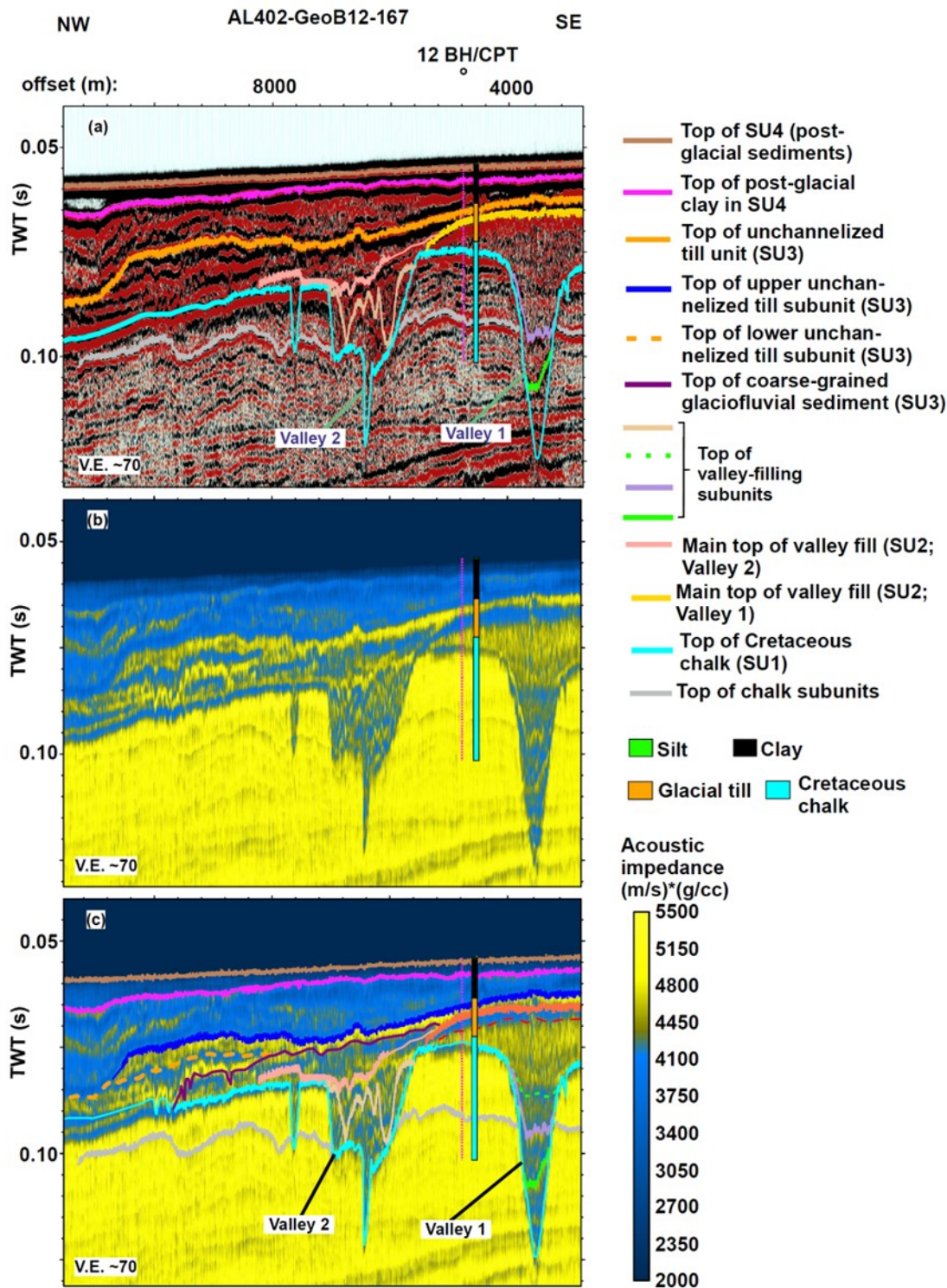


Figure 6-5: 2D seismic Profile AL402-GeoB12-167 tied to the lithologic log at Site 12 BH/CPT: a) Seismic amplitude section of the profile showing the horizons independently picked along the same unit boundaries that were interpreted in Ogunleye et al. (in prep., 2024a). These horizons formed the stratigraphic framework of an initial low-frequency impedance model employed in the band-limited approach; b) Un-interpreted absolute impedance section of the profile generated with the band-limited inversion approach. It corresponds to a part of Figure 6-3; c) Interpreted version of the seismic data in (b) correlated with sediment descriptions. The stippled red line is the top of the high-impedance interval within the uppermost subunit filling Valley 1. This high-impedance zone is characterized by anomalous lithologic and geotechnical properties within the valley. Notice how impedance anomalies show the detailed spatial distribution of lithologic units, thereby allowing improvements on the initial horizon interpretation shown in (a). Artifacts occur as vertical stripes on this impedance section. TWT = Two-Way Travel-time; SU = Seismic Unit (vertical exaggeration was calculated based on a velocity of 2000 m/s)

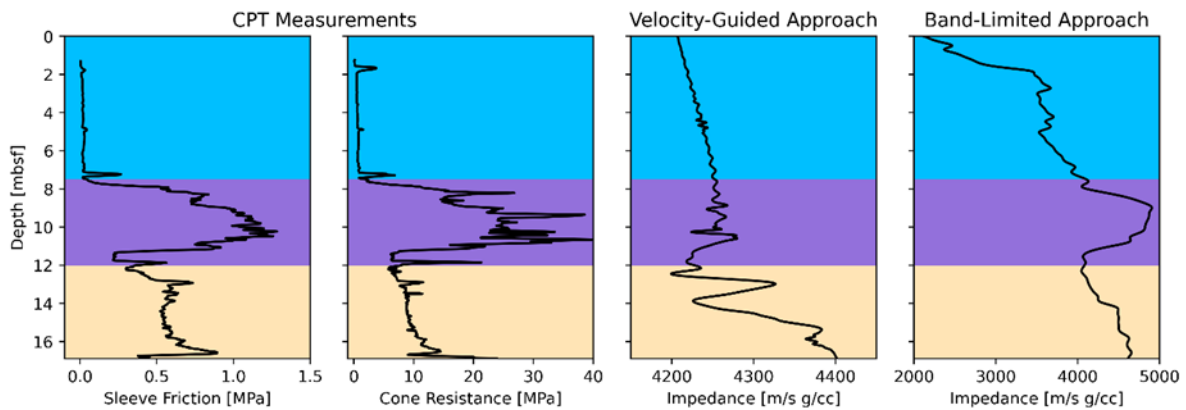


Figure 6-6: Raw data plot of the CPT measurements of sleeve friction and cone resistance and the impedance inversion results at Site 12 BH/CPT. Seismic Units SU4, SU3 and SU2 are shown with blue, purple and light brown backgrounds, respectively. Please note that the band-limited impedance is shifted upward by 1.07 m (the rationale for this decision is given in fig. 5.9).

6.4.3 Correlation of the Measured Cone Resistance and Sleeve Friction with the Predicted Absolute Acoustic Impedance - Velocity-Guided and Band-Limited Inversion Approaches

At Site 12 BH/CPT, the CPT profiles of measured cone resistance and sleeve friction were correlated with the acoustic impedance traces predicted by the velocity-guided and band-limited approaches (see Figure 6-6, Figure 6-7, and Figure 6-8).

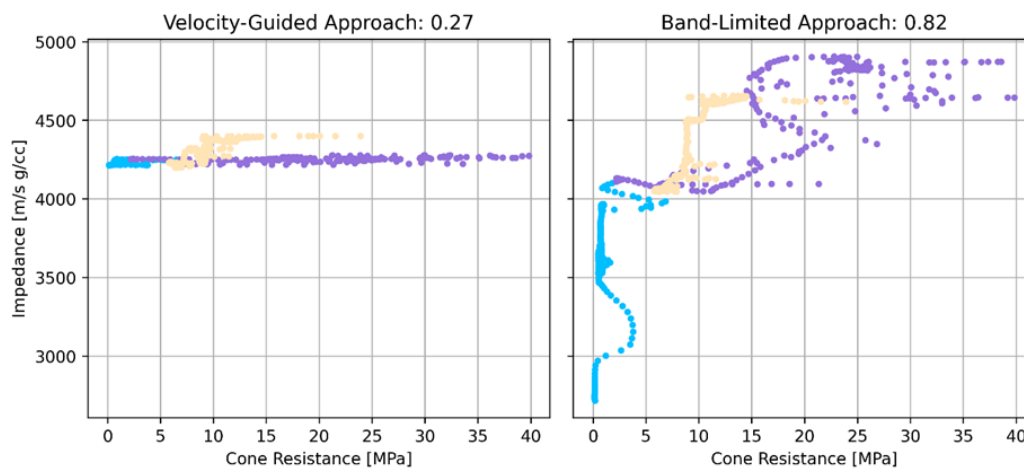


Figure 6-7: Cross plots of measured cone resistance and predicted impedance at Site 12 BH/CPT with a correlation coefficient of 0.27 for the velocity-guided results and 0.82 for the band-limited results. The colour code of the seismic units follows the code in Figure 6-6.

The measured sleeve friction and cone resistance in Seismic Unit SU4 show basically no variations (Figure 6-6). In addition, the resolution of the CPT data and acoustic impedance is at a different level. While the CPT data show very fine variations in the sub-meter scale, the seismic resolution is more at 0.5-1 m (Figure 6-6). This difference in resolution generally impacts CPT-to-impedance

correlation. Traversing from the shallower to deeper sections of the subsurface at Site 12 BH/CPT, it would be observed that the measured cone resistance and sleeve friction are relatively high in the un-channelized glacial till of SU3, and these CPT parameters decrease significantly into the Seismic Unit SU2, within which they progressively vary with depth.

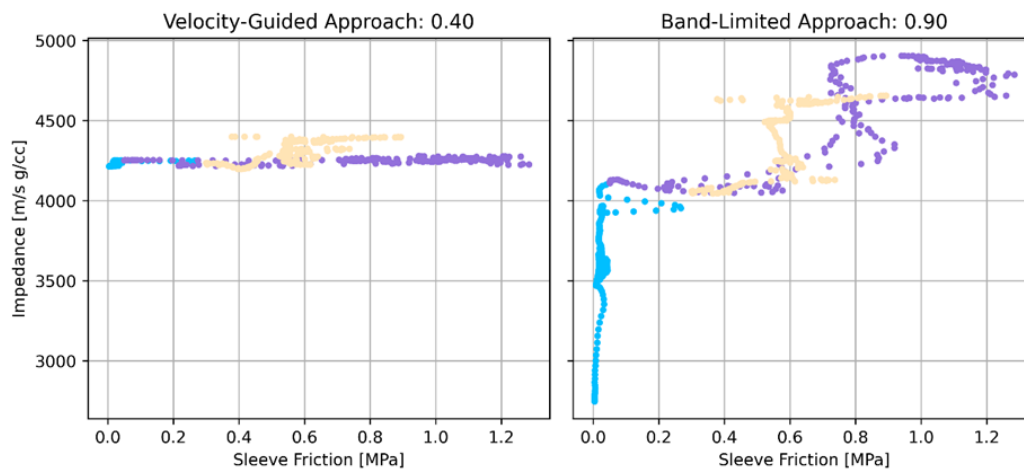


Figure 6-8: Cross plots of measured sleeve friction and predicted impedance at Site 12 BH/CPT with a correlation coefficient of 0.40 for the velocity-guided results and 0.90 for the band-limited results. The colour code of the seismic units follows the code in fig. Figure 6-6.

The cross plots between cone resistance measurements and predicted acoustic impedance at Site 12 BH/CPT indicate correlation coefficients of 0.27 and 0.82 for the velocity-guided and band-limited inversion approaches, respectively (Figure 6-7). In addition, the cross plots between sleeve friction and predicted impedance at the same site exhibit correlation coefficients of 0.40 and 0.90 for the velocity-guided and band-limited impedance inversions, respectively (Figure 6-8).

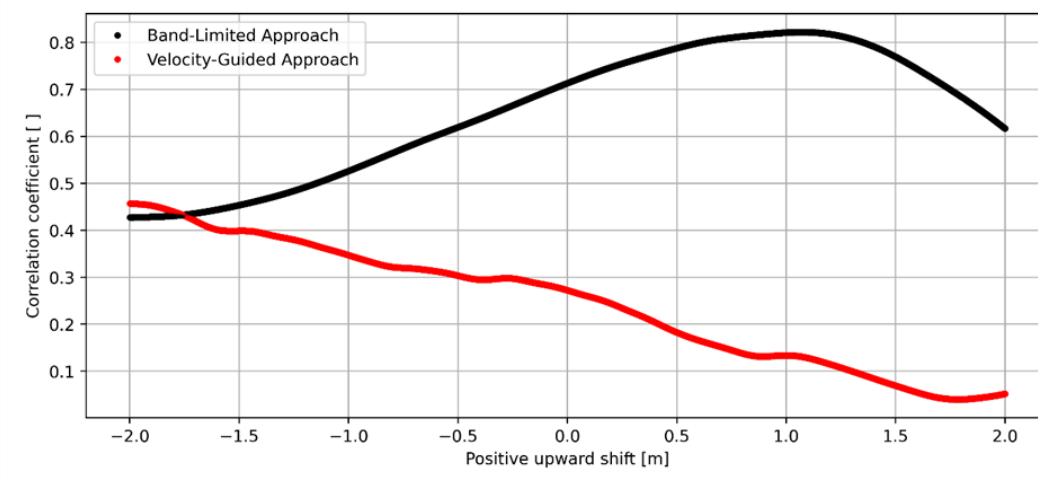


Figure 6-9: Correlation coefficient of measured cone resistance and predicted impedance as a function of constant depth shift at Site 12 BH/CPT.

Depth conversion in a strict sense requires some form of calibration and possibly some shifting. To test whether a potential vertical shift is affecting the correlation of impedance and CPT data, a constant shift was applied and the correlation coefficient was calculated. The result is given in Figure 6-9. While no clear indication for a potential up- or downward shift is visible for the velocity-guided result, it seems to be rather clear that the band-limited should be shifted by about 1 m to achieve a fit with the CPT data (Figure 6-6 and Figure 6-9).

6.5 Discussion

6.5.1 Resolving Stratigraphic and Structural Complexities in the Near-Surface Sedimentary Record of Southern Arkona Basin — Significance of Correlation Between Absolute Acoustic Impedance and Lithologic Ground Truth

Foremost, the four major seismic units and their subunits, which were correlated with borehole sediment descriptions in the study area in Ogunleye et al. (in prep., 2024a), have been delineated on the absolute acoustic impedance sections in our current research (Figure 6-3, Figure 6-4, and Figure 6-5). This finding agrees with Veeken and Da Silva (2004), who mentioned that interpretation of seismic inversion results helps to recognize significant geological boundaries in the subsurface. Besides, the succession of imaged geological units on the velocity-guided and band-limited impedance sections ties well with the lithologic succession described at Sites 7 and 12 BH/CPT (Figure 6-3b, c and Figure 6-5b, c).

The difference of the statistical values between the ground truth and impedance inversion results in Table 6-2 can partly be explained by the spatial restriction of the boreholes. While the unit statistics have been calculated for the entire profile for the impedance inversion results, those statistics are restricted to the borehole sites for the ground truthing. Thus a larger sample size and changing geologic settings are encountered for the impedance inversion results. The occurrence of the highest values of Z_P in the Cretaceous chalk on the impedance sections (e.g. Figure 6-3c and Figure 6-5c, Table 6-2) is supported by the trend observed in the median values of Z_P derived for the seismic units on the basis of a compilation of P-S logs in the area (Ogunleye et al., in prep., 2024b). Based on the report of fissures in the Cretaceous chalk at Site 11 B/CPT, it is evident that the lineaments seen in the chalk zone around the borehole on the acoustic impedance section of Profile AL402-GeoB12-168 (Figure 6-4) correspond to the surfaces of weakness which were interpreted as evidences of glaciotectonic brittle deformation within the bedrock chalk in Ogunleye et al. (in prep., 2024a).

On the seismic amplitude section of Profile AL402-GeoB12-167, three subunits of SU2 have been interpreted within Valley 1 (Figure 6-5a). On the corresponding band-limited Z_p profile, the shallowest of those three subunits could be further differentiated into a lower interval showing relatively low impedance values and an upper section with predominantly high Z_p , thereby indicating that four subunits of SU2 actually occur within Valley 1 (Figure 6-5b, c). Multiple units of Z_p anomalies separated by curved interfaces within the tunnel valleys constitute the sedimentary packages of SU2 produced during multiple depositional episodes in the valleys (Figure 6-3 and Figure 6-5). On the band-limited Z_p section of Profile AL402-GeoB12-167, the uppermost subunit of SU2 occurring in Valley 1 has Z_p that are predominantly higher than those of the three underlying valley-filling subunits (Figure 6-5b, c). Since Z_p of a formation is dependent on v_p and its ρ , and in turn on its fluid content, mean grain size, porosity and mineralogical composition (Veeken & Silva, 2004; Vardy, 2015), the predominantly higher Z_p observed in the uppermost subunit of SU2 in Valley 1 might have a multi-factorial cause which might include relative preponderance of coarser material, low porosity and/or high proportion of crystalline rock fragments. However, sufficient core data are not available for a more specific explanation.

On the Z_p sections, an interpretation of the areal coverage and morphology of the coarse-grained glaciofluvial interval at the base of SU3 is facilitated (Figure 6-4, Figure 6-5). This cobbly sedimentary interval would evidently have a relatively large mean grain size and low porosity, which might be expected to produce high Z_p . Therefore, the relatively low values of Z_p associated with this coarse-grained glaciofluvial unit (e.g. Figure 6-4c and Figure 6-5c) might be due to the effect of a relatively low fraction of crystalline material or inhomogeneous spatial distribution. An alternative explanation such as high gas contents is unlikely, as the presence of gas was not reported in this glaciofluvial unit. Moreover, the mapping of the top and base of impedance anomalies not only indicates the lateral extent of the lower un-channelized till subunit in SU3, but it also shows that the Pleistocene glacial till penetrated at 6 BH/CPT is the lateral equivalent of the lower un-channelized till subunit encountered at 11 BH/CPT (Figure 6-4). It is noteworthy that this lower till subunit is not uniform in lithologic properties. Variation of Z_p from its lower to upper parts indicates the occurrence of an intra-till boundary that compartmentalizes the subunit itself into two different sections vertically stacked on each other, with probable changes in lithologic properties occurring across the boundary (Figure 6-4). Thus, it was the upper compartment of this lower till subunit that was penetrated at 11 BH/CPT. This level of internal details in SU3 was not very evident on the corresponding seismic amplitude section (Figure 6-4).

Although there is limited ground truth for some units and subunits, the impedance inversion results can still depict the unit property changes and thus allow a more comprehensive interpretation. The surface of the lower till subunit of SU3 is undulating and irregular as evidenced from the configuration of impedance anomaly associated with it along the Profile AL402-GeoB12-168 (Figure 6-4b, c). Deposition in a Pleistocene glacial lake blanketed the rugged top of the lower till subunit with the glaciolacustrine clay encountered at 11 BH/CPT in the central part of the study area. Thickness variation of the low Z_P anomaly corresponding to this clay on the Z_P section of Profile AL402-GeoB12-168 indicates that the clay unit gradually thickens in the northwestern direction, only to taper out abruptly (Figure 6-4b, c). This explains why the glaciolacustrine clay was not observed at 6 BH/CPT. Similarly, due to the tapering out of the upper un-channelized till subunit in the northwestern direction along the Profile AL402-GeoB12-168, as revealed by the morphology of its Z_P anomaly, the upper till subunit was not penetrated at 6 BH/CPT (Figure 6-4b, c). Besides, the spatial mapping of the top and base of the lower and upper un-channelized till subunits as defined by Z_P anomalies showed that 7 BH/CPT penetrated the former till subunit, while the section of SU3 drilled at 12 BH/CPT was the latter till subunit (Figure 6-3b, c).

Furthermore, the lithologic variation in the post-glacial sediments particularly at Sites 6 and 7 BH/CPT can be correlated with significant Z_P changes (e.g. Figure 6-3b, c). On the Z_P sections, this correlation allows the discrimination of the silt unit, which extends to the seafloor, from the underlying post-glacial clay in areas not penetrated by boreholes. Along the Profile AL402-GeoB12-167, the internal structures of geological units, which can be seen on the seismic amplitude section, are equally evident on the corresponding Z_P sections. The velocity-guided and band-limited Z_P sections preserve and reveal the undulating structural features in the post-glacial clay unit along the profile (Figure 6-3, Figure 6-5).

6.5.2 Potential of Acoustic Impedance as an Attribute for Predicting Cone Resistance

According to Stoll (1989), the properties affecting the acoustic response of marine sediments include sediment structure, dynamic strain amplitude, overburden stress, lithification and grain size. These parameters also determine the cone resistance and sleeve friction during CPT measurements (Vardy et al., 2018). However, P-wave seismic data and geotechnical measurements are acquired under different strain regimes (Sauvin et al., 2019). While seismic data are collected under small strain conditions, conventional CPT measures large strain parameters. Besides, conventional seismic data have much lower resolution than geotechnical measurements (e.g. Figure 6-6), with the former and latter data types being recorded in time and depth domains, respectively. Noteworthy is that although events on seismic amplitude sections are interface-related, Z_P and

CPT measurements are both quantitative unit-based properties of formations. On the other hand, the difference in resolution between seismic and geotechnical measurements generally impacts the correlation between predicted Z_P and CPT data.

In our study, Z_P was derived from UHR seismic reflection data (central frequency ~ 350 Hz). The Z_P predicted by the band-limited and velocity-guided approaches show variations across unit boundaries from the Cretaceous chalk through valley fill and unchannelized till interval to post-glacial sediments (Figure 6-3, Figure 6-4, and Figure 6-5). Starting from 7.5 mbsf at Site 12 BH/CPT, measured cone resistance and sleeve friction increase drastically from SU4 to SU3, and their values decrease from SU3 to SU2 (Figure 6-6). At this site, Z_P predicted with the band-limited approach shows similar simultaneous changes across the boundaries of the seismic units (Figure 6-6). On the basis of the concurrent variations in predicted Z_P , measured cone resistance and sleeve friction across the seismic units as observed at Site 12 BH/CPT (Figure 6-6), we posit from a qualitative point of view that Z_P produced with the band-limited approach has the potential to serve as a predictor of cone resistance and sleeve friction during CPT data synthesis from UHR seismic data. This observation indicates that a risk for the generation of subsurface model can be mitigated. In general, there is a risk of missing potentially relevant units when a subsurface characterization was only based on boreholes (Henson & Sexton, 1991). In the case of the generation of integrated ground models incorporating inversion results, this risk is reduced as the lateral homogeneity and changes are revealed by the seismic data.

6.5.3 Assessment of the approaches for post-stack impedance estimation

Genetic algorithms have been employed for the two seismic inversion approaches in this study. The genetic algorithms used in the velocity-guided and band-limited approaches incur significantly higher computational costs compared to conventional deterministic optimization methods, but the benefits are threefold.

First, the algorithms' randomized initial generation of models results in a final Z_P model that is derived from field seismic data. Consequently, the ultimate Z_P model is more independent of interpreter bias, and the inversion algorithm autonomously determines an optimal model that offers the best global fitness solution from a statistical standpoint. Second, as the inversion explores a substantial portion of the solution space, it permits the calculation of statistically meaningful Probability Density Functions for each sample at every trace location. This enables the determination of confidence limits in addition to the statistically optimal solution. Third, stochastic optimization algorithms like genetic algorithms deliver robust optimization solutions, even in the

presence of significant noise contamination. For genetic algorithms, the mutation operator allows the algorithm to continuously explore a wide region of the parameter space, enabling it to overcome local minima in the optimization space and converge toward the global minimum.

In the two post-stack inversion approaches carried out in this study, a stationary wavelet was used and attenuation was not compensated. Due to the significant occurrence of fine grained sediments and chalk in the working area, Quality Factors $Q > 100$ are to be expected (Pinson et al., 2008). Considering the source signal of the air gun used in acquiring the seismic data, the source signal change due to attenuation is thought to be negligible for those high Q values. With relatively high Q values, the level of uncertainty introduced by attenuation is negligible as exemplified in Chapter 4.

The impedance sections produced by the band-limited and velocity-guided inversion approaches exhibit meaningful Z_P values that differentiate seismic units from one another along the same seismic line (Figure 6-3 and Figure 6-5). The numerical difference between the two inversion approaches (see section 6.4.2) could be due to: (1) difference in the wavelet used for convolution; (2) difference in the cost function for minimization; and (3) smoothing of a-priori Z_P model in the velocity-guided approach only. In the band-limited technique, a statistical wavelet extraction was performed on the post-stack seismic image by stacking the tapered seafloor reflection along the seismic line and this yielded a true, mixed phase wavelet that was used for the inversion.

Although the velocity-guided approach equally employed a statistical wavelet derived from the seismic data, the phase of the wavelet used in the approach was imposed to be zero. The zero phase wavelet used in the velocity-guided inversion scheme is therefore different from the mixed phase wavelet present in the actual seismic amplitude data. Thus, the lenticular low Z_P anomaly, which occurs within the uppermost subunit filling Valley 1 at the southeastern end of Profile AL402-GeoB12-167 (Figure 6-3b, c), might be an artifact partly or wholly caused by the difference between the phase of the wavelet used for inversion and that of the true wavelet.

Comparing the band-limited impedance section to its velocity-guided counterpart along the seismic Profile AL402-GeoB12-167, it appears that there is no significant difference in the mean Z_P values predicted for the till subunits of Seismic Unit SU3 (Table 6-2). However, at Site 12 BH/CPT and nearby areas, the impedance values of the SU3 till are generally higher in the band-limited product than in the velocity-guided section (Figure 6-3, Figure 6-5, and Figure 6-6). Thus, the similarity in the mean Z_P values of the SU3 till in both inversion products could be due to the presence of significantly lower values of Z_P within the till subunits in other parts of the band-limited product

than in the velocity-guided section, which leads to a much lower minimum value and broader range of impedance in the band-limited impedance section than in its velocity-guided counterpart within the SU3 till (Table 6-2).

At Site 12 BH/CPT, based on the correlation coefficients, both velocity-guided and band-limited approaches yielded a better correlation between the sleeve friction and predicted Z_P than between the measured cone resistance and predicted acoustic impedance (Figure 6-7, Figure 6-8). While the Z_P predicted by the band-limited approach highly correlates with the measured cone resistance and sleeve friction (correlation coefficients of 0.82 and 0.90, respectively), the velocity-guided approach yielded Z_P that have little to low correlation with the measured CPT parameters (Figure 6-7, Figure 6-8). Therefore, the band-limited approach yielded absolute acoustic impedance values that would better predict CPT data than the product of the velocity-guided inversion approach. This difference might be partly or wholly due to the difference between the phases of wavelets used in the inversion approaches. Consequently, the velocity-guided approach might be improved by utilizing the true wavelet of the seismic data in the inversion scheme. The high level of correlation between the band-limited impedance values and measured cone resistance and sleeve friction in our current study means Z_P generated with the band-limited approach can be used to reliably predict CPT parameters in the southern Arkona Basin. Sauvin et al. (2019) also reported a good correlation between measured and predicted tip resistance values when they used an artificial neural network in multi-attribute regression for tip resistance prediction. The regression was performed between Z_P and other seismic property on one hand and measured tip resistance on the other hand by training at multiple calibration sites. Besides, Chen et al. (2021) showed that Z_P generated by inverting ultrahigh-frequency (>2000 Hz) geophysical data can serve as a predictor of tip resistance for site characterizations.

Furthermore, in our study, horizons initially picked on seismic amplitude sections have been refined by re-picking them on the Z_P sections. Along Profile AL402-GeoB12-167, the Z_P sections produced with the two inversion approaches reveal remarkably similar stratigraphic and structural framework (compare Figure 6-3 and Figure 6-5). The interpreted geological features from both Z_P sections also correlate with lithologic ground truths at the associated borehole sites (Figure 6-3, Figure 6-4, and Figure 6-5). However, while the Z_P section generated with the velocity-guided approach is smooth, the product of the band-limited approach has vertical stripes that occur as artifacts (compare Figure 6-3 and Figure 6-5). This difference could be due to the smooth Z_P a-priori information which was applied in the former approach only and the abstaining of all kinds of smoothing in the latter approach.

6.6 Conclusion

Conventional seismic amplitude sections allow qualitative interpretation of stratigraphic and structural features based on interface-related seismic attributes. Our study has shown that such qualitative analysis of ultra-high-resolution seismic data should be checked and improved with seismic inversion results such as the post-stack absolute acoustic impedance Z_p .

In this research, Z_p of formations has been predicted using two different seismic inversion approaches based on stationary wavelets. Those approaches have been used to resolve subsoil geological complexity in the southern Arkona Basin. Impedance variation along seismic profiles has revealed anomalies that depicted not only the spatial extent and structure of stratigraphic intervals, but also the intra-unit boundary caused by internal lithologic variations which were not obvious on seismic amplitude sections. In our study, Z_p anomalies of formations accurately tied with lithologic ground truths at borehole locations in the southern Arkona Basin. This fostered the lateral correlation of lithologic units between boreholes and provided a detailed understanding of stratigraphic compartments, particularly within an un-channelized till unit. It also aided delineation of glaciofluvial rock fragments and glaciolacustrine clay. In the Cretaceous bedrock, fissures were depicted as lineaments on a Z_p section. The multiple sedimentary packages making up valley fills were represented as stacked units of impedance anomaly separated by curved interfaces across which there was a major Z_p contrast. The internal geomorphologic features seen on seismic amplitude sections within the post-glacial clay interval were equally preserved on Z_p profiles. Consequently, post-stack absolute acoustic impedance should be predicted through inversion of UHR seismic data and tied to lithologic logs to resolve near-surface stratigraphic and structural complexity, for example, in glaciated terrains consisting of Cretaceous bedrock chalk covered by glaciogenic sediments, which have in turn been succeeded by post-glacial clay and silt. Inversion of Z_p might have the potential to be used for predicting lithologic properties in the southern Arkona Basin.

Besides, we have shown that, in the southern Arkona Basin, qualitative changes in the measured cone resistance and sleeve friction across major unit boundaries within the post-glacial to glaciogenic interval occur concurrently with variations in the predicted Z_p . At a CPT site, the predicted Z_p from the band-limited inversion approach highly correlates with the measured cone resistance and sleeve friction values. We therefore conclude that when properly utilized, post-stack absolute acoustic impedance from UHR seismic reflection data has the potential to serve as an attribute for predicting geotechnical parameters - at least cone resistance and sleeve friction values - of subsoil units in the southern Arkona Basin.

The impedance inversion approaches used in this study - velocity-guided and band-limited approaches - were based on stationary wavelets, and they yielded meaningful results that variably tied with ground truths. However, it appears that an improved result might be realized with the velocity-guided approach, if the true wavelet and its actual phase are used for the inversion. It is equally apparent that attention should be given to improving the smoothness of predicted Z_p sections in the band-limited approach. In the implementation of a genetic algorithm for impedance inversion using stationary wavelets, the phase of the applied wavelet in relation to that of the true wavelet, cost function for minimization, and smoothing of acoustic impedance a-priori information are factors that might have an impact on predicted Z_p values.

6.7 Acknowledgements of Opeyemi Ogunleye

This study was funded through the project 'SynCore' (project number 03EE3020C) by the German Federal Ministry for Economic Affairs and Climate Action on the basis of a parliamentary resolution passed by the German Bundestag. The authors thank the partners in the project (Fraunhofer ITWM, GuD Geotechnik und Dynamik Consult GmbH, RWE Renewables GmbH) for their cooperation.

We also thank the captains and the crews of R/V Alkor for the successful conduction of the seismic data acquisition campaign during the research expeditions.

The geological, geophysical and geotechnical data as well as computers and IHS Kingdom license were made available by the University of Bremen for this study. The Norwegian Geotechnical Institute equally used its computing facility to carry out seismic inversion during and after a research placement of the first author at the institute. This research stay was funded by the MARUM graduate school GLOMAR. Our study benefited from fruitful discussions with Dr. Jean-Rémi Dujardin.

Chapter 7 Synthesis

The marine near surface, which describes the first tens to hundreds of meters below the seafloor, is of great societal and environmental relevance. But as of today, only a fraction of the world's ocean surface has been mapped by means of depth measurements and an even smaller proportion of the marine subsurface has been investigated. Of all available techniques, reflection seismics are a unique and extensively used method to structurally image the sub-seafloor. But the interpretation of seismic images only allows for an indirect and potentially ambiguous inference of the lithologies and associated depositional processes. Also, biases and misconceptions can arise during the interpretation. Especially in the near surface the possibilities to extract quantitative information from seismic data are underused.

Therefore, this thesis investigated how near surface seismic inversion can complement and improve subsurface studies adding quantitative information to the interpretation. Thereby, the focus was set on shallow water near surface seismic data and on the investigations for offshore wind energy farms. However, the general principles can be applied to diverse research questions regarding unconsolidated sediments. New insights and perspectives for future research are provided by this study, which are briefly summarised in the following.

7.1 Summary of the Conclusions

In general, it is shown that seismic inversion is a versatile tool to deduce quantitative information reaching beyond conventional, qualitative interpretation results. Integrating inversion, seismic interpretation is complemented by quantitative information and becomes less ambiguous. Also, seismic results can be communicated in a more suitable way to geologists and engineers, e.g., with the estimation of unit properties of interest, removal of spreading and wavelet effects and lithological classifications. Impedance (see Ogunleye et al., in prep., 2024b) is the most significant seismic parameter suitable to differentiate and classify unconsolidated near surface sediments. A range of empiric relations and correlations was compiled from available databases to convert impedance into quantitative values of sediment properties and to analyse and characterize the subseafloor. Extensive analyses confirm the applicability of the methods revealing low uncertainty. Applicability is further proven with case studies in different geologic settings such as primarily

sandy deposits in the North Sea (Chapter 4) and a sequence of chalk bedrock overlain by glaciogenic sediments and sandy to clayey post-glacial deposits in the Baltic Sea (Chapter 6). Because of their particular importance for offshore infrastructure installations, hazard assessment and distinction of lithologies, S-Wave velocities as the primary parameter were estimated using elastic pre-stack inversion (see Chapter 5). But the significance of the results and thus uncertainties need to be critically assessed, as S-Wave velocity has a limited effect on marine seismic data acquired with towed streamer systems. Additionally, the starting model of the pre-stack inversion is a major factor for the success of the inversion.

Seismic data acquisition is the first step and a critical point in a workflow, which includes apart from data acquisition, also data processing, qualitative interpretation, and quantitative interpretation facilitated by seismic inversion. In this study, for the first time, possible constraints posed by survey design, choice of sources and receivers and operational approaches as part of the data acquisition, were investigated to better understand the impact on quantification of physical properties of unconsolidated sediments (Chapter 3). Generally, acquisition effects such as source and receiver directivity and ghosts, and wave spreading phenomena including geometric spreading and inelastic attenuation are shown in this thesis to be more pronounced than the Amplitude Versus Angle effect. Since the Amplitude Versus Angle effect is the basis for the estimation of elastic properties with marine reflection seismic data, elastic inversion requires accurate modelling of all amplitude effects during the inversion process, or alternatively prior correction. Thus, source directivity of two types of seismic sources with particularly high frequency range, a very small volume airgun and an electric sparker system, were measured and analysed. For the sparker seismic source, not only the change of directive strength with incidence angle but also the source signal shape variation has been found to be a major factor. Accordingly, a measurement of the pitch and roll of such a source during data acquisition is suggested for a correction, but not yet established in survey design. For both high accuracy velocity analysis and elastic inversion, incidence angles are required to exceed 40° , as modelling and field data in this study confirm. Acquisition equipment, however, does not yet meet these requirements in commercial work. Additionally, the spatial extent of hydrophone groups in receiver strings must be limited to mitigate receiver directivity effects. From a sensitivity analysis of possible acquisition errors, it is concluded, that lateral and vertical positioning of receivers and sources has to be sufficiently precise, e.g., within offset errors < 2 m for Ultra-High Resolution sources. Finally, ranges of physical properties of unconsolidated sediments were investigated, revealing that typically used constraints and approximations are not valid for unconsolidated sediments violating prerequisites for inversion, if not replaced by appropriate relationships.

Beyond geophysics, detailed and calibrated source strength and directivity patterns are also important parameters to both estimate and mitigate potentially negative impacts of seismic data acquisition campaigns on marine life. A detailed workflow was developed to calculate a range of different metrics for impact assessment, and is documented in Appendix “B Additional Manuscript: Is it too loud? Approximations for Underwater Noise Impact Assessments and Reporting for Near Surface Seismic Campaigns”. Potentially negative impacts are approximated by a noise impact assessment, from which a safety zone around a source and vessel can be determined, e.g., a zone with a radius <260 m for a micro-GI airgun.

As ground truthing from geologic or geotechnical samples or well logs is sparsely distributed or often not available, it was an important objective to develop a workflow for impedance inversion which is exclusively based on near surface seismic data. In Chapter 4, it is demonstrated that travel time curve inversion can also provide a good basis for the low frequency trend estimation. With fitted empiric relations, velocity is converted to impedance. Furthermore, band-limited impedance is inverted from the post-stack reflection seismic image with a custom implementation of a stable and noise insensitive algorithm. Then, the low frequency trend is merged with band-limited impedance inversion results. In the merging operation accomplished with a further development of an existing algorithm, crossover filters avoid possible artefacts and scaling accounts for the unknown source strength, receiver sensitivities and processing artefacts. Especially, also an attenuation correction before inversion was developed to remove the effect of inelastic and frequency independent attenuation. The uncertainty has been quantified by the analysis of many randomly initialized inversion runs and has been found to be in the range of 5-9%. At last, a depth conversion algorithm was implemented, which allows for the optimization with depth control points, utilizing the velocity model generated by travel time curve inversion.

To ultimately analyse elastic properties of sediments in the near surface (Chapter 5), an elastic pre-stack inversion using amplitude corrected angle stacks as an input has been developed. To create an initial elastic model, empiric relations are fitted to estimate a P-Wave velocity, a S-Wave velocity, and a density model from the compressional impedance, based on travel time curve and impedance inversion. In contrast to existing algorithms, dipping strata and angle dependent source wavelets can be accounted for and the inversion is relatively noise insensitive by the use of angle stacks. The developed inversion can be integrated into standard processing and quality control workflows, as all processing steps employed are also beneficial for the quality of seismic imaging.

To proof the applicability of the impedance inversion methodology in relevant settings, the inversion approach developed in Chapter 4 has been applied to a seismic line from the Baltic Sea (Chapter 6). As interval velocity estimates were not available, the low frequency model generation was further developed and a layer cake low frequency model has been created based on stratigraphic horizons and well data. Through a collaboration with the Norwegian Geotechnical Institute, it was also possible to compare the here developed inversion approach with one of the few established impedance inversion approaches of the industry. Although the interpretation of the results is not concluded yet, it has been found that both inversion approaches generally yield similar results, correlate well to ground truthing data and could be used for the prediction of geotechnical parameters. However, the two absolute impedance values differ in the finer details. In conclusion, the generated impedance profiles resemble a significant improvement and capture intra-unit lithologic variations and property boundaries which are not evident on seismic amplitude images.

For the application of seismic inversion for offshore wind farm investigations it is critical, to achieve high Technology Readiness Levels (TRL). Regarding the more basic levels, the uncertainty estimates conducted and the analysis of possible limitations by data acquisition (TRL 3) or the operational environment (TRL 5) are essential aspects for the critical assessment of inversion methods. Also, the new development of the pre-stack inversion being sensitive to the S-Wave velocity range of interest is a critical step (TRL3). With the further development of the impedance inversion and the case studies in appropriate geologic and operational environment, the high level of TRL 7 is reached. But additionally, the need for further tests for the completion of the methodology is indicated.

7.2 Outlook

In the scientific framework of the overarching SynCore project, this thesis provided an important knowledge transfer and a significant step forward for the industrial application of seismic inversion for offshore wind farm investigations. It remains a challenge for the project partners and the industry to further qualify, establish, and actually employ the methodology. As it was possible within the framework of a previous project to establish diffraction imaging for boulder detection (Römer-Stange et al., 2022) and as there is strong interest by the industry, it is rather likely that near surface seismic inversion will enter the survey market relatively soon. In the case of impedance inversion, there are only little and mainly operational hurdles left and one can observe the onset of the broader application for windfarm investigations (Forsberg et al., 2022). So, if high quality data was acquired and processed, if a reliable low frequency model was generated, and if a representative

wavelet was extracted, the methods developed in this thesis could be employed for industrial applications. Especially if Ultra-Ultra High Resolution seismic sources are used, the attenuation model estimation and attenuation correction is an additional critical factor to be considered beforehand. Due to the high lateral, geologic variation described in the case studies, the importance for future 3D surveys is to be emphasized at this point. As the impedance inversion workflow is computationally very effective, this inversion is readily applied to 3D data sets. The direct investigation of shear properties by means of pre-stack inversion or full-waveform inversion remains a challenge. Further validation and demonstration in relevant and operational environments are needed. Therefore, further case studies in relevant areas with an optimized acquisition set up and reliable ground truthing data need to be conducted. As our results are reproducible and aim to solve several of the open questions, some important contributions for the qualification of the method are made.

With the establishment of inversion workflows in this thesis, the approaches can now be used to benefit research. On the one hand, more technical aims such as the planning of coring campaigns, the derisking of drilling operations or improved seismic well ties can be reached. On the other hand, more fundamental research questions like the interpretation of geological processes, or the identification and quantification of fluids in the subseafloor can be facilitated. Specific examples of prospective applications include, e.g., lithological classification of delta deposits to analyse the sedimentological processes, lithological classification of contouritic deposits for palaeoceanographic studies, the identification of weak layers for geohazard studies, the identification of hard layers such as volcanic sills and dykes to further understand volcanic processes, porosity estimation to identify seals and reservoirs for Carbon Capture and Storage studies, and gas or gas hydrate quantification to support the research on the carbon cycle. To unlock the full potential of seismic inversion it is essential to further improve the data acquisition and collect seismic data with wide reflection angles. Thus, it is suggested to take the next step in acquisition technology with solid and digital streamers comprising more than 96 channels and >100 m length for shallow waters.

The expertise developed in the working group can also benefit the academic education at the University of Bremen in the future. Inversion in general and marine near surface seismic inversion in particular are increasingly important topics and students should be able to acquire knowledge about inversion to improve their career chances. Due to the thematic proximity of inversion to machine learning and the software skills necessary for inversion, there are additional teaching benefits.

A promising strategy to assess shear properties of near surface sediments based on the forward scattered wavefield and direct S-Wave recordings with data acquisition systems deployed on the seafloor has not been considered in this thesis. The findings and algorithms presented in this thesis can contribute to further research in this area.

Acknowledgements

This dissertation was funded through the project 'SynCore' (project number 03EE3020C) by the German Ministry of Economics and Energy (BMWi) on the basis of a parliamentary resolution passed by the German Bundestag. I want to thank the project partners in the project namely Dr. Jan Hebig of the Fraunhofer IWES, Dr. Norman Ettrich of the Fraunhofer ITWM, Patrick Arnold and Sigrid Wilhelm of GuD Geotechnik und Dynamik Consult GmbH and Volker Herwig of RWE Renewables GmbH for their cooperation in the SynCore Project.

At this point I would like to express my deepest gratitude to Prof. Dr. Volkhard Spieß as my PhD supervisor and first reviewer. This project would have been impossible without your guidance and support. It will always amaze and fascinate me, that your gut feeling about geophysical problems tends to be correct in more than 95% of the cases. Thank you for both encouraging and challenging me, arousing my interest in seismics and the coffee machine in your office powering 80% of the text written.

Furthermore, I am much obliged to Prof. Dr. Serge A. Shapiro, who agreed to be the second reviewer of this thesis. Working on scattering and attenuation I often read your articles and thus I am very happy, that you bring your expertise into the committee.

The members of my thesis committee also played an important role, so I want to thank Prof. Dr. Thomas Bohlen, Dr. Hanno Keil, and Dr. Stefan Wenau for their willingness to spend their time in my lengthy meetings, read lengthy emails or drafts and provide crucial advice. Hanno deserves special thanks, as little to nothing would work without him in the working group. With enough time, I guess there is nothing you could not do. I highly value the time I am allowed to spend on all kinds of ships and work with you. Stefan is to be held accountable and thus to be thanked for pretty much my entire undergraduate seismic education, taking me on my first seismic cruise as well as a great deal of time we spent together on boulder detection.

At this point I also want to thank all members of the working group Marine Technology/ Environmental Research, which I did not mention yet. Namely and in alphabetical order: Aike Albers, Anna Baltz, Dr. Noemi Fekete, Angela Friedeberg, (Great) Max Merl, (Little) Max Meyer, Dr. Mohamed Mhmod, Opeyemi Ogunleye, Dr. Tilmann Schwenk. Sincere thanks are to be expressed to Tilmann, as the many coffee breaks with him saved my sanity and as I could always

rely on his opinion. After the time in the Corona home office, it was the greatest relief to get (Great) Max as a new colleague and office neighbour. Thank you for being my occasional rubber duck and your friendship.

I am also much obliged to all colleagues at the Fraunhofer IWES. My very special thanks befit Viola Bihler, Julia Haberkern, Natasha Morales, Aisgo Oguro, Dr. Benedict Preu, Carlos Ramos, and Lennart Siemann. I greatly appreciate the work with you, enjoyed the BSH night shifts and the occasional seismic deep dive, although some of you should read their emails more often. Bene is to be thanked additionally for his trust in the early versions of boulder detection and his great engagement to build a large seismic group at the IWES. A great deal of support and joy during my PhD is due to Carlos, Aisgo and Lennart as close friends. The importance of the seismic daydreaming with Carlos can also not be stressed enough, as it kept my fascination about seismics alive and is a great source of inspiration.

Seismic data acquisition, sound pressure and directivity measurements of the seismic sources were conducted during the expeditions AL546, AL566, AL581 and He569, so I duly thank the captains and the crews of R/V ALKOR and R/V HEINCKE for their engagement in the successful data acquisition campaign. He569 was part of the SEBAMO project funded by the German Federal Maritime and Hydrographic Agency.

I am also much obliged to Applied Acoustics (Michael Calvert, Neil MacDonald) and the IWES (Julia Haberkern, Rouven Brune, Tom Schaffarzyk) for their contribution to the sparker test data acquisition campaign in March 2022.

Several student assistants, most notably Aleksandra Zubkova, were involved in the processing of the Cone Penetration Test data at the Fraunhofer IWES and we duly thank those student assistants for their work.

On behalf of Opeyemi Ogunleye, I want to thank the GLOMAR graduate school for his funding of the research stay at the Norwegian Geotechnical Institute and Dr. Jean-Rémi Dujardin for his discussion input for the post-stack impedance inversions conducted for the Arkona Basin.

As I would not have started to work as a geophysicist, if this career did not involve going on cruises, I also want to thank the captains and the crews of R/V Heincke, R/V Alkor, VWFS Atair, and VWFS Wega for the successful conduction of the seismic data acquisition campaigns.

Before the start of my PhD and my time at the Fraunhofer IWES, I had the chance to be lectured by Prof. Dr. Gerhard Bohrmann and to be on several cruises with him. Those cruises, your comprehensive knowledge and your leadership are amongst the best experiences of my adult life. Thank you.

During my time as a PhD student, I had the chance to join the GLOMAR graduate school, so I duly thank Prof. Dr. Dierk Hebbeln, Dr Tina Klose and Sina Teumer for their work and support. Since Dierk was the first one to give me a student job and most importantly bring me on a research vessel, I want to use this chance to express my gratitude for his trust and support. Also, I very much appreciated the Data Train lectures and workshops, thank you Tanja Hörner and the whole Data Train team.

Last, but not least I want to thank all my friends and family for their whole-hearted support, interest, and appreciation of my work. Without your support, not a single page would have been written. All of you had to endure the cycles of agony and joy while programming, so please kindly excuse my mood swings.

References

- AAE. (2022). *Dura-Spark UHD Seismic Sound Source* (Product Specifications No. Issue 1) (p. 2). Great Yarmouth, United Kingdom: Applied Acoustic Engineering Ltd. Retrieved from <https://www.aatechnologiesgroup.com/applied-acoustics/products/sub-bottom-profiling/sound-source-sparkers/>
- Ainslie, M. A., & McColm, J. G. (1998). A simplified formula for viscous and chemical absorption in sea water. *The Journal of the Acoustical Society of America*, *103*(3), 1671–1672. <https://doi.org/10.1121/1.421258>
- Aki, K., & Richards, P. G. (2002). *Quantitative seismology*. (J. Ellis, Ed.) (2nd ed.). Sausalito, Calif.: University Science Books. Retrieved from http://katalog.suub.uni-bremen.de/DB=1/LNG=DU/CMD?ACT=SRCHA&IKT=8000&TRM=40206166*
- Aki, K., Christoffersson, A., & Husebye, E. S. (1977). Determination of the three-dimensional seismic structure of the lithosphere. *Journal of Geophysical Research (1896-1977)*, *82*(2), 277–296. <https://doi.org/10.1029/JB082i002p00277>
- Alcalde, J., & Bond, C. E. (2022). Chapter 5 - Subjective uncertainty and biases: The impact on seismic data interpretation. In R. Bell, D. Iacopini, & M. Vardy (Eds.), *Interpreting Subsurface Seismic Data* (pp. 103–123). Elsevier. <https://doi.org/10.1016/B978-0-12-818562-9.00002-9>
- Aleardi, M., & Tognarelli, A. (2016). The limits of narrow and wide-angle AVA inversions for high V_p/V_s ratios: An application to elastic seabed characterization. *Journal of Applied Geophysics*, *131*, 54–68. <https://doi.org/10.1016/j.jappgeo.2016.05.009>
- Amaechi, C. V., Reda, A., Butler, H. O., Ja'e, I. A., & An, C. (2022). Review on Fixed and Floating Offshore Structures. Part I: Types of Platforms with Some Applications. *Journal of Marine Science and Engineering*, *10*(8), 1074. <https://doi.org/10.3390/jmse10081074>
- Andrén, T., Björck, S., Andrén, E., Conley, D., Zillén, L., & Anjar, J. (2011). The Development of the Baltic Sea Basin During the Last 130 ka. In J. Harff, S. Björck, & P. Hoth (Eds.), *The Baltic Sea Basin* (pp. 75–97). Berlin, Heidelberg: Springer. https://doi.org/10.1007/978-3-642-17220-5_4
- Andresen, K. J., Hepp, D. A., Keil, H., & Spieß, V. (2022). Seismic morphologies of submerged late glacial to Early Holocene landscapes at the eastern Dogger Bank, central North Sea Basin – implications for geo-archaeological potential. *Geological Society, London, Special Publications*, *525*(1), SP525-2021–155. <https://doi.org/10.1144/SP525-2021-155>
- Anell, I., Thybo, H., & Rasmussen, E. (2012). A synthesis of Cenozoic sedimentation in the North Sea. *Basin Research*, *24*(2), 154–179. <https://doi.org/10.1111/j.1365-2117.2011.00517.x>
- Arfai, J., Franke, D., Lutz, R., Reinhardt, L., Kley, J., & Gaedicke, C. (2018). Rapid Quaternary subsidence in the northwestern German North Sea. *Scientific Reports*, *8*(1), 11524. <https://doi.org/10.1038/s41598-018-29638-6>

- Armstrong, K. (2015). Chapter 13 - Emerging Industrial Applications. In P. Styring, E. A. Quadrelli, & K. Armstrong (Eds.), *Carbon Dioxide Utilisation* (pp. 237–251). Amsterdam: Elsevier. <https://doi.org/10.1016/B978-0-444-62746-9.00013-X>
- Arshad, M., & O’Kelly, B. C. (2016). Analysis and Design of Monopile Foundations for Offshore Wind-Turbine Structures. *Marine Georesources & Geotechnology*, 34(6), 503–525. <https://doi.org/10.1080/1064119X.2015.1033070>
- Aster, R. C., Borchers, B., & Thurber, C. H. (2013a). Chapter 10 - Nonlinear Inverse Problems. In R. C. Aster, B. Borchers, & C. H. Thurber (Eds.), *Parameter Estimation and Inverse Problems (Second Edition)* (pp. 239–252). Boston: Academic Press. <https://doi.org/10.1016/B978-0-12-385048-5.00010-0>
- Aster, R. C., Borchers, B., & Thurber, C. H. (2013b). Chapter 11 - Bayesian Methods. In R. C. Aster, B. Borchers, & C. H. Thurber (Eds.), *Parameter Estimation and Inverse Problems (Second Edition)* (pp. 253–280). Boston: Academic Press. <https://doi.org/10.1016/B978-0-12-385048-5.00011-2>
- Atwood, T. B., Witt, A., Mayorga, J., Hammill, E., & Sala, E. (2020). Global Patterns in Marine Sediment Carbon Stocks. *Frontiers in Marine Science*, 7. <https://doi.org/10.3389/fmars.2020.00165>
- Avseth, P., Mukerji, T., & Mavko, G. (2005). *Quantitative Seismic Interpretation: Applying Rock Physics Tools to Reduce Interpretation Risk*. Cambridge: Cambridge University Press. <https://doi.org/10.1017/CBO9780511600074>
- AWI. (2017). Research Vessel HEINCKE Operated by the Alfred-Wegener-Institute. *Journal of Large-Scale Research Facilities JLSRF*, 3, A120–A120. <https://doi.org/10.17815/jlsrf-3-164>
- Aytun, K. (1999). The footsteps of the receiver ghost in the f-k domain. *GEOPHYSICS*, 64(5), 1618–1626. <https://doi.org/10.1190/1.1444666>
- Bacon, M., Simm, R., & Redshaw, T. (Eds.). (2003). 06 - Inversion. In *3-D Seismic Interpretation* (pp. 155–171). Cambridge: Cambridge University Press. <https://doi.org/10.1017/CBO9780511802416.007>
- Badiey, M., Cheng, A. H.-D., & Mu, Y. (1998). From geology to geoacoustics—Evaluation of Biot–Stoll sound speed and attenuation for shallow water acoustics. *The Journal of the Acoustical Society of America*, 103(1), 309–320. <https://doi.org/10.1121/1.421136>
- Barros, T., Ferrari, R., Krummenauer, R., & Lopes, R. (2015). Differential evolution-based optimization procedure for automatic estimation of the common-reflection surface traveltime parameters. *GEOPHYSICS*, 80(6), WD189–WD200. <https://doi.org/10.1190/geo2015-0032.1>
- Barton, P., & Wood, R. (1984). Tectonic evolution of the North Sea basin: crustal stretching and subsidence. *Geophysical Journal International*, 79(3), 987–1022. <https://doi.org/10.1111/j.1365-246X.1984.tb02880.x>
- Batchelor, C. L., Margold, M., Krapp, M., Murton, D. K., Dalton, A. S., Gibbard, P. L., et al. (2019). The configuration of Northern Hemisphere ice sheets through the Quaternary. *Nature Communications*, 10(1), 3713. <https://doi.org/10.1038/s41467-019-11601-2>

- Bauer, J. E., Cai, W.-J., Raymond, P. A., Bianchi, T. S., Hopkinson, C. S., & Regnier, P. A. G. (2013). The changing carbon cycle of the coastal ocean. *Nature*, *504*(7478), 61–70. <https://doi.org/10.1038/nature12857>
- Bednar, J. B. (2005). A brief history of seismic migration. *GEOPHYSICS*, *70*(3), 3MJ-20MJ. <https://doi.org/10.1190/1.1926579>
- Bendixen, C., Lamb, R. M., Huuse, M., Boldreel, L. O., Jensen, J. B., & Clausen, O. R. (2018). Evidence for a grounded ice sheet in the central North Sea during the early Middle Pleistocene Donian Glaciation. *Journal of the Geological Society*, *175*(2), 291–307. <https://doi.org/10.1144/jgs2017-073>
- Bendixen, M., Iversen, L. L., Best, J., Franks, D. M., Hackney, C. R., Latrubesse, E. M., & Tusting, L. S. (2021). Sand, gravel, and UN Sustainable Development Goals: Conflicts, synergies, and pathways forward. *One Earth*, *4*(8), 1095–1111. <https://doi.org/10.1016/j.oneear.2021.07.008>
- Ben-Menahem, A. (1995). A concise history of mainstream seismology: Origins, legacy, and perspectives. *Bulletin of the Seismological Society of America*, *85*(4), 1202–1225. <https://doi.org/10.1785/BSSA0850041202>
- Bennett, M. R. (2001). The morphology, structural evolution and significance of push moraines. *Earth-Science Reviews*, *53*(3), 197–236. [https://doi.org/10.1016/S0012-8252\(00\)00039-8](https://doi.org/10.1016/S0012-8252(00)00039-8)
- Beylkin, G. (1985). Imaging of discontinuities in the inverse scattering problem by inversion of a causal generalized Radon transform. *Journal of Mathematical Physics*, *26*(1), 99–108. <https://doi.org/10.1063/1.526755>
- Bickel, S. H., & Natarajan, R. R. (1985). Plane-wave Q deconvolution. *GEOPHYSICS*, *50*(9), 1426–1439. <https://doi.org/10.1190/1.1442011>
- Biot, M. A. (1956). Theory of Propagation of Elastic Waves in a Fluid-Saturated Porous Solid. I. Low-Frequency Range. *The Journal of the Acoustical Society of America*, *28*(2), 168–178. <https://doi.org/10.1121/1.1908239>
- Bishop, T. N., Bube, K. P., Cutler, R. T., Langan, R. T., Love, P. L., Resnick, J. R., et al. (1985). Tomographic determination of velocity and depth in laterally varying media. *GEOPHYSICS*, *50*(6), 903–923. <https://doi.org/10.1190/1.1441970>
- Björck, S. (1995). A review of the history of the Baltic Sea, 13.0-8.0 ka BP. *Quaternary International*, *27*, 19–40. [https://doi.org/10.1016/1040-6182\(94\)00057-C](https://doi.org/10.1016/1040-6182(94)00057-C)
- BMWi. Forschung für eine umweltschonende, zuverlässige und bezahlbare Energieversorgung, BAnz AT 30.12.2014 B1 § (2014). Retrieved from https://www.bmwi.de/Redaktion/DE/Downloads/B/bekanntmachung-forschungsfoerderung-im-6-energieforschungsprogramm.pdf?__blob=publicationFile&cv=3
- BMWK. (2022, November 1). Marine conservation: Germany will not sponsor deep-sea mining until further notice. *Joint Press Release Federal Ministry for Economic Affairs and Climate Action*. Retrieved from

- <https://www.bmwk.de/Redaktion/EN/Pressemitteilungen/2022/11/20221101-marine-conservation-germany-will-not-sponsor-deep-sea-mining-until-further-notice.html>
- Boehm, G., Carcione, J. M., & Vesnaver, A. (1996). Reflection tomography versus stacking velocity analysis. *Journal of Applied Geophysics*, *35*(1), 1–13. [https://doi.org/10.1016/0926-9851\(95\)00025-9](https://doi.org/10.1016/0926-9851(95)00025-9)
- BOEM. (2014). *Marine Mammal Hearing and Sensitivity to Acoustic Impacts* (Meeting Submission No. Appendix H) (p. 30). London, UK: Bureau of Ocean Energy Management. Retrieved from <https://www.cbd.int/doc/meetings/mar/mcbem-2014-01/other/mcbem-2014-01-submission-boem-02-en.pdf>
- Bohlen, T. (2002). Parallel 3-D viscoelastic finite difference seismic modelling. *Computers & Geosciences*, *28*(8), 887–899. [https://doi.org/10.1016/S0098-3004\(02\)00006-7](https://doi.org/10.1016/S0098-3004(02)00006-7)
- Bohlen, T., Kugler, S., Klein, G., & Theilen, F. (2004). 1.5D inversion of lateral variation of Scholte-wave dispersion. *GEOPHYSICS*, *69*(2), 330–344. <https://doi.org/10.1190/1.1707052>
- Boiero, D., Wiarda, E., & Vermeer, P. (2013). Surface- and guided-wave inversion for near-surface modeling in land and shallow marine seismic data. *The Leading Edge*, *32*(6), 638–646. <https://doi.org/10.1190/tle32060638.1>
- Bonne, W. M. I. (2010). European Marine Sand and Gravel Resources: Evaluation and Environmental Impacts of Extraction - an Introduction. *Journal of Coastal Research*, i–vi.
- Borland, H. P., Gilby, B. L., Henderson, C. J., Leon, J. X., Schlacher, T. A., Connolly, R. M., et al. (2021). The influence of seafloor terrain on fish and fisheries: A global synthesis. *Fish and Fisheries*, *22*(4), 707–734. <https://doi.org/10.1111/faf.12546>
- Boudreau, B. P. (2000). The mathematics of early diagenesis: From worms to waves. *Reviews of Geophysics*, *38*(3), 389–416. <https://doi.org/10.1029/2000RG000081>
- Breitzke, M. (1997). *Elastische Wellenausbreitung in marinen Sedimenten - Neue Entwicklungen der Ultraschall Sedimentphysik und Sedimentechographie* (Vol. 104). Bremen, Germany: Fachbereich 5, Universität Bremen. Retrieved from <https://media.suub.uni-bremen.de/handle/elib/3777?locale=de>
- Breitzke, M. (2000). Acoustic and elastic characterization of marine sediments by analysis, modeling, and inversion of ultrasonic P wave transmission seismograms. *Journal of Geophysical Research: Solid Earth*, *105*(B9), 21411–21430. <https://doi.org/10.1029/2000JB900153>
- Breitzke, M. (2006). Physical Properties of Marine Sediments. In H. D. Schulz & M. Zabel (Eds.), *Marine Geochemistry* (pp. 27–71). Berlin, Heidelberg: Springer. https://doi.org/10.1007/3-540-32144-6_2
- Brossier, R., Operto, S., & Virieux, J. (2009). Seismic imaging of complex onshore structures by 2D elastic frequency-domain full-waveform inversion. *GEOPHYSICS*, *74*(6), WCC105–WCC118. <https://doi.org/10.1190/1.3215771>

- Brotons, V., Tomás, R., Ivorra, S., Grediaga, A., Martínez-Martínez, J., Benavente, D., & Gómez-Heras, M. (2016). Improved correlation between the static and dynamic elastic modulus of different types of rocks. *Materials and Structures*, 49(8), 3021–3037. <https://doi.org/10.1617/s11527-015-0702-7>
- BSH. (2021, July 26). PINTA [Data hub]. Retrieved July 26, 2021, from <https://pinta.bsh.de/>
- Buiting, J. J. M., & Bacon, M. (1999). Seismic inversion as a vehicle for integration of geophysical, geological and petrophysical information for reservoir characterization: some North Sea examples. *Geological Society, London, Petroleum Geology Conference Series*, 5(1), 1271–1280. <https://doi.org/10.1144/0051271>
- Buland, A., & Omre, H. (2003). Bayesian linearized AVO inversion. *GEOPHYSICS*, 68(1), 185–198. <https://doi.org/10.1190/1.1543206>
- Bull, J. M., Quinn, R., & Dix, J. K. (1998). Reflection Coefficient Calculation from Marine High Resolution Seismic Reflection (Chirp) Data and Application to an Archaeological Case Study. *Marine Geophysical Researches*, 20(1), 1–11. <https://doi.org/10.1023/A:1004373106696>
- Burd, H. J., Byrne, B. W., McAdam, R., Houlsby, G. T., Martin, C. M., Beuckelaers, W., et al. (2017). Foundation Design of Offshore Wind Structures. In *TC209 Workshop on Foundation Design of Offshore Wind Structures, 19th International Conference on Soil Mechanics and Geotechnical Engineering*. Retrieved from <http://spiral.imperial.ac.uk/handle/10044/1/55424>
- Butler, D. K. (2005). 1. What Is Near-Surface Geophysics? In *Near-Surface Geophysics* (Vols. 1–0, pp. 1–6). Society of Exploration Geophysicists. <https://doi.org/10.1190/1.9781560801719.ch1>
- BVG, A. (2019). *Guide to an offshore wind farm* (p. 128). Swindon, UK: The Crown Estate, CATAPULT Offshore Renewable Energy. Retrieved from <https://guidetoanoffshorewindfarm.com>
- Cameron, M., Fomel, S., & Sethian, J. (2008). Time-to-depth conversion and seismic velocity estimation using time-migration velocity. *GEOPHYSICS*, 73(5), VE205–VE210. <https://doi.org/10.1190/1.2967501>
- Canals, M., Lastras, G., Urgeles, R., Casamor, J. L., Mienert, J., Cattaneo, A., et al. (2004). Slope failure dynamics and impacts from seafloor and shallow sub-seafloor geophysical data: case studies from the COSTA project. *Marine Geology*, 213(1), 9–72. <https://doi.org/10.1016/j.margeo.2004.10.001>
- Carbon Trust. (2020). *Guidance for geophysical surveying for UXO and boulders supporting cable installations (Offshore Wind Accelerator)* (p. 103). London, UK. Retrieved from <https://www.carbontrust.com/de/node/1233>
- Carcione, J. M., & Picotti, S. (2006). P-wave seismic attenuation by slow-wave diffusion: Effects of inhomogeneous rock properties. *GEOPHYSICS*, 71(3), O1–O8. <https://doi.org/10.1190/1.2194512>
- Cevatoglu, M., Bull, J. M., Vardy, M. E., Gernon, T. M., Wright, I. C., & Long, D. (2015). Gas migration pathways, controlling mechanisms and changes in sediment acoustic properties

- observed in a controlled sub-seabed CO₂ release experiment. *International Journal of Greenhouse Gas Control*, 38, 26–43. <https://doi.org/10.1016/j.ijggc.2015.03.005>
- Charles, J. A., Gourvenec, S. M., & Vardy, M. E. (2022). Coupling site wide CPT profiles and genetic algorithms for whole-site offshore windfarm layout optimization. In Gottardi & Tonni (Eds.), *Cone Penetration Testing 2022* (pp. 870–875). Bologna, Italy: CRC Press. <https://doi.org/10.1201/9781003308829-129>
- Chen, R., Tran, K. T., & Wang, Y. (2021). 2D time-domain full-waveform inversion of SH- and Love-waves for geotechnical site characterization. *Near Surface Geophysics*, 19(3), 283–295. <https://doi.org/10.1002/nsg.12137>
- Chopra, S., & Castagna, J. P. (2014). *AVO*. (M. N. Nabighian, Ed.). Tulsa, Okla: Society of Exploration Geophysics. Retrieved from <https://doi.org/10.1190/1.9781560803201>
- Chopra, S., & Marfurt, K. J. (2007). *Seismic Attributes for Prospect Identification and Reservoir Characterization*. Society of Exploration Geophysicists and European Association of Geoscientists and Engineers. <https://doi.org/10.1190/1.9781560801900>
- Chotiros, N. P. (1994). Reflection and reverberation in normal incidence echo-sounding. *The Journal of the Acoustical Society of America*, 96(5), 2921–2929. <https://doi.org/10.1121/1.411301>
- Claerbout, J. F. (1986). *Imaging the Earth's Interior* (Stanford Exploration Project No. 40). Stanford, California (USA): Stanford University. Retrieved from <https://sepwww.stanford.edu/sep/prof/iei2/>
- Claerbout, J. F. (2010). *Basic Earth Imaging* (11th ed.). Stanford University, California (USA): SEPM. Retrieved from <http://sepwww.stanford.edu/sep/prof/>
- Clare, M. A., Vardy, M. E., Cartigny, M. J. B., Talling, P. J., Himsforth, M. D., Dix, J. K., et al. (2017). Direct monitoring of active geohazards: emerging geophysical tools for deep-water assessments. *Near Surface Geophysics*, 15(4), 427–444. <https://doi.org/10.3997/1873-0604.2017033>
- Clementi, M., Boiero, D., Leone, C., & Masnaghetti, L. (2022). Towards Holistic Characterization of the Near Seabed for Renewable Energy Installations in Shallow Marine Environments (Vol. 2022, pp. 1–5). Presented at the EAGE GET 2022, European Association of Geoscientists & Engineers. <https://doi.org/10.3997/2214-4609.202221112>
- Cofaigh, C. Ó. (1996). Tunnel valley genesis. *Progress in Physical Geography: Earth and Environment*, 20(1), 1–19. <https://doi.org/10.1177/030913339602000101>
- Connolly, P. (1999). Elastic impedance. *The Leading Edge*, 18(4), 438–452. <https://doi.org/10.1190/1.1438307>
- Cook, M., Barwise, A., Hobbs, R., Hodgson, T., Leo, J., Jenner, C., et al. (2014). *Guidance Notes for the Planning and Execution of Geophysical and Geotechnical Ground Investigations for Offshore Renewable Energy Developments* (Guidance Note) (p. 49). London, UK: The Society of Underwater Technology. Retrieved from https://www.sut.org/wp-content/uploads/2014/07/OSIG-Guidance-Notes-2014_web.pdf

- Cooke, D., & Cant, J. (2010). Model-based Seismic Inversion: Comparing deterministic and probabilistic approaches. *CSEG Recorder*, 4(35), 12.
- Cooke, D. A., & Schneider, W. A. (1983). Generalized linear inversion of reflection seismic data. *GEOPHYSICS*, 48(6), 665–676. <https://doi.org/10.1190/1.1441497>
- Coughlan, M., Fleischer, M., Wheeler, A. J., Hepp, D. A., Hebbeln, D., & Mörz, T. (2018). A revised stratigraphical framework for the Quaternary deposits of the German North Sea sector: a geological-geotechnical approach. *Boreas*, 47(1), 80–105. <https://doi.org/10.1111/bor.12253>
- Cruse, E., Pica, A., Noble, M., McDonald, J., & Tarantola, A. (1990). Robust elastic nonlinear waveform inversion: Application to real data. *GEOPHYSICS*, 55(5), 527–538. <https://doi.org/10.1190/1.1442864>
- Crocker, S. E., & Fratantonio, F. D. (2016). *Characteristics of Sounds Emitted During High-Resolution Marine Geophysical Surveys* (Technical Report No. 12,203 (BOEM 2016-044)) (p. 266). Newport, Rhode Island: Naval Undersea Warfare Center Division.
- Dan, G., Sultan, N., & Savoye, B. (2007). The 1979 Nice harbour catastrophe revisited: Trigger mechanism inferred from geotechnical measurements and numerical modelling. *Marine Geology*, 245(1), 40–64. <https://doi.org/10.1016/j.margeo.2007.06.011>
- Danbom, S. H. (2005). 2. Special Challenges Associated with the Near Surface. In *Near-Surface Geophysics* (Vols. 1–0, pp. 7–30). Society of Exploration Geophysicists. <https://doi.org/10.1190/1.9781560801719.ch2>
- DFG. Statutes of the Deutsche Forschungsgemeinschaft, Register of Associations § VR 2030 (2023). Retrieved from https://www.dfg.de/download/pdf/dfg_im_profil/satzung/dfg_satzung_en.pdf
- Diesing, M. (2020). Deep-sea sediments of the global ocean. *Earth System Science Data*, 12(4), 3367–3381. <https://doi.org/10.5194/essd-12-3367-2020>
- Dondurur, D. (2018). *Acquisition and Processing of Marine Seismic Data*. Elsevier. <https://doi.org/10.1016/C2016-0-01591-7>
- Dooling, R. J., & Therrien, S. C. (2012). Hearing in Birds: What Changes From Air to Water. In A. N. Popper & A. Hawkins (Eds.), *The Effects of Noise on Aquatic Life* (pp. 77–82). New York, NY: Springer. https://doi.org/10.1007/978-1-4419-7311-5_17
- Downton, J. E. (2005). *Seismic parameter estimation from AVO inversion* (Doctor of Science). University of Calgary, Calgary, Alberta (Canada). Retrieved from CREWES.
- Downton, J. E., & Lines, L. R. (2004). Three term AVO waveform inversion. In *SEG International Exposition and Annual Meeting* (p. SEG-2004). SEG. Retrieved from <https://onepetro.org/SEGAM/proceedings-abstract/SEG04/All-SEG04/92033>
- Downton, J. E., Pickford, S., & Lines, L. R. (2001). Constrained three parameter AVO inversion and uncertainty analysis. In *SEG International Exposition and Annual Meeting* (p. SEG-2001). SEG. Retrieved from <https://onepetro.org/SEGAM/proceedings-abstract/SEG01/All-SEG01/89192>

- Dragoset, B. (2005). A historical reflection on reflections. *The Leading Edge*, 24(s1), s46–s70. <https://doi.org/10.1190/1.2112392>
- Duarte, H., Wardell, N., & Monrigal, O. (2017). Advanced processing for UHR3D shallow marine seismic surveys. *Near Surface Geophysics*, 15(4), 347–358. <https://doi.org/10.3997/1873-0604.2017022>
- Duncan, A. J., & Parsons, M. J. G. (2011). How Wrong Can You Be? Can a Simple Spreading Formula Be Used to Predict Worst-Case Underwater Sound Levels?, 8.
- Duveneck, E. (2004). *Tomographic determination of seismic velocity models with kinematic wavefield attributes* (Dr. rer. nat.). Universität Karlsruhe, Karlsruhe. Retrieved from <https://core.ac.uk/download/pdf/197565385.pdf>
- Dvorkin, J., Prasad, M., Sakai, A., & Lavoie, D. (1999). Elasticity of marine sediments: Rock physics modeling. *Geophysical Research Letters*, 26(12), 1781–1784. <https://doi.org/10.1029/1999GL900332>
- Dvorkin, J., Gutierrez, M. A., & Grana, D. (2014). *Seismic Reflections of Rock Properties*. Cambridge: Cambridge University Press. <https://doi.org/10.1017/CBO9780511843655>
- Ehlers, J. (2022). *The Ice Age*. Springer Berlin Heidelberg. Retrieved from <https://doi.org/10.1007/978-3-662-64590-1>
- Ehlers, J., Grube, A., Stephan, H.-J., & Wansa, S. (2011). Chapter 13 - Pleistocene Glaciations of North Germany—New Results. In J. Ehlers, P. L. Gibbard, & P. D. Hughes (Eds.), *Developments in Quaternary Sciences* (Vol. 15, pp. 149–162). Elsevier. <https://doi.org/10.1016/B978-0-444-53447-7.00013-1>
- Elmer, K.-H., Betke, K., & Neumann, T. (2007). *Standardverfahren zur Ermittlung und Bewertung der Belastung der Meeresumwelt durch Schallimmission von Offshore-Windenergieanlagen : Abschlussbericht zum BMU-Forschungsvorhaben 0329947 ; [Verbundprojekt]*. Hannover.
- Espin, I., Salaun, N., & Jiang, H. (2022). From Conventional Acquisition to UHR Image Using FWI in the Barents Sea (Vol. 2022, pp. 1–5). Presented at the EAGE GET 2022, European Association of Geoscientists & Engineers. <https://doi.org/10.3997/2214-4609.202221035>
- European Commission. Commission Decision (EU) 2017/848 of 17 May 2017 laying down criteria and methodological standards on good environmental status of marine waters and specifications and standardised methods for monitoring and assessment, and repealing Decision 2010/477/EU (Text with EEA relevance.), 125 OJ L § (2017). Retrieved from <http://data.europa.eu/eli/dec/2017/848/oj/eng>
- Fatti, J. L., Smith, G. C., Vail, P. J., Strauss, P. J., & Levitt, P. R. (1994). Detection of gas in sandstone reservoirs using AVO analysis: A 3-D seismic case history using the Geostack technique. *GEOPHYSICS*, 59(9), 1362–1376. <https://doi.org/10.1190/1.1443695>
- Fawad, M., Hansen, J. A., & Mondol, N. H. (2020). Seismic-fluid detection-a review. *Earth-Science Reviews*, 210, 103347. <https://doi.org/10.1016/j.earscirev.2020.103347>

- Ferguson, R. J., & Margrave, G. F. (1996). *A simple algorithm for band-limited impedance inversion* (CREWES Research Report No. 8) (p. 10).
- Fichtner, A. (2011). *Full Seismic Waveform Modelling and Inversion*. Berlin, Heidelberg: Springer Berlin Heidelberg. <https://doi.org/10.1007/978-3-642-15807-0>
- Filippova, K., Kozhenkov, A., & Alabushin, A. (2011). Seismic inversion techniques: choice and benefits. *First Break*, 29(5). Retrieved from <https://www.earthdoc.org/content/journals/0.3997/1365-2397.29.5.49948>
- Fischer, J., Jost, O., Richter, M., Wiemann, J., & Fichtner Water & Transportation GmbH (Hamburg). (2019). *Presentation and Comparison of Site Investigation Methods for Offshore Wind Energy in the European North Seas Countries in the Context of the EU North Seas Energy Cooperation* (Final Report No. FB000323/ENG) (p. 99). Dessau-Roßlau, Germany: German Environment Agency. Retrieved from ISSN 1862-4804
- Fitzsimons, S., & Howarth, J. (2018). Chapter 9 - Glaciolacustrine Processes. In John Menzies & J. J. M. van der Meer (Eds.), *Past Glacial Environments (Second Edition)* (pp. 309–334). Elsevier. <https://doi.org/10.1016/B978-0-08-100524-8.00009-9>
- Fjær, E. (2019). Relations between static and dynamic moduli of sedimentary rocks. *Geophysical Prospecting*, 67(1), 128–139. <https://doi.org/10.1111/1365-2478.12711>
- Forsberg, C. F., Sauvin, G., Klinkvort, R. T., Vardy, M. E., Vanneste, M., & Kort, A. (2022). *Integrated Ground Model Report* (Ministerie van Economische Zaken en Klimaat, Rijksdienst voor Ondernemend Nederland No. 20190798- 04- R) (p. 964). Oslo, Norway: Norwegian Geotechnical Institute.
- Friedlingstein, P., O’Sullivan, M., Jones, M. W., Andrew, R. M., Gregor, L., Hauck, J., et al. (2022). Global Carbon Budget 2022. *Earth System Science Data*, 14(11), 4811–4900. <https://doi.org/10.5194/essd-14-4811-2022>
- Fu, F. (2018). Chapter Eight - Design of Offshore Structures. In F. Fu (Ed.), *Design and Analysis of Tall and Complex Structures* (pp. 251–293). Butterworth-Heinemann. <https://doi.org/10.1016/B978-0-08-101018-1.00008-3>
- Fuchs, K., & Müller, G. (1971). Computation of Synthetic Seismograms with the Reflectivity Method and Comparison with Observations. *Geophysical Journal International*, 23(4), 417–433. <https://doi.org/10.1111/j.1365-246X.1971.tb01834.x>
- FUGRO. (2020). *Synthetic CPT Profiles Hollandse Kust (west) Wind Farm Zone Dutch Sector, North Sea* (Geotechnical Report No. WOZ2190152) (p. 104). Utrecht, Netherlands: Rijksdienst voor Ondernemend Nederland. Retrieved from <https://offshorewind.rvo.nl/generalw>
- Gardner, G. H. F., Gardner, L. W., & Gregory, A. R. (1974). Formation velocity and density—the diagnostic basics for stratigraphic traps. *GEOPHYSICS*, 39(6), 770–780. <https://doi.org/10.1190/1.1440465>
- Geldart, L. P., & Sheriff, R. E. (2004). 5. Seismic Velocity. In *Problems in Exploration Seismology and their Solutions* (pp. 141–180). Society of Exploration Geophysicists. <https://doi.org/10.1190/1.9781560801733.ch5>

- Graham, A. G. C., Stoker, M. S., Lonergan, L., Bradwell, T., & Stewart, M. (2011). Chapter 21 - The Pleistocene Glaciations of the North Sea Basin. In P. L. G. and P. D. H. Jürgen Ehlers (Ed.), *Developments in Quaternary Sciences* (Vol. 15, pp. 261–278). Elsevier. Retrieved from <http://www.sciencedirect.com/science/article/pii/B9780444534477000210>
- Green, D. M., DeFerrari, H., McFadden, D., Pearse, J. S., Popper, A. N., Richardson, W. J., et al. (1994). *Low-Frequency Sound and Marine Mammals: Current Knowledge and Research Needs*. Washington, D.C.: National Research Council (US) Committee on Low-Frequency Sound and Marine Mammals. Retrieved from <https://www.ncbi.nlm.nih.gov/books/NBK236693/>
- Guigné, J. Y., & Blondel, P. (2017). *Acoustic Investigation of Complex Seabeds*. Springer. Retrieved from <http://www.springer.com/us/book/9783319025780>
- Guo, Y.-G., Li, F.-H., Liu, J.-J., & Li, Z.-L. (2006). Time-Domain Geoacoustic Inversion Based on Normal Incidence Reflection from Layered Sediment. *Chinese Physics Letters*, 23(9), 2483–2486. <https://doi.org/10.1088/0256-307X/23/9/037>
- Gutowski, M., Breitzke, M., & Spieß, V. (2002). Fast static correction methods for high-frequency multichannel marine seismic reflection data: A high-resolution seismic study of channel-levee systems on the Bengal Fan. *Marine Geophysical Researches*, 23(1), 57–75. <https://doi.org/10.1023/A:1021240415963>
- Gutowski, M., Bull, J. M., Dix, J. K., Henstock, T. J., Hogarth, P., Hiller, T., et al. (2008). 3D high-resolution acoustic imaging of the sub-seabed. *Applied Acoustics*, 69(3), 262–271. <https://doi.org/10.1016/j.apacoust.2006.08.010>
- Hamilton, E. L. (1970). Sound velocity and related properties of marine sediments, North Pacific. *Journal of Geophysical Research (1896-1977)*, 75(23), 4423–4446. <https://doi.org/10.1029/JB075i023p04423>
- Hamilton, E. L. (1972). COMPRESSIONAL-WAVE ATTENUATION IN MARINE SEDIMENTS. *GEOPHYSICS*, 37(4), 620–646. <https://doi.org/10.1190/1.1440287>
- Hampson, D. P., Russell, B. H., & Bankhead, B. (2005). Simultaneous inversion of pre-stack seismic data. In *SEG Technical Program Expanded Abstracts 2005* (pp. 1633–1637). Society of Exploration Geophysicists. <https://doi.org/10.1190/1.2148008>
- Harris, P. T., Macmillan-Lawler, M., Rupp, J., & Baker, E. K. (2014). Geomorphology of the oceans. *Marine Geology*, 352, 4–24. <https://doi.org/10.1016/j.margeo.2014.01.011>
- Heffernan, O. (2023, September 1). Deep-Sea Mining Could Begin Soon, Regulated or Not. *Scientific American*. <https://doi.org/10.1038/scientificamerican0923-34>
- Hein, J. R., Koschinsky, A., & Kuhn, T. (2020). Deep-ocean polymetallic nodules as a resource for critical materials. *Nature Reviews Earth & Environment*, 1(3), 158–169. <https://doi.org/10.1038/s43017-020-0027-0>
- Henson, H., & Sexton, J. L. (1991). Premine study of shallow coal seams using high-resolution seismic reflection methods. *GEOPHYSICS*, 56(9), 1494–1503. <https://doi.org/10.1190/1.1443171>

- Hertweck, T., Jäger, C., Mann, J., Duveneck, E., & Heilmann, Z. (2004). A seismic reflection imaging workflow based on the Common Reflection Surface (CRS) stack: Theoretical background and case study. In *SEG Technical Program Expanded Abstracts 2004* (Vols. 1–0, pp. 2032–2035). Society of Exploration Geophysicists. <https://doi.org/10.1190/1.1845195>
- Hesse, R., & Schacht, U. (2011). Chapter 9 - Early Diagenesis of Deep-Sea Sediments. In H. HüNeke & T. Mulder (Eds.), *Developments in Sedimentology* (Vol. 63, pp. 557–713). Elsevier. <https://doi.org/10.1016/B978-0-444-53000-4.00009-3>
- Hovem, J. M., Richardson, M., & Stoll, R. D. (Eds.). (1991). *Shear Waves in Marine Sediments*. Springer Netherlands. <https://doi.org/10.1007/978-94-011-3568-9>
- Huuse, M., & Clausen, O. R. (2001). Morphology and origin of major Cenozoic sequence boundaries in the eastern North Sea Basin: top Eocene, near-top Oligocene and the mid-Miocene unconformity. *Basin Research*, 13(1), 17–41. <https://doi.org/10.1046/j.1365-2117.2001.00123.x>
- Huuse, M., & Lykke-Andersen, H. (2000a). Large-scale glaciotectonic thrust structures in the eastern Danish North Sea. *Geological Society, London, Special Publications*, 176(1), 293–305. <https://doi.org/10.1144/GSL.SP.2000.176.01.22>
- Huuse, M., & Lykke-Andersen, H. (2000b). Overdeepened Quaternary valleys in the eastern Danish North Sea: morphology and origin. *Quaternary Science Reviews*, 19(12), 1233–1253. [https://doi.org/10.1016/S0277-3791\(99\)00103-1](https://doi.org/10.1016/S0277-3791(99)00103-1)
- IAU. (2001). *Assessment of plans and projects significantly affecting Natura 2000 Sites - Methodological guidance on the provisions of Article 6(3) and (4) of the Habitats Directive 92/43/EEC* (p. 81). Luxembourg: Impacts Assessment Unit, School of Planning Oxford Brookes University. Retrieved from https://ec.europa.eu/environment/nature/natura2000/management/docs/art6/natura_2000_assess_en.pdf
- IPCC. (2005). *IPCC Special Report on Carbon Dioxide Capture and Storage* (Prepared by Working Group III of the Intergovernmental Panel on Climate Change [Metz, B., O. Davidson, H. C. de Coninck, M. Loos, and L. A. Meyer (eds.)]) (p. 422). Retrieved from www.cambridge.org/9780521863360
- IPCC. (2021). *Climate Change 2021: The Physical Science Basis. Contribution of Working Group I to the Sixth Assessment Report of the Intergovernmental Panel on Climate Change* (Vol. In Press). Cambridge, United Kingdom and New York, NY, USA: Cambridge University Press. <https://doi.org/10.1017/9781009157896>
- IPCC. (2022). *The Ocean and Cryosphere in a Changing Climate: Special Report of the Intergovernmental Panel on Climate Change*. Cambridge: Cambridge University Press. <https://doi.org/10.1017/9781009157964>
- ISA. (2010). *A Geological Model of Polymetallic Nodule Deposits in the Clarion-Clipperton Fracture Zone*. International Seabed Authority.
- Ismail, A., Smith, E., Phillips, A., & Stumpf, A. (2012). Pitfalls in interpretation of shallow seismic data. *Applied Geophysics*, 9(1), 87–94. <https://doi.org/10.1007/s11770-012-0318-4>

- ISO 14688-1. (2017). Geotechnical investigation and testing — Identification and classification of soil — Part 1: Identification and description. Geneva, Switzerland. Retrieved from <https://www.iso.org/obp/ui/en/#iso:std:iso:14688:-1:ed-2:v1:en>
- ISO 14688-2. (2017). Geotechnical investigation and testing — Identification and classification of soil — Part 2: Principles for a classification. Geneva, Switzerland. Retrieved from <https://www.iso.org/standard/66346.html>
- ISO 19901-10. (2021, March). Petroleum and natural gas industries — Specific requirements for offshore structures — Part 10: Marine geophysical investigations. ISO Standard, Geneva, Switzerland: International Organisation for Standardization. Retrieved from <https://www.iso.org/standard/77017.html>
- ISO 22476-1. (2022). Geotechnical investigation and testing — Field testing — Part 1: Electrical cone and piezocone penetration test. Geneva, Switzerland. Retrieved from <https://www.iso.org/standard/75661.html>
- Jaeger, J. M., & Koppes, M. N. (2016). The role of the cryosphere in source-to-sink systems. *Earth-Science Reviews*, 153, 43–76. <https://doi.org/10.1016/j.earscirev.2015.09.011>
- Jäger, R., Mann, J., Höcht, G., & Hubral, P. (2001). Common-reflection-surface stack: Image and attributes. *GEOPHYSICS*, 66(1), 97–109. <https://doi.org/10.1190/1.1444927>
- Jannane, M., Beydoun, W., Crase, E., Cao, D., Koren, Z., Landa, E., et al. (1989). Wavelengths of earth structures that can be resolved from seismic reflection data. *Geophysics*, 54(7), 906–910. <https://doi.org/10.1190/1.1442719>
- Jannsen, D., Voss, J., & Theilen, F. (1985). COMPARISON OF METHODS TO DETERMINE Q IN SHALLOW MARINE SEDIMENTS FROM VERTICAL REFLECTION SEISMOGRAMS*. *Geophysical Prospecting*, 33(4), 479–497. <https://doi.org/10.1111/j.1365-2478.1985.tb00762.x>
- JNCC. (2017). *JNCC guidelines for minimising the risk of injury to marine mammals from geophysical surveys* (p. 28). Joint Nature Conservation Committee. Retrieved from <http://data.jncc.gov.uk/data/e2a46de5-43d4-43f0-b296-c62134397ce4/jncc-guidelines-seismicsurvey-aug2017-web.pdf>
- Joshi, R. P., & Thagard, S. M. (2013). Streamer-Like Electrical Discharges in Water: Part I. Fundamental Mechanisms. *Plasma Chemistry and Plasma Processing*, 33(1), 1–15. <https://doi.org/10.1007/s11090-012-9425-5>
- Kallehave, D., Byrne, B. W., LeBlanc Thilsted, C., & Mikkelsen, K. K. (2015). Optimization of monopiles for offshore wind turbines. *Philosophical Transactions of the Royal Society A: Mathematical, Physical and Engineering Sciences*, 373(2035), 20140100. <https://doi.org/10.1098/rsta.2014.0100>
- Kallweit, R. S., & Wood, L. C. (1982). The limits of resolution of zero-phase wavelets. *GEOPHYSICS*, 47(7), 1035–1046. <https://dx.doi.org/10.1190/1.1441367>
- Kaminski, P., Urlaub, M., Grabe, J., & Berndt, C. (2020). Geomechanical behaviour of gassy soils and implications for submarine slope stability: a literature analysis. *Geological Society, London, Special Publications*, 500(1), 277–288. <https://doi.org/10.1144/SP500-2019-149>

- Kastelein, R., Helder-Hoek, L., & Van de Voorde, S. (2017). Hearing thresholds of a male and a female harbor porpoise (*Phocoena phocoena*). *The Journal of the Acoustical Society of America*, *142*(2), 1006. <https://doi.org/10.1121/1.4997907>
- Kastelein, R., Helder-Hoek, L., Van de Voorde, S., von Benda-Beckmann, A. M., Lam, F.-P. A., Jansen, E., et al. (2017). Temporary hearing threshold shift in a harbor porpoise (*Phocoena phocoena*) after exposure to multiple airgun sounds. *The Journal of the Acoustical Society of America*, *142*(4), 2430–2442. <https://doi.org/10.1121/1.5007720>
- Kastelein, R., Voorde, S., & Jennings, N. (2018). Swimming Speed of a Harbor Porpoise (*Phocoena phocoena*) During Playbacks of Offshore Pile Driving Sounds. *Aquatic Mammals*, *44*, 92–99. <https://doi.org/10.1578/AM.44.1.2018.92>
- Kastelein, R., Hoek, L., Cornelisse, S., von Benda-Beckmann, S., Lam, F.-P., Jong, C., & Ketten, D. (2020). Lack of reproducibility of temporary hearing threshold shifts in a harbor porpoise after exposure to repeated airgun sounds. *The Journal of the Acoustical Society of America*, *148*, 556–565. <https://doi.org/10.1121/10.0001668>
- Keil, H., Hepp, D., & Andresen, K. (2021). *Changing North Sea, Cruise No. HE569, February 03 - February 27, 2021, Bremerhaven (Germany) - Bremerhaven (Germany)* (Heincke Berichte) (p. 60). Bonn. https://doi.org/10.48433/cr_he569
- Ker, S., Le Gonidec, Y., & Gibert, D. (2013). Multiresolution seismic data fusion with a generalized wavelet-based method to derive seabed acoustic properties. *Geophysical Journal International*, *195*(2), 1370–1383. <https://doi.org/10.1093/gji/ggt317>
- Kiyota, T., Maekawa, Y., & Wu, C. (2019). Using in-situ and laboratory-measured shear wave velocities to evaluate the influence of soil fabric on in-situ liquefaction resistance. *Soil Dynamics and Earthquake Engineering*, *117*, 164–173. <https://doi.org/10.1016/j.soildyn.2018.11.016>
- Klein, G., Bohlen, T., Theilen, F., Kugler, S., & Forbriger, T. (2005). Acquisition and Inversion of Dispersive Seismic Waves in Shallow Marine Environments. *Marine Geophysical Researches*, *26*(2), 287–315. <https://doi.org/10.1007/s11001-005-3725-6>
- Knott, C. G. (1899). III. Reflexion and refraction of elastic waves, with seismological applications. *The London, Edinburgh, and Dublin Philosophical Magazine and Journal of Science*, *48*(290), 64–97. <https://doi.org/10.1080/14786449908621305>
- Köhn, D. (2011). *Time Domain 2D Elastic Full Waveform Tomography* (PhD Thesis). Kiel University, Kiel (Germany). Retrieved from https://macau.uni-kiel.de/receive/diss_mods_00006786
- Köhn, D., De Nil, D., Kurzmann, A., Przebindowska, A., & Bohlen, T. (2012). On the influence of model parametrization in elastic full waveform tomography. *Geophysical Journal International*, *191*(1), 325–345. <https://doi.org/10.1111/j.1365-246X.2012.05633.x>
- Kooi, H., Hettema, M., & Cloetingh, S. (1991). Lithospheric dynamics and the rapid pliocene-quadernary subsidence phase in the southern north sea basin. *Tectonophysics*, *192*(3), 245–259. [https://doi.org/10.1016/0040-1951\(91\)90102-X](https://doi.org/10.1016/0040-1951(91)90102-X)

- Kortekaas, M., Murray, A. S., Sandgren, P., & Björck, S. (2007). OSL chronology for a sediment core from the southern Baltic Sea: A continuous sedimentation record since deglaciation. *Quaternary Geochronology*, 2(1), 95–101. <https://doi.org/10.1016/j.quageo.2006.05.036>
- Kräutner, T., Albrecht, B., Puhl, D., & Hüttl, H. (2022). *Sand - ein unterschätzter Rohstoff?* (Geopolitische Information No. 1/2022) (p. 36). Geoinformationsdienst der Bundeswehr. Retrieved from <https://www.bundeswehr.de/resource/blob/5522616/5e682b7704e325e3a46048cfdc5141af/2022-1-geopolitische-information-web-data.pdf>
- ten Kroode, F., Bergler, S., Corsten, C., de Maag, J. W., Strijbos, F., & Tjihof, H. (2013). Broadband seismic data — The importance of low frequencies. *GEOPHYSICS*, 78(2), WA3–WA14. <https://doi.org/10.1190/geo2012-0294.1>
- Kugler, S., Bohlen, T., Forbriger, T., Bussat, S., & Klein, G. (2007). Scholte-wave tomography for shallow-water marine sediments. *Geophysical Journal International*, 168(2), 551–570. <https://doi.org/10.1111/j.1365-246X.2006.03233.x>
- Kuhlmann, G., de Boer, P. L., Pedersen, R. B., & Wong, T. E. (2004). Provenance of Pliocene sediments and paleoenvironmental changes in the southern North Sea region using Samarium–Neodymium (Sm/Nd) provenance ages and clay mineralogy. *Sedimentary Geology*, 171(1–4), 205–226. <https://doi.org/10.1016/j.sedgeo.2004.05.016>
- Kurzmann, A., Przebindowska, A., Köhn, D., & Bohlen, T. (2013). Acoustic full waveform tomography in the presence of attenuation: a sensitivity analysis. *Geophysical Journal International*, 195(2), 985–1000. <https://doi.org/10.1093/gji/ggt305>
- Lackschewitz, K., & Heinitz, M. (2015). Research Vessel ALKOR. *Journal of Large-Scale Research Facilities JLSRF*, 1, A35–A35. <https://doi.org/10.17815/jlsrf-1-61>
- Lailly, P. (1984). The seismic inverse problem as a sequence of before stack migrations. In J. B. Bednar, E. Robinson, & A. B. Weglein (Eds.), *Inverse Scattering. Theory and Application (SLAM)* (pp. 206–220). Philadelphia.
- Lamb, R. M., Huuse, M., & Stewart, M. (2017). Early Quaternary sedimentary processes and palaeoenvironments in the central North Sea. *Journal of Quaternary Science*, 32(2), 127–144. <https://doi.org/10.1002/jqs.2894>
- Lamb, R. M., Harding, R., Huuse, M., Stewart, M., & Brocklehurst, S. H. (2018). The early Quaternary North Sea Basin. *Journal of the Geological Society*, 175(2), 275–290. <https://doi.org/10.1144/jgs2017-057>
- Larsen, B., & Andersen, L. T. (2005). Late Quaternary stratigraphy and morphogenesis in the Danish eastern North Sea and its relation to onshore geology. *Geologie En Mijnbouw/Netherlands Journal of Geosciences*, 84(2), 113–128. <https://doi.org/10.1017/S0016774600023003>
- Lebedeva-Ivanova, N., Polteau, S., Bellwald, B., Planke, S., Berndt, C., & Stokke, H. H. (2018). Toward one-meter resolution in 3D seismic. *The Leading Edge*, 37(11), 818–828. <https://doi.org/10.1190/tle37110818.1>

- Lee, M. W. (2006). A simple method of predicting S-wave velocity. *GEOPHYSICS*, 71(6), F161–F164. <https://doi.org/10.1190/1.2357833>
- Lei, X., & Morgan, E. C. (2015). Characterization of Gas-charged Sediments from Joint Inversion of Qp and Qs. In *SEG Technical Program Expanded Abstracts 2015* (pp. 2765–2770). Society of Exploration Geophysicists. <https://doi.org/10.1190/segam2015-5904497.1>
- Lesny, K., & Richwien, W. (2011). 16 - Design, construction and installation of support structures for offshore wind energy systems. In J. D. Sørensen & J. N. Sørensen (Eds.), *Wind Energy Systems* (pp. 479–518). Woodhead Publishing. <https://doi.org/10.1533/9780857090638.4.479>
- Lesny, K., Atzler, R., Bartholomä, A., Bellmer, H., Geduhn, M., Gehrman-Vorbau, J., et al. (2014). *Standard Ground Investigations - Minimum requirements for geotechnical surveys and investigations into offshore wind energy structures, offshore stations and power cables* (Standard No. BSH-No 7004) (p. 41). Hamburg and Rostock, Germany: Federal Maritime and Hydrographic Agency (BSH). Retrieved from https://www.bsh.de/DE/PUBLIKATIONEN/_Anlagen/Downloads/Offshore/Standards/Standard-Ground-investigation-for-offshore-wind-energy_en.pdf?__blob=publicationFile&v=6
- L'Heureux, J. S. (2016). Correlations between shear wave velocity and geotechnical parameters in Norwegian clays. In *Proceedings of the 17th Nordic Geotechnical Meeting* (p. 10). Reykjavik, Iceland.
- Lindseth, R. O. (1972). Approximation of acoustic logs from seismic traces. *Canadian Well Logging Society*, 5, 13–26.
- Lindseth, R. O. (1979). Synthetic sonic logs—a process for stratigraphic interpretation. *GEOPHYSICS*, 44(1), 3–26. <https://doi.org/10.1190/1.1440922>
- Linkwitz, S. H. (1978). Passive Crossover Networks for Noncoincident Drivers. *Journal of the Audio Engineering Society*, 26(3), 149–150.
- Lisiecki, L. E., & Raymo, M. E. (2005). A Pliocene-Pleistocene stack of 57 globally distributed benthic $\delta^{18}\text{O}$ records. *Paleoceanography*, 20(1). <https://doi.org/10.1029/2004PA001071>
- Lisiecki, L. E., & Raymo, M. E. (2007). Plio–Pleistocene climate evolution: trends and transitions in glacial cycle dynamics. *Quaternary Science Reviews*, 26(1), 56–69. <https://doi.org/10.1016/j.quascirev.2006.09.005>
- Lloyd, H. J. E. (2013). *An Investigation of the Role of Low Frequencies in Seismic Impedance Inversion* (Master). University of Calgary, Calgary, Alberta (Canada). Retrieved from https://www.crewes.org/ResearchLinks/GraduateTheses/2013/Lloyd_MSc_2013.pdf
- Lohrberg, A., Schwarzer, K., Unverricht, D., Omlin, A., & Krastel, S. (2020). Architecture of tunnel valleys in the southeastern North Sea: new insights from high-resolution seismic imaging. *Journal of Quaternary Science*, 35(7), 892–906. <https://doi.org/10.1002/jqs.3244>
- Lohrberg, A., Krastel, S., Unverricht, D., & Schwarzer, K. (2022). The Heligoland Glacitectonic Complex in the southeastern North Sea: indicators of a pre- or early-Elsterian ice margin. *Boreas*, 51(1), 100–117. <https://doi.org/10.1111/bor.12551>

- Lombardi, D., Bhattacharya, S., & Nikitas, G. (2017). Chapter 17 - Physical Modeling of Offshore Wind Turbine Model for Prediction of Prototype Response. In T. M. Letcher (Ed.), *Wind Energy Engineering* (pp. 353–374). Academic Press. <https://doi.org/10.1016/B978-0-12-809451-8.00017-5>
- Longva, O., Janbu, N., Blikra, L. H., & Bøe, R. (2003). The 1996 Finneidfjord Slide; Seafloor Failure and Slide Dynamics. In J. Locat, J. Mienert, & L. Boisvert (Eds.), *Submarine Mass Movements and Their Consequences: 1st International Symposium* (pp. 531–538). Dordrecht: Springer Netherlands. https://doi.org/10.1007/978-94-010-0093-2_58
- Ludwig, W. J., Nafe, J. E., & Drake, C. L. (1970). Seismic refraction. In E. Maxwell (Ed.), *The Sea* (Vol. Vol. 4, Part 1, pp. 53–84). New York: Wiley-Interscience.
- Lunne, T., Robertson, P. K., & Powell, J. J. M. (2002). *Cone penetration testing in geotechnical practice*. London, UK: E & FN Spon. Retrieved from http://katalog.suub.uni-bremen.de/DB=1/LNG=DU/CMD?ACT=SRCHA&IKT=8000&TRM=1780608438*
- Lurton, X. (2016). Modelling of the sound field radiated by multibeam echosounders for acoustical impact assessment. *Applied Acoustics*, 101, 201–221. <https://doi.org/10.1016/j.apacoust.2015.07.012>
- Lutz, R. K., Gaedicke, C., Reinhardt, L., & Winsemann, J. (2009). Pleistocene tunnel valleys in the German North Sea: spatial distribution and morphology. *Zeitschrift Der Deutschen Gesellschaft Für Geowissenschaften*, 160(3), 225–235. <https://doi.org/10.1127/1860-1804/2009/0160-0225>
- Ma, X. (2002). Simultaneous inversion of prestack seismic data for rock properties using simulated annealing. *GEOPHYSICS*, 67(6), 1877–1885. <https://doi.org/10.1190/1.1527087>
- Mankins, J. (1995). *Technology Readiness Levels-A White Paper* (White Paper). Washington, D.C.: NASA. Retrieved from <https://www.semanticscholar.org/paper/Technology-Readiness-Levels-A-White-Paper-Mankins/3072b8cfdbfbec59c53e212c8876ef1d087489d9>
- Margrave, G. F., & Lamoureaux, M. P. (Eds.). (2019). Velocity Measures and Ray Tracing. In *Numerical Methods of Exploration Seismology: With Algorithms in MATLAB®* (pp. 309–350). Cambridge: Cambridge University Press. <https://doi.org/10.1017/9781316756041.007>
- Marsset, Missiaen, Roeck, D., Noble, Versteeg, & Henriët. (1998). Very high resolution 3D marine seismic data processing for geotechnical applications. *Geophysical Prospecting*, 46(2), 105–120. <https://doi.org/10.1046/j.1365-2478.1998.00076.x>
- Masoli, C. A., Petronio, L., Gordini, E., Deponte, M., Boehm, G., Cotterle, D., et al. (2020). Near-shore geophysical and geotechnical investigations in support of the Trieste Marine Terminal extension. *Near Surface Geophysics*, 18(1), 73–89. <https://doi.org/10.1002/nsg.12084>
- Masson, Canals, Alonso, Urgeles, & Huhnerbach. (1998). The Canary Debris Flow: source area morphology and failure mechanisms. *Sedimentology*, 45(2), 411–432. <https://doi.org/10.1046/j.1365-3091.1998.0165f.x>

- Masson, D. G., Harbitz, C. B., Wynn, R. B., Pedersen, G., & Løvholt, F. (2006). Submarine Landslides: Processes, Triggers and Hazard Prediction. *Philosophical Transactions: Mathematical, Physical and Engineering Sciences*, 364(1845), 2009–2039.
- Masson, D. G., Wynn, R. B., & Talling, P. J. (2010). Large Landslides on Passive Continental Margins: Processes, Hypotheses and Outstanding Questions. In D. C. Mosher, R. C. Shipp, L. Moscardelli, J. D. Chaytor, C. D. P. Baxter, H. J. Lee, & R. Urgeles (Eds.), *Submarine Mass Movements and Their Consequences* (pp. 153–165). Dordrecht: Springer Netherlands. https://doi.org/10.1007/978-90-481-3071-9_13
- Mathys, M., Thießen, O., Theilen, F., & Schmidt, M. (2005). Seismic Characterisation of Gas-rich Near Surface Sediments in the Arkona Basin, Baltic Sea. *Marine Geophysical Researches*, 26(2), 207–224. <https://doi.org/10.1007/s11001-005-3719-4>
- Mayer, L., Jakobsson, M., Allen, G., Dorschel, B., Falconer, R., Ferrini, V., et al. (2018). The Nippon Foundation—GEBCO Seabed 2030 Project: The Quest to See the World's Oceans Completely Mapped by 2030. *Geosciences*, 8(2), 63. <https://doi.org/10.3390/geosciences8020063>
- Mayne, P. W. (2014). Interpretation of geotechnical parameters from seismic piezocone tests. In *Proceedings, 3rd International Symposium on Cone Penetration Testing* (Vol. ISSMGE Technical Committee TC 102, pp. 47–73). Las Vegas, USA. Retrieved from www.cpt14.com
- McCann, C., & McCann, D. M. (1969). The attenuation of compressional waves in marine sediments. *GEOPHYSICS*, 34(6), 882–892. <https://doi.org/10.1190/1.1440059>
- Menzies, J., van der Meer, J. J. M., & Shilts, W. W. (2018). Chapter 5 - Subglacial Processes and Sediments. In John Menzies & J. J. M. van der Meer (Eds.), *Past Glacial Environments (Second Edition)* (pp. 105–158). Elsevier. <https://doi.org/10.1016/B978-0-08-100524-8.00004-X>
- Merouane, A., & Yilmaz, O. (2017). Time-varying Q estimation on reflection seismic data in the presence of amplitude variations. In *SEG Technical Program Expanded Abstracts 2017* (pp. 3552–3556). Houston, Texas: Society of Exploration Geophysicists. <https://doi.org/10.1190/segam2017-17782597.1>
- Miller, K. A., Thompson, K. F., Johnston, P., & Santillo, D. (2018). An Overview of Seabed Mining Including the Current State of Development, Environmental Impacts, and Knowledge Gaps. *Frontiers in Marine Science*, 4. Retrieved from <https://www.frontiersin.org/articles/10.3389/fmars.2017.00418>
- Mintrop, L. (1930). *II. On The History of the Seismic Method for the Investigation of Underground Formations and Mineral Deposits*. Hannover, Germany: Seismos GmbH. Retrieved from http://wdiehl.de/PS/PS_HTML/Report/Mintrop/ps_sonderdruck_mintrop_db_liste.php
- Missiaen, T. (2005). VHR Marine 3D Seismics for Shallow Water Investigations: Some Practical Guidelines. *Marine Geophysical Researches*, 26(2), 145–155. <https://doi.org/10.1007/s11001-005-3708-7>
- Monk, D. J. (1993). Wave-Equation Multiple Suppression Using Constrained Gross-Equalization1. *Geophysical Prospecting*, 41(6), 725–736. <https://doi.org/10.1111/j.1365-2478.1993.tb00880.x>

- Monrigal, O., Jong, I. de, & Duarte, H. (2017). An ultra-high-resolution 3D marine seismic system for detailed site investigation. *Near Surface Geophysics*, *15*(4), 335–345. <https://doi.org/10.3997/1873-0604.2017025>
- Mora, P. (1987). Nonlinear two-dimensional elastic inversion of multioffset seismic data. *GEOPHYSICS*, *52*(9), 1211–1228. <https://doi.org/10.1190/1.1442384>
- Mora, P. (1989). Inversion=migration+tomography. In G. A. van Zee & J. G. G. van de Vorst (Eds.), *Parallel Computing 1988* (pp. 78–101). Berlin, Heidelberg: Springer. https://doi.org/10.1007/3-540-51604-2_6
- Morgan, E., Vanneste, M., & Vardy, M. (2014). Characterization of the Slope-destabilizing Effects of Gas-charged Sediment via Seismic Surveys. Presented at the Offshore Technology Conference, Offshore Technology Conference. <https://doi.org/10.4043/25196-MS>
- Morgan, E. C., Vanneste, M., Lecomte, I., Baise, L. G., Longva, O., & McAdoo, B. (2012). Estimation of free gas saturation from seismic reflection surveys by the genetic algorithm inversion of a P-wave attenuation model. *GEOPHYSICS*, *77*(4), R175–R187. <https://doi.org/10.1190/geo2011-0291.1>
- Moros, M., Lemke, W., Kuijpers, A., Endler, R., Jensen, J. B., Bennike, O., & Gingele, F. (2002). Regressions and transgressions of the Baltic basin reflected by a new high-resolution deglacial and postglacial lithostratigraphy for Arkona Basin sediments (western Baltic Sea). *Boreas*, *31*(2), 151–162. <https://doi.org/10.1111/j.1502-3885.2002.tb01063.x>
- Muskulus, M., & Schafhirt, S. (2014). Design Optimization of Wind Turbine Support Structures—A Review. *Journal of Ocean and Wind Energy*, *1*(1), 11.
- Naser, M., Ahmed, A., & Ismail, K. (2022). Ultimate Lateral Capacity of Large Diameter Monopiles Embedded in Sand. *Indian Geotechnical Journal*, *52*(1), 113–124. <https://doi.org/10.1007/s40098-021-00556-1>
- Neep, J. P. (2008). Benchmarking Prestack AVO Inversion (p. cp). Presented at the 70th EAGE Conference and Exhibition incorporating SPE EUROPEC 2008, European Association of Geoscientists & Engineers. <https://doi.org/10.3997/2214-4609.20147797>
- Negro, V., López-Gutiérrez, J.-S., Esteban, M. D., Alberdi, P., Imaz, M., & Serracarla, J.-M. (2017). Monopiles in offshore wind: Preliminary estimate of main dimensions. *Ocean Engineering*, *133*, 253–261. <https://doi.org/10.1016/j.oceaneng.2017.02.011>
- Nemtsov, V. S. (2019). A Comparison of Calculation Methods for Non-Elastic Absorption Coefficients Using the Model Seismic Data Pattern. *Moscow University Geology Bulletin*, *74*(5), 490–495. <https://doi.org/10.3103/S0145875219050077>
- Nikitas, G., Bhattacharya, S., & Vimalan, N. (2020). 16 - Wind Energy. In T. M. Letcher (Ed.), *Future Energy (Third Edition)* (pp. 331–355). Elsevier. <https://doi.org/10.1016/B978-0-08-102886-5.00016-5>
- Obst, K., Nachtweide, C., & Müller, U. (2017). Late Saalian and Weichselian glaciations in the German Baltic Sea documented by Pleistocene successions at the southeastern margin of the Arkona Basin. *Boreas*, *46*(1), 18–33. <https://doi.org/10.1111/bor.12212>

- OGP. (2017). *Guidelines for the conduct of offshore drilling hazard site surveys* (Geomatics Guidance Note 18-1 No. 373-18– 1 Version 2) (p. 46). London, UK: International Association of Oil & Gas Producers. Retrieved from <https://www.iogp.org/bookstore/portfolio-item/geomatics/>
- O’Kelly, B. C., & Arshad, M. (2016). 20 - Offshore wind turbine foundations – analysis and design. In C. Ng & L. Ran (Eds.), *Offshore Wind Farms* (pp. 589–610). Woodhead Publishing. <https://doi.org/10.1016/B978-0-08-100779-2.00020-9>
- Oldenburg, D. W., Scheuer, T., & Levy, S. (1983). Recovery of the acoustic impedance from reflection seismograms. *GEOPHYSICS*, 48(10), 1318–1337. <https://doi.org/10.1190/1.1441413>
- Oldenburg, Douglas W., & Li, Y. (2005). 5. Inversion for Applied Geophysics: A Tutorial. In *Near-Surface Geophysics* (Vols. 1–0, pp. 89–150). Society of Exploration Geophysicists. <https://doi.org/10.1190/1.9781560801719.ch5>
- Oliveira, S., Loures, L., Moraes, F., & Theodoro, C. (2009). Nonlinear impedance inversion for attenuating media. *GEOPHYSICS*, 74(6), R111–R117. <https://doi.org/10.1190/1.3256284>
- O’Neill, M. P., Osuchowski, A. L., Cai, Y., Bransby, M. F., Watson, P. G., Gaudin, C., et al. (2023). Integrated and data Science-informed seabed characterisation for optimised foundation design. *Ocean Engineering*, 284, 115095. <https://doi.org/10.1016/j.oceaneng.2023.115095>
- Operto, S., Gholami, Y., Prieux, V., Ribodetti, A., Brossier, R., Metivier, L., & Virieux, J. (2013). A guided tour of multiparameter full-waveform inversion with multicomponent data: From theory to practice. *The Leading Edge*, 32(9), 1040–1054. <https://doi.org/10.1190/tle32091040.1>
- OSPAR. (2016). *OSPAR inventory of measures to mitigate the emission and environmental impact of underwater noise* (p. 72). Convention for the Protection of the Marine Environment of the North East Atlantic. Retrieved from <https://www.ospar.org/documents?v=37745>
- Ottesen, D., Dowdeswell, J. A., & Bugge, T. (2014). Morphology, sedimentary infill and depositional environments of the Early Quaternary North Sea Basin (56°–62°N). *Marine and Petroleum Geology*, 56, 123–146. <https://doi.org/10.1016/j.marpetgeo.2014.04.007>
- Overeem, I., Weltje, G. J., Bishop-Kay, C., & Kroonenberg, S. B. (2001). The Late Cenozoic Eridanos delta system in the Southern North Sea Basin: a climate signal in sediment supply?: *The Cenozoic Eridanos delta, southern North Sea. Basin Research*, 13(3), 293–312. <https://doi.org/10.1046/j.1365-2117.2001.00151.x>
- Owen, A. (2020). 17 - Tidal Current Energy: Origins and Challenges. In T. M. Letcher (Ed.), *Future Energy (Third Edition)* (pp. 357–374). Elsevier. <https://doi.org/10.1016/B978-0-08-102886-5.00017-7>
- Özmaral, A., Abegunrin, A., Keil, H., Hepp, D. A., Schwenk, T., Lantzsch, H., et al. (2022). The Elbe Palaeovalley: Evolution from an ice-marginal valley to a sedimentary trap (SE North Sea). *Quaternary Science Reviews*, 282, 107453. <https://doi.org/10.1016/j.quascirev.2022.107453>

- Panda, S., LeBlanc, L. R., & Schock, S. G. (1994). Sediment classification based on impedance and attenuation estimation. *The Journal of the Acoustical Society of America*, 96(5), 3022–3035. <https://doi.org/10.1121/1.411266>
- Paraska, D. W., Hipsey, M. R., & Salmon, S. U. (2014). Sediment diagenesis models: Review of approaches, challenges and opportunities. *Environmental Modelling & Software*, 61, 297–325. <https://doi.org/10.1016/j.envsoft.2014.05.011>
- Paulus, E. (2021). Shedding Light on Deep-Sea Biodiversity—A Highly Vulnerable Habitat in the Face of Anthropogenic Change. *Frontiers in Marine Science*, 8. Retrieved from <https://www.frontiersin.org/articles/10.3389/fmars.2021.667048>
- Pedersen, S. A. S. (1987). Comparative studies of gravity tectonics in Quaternary sediments and sedimentary rocks related to fold belts. *Geological Society, London, Special Publications*, 29(1), 165–179. <https://doi.org/10.1144/GSL.SP.1987.029.01.14>
- Pein, T., Werpup Oguro, A., Keil, H., Spieß, V., Preu, B., Herwig, V., & Wenau, S. (2020). Interpolation of CPT Data Supported by 3D Seismic Data for Offshore Soil Characterization. In *NSG2020 4th Applied Shallow Marine Geophysics Conference* (pp. 1–5). ;: European Association of Geoscientists & Engineers. <https://doi.org/10.3997/2214-4609.202020155>
- Pereira, J. J., Ng, T. F., & Hunt, J. (2021). Climate Action. In J. C. Gill & M. Smith (Eds.), *Geosciences and the Sustainable Development Goals* (pp. 313–337). Cham: Springer International Publishing. https://doi.org/10.1007/978-3-030-38815-7_13
- Petterson, M. G., Kim, H.-J., & Gill, J. C. (2021). Conserve and Sustainably Use the Oceans, Seas, and Marine Resources. In J. C. Gill & M. Smith (Eds.), *Geosciences and the Sustainable Development Goals* (pp. 339–367). Cham: Springer International Publishing. https://doi.org/10.1007/978-3-030-38815-7_14
- Pinson, L. J. W., Henstock, T. J., Dix, J. K., & Bull, J. M. (2008). Estimating quality factor and mean grain size of sediments from high-resolution marine seismic data. *GEOPHYSICS*, 73(4), G19–G28. <https://doi.org/10.1190/1.2937171>
- Preine, J., Schwarz, B., Bauer, A., & Hübscher, C. (2020). When There Is No Offset: A Demonstration of Seismic Diffraction Imaging and Depth-Velocity Model Building in the Southern Aegean Sea. *Journal of Geophysical Research: Solid Earth*, 125(9), e2020JB019961. <https://doi.org/10.1029/2020JB019961>
- Provenzano, G., Vardy, M. E., & Henstock, T. J. (2016). Pre-stack Waveform Inversion of VHF Marine Seismic Reflection Data - A Case Study in Norway (Vol. 2016, pp. 1–5). Presented at the Near Surface Geoscience 2016 - Second Applied Shallow Marine Geophysics Conference, European Association of Geoscientists & Engineers. <https://doi.org/10.3997/2214-4609.201602147>
- Provenzano, G., Vardy, M. E., & Henstock, T. J. (2017). Pre-stack full waveform inversion of ultra-high-frequency marine seismic reflection data. *Geophysical Journal International*, 209(3), 1593–1611. <https://doi.org/10.1093/gji/ggx114>
- Provenzano, G., Vardy, M. E., & Henstock, T. J. (2018). Decimetric-resolution stochastic inversion of shallow marine seismic reflection data: dedicated strategy and application to a geohazard

- case study. *Geophysical Journal International*, 214(3), 1683–1700. <https://doi.org/10.1093/gji/ggy221>
- Provenzano, G., Zervos, A., Vardy, M. E., & Henstock, T. J. (2019). Characterization of shallow overpressure in consolidating submarine slopes via seismic full waveform inversion. *Quarterly Journal of Engineering Geology and Hydrogeology*. <https://doi.org/10.1144/qjegh2019-019>
- Provenzano, G., Henstock, T. J., Bull, J. M., & Bayrakci, G. (2020). Attenuation of receiver ghosts in variable-depth streamer high-resolution seismic reflection data. *Marine Geophysical Research*, 41(2), 11. <https://doi.org/10.1007/s11001-020-09407-9>
- Ramsey, N. (2002). A Calibrated Model For The Interpretation Of Cone Penetration Tests (Cpts) In North Sea Quaternary Soils. Presented at the Offshore Site Investigation and Geotechnics “Diversity and Sustainability”; Proceedings of an International Conference, Society of Underwater Technology. Retrieved from <https://www.onepetro.org/conference-paper/SUT-OSIG-02-341>
- Rasmussen, E. S. (2004). The interplay between true eustatic sea-level changes, tectonics, and climatic changes: what is the dominating factor in sequence formation of the Upper Oligocene–Miocene succession in the eastern North Sea Basin, Denmark? *Global and Planetary Change*, 41(1), 15–30. <https://doi.org/10.1016/j.gloplacha.2003.08.004>
- Raymer, L., Hunt, E., & Gardner, J. (1980). An improved sonic transit time-to-porosity transform. In *SPWLA 21st Annual Logging Symposium* (pp. 1–13).
- Raymo, M. E., & Ruddiman, W. F. (1992). Tectonic forcing of late Cenozoic climate. *Nature*, 359(6391), 117–122. <https://doi.org/10.1038/359117a0>
- Reiche, S., Berkels, B., & Weiß, B. (2020). Automated static and moveout corrections of high-resolution seismic data from the Baltic Sea. *Near Surface Geophysics*, 18(1), 23–37. <https://doi.org/10.1002/nsg.12068>
- Richards, A. F., Palmer, H. D., & Perlow, M. (1975). Review of continental shelf marine geotechnics: Distribution of soils, measurement of properties, and environmental hazards. *Marine Geotechnology*, 1(1), 33–67. <https://doi.org/10.1080/10641197509388151>
- Riedel, M., & Theilen, F. (2001). AVO investigations of shallow marine sediments. *Geophysical Prospecting*, 49(2), 198–212. <https://doi.org/10.1046/j.1365-2478.2001.00246.x>
- Riedel, M., Dosso, S. E., & Beran, L. (2003). Uncertainty estimation for amplitude variation with offset (AVO) inversion. *GEOPHYSICS*, 68(5), 1485–1496. <https://doi.org/10.1190/1.1620621>
- Robb, G. B. N., Best, A. I., Dix, J. K., Bull, J. M., Leighton, T. G., & White, P. R. (2006). The frequency dependence of compressional wave velocity and attenuation coefficient of intertidal marine sediments. *The Journal of the Acoustical Society of America*, 120(5), 2526–2537. <https://doi.org/10.1121/1.2345908>
- Robertson, P. K. (2009). Interpretation of cone penetration tests — a unified approach. *Canadian Geotechnical Journal*, 46(11), 1337–1355. <https://doi.org/10.1139/T09-065>

- Robertson, P. K. (2016). Cone penetration test (CPT)-based soil behaviour type (SBT) classification system — an update. *Canadian Geotechnical Journal*, 53(12), 1910–1927. <https://doi.org/10.1139/cgj-2016-0044>
- Robertson, P. K., & Cabal, K. L. (2015). *Guide to Cone Penetration Testing* (No. 6th Edition) (p. 143). Signal Hill, California (USA): Gregg Drilling & Testing, Inc. Retrieved from <https://www.greggdrilling.com/news/6th-edition-of-guide-to-cone-penetration-testing-now-available/>
- Römer, M., Wenau, S., Mau, S., Veloso, M., Greinert, J., Schlüter, M., & Bohrmann, G. (2017). Assessing marine gas emission activity and contribution to the atmospheric methane inventory: A multidisciplinary approach from the Dutch Dogger Bank seep area (North Sea). *Geochemistry, Geophysics, Geosystems*, 18(7), 2617–2633. <https://doi.org/10.1002/2017GC006995>
- Römer, M., Blumenberg, M., Heeschen, K., Schloemer, S., Müller, H., Müller, S., et al. (2021). Seafloor Methane Seepage Related to Salt Diapirism in the Northwestern Part of the German North Sea. *Frontiers in Earth Science*, 9, 319. <https://doi.org/10.3389/feart.2021.556329>
- Römer-Stange, N., Wenau, S., Bihler, V., Keil, H., Ramos Córdova, C. A., & Spieß, V. (2022). Boulder Detection in the Shallow Sub-Seafloor by Diffraction Imaging With Beamforming on Ultra-High Resolution Seismic Data—A Feasibility Study. *Earth and Space Science*, 9(6), e2021EA002156. <https://doi.org/10.1029/2021EA002156>
- Russell, B. H. (2014). Prestack seismic amplitude analysis: An integrated overview. *Interpretation*, 2(2), SC19–SC36. <https://doi.org/10.1190/INT-2013-0122.1>
- Rutgers, W. R., & de Jong, I. (2003). Multi-tip sparker for the generation of acoustic pulses. *Sensor Review*, 23(1), 55–59. <https://doi.org/10.1108/02602280310457974>
- Santoso, D., Alam, S., Hendrajaya, L., Alfian, Munadi, S., & Purwoko. (1996). Reservoir fluid identification and elastic modulus determination using AVO. *Journal of Applied Geophysics*, 35(2), 159–165. [https://doi.org/10.1016/0926-9851\(96\)00017-1](https://doi.org/10.1016/0926-9851(96)00017-1)
- Sauvin, G., Vanneste, M., & Madshus, C. (2018). High-Resolution Quantitative Ground-Model for Shallow Subsurface. Presented at the 3rd Applied Shallow Marine Geophysics Conference, Porto, Portugal. <https://doi.org/10.3997/2214-4609.201802659>
- Sauvin, G., Vanneste, M., Vardy, M. E., Klinkvort, R. T., & Carl Fredrik, F. (2019). Machine Learning and Quantitative Ground Models for Improving Offshore Wind Site Characterization. Presented at the Offshore Technology Conference, Offshore Technology Conference. <https://doi.org/10.4043/29351-MS>
- Sayers, C., Dasgupta, S., Gofer, E., Hearn, R., Koesoemadinata, A., & Sudhakar, V. (2020). Seismic Inversion for Risk Reduction in Drilling and Production in Unconventional Reservoirs. Presented at the SPE Annual Technical Conference and Exhibition, OnePetro. <https://doi.org/10.2118/201530-MS>
- Schack, H., Ruiz, M., Andersson, M., & Zweifel, U. L. (2019). *Noise sensitivity of animals in the Baltic Sea* (Underwater noise No. 167) (p. 46). Helsinki, Finland: Helsinki Commission -

- HELCOM. Retrieved from <https://www.helcom.fi/wp-content/uploads/2019/08/BSEP167.pdf>
- Schmoor, K. A., & Achmus, M. (2015). Optimum Geometry of Monopiles With Respect to the Geotechnical Design. *Journal of Ocean and Wind Energy*, 2(1).
- Schock, S. G., LeBlanc, L. R., & Mayer, L. A. (1989). Chirp subbottom profiler for quantitative sediment analysis. *GEOPHYSICS*, 54(4), 445–450. <https://doi.org/10.1190/1.1442670>
- Sclater, J. G., & Christie, P. a. F. (1980). Continental stretching: An explanation of the Post-Mid-Cretaceous subsidence of the central North Sea Basin. *Journal of Geophysical Research: Solid Earth*, 85(B7), 3711–3739. <https://doi.org/10.1029/JB085iB07p03711>
- Selley, R. C. (2000). 5 - Sedimentary Structures. In R. C. Selley (Ed.), *Applied Sedimentology (Second Edition)* (pp. 130–180). San Diego: Academic Press. <https://doi.org/10.1016/B978-012636375-3/50006-9>
- Sen, M., & Stoffa, P. (1992). Rapid sampling of model space using genetic algorithms: Examples from seismic waveform inversion. *Geophysical Journal International*, 108, 281–292. <https://doi.org/10.1111/j.1365-246X.1992.tb00857.x>
- Seong, W., & Park, C. (2001). Geoacoustic Inversion via Genetic Algorithm and Its Application to Manganese Sediment Identification. *Marine Georesources & Geotechnology*, 19(1), 37–50. <https://doi.org/10.1080/10641190109353803>
- Sercel. (2022). *Mini GI-Source* (Product Specifications) (p. 12). Houston, Texas: Sercel Inc. Retrieved from <https://www.sercel.com/products/Pages/MiniG-Gun.aspx>
- Sheen, D.-H., Tuncay, K., Baag, C.-E., & Ortoleva, P. J. (2006). Time domain Gauss-Newton seismic waveform inversion in elastic media. *Geophysical Journal International*, 167(3), 1373–1384. <https://doi.org/10.1111/j.1365-246X.2006.03162.x>
- Shumway, G. (1960). Sound speed and absorption studies of marine sediments by a resonance method. *GEOPHYSICS*, 25(2), 451–467. <https://doi.org/10.1190/1.1438717>
- Simm, R., & Bacon, M. (2014). *Seismic Amplitude: An Interpreter's Handbook*. Cambridge University Press.
- Sirgue, L., & Pratt, R. G. (2004). Efficient waveform inversion and imaging: A strategy for selecting temporal frequencies. *GEOPHYSICS*, 69(1), 231–248. <https://doi.org/10.1190/1.1649391>
- Sirgue, L., Barkved, O. I., Dellinger, J., Etgen, J., Albertin, U., & Kommedal, J. H. (2010). Full waveform inversion: the next leap forward in imaging at Valhall. *First Break*, 28. <https://doi.org/10.3997/1365-2397.2010012>
- Smith, M., & Bricker, S. (2021). Sustainable Cities and Communities. In J. C. Gill & M. Smith (Eds.), *Geosciences and the Sustainable Development Goals* (pp. 259–282). Cham: Springer International Publishing. https://doi.org/10.1007/978-3-030-38815-7_11

- Sobreira, J. F. F., Lipski, M., Carvalho, L. A., & Márquez, E. (2010). Geotechnical characterization based on seismic data approaches applied in Campos Basin, southeastern Brazilian Margin. *The Leading Edge*, 29(7), 842–846. <https://doi.org/10.1190/1.3462788>
- Southall, B. L., Bowles, A. E., Ellison, W. T., Finneran, J. J., Gentry, R. L., Greene, C. R., et al. (2007). MARINE MAMMAL NOISE-EXPOSURE CRITERIA: INITIAL SCIENTIFIC RECOMMENDATIONS. *Bioacoustics*, 17(1–3), 273–275. <https://doi.org/10.1080/09524622.2008.9753846>
- Southall, B. L., Finneran, J. J., Reichmuth, C., Nachtigall, P. E., Ketten, D. R., Bowles, A. E., et al. (2019). Marine Mammal Noise Exposure Criteria: Updated Scientific Recommendations for Residual Hearing Effects. *Aquatic Mammals*, 45(2), 125–232. <https://doi.org/10.1578/AM.45.2.2019.125>
- Spieß, V., Nkemata, A. F., Olayanju, G., Raza, A., Sanila, N., Soyombo, O., et al. (2022). *Student Cruise - Marine Geology of the Baltic Sea - Cruise No. AL546* (Fahrtbericht No. doi:10.3289/CR_AL546). Bremen, Germany: Universität Bremen. Retrieved from <https://oceanrep.geomar.de/id/eprint/57301/>
- Sternlicht, D. D., & de Moustier, C. P. (2003). Remote sensing of sediment characteristics by optimized echo-envelope matching. *The Journal of the Acoustical Society of America*, 114(5), 2727–2743. <https://doi.org/10.1121/1.1608019>
- Stevenson, I. R., McCann, C., & Runciman, P. B. (2002). An attenuation-based sediment classification technique using Chirp sub-bottom profiler data and laboratory acoustic analysis. *Marine Geophysical Researches*, 23(4), 277–298. <https://doi.org/10.1023/A:1025708024518>
- Stewart, I., Capello, M. A., Mouri, H., Mhopjeni, K., & Raji, M. (2023). Three Horizons for Future Geoscience. *Earth Science, Systems and Society*, 3, 10079. <https://doi.org/10.3389/esss.2023.10079>
- Stoffa, P. L., & Sen, M. K. (1991). Nonlinear multiparameter optimization using genetic algorithms: Inversion of plane-wave seismograms. *GEOPHYSICS*, 56(11), 1794–1810. <https://doi.org/10.1190/1.1442992>
- Stoll, R. D. (1977). Acoustic waves in ocean sediments. *Geophysics*, 42(4), 715–725. <https://doi.org/10.1190/1.1440741>
- Storn, R., & Price, K. (1997). Differential Evolution – A Simple and Efficient Heuristic for global Optimization over Continuous Spaces. *Journal of Global Optimization*, 11(4), 341–359. <https://doi.org/10.1023/A:1008202821328>
- Tarantola, A. (1986). A strategy for nonlinear elastic inversion of seismic reflection data. *Geophysics*, 51(10), 1893–1903. <https://doi.org/10.1190/1.1442046>
- Telford, W. M., Geldart, L. P., & Sheriff, R. E. (2004). *Applied Geophysics*. Cambridge: Cambridge Univ. Press. Retrieved from http://katalog.suub.uni-bremen.de/DB=1/LNG=DU/CMD?ACT=SRCHA&IKT=8000&TRM=1194005055*
- Terente, V. A., Owen, M. J., Higgs, D. M., & Ellery, G. (2016). Derivation of Ground Models and Characteristic Geotechnical Profiles in Offshore Wind Farms at pre-FID stage. Presented

- at the The 26th International Ocean and Polar Engineering Conference, International Society of Offshore and Polar Engineers. Retrieved from <https://www.onepetro.org/conference-paper/ISOPE-I-16-411>
- Thiel, N., Hertweck, T., & Bohlen, T. (2019). Comparison of acoustic and elastic full-waveform inversion of 2D towed-streamer data in the presence of salt. *Geophysical Prospecting*, *67*(2), 349–361. <https://doi.org/10.1111/1365-2478.12728>
- Thöle, H., Gaedicke, C., Kuhlmann, G., & Reinhardt, L. (2014). Late Cenozoic sedimentary evolution of the German North Sea – A seismic stratigraphic approach. *Newsletters on Stratigraphy*, *47*(3), 299–329. <https://doi.org/10.1127/0078-0421/2014/0049>
- Thorne, J. A., & Watts, A. B. (1989). Quantitative Analysis of North Sea Subsidence. *AAPG Bulletin*, *73*(1), 88–116. <https://doi.org/10.1306/703C9AF0-1707-11D7-8645000102C1865D>
- Tóth, Z., Spieß, V., Mogollón, J. M., & Jensen, J. B. (2014). Estimating the free gas content in Baltic Sea sediments using compressional wave velocity from marine seismic data. *Journal of Geophysical Research: Solid Earth*, *119*(12), 8577–8593. <https://doi.org/10.1002/2014JB010989>
- Tougaard, J. (2014). *Vurdering af effekter af undervandsstøj på marine organismer* (Technical Report No. Del 2-Påvirkninger) (p. 51). Aarhus Universitet, DCE – Nationalt Center for Miljø og Energi. Retrieved from <http://dce2.au.dk/pub/TR45.pdf>
- Tougaard, J. (2016). *Input to revision of guidelines regarding underwater noise from oil and gas activities - effects on marine mammals and mitigation measures* (Background document No. 202) (p. 52). Aarhus, Denmark: Aarhus University, Department of Bioscience. Retrieved from <http://dce2.au.dk/pub/SR202.pdf>
- Tougaard, J., Wright, A. J., & Madsen, P. T. (2015). Cetacean noise criteria revisited in the light of proposed exposure limits for harbour porpoises. *Marine Pollution Bulletin*, *90*(1), 196–208. <https://doi.org/10.1016/j.marpolbul.2014.10.051>
- Tromp, J. (2020). Seismic wavefield imaging of Earth's interior across scales. *Nature Reviews Earth & Environment*, *1*(1), 40–53. <https://doi.org/10.1038/s43017-019-0003-8>
- Tucker, P. M., & Yorston, H. J. (1973). 1. Pitfalls in Seismic Interpretation. In *Pitfalls in Seismic Interpretation* (Vols. 1–0, pp. i–57). Society of Exploration Geophysicists. <https://doi.org/10.1190/1.9781560802365.ch1>
- Ursin, B. (1990). Offset-dependent geometrical spreading in a layered medium. *GEOPHYSICS*, *55*(4), 492–496. <https://doi.org/10.1190/1.1442860>
- Van Dover, C. L. (2019). Inactive Sulfide Ecosystems in the Deep Sea: A Review. *Frontiers in Marine Science*, *6*. Retrieved from <https://www.frontiersin.org/articles/10.3389/fmars.2019.00461>
- Vanneste, M., Forsberg, C. F., Knudsen, S., Kvalstad, T. J., L'Heureux, J. S., Lunne, T., et al. (2015). Integration of very-high-resolution seismic and CPTU data from a coastal area affected by shallow landsliding - The finneidfjord natural laboratory. In *Frontiers in Offshore Geotechnics III - 3rd International Symposium on Frontiers in Offshore Geotechnics, ISFOG 2015* (pp. 1017–1022). CRC Press/Balkema. Retrieved from

- <https://pennstate.pure.elsevier.com/en/publications/integration-of-very-high-resolution-seismic-and-cptu-data-from-a->
- Vardy, M. E. (2015). Deriving shallow-water sediment properties using post-stack acoustic impedance inversion. *Near Surface Geophysics*, 13(2), 143–154. <https://doi.org/10.3997/1873-0604.2014045>
- Vardy, M. E. (2020, May 26). Marine Site Investigation and Reducing Risk - The evolving role of seismic reflection data within offshore site investigation. *GEO ExPro*, 17(2). Retrieved from <http://www.geoexpro.com/articles/2020/05/marine-site-investigation-and-reducing-risk>
- Vardy, M. E., L'Heureux, J.-E., Vanneste, M., Longva, O., Steiner, A., Forsberg, C. F., et al. (2012). Multidisciplinary investigation of a shallow near-shore landslide, Finneidfjord, Norway. *Near Surface Geophysics*, 10(4), 267–277. <https://doi.org/10.3997/1873-2012022>
- Vardy, M. E., Vanneste, M., Henstock, T. J., Morgan, E. C., & Pinson, L. J. W. (2015). Can high-resolution marine geophysical data be inverted for soil properties? *Proceedings of the Institute of Acoustics*, 37(1), 149–156.
- Vardy, M. E., Vanneste, M., Henstock, T. J., Clare, M. A., Forsberg, C. F., & Provenzano, G. (2017). State-of-the-art remote characterization of shallow marine sediments: the road to a fully integrated solution. *Near Surface Geophysics*, 15(4), 387–402. <https://doi.org/10.3997/1873-0604.2017024>
- Vardy, M. E., Clare, M. A., Vanneste, M., Forsberg, C. F., & Dix, J. K. (2018). Seismic Inversion for Site Characterization: When, Where and Why Should We Use It? Presented at the Offshore Technology Conference, Offshore Technology Conference. <https://doi.org/10.4043/28730-MS>
- Veeken, P. C. H., & Silva, M. D. (2004). Seismic Inversion Methods and some of their constraints. *First Break*, 22(6). <https://doi.org/10.3997/1365-2397.2004011>
- van der Vegt, P., Janszen, A., & Moscariello, A. (2012). Tunnel valleys: current knowledge and future perspectives. In M. Huuse, J. Redfern, D. P. L. Heron, R. J. Dixon, A. Moscariello, & J. Craig (Eds.), *Glaciogenic Reservoirs and Hydrocarbon Systems* (Vol. 368, p. 0). Geological Society of London. <https://doi.org/10.1144/SP368.13>
- Vermeer, G. J. O. (1999). Factors affecting spatial resolution. *GEOPHYSICS*, 64(3), 942–953. <https://doi.org/10.1190/1.1444602>
- Virieux, J., & Operto, S. (2009). An overview of full-waveform inversion in exploration geophysics. *GEOPHYSICS*, 74(6), WCC1–WCC26. <https://doi.org/10.1190/1.3238367>
- Virieux, J., Asnaashari, A., Brossier, R., Métivier, L., Ribodetti, A., & Zhou, W. (2014). 6. An introduction to full waveform inversion. In *Encyclopedia of Exploration Geophysics* (pp. R1-1-R1-40). Society of Exploration Geophysicists. <https://doi.org/10.1190/1.9781560803027.entry6>
- Wang, J., & Stewart, R. (2015). Inferring marine sediment type using chirp sonar data: Atlantis field, Gulf of Mexico. In *SEG Technical Program Expanded Abstracts 2015* (Vols. 1–0, pp. 2385–2390). Society of Exploration Geophysicists. <https://doi.org/10.1190/segam2015-5918190.1>

- Wang, Y. (2003). Multiple subtraction using an expanded multichannel matching filter. *Geophysics*, 68. <https://doi.org/10.1190/1.1543220>
- Wang, Y. (2004). Q analysis on reflection seismic data. *Geophysical Research Letters*, 31(17). <https://doi.org/10.1029/2004GL020572>
- Wang, Y. (2008). *Seismic inverse Q filtering*. Malden, MA: Blackwell Pub. Retrieved from http://katalog.suub.uni-bremen.de/DB=1/LNG=DU/CMD?ACT=SRCHA&IKT=8000&TRM=91130385*
- Weglein, A. B. (2013). A timely and necessary antidote to indirect methods and so-called P-wave FWI. *The Leading Edge*, 32(10), 1192–1204. <https://doi.org/10.1190/tle32101192.1>
- Whitcombe, D. N., Connolly, P. A., Reagan, R. L., & Redshaw, T. C. (2002). Extended elastic impedance for fluid and lithology prediction. *GEOPHYSICS*, 67(1), 63–67. <https://doi.org/10.1190/1.1451337>
- Whiteley, R. J. (2005). 15. Gravity Mapping and Seismic Imaging of Paleochannels on Large Tunnel Routes in Sydney, Australia. In *Near-Surface Geophysics* (Vols. 1–0, pp. 503–512). Society of Exploration Geophysicists. <https://doi.org/10.1190/1.9781560801719.ch15>
- Wichtmann, T., Kimmig, I., & Triantafyllidis, T. (2017). On correlations between “dynamic” (small-strain) and “static” (large-strain) stiffness moduli – An experimental investigation on 19 sands and gravels. *Soil Dynamics and Earthquake Engineering*, 98, 72–83. <https://doi.org/10.1016/j.soildyn.2017.03.032>
- Widess, M. B. (1973). HOW THIN IS A THIN BED? *GEOPHYSICS*, 38(6), 1176–1180. <https://doi.org/10.1190/1.1440403>
- Winsemann, J., Koopmann, H., Tanner, D. C., Lutz, R., Lang, J., Brandes, C., & Gaedicke, C. (2020). Seismic interpretation and structural restoration of the Heligoland glaciotectionic thrust-fault complex: Implications for multiple deformation during (pre-)Elsterian to Warthian ice advances into the southern North Sea Basin. *Quaternary Science Reviews*, 227, 106068. <https://doi.org/10.1016/j.quascirev.2019.106068>
- Winterhalter, B., Flodén, T., Ignatius, H., Axberg, S., & Niemistö, L. (1981). Chapter 1 Geology of the Baltic Sea. In A. Voipio (Ed.), *Elsevier Oceanography Series* (Vol. 30, pp. 1–121). Elsevier. [https://doi.org/10.1016/S0422-9894\(08\)70138-7](https://doi.org/10.1016/S0422-9894(08)70138-7)
- Woodward, M. J., Nichols, D., Zdraveva, O., Whitfield, P., & Johns, T. (2008). A decade of tomography. *GEOPHYSICS*, 73(5), VE5–VE11. <https://doi.org/10.1190/1.2969907>
- Yao, G., Wu, D., & Wang, S.-X. (2020). A review on reflection-waveform inversion. *Petroleum Science*, 17(2), 334–351. <https://doi.org/10.1007/s12182-020-00431-3>
- Yilmaz, Ö. (1991). *Seismic data processing*. Tulsa, Okla.: Soc. of Exploration Geophysicists. Retrieved from http://katalog.suub.uni-bremen.de/DB=1/LNG=DU/CMD?ACT=SRCHA&IKT=8000&TRM=16657336*
- Yilmaz, Ö. (2001). *Seismic Data Analysis: Processing, Inversion, and Interpretation of Seismic Data*. Society of Exploration Geophysicists. <https://doi.org/10.1190/1.9781560801580>

- Yuan, S., Wang, S., Luo, Y., Wei, W., & Wang, G. (2019). Impedance inversion by using the low-frequency full-waveform inversion result as an a priori model. *GEOPHYSICS*, *84*(2), R149–R164. <https://doi.org/10.1190/geo2017-0643.1>
- Zeiler, M., Schulz-Ohlberg, J., & Figge, K. (2000). Mobile sand deposits and shoreface sediment dynamics in the inner German Bight (North Sea). *Marine Geology*, *170*(3), 363–380. [https://doi.org/10.1016/S0025-3227\(00\)00089-X](https://doi.org/10.1016/S0025-3227(00)00089-X)
- Zeiler, M., Schwarter, K., Ricklefs, K., & Bartholomä, A. (2008). Seabed Morphology and Sediment Dynamics. *Die Küste*, *74*, 31–44.
- Zhang, Z., & Digby, A. (2013). Analysis of amplitude, reflection strength, and acoustic impedance of AUV sub-bottom profiles with application to deepwater near-surface sediments. Presented at the Offshore Technology Conference, OnePetro. <https://doi.org/10.4043/23978-MS>
- Ziegler, P. A. (1990). *Geological atlas of Western and Central Europe*. Den Haag: Shell Internationale Petroleum Maatschappij BV. Retrieved from http://katalog.suub.uni-bremen.de/DB=1/LNG=DU/CMD?ACT=SRCHA&IKT=8000&TRM=74153914*
- Zoback, M. D., & Gorelick, S. M. (2012). Earthquake triggering and large-scale geologic storage of carbon dioxide. *Proceedings of the National Academy of Sciences*, *109*(26), 10164–10168. <https://doi.org/10.1073/pnas.1202473109>
- Zoeppritz, K. (1919). VII b. Über Reflexion und Durchgang seismischer Wellen durch Unstetigkeitsflächen. *Nachrichten von Der Gesellschaft Der Wissenschaften Zu Göttingen, Mathematisch-Physikalische Klasse*, *1919*, 66–84.

List of Figures

Figure 1-1: Overview of the marine near surface (equal area Eckert IV projection; ESRI 54012). A) Geomorphic features of the world's ocean redrawn and modified from Harris et al. (2014). B) Deep sea sediments of the world's oceans redrawn and modified from Diesing (2020)....2

Figure 1-2: Viscoelastic properties of unconsolidated near surface sediments and empirical relations relating the properties reproducing Breitzke et al. (2000) and Pinson et al. (2008). The measurements shown are taken from McCann & McCann (1969), Shumway (1960), Hamilton (1970, 1972), Breitzke et al. (2000), Stevenson et al. (2002), Robb et al. (2006), while the P-S Logging data shown is taken from the BSH Pinta Data Base (2021) for the wind parks N0307, N0308 and O0103. A) Cross-plot of the wet-bulk density and the compressional or P-Wave velocity with an overlay of the empiric density to P-Wave velocity relationship by Raymer et al. (1980), Gardner (1974), and (Ludwig et al., 1970). Below velocities of about 1600 m/s, the variation in density is significantly larger than the velocity variation. B) Cross-plot of the wet-bulk density and the Shear or S-Wave velocity with an overlay of the empiric S-wave velocity estimation by Lee (2006) applied on the fit of the measurements to the Raymer et al. (1980) equation. A clear discrepancy of the P-S Logging data and the measurements as well as the empiric estimation is observed. It is to be noted that only the Breitzke et al. (2000) measurements are shown, as the other measurements lack S-Wave velocity information. C) Cross plot of the grain size and the attenuation quality factor. The grain size is expressed in the Φ -scale according to which the diameter is defined as $D = 1 \text{ mm} \cdot 2^{-\Phi}$ leading to $D(\Phi = 0) = 1 \text{ mm}$, $D(\Phi = 4) = 0.0625 \text{ mm}$, or $D(\Phi = 8) = 0.0039 \text{ mm}$. The quality factor Q is the ratio of the total energy of the seismic wave and the energy lost during one cycle of the wave due to intrinsic attenuation and scattering. Thus, the higher the quality factor, the lower the observed energy loss. So, it is shown in the plot, that attenuation is high for large grain sizes and lower attenuation is expected at small grain sizes.....5

Figure 1-3: Paleogeographic maps taken from (Winsemann et al., 2020) depicting the glacial history of the study area and showing the tunnel valleys in the surrounding of the study area. A) First deformation phase in which a pre- or early Elsterian ice advance towards the West formed the Heligoland and possibly the Fanø Bugt glaciotectonic complex. B) During the Elsterian (MIS 12 or MIS 19) deep tunnel valleys have been incised at the margins of ice advances from the North. C) Second deformation phase during the Saalian Drenthe ice-advance (MIS 6)

during which shallow, westward-dipping thrusts formed. D) Third deformation phase during the Saalian late Drenthe or Warthe 1 ice advance during which shallow east-west-trending tunnel valleys formed and during which the glaciotectonic complexes and previously incised tunnel are deformed.....9

Figure 1-4: Shot gathers and corresponding ray paths with a P-Wave velocity v_P profile increasing stepwise or continuously with depth z A) a conventional marine seismic survey with a hydrophone streamer and a source towed behind a ship and B) an ocean bottom recording survey with receivers deployed on the seafloor and a source towed behind a ship modified after Klein et al. (2005), Dondurur (2018) and Clementi et al. (2022).11

Figure 1-5: Notation of the possible reflection and transmission coefficients of incident P-Waves and S-Waves at interfaces between solid and fluid half-spaces modified after Aki & Richards (2002). As seawater is inviscid for seismic waves, only P-Wave phases occur in the fluid half-space.12

Figure 1-6: Visualization of optimization principles modified after Köhn (2011). A) Definition of the data residual Δd_1 of the initial subsurface model m_1 as the difference between the calculated seismic data $d_{cal}(m_1)$ and the observed seismic data d_{obs} . B) Minimization of the objective function in the parameter space of the P-Wave velocity v_P and S-Wave velocity v_S with gradient descent methods in which every iteration step updates the subsurface model until the final model m^* is reached. Ideally, m^* is equivalent to the global minimum of the objective function.....17

Figure 1-7: Addition of the low frequency trend to the band limited impedance to restore a full bandwidth impedance estimate modified from (Ferguson & Margrave, 1996). A) Spectrum and time series of the low frequency trend, e.g., resulting from velocity analysis or logging data. B) Spectrum and time series of the band-limited impedance. Both the high and low frequencies outside the frequency range of the wavelet are missing and the relative scaling factor λ of the band-limited impedance relative to the low frequency trend are unknown. In the time series the factor is already applied, but due to the band limitation, the impedance resembles a variation around zero. C) Restored impedance in which the low frequency trend has been added to the band-limited impedance. The missing high frequency are not restored leading to a limited resolution.20

Figure 1-8: Comparison of inversion results with qualitative interpretation for a boomer seismic reflection section from the Walney I wind farm site in the Eastern Irish Sea, taken and modified from Vardy et al. (2018) and Vardy (2020). A) Impedance inversion section retaining

the full details of the B) Post-stack seismic image. C) Ground model after geologic interpretation showing four distinctive units whose boundaries are indicated in (A) with red, stippled lines. D) Seismic data equivalent of the four layer model in (C) which resembles considerable information loss compared to the seismic image in (B).21

Figure 1-9: Workflow of pre-stack inversion taken from Simm & Bacon (2014), in which angle stacks are modelled and compared to the observed seismic data. Unless the misfit is below a stopping criterion, the model is updated to reduce the misfit. To stabilize the optimization process a number of constraints such as the Gardner relation of constant P-Wave to S-Wave velocity ratio can be introduced.22

Figure 1-10: Pre-stack inversion result achieved with simulated annealing from a commercial North Sea 3D seismic data set modified after Ma (2002) showing A) the real offset gather of a deep (approximately 2-2.8 km assuming $v_P = 2000$ m/s) seismic section with offsets exceeding 2 km; B) The corresponding reconstruction after the pre-stack inversion; C) The misfit or likewise the difference between (A) and (B); D) the shear impedance ($Z_S = v_S \cdot \rho$) result of the inversion as a black solid line in comparison to the initial model as a grey dotted line and the ground truth from logging data as a grey dashed line.23

Figure 2-1: Overview map of the data collected during research expedition He569, modified after Keil et al. (2021).30

Figure 2-2: Acquisition layout for the Profile He569-GeoB21-033 acquired during the research expedition He569 redrawn after Keil et al. (2021). The main elements of the acquisition system are two seismic sources including a Sercel micro-GI airgun and an Applied Acoustics Dura-Spark UHD 400 sparker, and a 96 channel single hydrophone streamer with variable channel spacing.32

Figure 2-3: Illustration of data spaces to visualize seismic data for processing and quality control purposes and the effect of important processing steps. A) Shot gather in which all channels for one shot of the seismic source sorted by source-receiver distance (offset d_{off}) or by channel number are displayed. Events such as the direct wave, or backscattered waves appear at the uncorrected Two-Way-Traveltime TWT . B) Constant offset gathers display the traces of one channel for a number of consecutive shots along the length of a profile dl . The seismic events appear at the uncorrected TWT . Dipping reflected and diffractions events appear not at the true position. C) Assuming that reflection originate from the midpoint between source-receiver pairs, all traces whose midpoints falls within a certain section of the profile are collected in Common Mid Point (CMP) gathers. When the Normal Move Out (NMO) is

corrected, reflection events from horizontal reflectors appear at the true subsurface position and are flattened using true average velocity. The NMO velocity of dipping events, in contrast, is not equivalent to the average velocity to the reflector and dipping reflectors are not positioned at the true subsurface location by NMO correction. The assumption that the midpoint is the reflection point is violated for dipping reflectors. Stacking describes the summation of all traces inside a CMP to determine the average trace. With post-stack migration, dipping reflectors are moved to their true subsurface position. D) With pre-stack migration, all traces within a certain distance also called aperture around a CMP are gathered and all backscattering events are corrected to their true subsurface position.35

Figure 2-4: Effect of the seismic data processing on the Profile He569-GeoB21-033 in terms of the suppression of the seafloor multiples, the enhancement of the reflections, suppression of noise and correction to the true subsurface position. To allow for a better comparison of the relative amplitudes, an Automatic Gain Control in a 200 ms window has been applied and then the seismic sections are scaled to the same amplitudes. For further details on the principles refer to Figure 2-3 and for further processing details refer to the main text (Section “2.1.3 Seismic Data Processing”). The panels from A-E reflect the enhancement of the seismic image with progress in the processing flow.....37

Figure 2-5: Synthetic seismogram generation with SOFI2D for a 250 Hz Ricker wavelet. A) Model parameters for the visco-elastic modelling defined by the P-Wave velocity v_p , the S-Wave velocity v_s , density, and attenuation quality factor Q . B) Synthetic seismogram calculated with the model parameters in (A). C) Annotated snapshot of the wavefield at approximately 95 ms. Damping model boundaries are implemented with a width of about 10 m. Thus, the source and the receivers are placed in a depth of 20 m and the model region is extended beyond the area of interest to avoid model edge artefacts.....38

Figure 2-6: Graphic representation of ravel time curve calculation methods taken from Duveneck (2004). A) The travel time for a plane reflector depending on the offset $h = off$ in a homogenous medium with P-Wave velocity v is exactly described by Equation 2-1. B) The travel time curve for a curved, dipping reflector in a smooth laterally inhomogeneous medium with the P-Wave velocity $v(x, z)$ is described by Equation 2-3.40

Figure 2-7: Illustration of the equivalent one-way raypath in a stack of laterally homogenous layers for a P-P reflection at the location of the dashed line taken from Margrave & Lamoureux (2019). A) Source-Receiver raypath for a P-P reflection. B) Equivalent one-way raypath to the two-way raypath shown in (A).41

- Figure 2-8: Optimization procedure for the travel time curve inversion. As a starting point, a number of random velocity v and depth z models is initiated. Then synthetic travel time curves are calculated for every individual in the population of models and compared to the picked travel time curves. Based on the error, the individuals are optimized with a differential evolution scheme and a new generation of synthetic travel time curves is calculated. This procedure continues until a stopping criterion is reached. The final model is determined from the population of optimized models.42
- Figure 2-9: Optimization procedure for the impedance inversion. Every stacked trace of each CMP is inverted independently. As a starting point, a number of random reflectivity models is initiated. Then synthetic data is calculated for every individual in the population of models and compared to stacked data. Based on the error, the individuals are optimized with a stochastic remainder scheme. This procedure continues until a stopping criterion is reached. The final model is determined from the population of optimized models and the impedance is calculated from the reflectivity.46
- Figure 2-10: Matrix operation representation of a stationary and non-stationary convolution with a NMO stretch operator modified after Downton and Lines (2004) and Claerbout (2010). A) For a stationary convolution, the column vector of the reflectivity r_{PP} with the length of N_{TWT} time samples is multiplied with the convolution matrix of the size N_{TWT} by N_{TWT} to model the seismic trace column vector d of the length N_{TWT} . B) To approximate the seismic trace with the effect of NMO stretch d' , r_{PP} is multiplied with the convolution matrix W' which includes the stretch. The calculation of the matrix W' is based on the NMO interpolation matrix N of the size N_{TWT} by N_{TWT} . This matrix contains all zeros except for the trajectory of the NMO hyperbola being ones. The matrix for the inverse NMO correction is the transpose N^T . The non-stationary convolution matrix is calculated by the matrix multiplication of $N * W * N^T$49
- Figure 3-1: Initial model for the traveltime curve inversion experiments. A) Hyperbolic traveltime curves of the Two-Way-Traveltime (TWT) plotted on an offset axis. B) Ground model including six horizontal layers of 10 m thickness of stepwise increasing velocity.60
- Figure 3-2: Characteristics of a Sercel micro-GI airgun with a volume of 2 x 0.1 L towed in approximately 1.0 m depth in terms of A) the signal shape in the time domain on the left side and normalized frequency spectrum on the right side. B) Peak Sound Pressure Levels (SPL_{peak}) of the Sercel micro-GI and mini-GI airguns depending on the air pressure supplied to the sources. The values for the Mini-GI airgun with 2 x 0.454 L volume, mini-GI airgun with

- reducers limiting the volume to 2×0.227 L and the array of two mini-GI airguns with a total volume of $2 \times (2 \times 0.454)$ L are taken from Crocker & Fratantonio (2016) and Crocker et al. The SPL_{peak} of the micro-GI airgun with a volume of 2×0.1 L has been measured during the research expedition AL581.63
- Figure 3-3: Source characteristics of an Applied Acoustics (AA) Dura-Spark UHD 400 with the tip banks at 0.2 m depth. A) Signal shape in the time domain on the left and the normalized frequency spectrum on the right depending on the supplied electric energy. B) Peak Sound Pressure Level SPL_{peak} as a function of the supplied electric energy. C) Sparker signals characteristics exemplified for two different depths of the tip banks.65
- Figure 3-4: Comparison of the directivity of the Sercel micro-GI airgun and the Applied Acoustics Dura-Spark UHD 400 (AADS400). A, D) Schematic drawing of the sources towed behind a vessel (not to scale) including a normalized angle gathers of the emitted wavelets. B, E) Normalized frequency spectra of the wavelets shown above sharing the colour code. C, F) Measurements of the directional strength of the sources corrected for spherical divergence.66
- Figure 3-5: Wavelets of the Sercel micro-GI airgun and the Applied Acoustics Dura-Spark UHD 400 sparker extracted of the seafloor reflection of Profile He569-GeoB21-033. A) Time series of the wavelets. B) Normalized frequency spectra.67
- Figure 3-6: Schematic illustration of relevant acquisition parameters for near surface seismic inversion and the impact of the acquisition efforts on the velocity estimation accuracy. A) Acquisition setting for near surface seismics with a seismic source depicted as a micro-GI airgun in this case and a streamer towed behind a vessel. The references in the illustration link to figures in which the parameter is discussed. B) Impact of acquisition parameters and efforts on the traveltimes curve inversion accuracy.68
- Figure 3-7: Analysis of the range of possible Amplitude Versus Angle (AVA) curves of reflected P-waves. A) Expected range of AVA curves calculated with the Zoeppritz equation for all possible interfaces between sediments of Soil Behaviour Type 3-7 taken from Table 3-1. B) Comparison of AVA simplifications to the Zoeppritz equation using the Pearson's Correlation Coefficient and the Root Mean Square (RMS) error. The simplifications are only valid to a certain maximum incidence angle according to their definition (Chopra & Castagna, 2014). Accordingly, grey numbers in the table indicate, that the simplification is invalid for the incidence angle range in the row of the table according to the literature. The coloured boxes show whether the correlation coefficient and the RMS error indicate to be valid for the soil type tested.70

- Figure 3-8: Comparison of wave spreading and acquisition effects on the seismic amplitude. A) The ground model for this example includes two sand bodies of 10 m thickness separated by a 10 m thick clay layer at 20 m water depth. Three interfaces (water-sand: blue; sand-clay: orange; clay-sand: green) are investigated. The sediment properties in terms of P-Wave velocity v_p , S-Wave velocity v_s , density ρ , and attenuation quality factor Q are taken from Table 3-1. B) Comparison of the different effects on the seismic amplitude. The Amplitude Versus Angle (AVA) effect can be used to deduct shear properties. This effect is masked by a range of acquisition and wave spreading effects, e.g., the geometric spreading of the seismic wave, which is modelled by spherical spreading here. For the attenuation it assumed, that Q is constant for the frequency range of interest. Nevertheless, the attenuation effect is depending on the source signal, so a sparker source is attenuated twice as much compared to the micro-GI. The directivity functions of the sources are generated from the measurements shown in Figure 3-4. The use of receiver groups and the receiver ghost introduce additional effects.77
- Figure 3-9: Summary of the requirements and boundary conditions for near surface reflection seismic inversion for target depths of up to 80-100 m. The classification of the sources follows ISO 19901-10 (2021) High Resolution (HR, 75-300 Hz), Ultra-High-Resolution (UHR, 250-800 Hz) and Ultra-Ultra-High-Resolution (UUHR, 750-2000 Hz)84
- Figure 4-1: Sketch of the possible discrepancy of the interpretation based on one-dimensional information to actual, complex and small scale features, modified and extended from Henson and Sexton (1991). If dipping or folded strata or small-scale features such as channels are encountered in the subsurface, adjacent boreholes will show low correlation.88
- Figure 4-2: Time domain (top row) and frequency domain (bottom row) representation of the convolutional model of a seismic trace. In a vertical incidence scenario without attenuation and geometric spreading, impedance contrasts define the reflectivity of interfaces, and a seismic trace can be modelled by the convolution of the reflection time series with the time series of the wavelet. In the frequency domain, this convolution is represented by the multiplication of the spectra.89
- Figure 4-3: Methodological flow chart to derive quantitative ground models with near surface seismic inversion and Cone Penetration Test (CPT) data. Seismic data is acquired, processed, and inverted as time series data, while CPTs are recorded in depth. After CPT and seismic results are brought together in a joint interpretation step, the seismic results can be converted to depth. The depth converted results can further be used for the generation of ground models.94

- Figure 4-4: A) Traveltime curves of four reflection events and B) corresponding inversion results for CMP 492 of the Profile He569-GeoB21-033 which is adjacent to the location of CPT 3. The uncertainty is quantified by the standard error of the mean (dashed lines in B).97
- Figure 4-5: Exemplary bandlimited impedance inversion of CMP492 adjacent to CPT 3. A) Comparison of the seismic amplitudes of the original trace and the inversion result with a correlation coefficient (Pearson's R) of 0.96. For the example shown here, the attenuation has not been corrected. The results of the inversion are the (B) inverted reflectivity and the (C) bandlimited inverted acoustic impedance.....99
- Figure 4-6: Example of the raw CPT data cleaning process. Measured cone resistance (q_c), sleeve friction (f_s) and pore pressure (u_2) from CPT 2. The blue curves show the raw values, and the dashed orange line indicates de cleaned curves.....103
- Figure 4-7: Reflection seismic image He569-GeoB21-033 and the corresponding interpretation. A) Location map of the profile in the German North Sea in the north of the island Heligoland. The profile is approximately west-east oriented and 9.0 km long. B) Seismic image in the form of a migrated angle stack with an angle range of 0-30°, which is the basis for the inversion. C) Interpreted seismic image with four main Units U1-U4, which are bounded by the seafloor (SF) at about 40 ms and the Horizons H1-H3. Horizons H2 and H3 show a prominent, U-shaped erosional feature around profile distance 7 km. Remnants of the seafloor multiple are visible around 80 ms, while a peg-leg multiple following H2 at 40 ms distance is observed between 110-140 ms. The tip resistance q_t of the Cone Penetration Test (CPT) is overlain on the seismic image using a brute processing velocity model for the time-depth conversion.106
- Figure 4-8: Cross-plot of the sediment density and P-Wave Velocity taken from McCann & McCann (1969), Shumway (1960), Hamilton (1970, 1972), Breitzke et al. (2000), Stevenson et al. (2002), Robb et al. (2006) and the BSH Pinta Data Base (2021) for the wind parks N0307, N0308 and O0103 with an overlay of the empiric density to P-Wave velocity relationship by Raymer et al. (1980) whose parameters are given in Table 4-4108
- Figure 4-9: Low frequency model derived from the travel time curve inversion. A) Upper part of the interpreted seismic image of He569-GeoB21-033 matching to Figure 4-7. The tip resistance q_c of the Cone Penetration Test (CPT) measurements is overlain using a brute processing velocity model for the time-depth conversion. B) Low frequency impedance model derived from the interval velocity estimation and impedance transformation. The impedances shown are typical for sandy deposits. Highest impedances are found in U3 and U2.....109

Figure 4-10: Attenuation Quality Factor Q estimation at CPT 3 for an averaged section of 0.2 km from profile length 5.2-5.4 km (CMP 480-500 with a spacing of 10 m). A) Normalized frequency spectra of the averaged autocorrelations showing a clear shift to lower frequencies for the Horizons H2 and H1 compared to the seafloor reflection. B) Probability Density Function (PDF) of the average Q -Factor estimation indicating values around 40 for H2 and 95 for H1. C) Average and interval Q estimates with an uncertainty estimation (68.3% confidence intervals). Low Q values corresponding to high attenuation are observed for the Unit U4 and U3 between SF and H2. Moderately high Q values are observed for U2 between H2 and H1. The range of errors, especially for the upper limit of the uncertainty is larger than the mean value.110

Figure 4-11: Average and interval attenuation Quality Factor Q estimation for the Profile He569-GeoB21-033, see Figure 4-7 for a location map and uninterpreted seismic image. A) Average Q -values at the Horizons H2 and H1. H3 is indicated by a stiped line as this horizon has not been included for the attenuation estimation. The autocorrelations of 20 CMPs in intervals of 10 CMPs have been averaged to determine the average Q . B) Boxplots of the interval Q estimates for the Units U2 and U3+4 inverted from the average Q values in (A). Assuming that the Q -values in the units are constant, those boxplots can be used to determine the layer properties and to build an attenuation model. Interval Q -values above 300 are excluded from the boxplots and plotted as red crosses, as such high Q -values are outside the range of possible values.111

Figure 4-12: Uncertainty estimation of the absolute impedance based on 1000 repetitive inversion runs of the inversion work flow (Figure 4-3) at CPT 3 (CMP 492) using probability density functions of the attenuation Quality Factor Q and the interval velocity as input. The density is derived from the interval velocity based on the transformation curve shown in Figure 4-8. The Q -Factor is used to scale the post-stack seismic trace before the bandlimited impedance inversion. The probability density function of the seismic amplitude shows the occurrence of the modelled seismic traces after inversion. The band limited impedance is not properly scaled, the low frequency trend is wrongly estimated and there is a strongly increasing uncertainty with depth. After the merging and scaling of the inversion results, an absolute impedance estimation is reached.113

Figure 4-13: Time domain inversion results for the profile He569-GeoB21-033. A) Interpreted seismic image as shown in Figure 4-7. The tip resistance q_t of the Cone Penetration Test (CPT) measurements is overlain using a brute processing velocity model for the time-depth

conversion. B) Impedance inversion result in which the band limited impedance has been merged with the low frequency trend with a 10 Hz Linkwitz-Riley Filter.....115

Figure 4-14: Horizon depths and depth uncertainty estimate. For the depth conversion the fix points listed in Table 4-5 are used. The uncertainty of the depth estimate is determined by the seismic resolution, the depth conversion fit and an estimated velocity error for intervals without depth fix points. The maximum uncertainty of the interval velocity estimate is 25 m/s (see “Low Frequency Model by Traveltime Curve Inversion and Density Estimation”) and thus a maximum error of 2% is assumed.117

Figure 4-15: Comparison of (A) the absolute impedance Z_p estimation and (B) the tip resistance q_t of the Cone Penetration Testing for location CPT 3. The band limited impedance has been merged with the low frequency trend at a characteristic frequency $f_c = 10$ Hz. Although there is more high frequent variation observed on q_t , the general pattern match with a moderately high correlation of 0.69 (Pearson’s correlation coefficient). Especially the low impedance layer below 70 m matches very well to low tip resistance.....118

Figure 4-16: Depth converted seismic image and inversion result. A) Interpreted seismic image corrected for attenuation and converted to depth, see Figure 4-7 for location map and seismic time image. The tip resistance q_c of the Cone Penetration Test (CPT) measurements is overlain. B) Smoothed impedance inversion section generated with a 40 Hz Linkwitz-Riley Filter to merge the band limited impedance with the low frequency trend. Small scale impedance anomalies are more easily interpreted in this smoother impedance section, while the impedances rise more steeply directly below the seafloor compared to Figure 4-13.122

Figure 4-17: Detail of the seismic image and the inversion results. The tip resistance q_c and the normalized Soil Behaviour Type SBT_n of the Cone Penetration Test at location 1 (CPT 1) are overlain. A) Interpreted seismic image corrected for attenuation and converted to depth, see Figure 4-16 for full scale image and location overview. The determined attenuation quality factor Q with the corresponding lithological interpretation is shown for the units on the right side of the plot. Important features such as small scale channel incisions and the peat and clay layer are highlighted. B) Smooth impedance inversion result in which the band limited impedance has been merged with the low frequency trend with a 40 Hz Linkwitz-Riley Filter. C) Classification of SBT based on the impedance shown based on limits taken from Chapter 3 which are built on the sediment properties data sets listed in “4.2 Low Frequency Model” and shown in the legend. Overall a very good match of the CPT SBT_n and the SBT from the impedance can be reached. The small SBT_n at H3 of CPT 1 does not have a direct equivalent

- in the seismics. But there generally are channel incisions with low SBT observed at H3 and the CPT is located at 20 m distance to the seismic line.....124
- Figure 5-1: S-Wave velocity prediction based on P-Wave velocities as suggested by Lee (2006) for the BSH Pinta Data Base (2021) PS-Logging data of the wind farm sites N0307, N0308 and O0103.....136
- Figure 5-2: Super gather around CMP 492 of the Profile He569-GeoB21-033. Four strong and consistent reflection events have been picked and the picks are superimposed as black dots. Spherical divergence correction has been applied.137
- Figure 5-3: Impedance inversion to generate a starting model for the pre-stack inversion. A) Angle stack in the range 10-30° showing a pronounced seafloor reflection and two events with a higher amplitude. B) Low frequency impedance model (blue line) and impedance inversion result (orange line). Below the seafloor a gradient zone followed by two negative impedance steps is observed. A further and pronounced negative impedance step is found at 90 ms. 139
- Figure 5-4: Pre-stack inversion on synthetic data. The upper panels of (A)-(D) show angle stacks in the range 10°-40° in 5° steps which are scaled to the same amplitude, while the lower panels of (A)-(D) show the corresponding compressional impedance Z_P as well as the shear impedance Z_S models. A) True model of the synthetic test. The time interval which is used for the sensitivity analysis shown in Figure 5-5 is indicated by a grey bar. B) Initial Model for the inversion, which is the true model in (A) filtered with a 6.25 ms long running median filter. C) Inverted model after 375 iterations. The true impedances are underlying the inverted impedances and are displayed as black lines. D) Optimization progress showing the decreasing L_2 -norm with increasing number of iterations. The subordinate plot shows a zoom on the iterations 100-375.....140
- Figure 5-5: Sensitivity analysis of the pre-stack inversion regarding the model parameters P-Wave velocity, S-Wave velocity, and density relative to the true model of the synthetic inversion test (Figure 5-4). To test the impact of the change of a single parameter, the remaining parameters are fixe to the true model and the parameters in a 2 ms interval were changed as shown in the upper panels. The change of the L_2 -norm in respect to the true model is displayed in the lower panels. A) P-Wave velocity sensitivity showing a steep L_2 -norm increase for both higher and lower velocities. B) S-Wave velocity sensitivity showing a steep L_2 -norm increase for higher velocities. C) Density sensitivity showing a steep L_2 -norm increase for both higher and lower densities.....141

- Figure 5-6: Pre-stack inversion of the angle stack at CMP 492 of Profile He569-GeoB21-033. In (A) and the upper panels of (B) and (C) angle stacks scaled to the same amplitude are displayed, while the lower panels in (B) and (C) show the corresponding shear impedance Z_S and compressional impedance Z_P models. A) Observed angle stacks. B) Initial model derived from the post-stack impedance inversion (equivalent to Figure 5-4B). C) Inverted model after 375 iterations. The impedance models after pre-stack inversion generally resemble the post-stack impedance based estimates, although more dynamic variation is observed on the pre-stack inversion results.142
- Figure 5-7: Comparison of the Cone Penetration Testing (CPT) and pre-stack inversion results in respect to the Soil Behaviour Type (SBT) and S-Wave velocity v_S . At about 60 m depth, the remnant of the multiple after the multiple suppression is to be observed. A) Section of the attenuation corrected, and depth converted Profile He569-GeoB21-033 taken from Chapter 4 with an overlay of the inversion and CPT result at the well location. B) Crossplot of v_S derived by the CPT measurements and the pre-stack inversion. The outliers marked with a red oval correspond to the high v_S values of the CPT measurements at the bottom of the well in (A), which are also marked with a red oval.143
- Figure 6-1: Map of the study area (red outline in inset) in the southern Arkona Basin showing the 2D seismic reflection profiles that were inverted in this study and sites with sediment descriptions, velocity logs and Cone Penetration Test (CPT) data. The sites are shown as dots (black dots represent sites located on the inverted seismic profiles; red dot indicates an additional site utilized in Ogunleye et al., in prep., 2024a and 2024b). The name of each site is the number shown in the figure (numbers follow the order introduced in Ogunleye et al., in prep., 2024a) followed by BH/CPT at the locations with CPT data; Site 1 has no CPT data, so its name is 1 BH. 1 BH and 2, 3, 4, 6 and 11 BH/CPT have velocity logs which were utilized in Ogunleye et al., in prep., 2024b for estimating median physical properties of geological units. Pre-Quaternary faults of the Tornquist Zone are depicted (Obst et al., 2017). EMODnet Bathymetry Consortium (2020) is the basis of the water depth values. Map coordinates are in UTM 33N (Modified from Ogunleye et al., in prep., 2024a).151
- Figure 6-2: Workflow of the band-limited acoustic impedance inversion approach in which a band-limited impedance result is merged with a layer cake low-frequency Z_P model.153
- Figure 6-3: 2D seismic Profile AL402-GeoB12-167 tied to the lithologic logs at Sites 7 and 12 BH/CPT (see Figure 6-1 for location): a) Interpreted seismic amplitude section showing the major near-surface seismic units and their lithologic characterization in our study area based on the work presented in Ogunleye et al. (in prep., 2024a); b) Un-interpreted absolute acoustic

impedance section of the profile generated with the velocity-guided inversion approach; c) Interpreted version of the impedance section in (b) which has been correlated with sediment descriptions. Notice how impedance anomalies indicate the lateral extent and vertical stacking of stratigraphic units. Two Pleistocene valleys are depicted as cutting into the Cretaceous chalk. Stippled red lines delineate a lenticular zone with relatively low impedance values in a valley fill. TWT = Two-Way Travel-time; SU = Seismic Unit (vertical exaggeration was calculated based on a velocity of 2000 m/s)155

Figure 6-4: 2D seismic Profile AL402-GeoB12-168 tied to the lithologic logs at Sites 6 and 11 BH/CPT (see Figure 6-1 for location): a) Un-interpreted seismic amplitude section along the profile; b) Un-interpreted absolute acoustic impedance section generated from data shown in (a) with the velocity-guided inversion approach; c) Interpreted version of the impedance section in (b) showing the spatial distribution of lithologic units, an intra-till property boundary, and the structural features of geological intervals. TWT = Two-Way Travel-time; SU = Seismic Unit (vertical exaggeration was calculated based on a velocity of 2000 m/s).157

Figure 6-5: 2D seismic Profile AL402-GeoB12-167 tied to the lithologic log at Site 12 BH/CPT: a) Seismic amplitude section of the profile showing the horizons independently picked along the same unit boundaries that were interpreted in Ogunleye et al. (in prep., 2024a). These horizons formed the stratigraphic framework of an initial low-frequency impedance model employed in the band-limited approach; b) Un-interpreted absolute impedance section of the profile generated with the band-limited inversion approach. It corresponds to a part of Figure 6-3; c) Interpreted version of the seismic data in (b) correlated with sediment descriptions. The stippled red line is the top of the high-impedance interval within the uppermost subunit filling Valley 1. This high-impedance zone is characterized by anomalous lithologic and geotechnical properties within the valley. Notice how impedance anomalies show the detailed spatial distribution of lithologic units, thereby allowing improvements on the initial horizon interpretation shown in (a). Artifacts occur as vertical stripes on this impedance section. TWT = Two-Way Travel-time; SU = Seismic Unit (vertical exaggeration was calculated based on a velocity of 2000 m/s).....160

Figure 6-6: Raw data plot of the CPT measurements of sleeve friction and cone resistance and the impedance inversion results at Site 12 BH/CPT. Seismic Units SU4, SU3 and SU2 are shown with blue, purple and light brown backgrounds, respectively. Please note that the band-limited impedance is shifted upward by 1.07 m (the rationale for this decision is given in fig. 5.9).161

- Figure 6-7: Cross plots of measured cone resistance and predicted impedance at Site 12 BH/CPT with a correlation coefficient of 0.27 for the velocity-guided results and 0.82 for the band-limited results. The colour code of the seismic units follows the code in Figure 6-6.....161
- Figure 6-8: Cross plots of measured sleeve friction and predicted impedance at Site 12 BH/CPT with a correlation coefficient of 0.40 for the velocity-guided results and 0.90 for the band-limited results. The colour code of the seismic units follows the code in fig. Figure 6-6. ...162
- Figure 6-9: Correlation coefficient of measured cone resistance and predicted impedance as a function of constant depth shift at Site 12 BH/CPT.162

List of Tables

Table 1-1: Examples of offshore structures updated from Richards et al. (1975) including information taken from Lesny et al. (2014), Nikitas et al. (2020), Owen (2020) and Amaechi et al. (2022). Items marked in red are elements of offshore wind energy generation systems.	4
Table 2-1: Seismic Data Acquisition Parameters of He569-GeoB21-033.	31
Table 3-1: Geophysical parameters in comparison to the Cone Penetration Testing (CPT) Soil Behaviour Types (SBT) for the near surface sediments of the North Sea and Baltic Sea derived from (1) Robertson (2009) and Robertson & Cabal (2015); (2) BSH Pinta Database (2021) for N0307, N0308, O0103 or likewise (*) Breitzke (1997); (3) Biot-Stoll Modelling (Hovem et al., 1991; Badiey et al., 1998; Dvorkin et al., 1999; Breitzke, 2006; Carcione & Picotti, 2006); (4) Pinson et al. (2008).	62
Table 3-2: Minimum parameter accuracy necessary for inversion to differentiate the expected Soil Behaviour Types (SBT) 3-7 given in Table 3-1. As SBT 1-2 and SBT 8-9 are characterized by comparatively larger contrasts, the accuracy restrictions to differentiate those SBTs are less strict.	72
Table 3-3: Estimation of the vertical resolution in time T_{res} and depth D_{res} and the lateral resolution after migration which is equal to the dominant wavelength λ_D . Estimates are based on Kallweit and Wood (1982) as described in the appendix “C.2 Biot-Stoll Modelling” and given for a lower boundary with a high P-Wave velocity $v_P = 1800$ m/s and a upper boundary with $v_P = 1500$ m/s. Peak f_C and predominant f_D frequencies are reported. The classification of the sources follows ISO 19901-10 (2021) High Resolution (HR, 75-300 Hz), Ultra-High-Resolution (UHR, 250-800 Hz) and Ultra-Ultra-High-Resolution (UUHR, 750-2000 Hz).	74
Table 4-1: Seismic Data Acquisition Parameters of He569-GeoB21-033.	95
Table 4-2: Parametrisation of the genetic algorithm for impedance inversion. For the uncertainty estimate 1000 repetitions with the given parameters were executed.	100
Table 4-3: General acquisition information from the used in-situ testing CPT and borehole sampling data. The water depth is referred to the echosounder depth reduced to the Lowest Astronomical Tide (LAT). The distance to profile was measured in a straight line, orthogonal to the location of the seismic Profile He569-GeoB21-033.	102

Table 4-4: Parameters for the empiric velocity-density relation by Raymer et al. (1980). The parameters were manually optimized to fit to the properties of near surface sediments taken from McCann & McCann (1969), Shumway (1960), Hamilton (1970, 1972), Breitzke (2000), Stevenson et al. (2002), Robb et al. (2006) and the BSH Pinta Data Base (2021) for the wind farms N0307, N0308 and O0103.	107
Table 4-5: Calibration points for depth conversion. The thick, dominant clay layer at the Cone Penetration Test locations and the low impedance layer below Horizon H2 are correlated for depth conversion.....	116
Table 5-1: Estimates from velocity and attenuation estimation.	138
Table 6-1: Impedance inversion parameters for genetic algorithm and merging of band limited impedance with low-frequency model in a layer cake approach.	154
Table 6-2: Measured and predicted statistical estimates of acoustic impedance Z_P for each seismic unit. The ground truth (measured) values are based on a compilation of velocity logs as shown in chapter 4, while the velocity-guided and band-limited values are based on the impedance predicted in each seismic unit along the entire section of Profile AL402-GeoB12-167. The velocity-guided and band-limited values for each seismic unit are calculated by summing the products of mean impedance and sample size at each trace location and dividing this sum by the total number of samples for all the locations. The unit of the statistical measures is (m/s)*(g/cc). The estimated mean values are grand means. Min. = Minimum Value; Max. = Maximum Value; SU = Seismic Unit	159

Appendix

A Abbreviations and Nomenclature

AVA	Amplitude Versus Angle
AVO	Amplitude Versus Offset
CMP	Common Mid Point
CPT	Cone Penetration Testing
CRS	Common Reflection Surface
FFT	Fast Fourier Transform
FWI	Full Waveform Inversion
FWT	Full Waveform Tomography
mbsf	Meter Below Seafloor
MIS	Marine Isotope Stage
MTU	Working Group MeeresTechnik / Umweltforschung (Marine Technology / Environmental Research) at the University of Bremen
NMO	Normal Move Out
RMS	Root Mean Square
RWI	Reflection Waveform Inversion
SNR	Signal to Noise Ratio
SynCore	Synthetic Coring
TWT	Two-Way Traveltime
TRL	Technology Readiness Level

Table A-1: Nomenclature as an alphabetical list.

α	Dip angle of a seismic horizon
A_{loss}	Loss function (amplitude spectrum) due to intrinsic, anelastic attenuation
A_{refl}	Amplitude spectrum at a reference reflector, obtained from autocorrelation
A_{sf}	Amplitude spectrum at the seafloor, obtained from autocorrelation
Dr	CPT relative density
d	Seismic response of the Earth, seismic data
d_{obs}	Recorded seismic data
$d_{cal}(m)$	Modelled seismic data with elastic model m
$\Delta d = d_{cal}(m) - d_{obs}$	Data-misfit vector
$F(m)$	Non-linear functional to generate seismic data from an elastic model
Fr	CPT friction ratio
f	Frequency vector, e.g., of an amplitude spectrum
fs	CPT sleeve friction
$g(TWT_0, off = 0 m)$	Offset dependent geometrical spreading correction function
h_{off}	Half-Offset, half of the source receiver distance
h_{md}	Trace-midpoint displacement, distance of trace to image point
μ	Step length for the steepest descent optimization
m	Elastic earth model defined by v_s, v_p and ρ
m^*	Elastic model with minimum misfit function
m_n	Elastic model in optimization step n
$m_{n,p}$	Elastic model in optimization step n , perturbed at a certain TWT
ν_{PR}	Poisson's Ratio
off	Offset, Source-Receiver distance
$PDF(Q)$	Probability Density Function of Quality Factor Q
p_μ	Step length factor
p_G	Damping constant for attenuation correction
ρ	Density
Q	Quality Factor, measure of intrinsic, anelastic attenuation of a P-Wave
Q_{ave}	Average Quality Factor estimated or calculated
Q_i	Interval Quality Factor, characteristic value within a certain unit or layer
Qt	CPT normalized cone resistance
qc	CPT cone resistance
qt	CPT corrected cone resistance
$r_{pp}(\theta)$	Angle dependent reflection coefficient from a down-going to an up-going pressure wave
R	Receivers
SBT	CPT soil behaviour type
$SBTn$	CPT normalize soil behaviour type
S_d	Misfit function
$S_d(m^*)$	Solution of the inverse problem; Minimum of the misfit function with optimized elastic model
ΔS_d	Gradient of the misfit function
θ	Incidence angle measured from the vertical
TWT	Two Way Traveltime
$TWT_0 = TWT(off = 0)$	Vertical Two Way Traveltime
TWT_{CRS}	Two Way Traveltime calculated with Common Reflection Surface method
TWT_{sf}	Two Way Traveltime to the seafloor reflection
TWT_{horz}	Two Way Traveltime to a specific reflector
u_2	CPT pore pressure
v_0	Pressure wave velocity at the surface layer, water column velocity
v_i	Interval velocity, characteristic value within a certain unit or layer
v_{NMO}	Pressure wave velocity for optimum Normal Move Out Correction
v_p	P-Wave (primary, pressure wave) velocity

v_{RMS}	Root Mean Square velocity
v_s	S-Wave (Secondary, shear wave) velocity
w	Wavelet, seismic source signature
Z_p	P-Wave impedance
z	Depth

B Additional Manuscript: Is it too loud? Approximations for Underwater Noise Impact Assessments and Reporting for Near Surface Seismic Campaigns

Nikolas Römer-Stange¹, Maximilian Merl¹, Hanno Keil¹, Volkhard Spieß¹

¹Department of Geosciences, University of Bremen, Klagenfurter Str. 2-4, D-28359 Bremen, Germany

In preparation for SoftwareX or First Break. Format and references have been adopted to match the thesis.

Keywords

Underwater Noise; Near Surface Seismics; Modelling; Seismic Data Acquisition; Environmental Impact Assessment

Abstract

Marine seismic acquisition campaigns using high energy sound sources are a potential threat to marine animals. Consequently, it became mandatory for acquisition campaigns to conduct impact assessments and to report on the emitted sound. Nevertheless, there is no established workflow or software package for those tasks. Building on continued discussions on the usage of appropriate sound exposure metrics and the definition of general limits for the onset of physiological and behavioural effects, a basis and a workflow for underwater noise impact assessments in the North and Baltic Sea is established for near surface and high resolution seismics. For the example of a Sercel micro GI airgun and harbour porpoises belonging to the functional hearing group of very high frequency cetaceans, the data sets necessary and the basis for the reports are shown. The auditory weighting and especially the geometric spreading function have been found to have the greatest influence on the extent of the safety distances to avoid negative impacts. Most importantly, no strong behavioural effects are to be expected at distances greater than 260 m for the chosen example. Consequently, the impact of high resolution seismic surveys on marine animals in the North and Baltic Sea is comparatively small.

B.1 Introduction

Human action such as the emission of underwater noise has the potential to severely impact the marine environment (Green et al., 1994; Schack et al., 2019; Southall et al., 2007, 2019). Consequently, there is a moral obligation for the planning of seismic acquisition campaigns to include an assessment of environmental impacts to avoid and mitigate negative effects on the marine flora and fauna. This requisite is also documented in international laws e.g. in the Commission Decision (EU) 2017/848 of 17 May 2017 (European Commission, 2017). It has also been fixed in this law, that underwater noise registries like the MarineEars system in Germany (marineears.bsh.de) have to be established. Such registries are gaining additional importance due to the increasing noise exposure in coastal waters, e.g., due to the development of offshore wind farms. For seismic surveys, Best Available Technique and Best Environmental Practices are documented in IAU (2001) and OSPAR (2016).

Noise assessments are based on the calculation of different metrics for a range possible negative impacts. Those types of impacts include permanent hearing damage (Permanent Threshold Shift: PTS), temporary hearing damage (Temporary Threshold Shift: TTS) and potential behavioral or physiological response with decreasing severity as shown in Figure A-1. To find quantitative limits for PTS and TTS, dual exposure metrics are determined for impulsive noise (Southall et al., 2007, 2019). On the one hand, the unweighted peak sound pressure level $[SPL_{uw,peak}] = 1 \text{ dB (re } 1 \mu\text{Pa)}$ is considered. On the other hand, the weighted and cumulative sound exposure level $[SEL_{w,cum}] = 1 \text{ dB (re } 1 \mu\text{Pa}^2\text{s)}$ has to be taken into account. The onset limit of possible negative impacts for PTS and TTS is either SEL or SPL, whichever is more restrictive. The weighted Root-Mean-Square SPL $[SPL_{rms}] = 1 \text{ dB (re } 1 \mu\text{Pa)}$ with an averaging time of 125 ms can be used for the determination of the onset of potential behavioral response as suggested by Tougaard (2014; 2015; 2016).

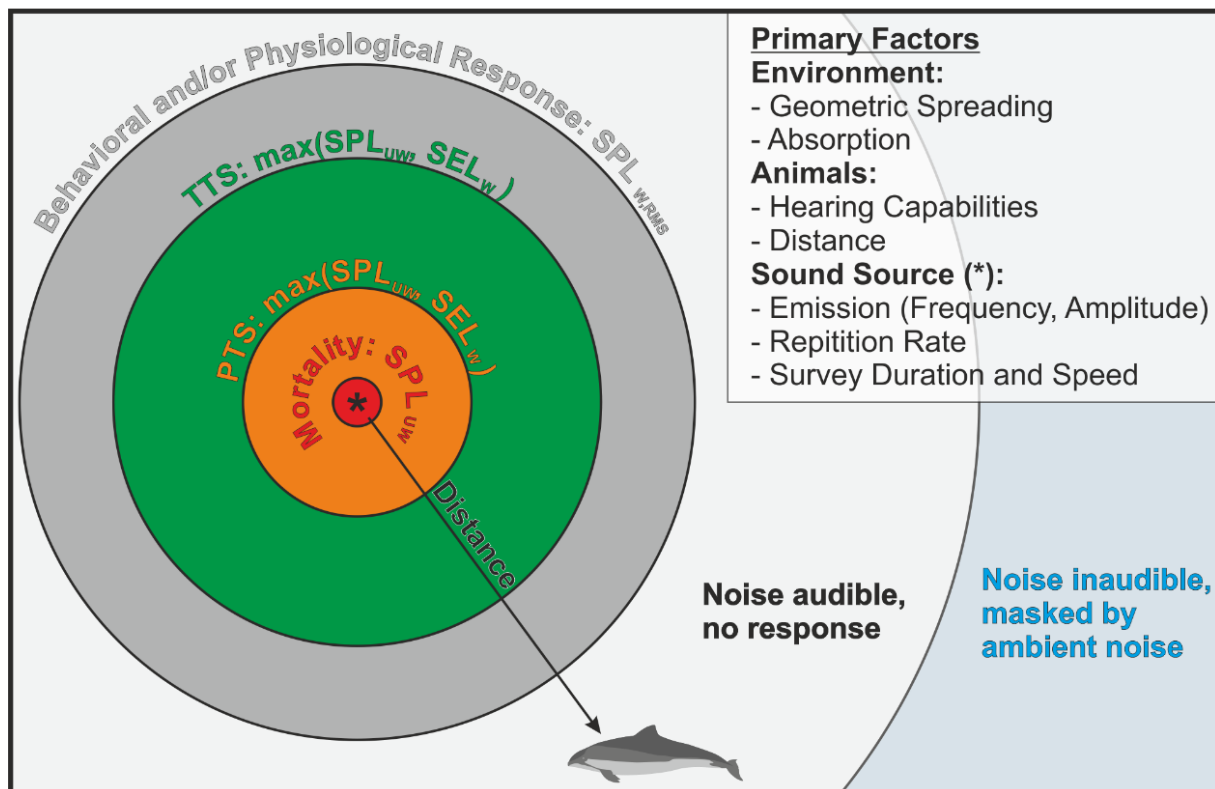


Figure A-1: Impact of noise emissions relative to the distance to the noise source adopted from Dooling and Therrien (2012). The estimation of the onset limit of possible negative effects is defined by three different metrics, which are primarily depending on the distance of an animal to the sound source, environmental, animal specific and sound source specific factors given in the upper right corner. Mortality is to be expected exceeding certain unweighted Sound Pressure Levels (SPL_{UW}). Permanent Threshold Shift (PTS) or Temporary Threshold Shift (TTS) are likely to occur above certain SPL_{UW} or weighted Sound Exposure Levels (SEL_w) as shown in Southall et al. (2007, 2019). Behavioral or likewise physiological responses have been found to be linked to the weighted Root Mean Square SPL ($SPL_{W,RMS}$) with an averaging time of 125 ms as suggested by Tougaard (2014; 2015; 2016). The weights for both SPL and SEL are Auditory Weighting Functions as defined in Southall et al. (2007, 2019).

For the North and Baltic Sea, harbor porpoises (*Phocoena phocoena*) serve as an important case study for impact assessments. Harbor Porpoises have been identified by Schack et al. (2019) as a priority noise sensitive species due to their high hearing sensitivity, the potential impact of noise on this species and their vulnerable/critically endangered status. Also, the data availability is relatively good. Following the standard approach given in Southall et al. (2007, 2019) harbor porpoises are classified to belong to the functional hearing group of Very High Frequency cetaceans (VHF) and the limits of PTS and TTS are defined accordingly and given in Table A-2. There is only very limited literature data on the onset of behavioral impacts for VHF. After consultation Jakob Tougaard (pers. communication) a limit of $SPL_{W,RMS}(125\text{ ms}) = 100\text{ dB}$ (re 1 μ Pa) for behavioral change of VHF is considered and reported in Table A-2. Nevertheless, recent experiments with harbor porpoises (Kastelein, Helder-Hoek, & Van de Voorde, 2017; Kastelein, Helder-Hoek, Van de Voorde, et al., 2017; Kastelein et al., 2018, 2020) showed, that only low level TTS are induced

with small airguns and that the harbor porpoises are able to self-mitigate noise exposure so no TTS is induced by increased swimming speed (7.1 km/h), changes of the head orientation and alteration of the hearing threshold by processes in the ear of nervous system. Especially at high frequency, the hearing of harbor porpoises is highly directional (Schack et al., 2019).

Table A-2: Onset limits of potential effects on harbor porpoises (*Phocoena phocoena*) belonging to the functional hearing group of Very High Frequency Cetaceans compiled from Southall et al. (2007, 2019); BOEM (2014) ; Tougaard et al. (2014; 2015; 2016); Schack et al. (2019).

Potential Effect on Harbor Porpoises	Unweighted Sound Pressure Level Limit: SPL _{UW} [dB re 1 μPa peak]	Weighted Sound Exposure Level Limit: SEL _w [dB re 1 μPa ² s]	Weighted Root Mean Square Sound Pressure Level Limit averaging period of 125 ms: SPL _{w,RMS} (125 ms) [dB re 1 μPa peak]
Mortality	>>230	Not applicable	Not applicable
Permanent Threshold Shift	202	155	Not applicable
Temporary Threshold Shift	196	140	Not applicable
Strong behavioral effect	Not applicable	Not applicable	100

Both the impact assessments before and the reporting after seismic or hydroacoustic acquisition campaigns are vital to safely conduct such projects and ensure a sustainable use of marine resources. Nonetheless, there is no established and freely available software package to help produce those reports. For many target areas, detailed reports have not been necessary in the past. As the reports are becoming mandatory now, a lot of new and additional efforts have to be spent to establish workflows and to collect the data necessary. The situation is aggravated by the fact that the sources of information are scattered and partially contradicting. Especially for universities and other research facilities with limited budgets it is often impossible to commission specialists to those tasks. Additionally, it is problematic for those institutions, that there is a lack of differentiation in the public opinion and regimentation between industrial seismic campaigns for the oil and gas exploration and near surface or academic seismic data acquisition.

Therefore, we aim to show and establish a basis and a workflow for the underwater noise impact assessment in the North and Baltic Sea. Also, we demonstrate what kind of data sets are necessary for the reports. This workflow is implemented in a PYTHON package, which is freely available via GIT (<https://github.com/roestanik/WhaleWatchWorkhorse>) and can consequently be used and improved by the community. Performing this assessment for a near surface research campaign, we can show, that this survey has only little impact on the marine environment.

B.2 Material and Methods

Calculation of the Sound Metrics

The basis of the different sound metrics is the noise signal $[p(t)]=1$ Pa with its specific amplitude and frequency content recorded as a time t series. As shown in Figure A-1 and Formula 1 and 2, p also depends on the distance d to account for geometric spreading $G(d)$, the absorption $A(f,d)$ of the noise in the water as a function of the instantaneous frequency f and d . For the weighted metrics, an animal group specific auditory weighting function $V(f)$ is included. The calculations require a forward and inverse transformation to the frequency domain F , commonly in the form of a Fast Fourier Transform.

$$p(t, d) = F^{-1}\{Fp(t) \cdot A(f, d) \cdot G(d)\} \quad (1)$$

$$p_w(t, d) = F^{-1}\{Fp(t) \cdot V(f) \cdot A(f, d) \cdot G(d)\} \quad (2)$$

The original weighting function $W(f)$ by Southall et al. (2019) with its parameters C , a , b , f_1 and f_2 are defined by:

$$W(f) = C + 10 \log_{10} \left\{ \frac{(f/f_1)^{2a}}{[1+(f/f_1)^2]^a [1+(f/f_2)^2]^b} \right\} \quad (3)$$

As $W(f)$ returns decibel (dB) amplitudes, the weighting function is transformed to the weighting function $V(f)$:

$$V(f) = 10^{\lfloor W(f)/20 \rfloor} \quad (4)$$

An approximation for chemical absorption in sea water $[a(f)]=1$ dB/km is e.g. given by Ainslie and McColm (1998). This approximation needs to be converted similarly to Formula 4:

$$A(f, d) = 10^{\{[a(f) \cdot d]/(1000 \cdot 20)\}} \quad (5)$$

A range of different options are available for the geometric spreading approximation. For deep water a spherical spreading approximation can be used:

$$g_{sph}(d) = 20 \log_{10} \left(\frac{1}{d} \right) \quad (6)$$

For very shallow water it would be most conservative to assume cylindrical spreading:

$$g_{cyl}(d) = 10 \log_{10} \left(\frac{1}{d} \right) \quad (7)$$

More realistic approximations for geometric spreading in shallow water are given by Elmer et al. (2007) or Duncan and Parsons (2011). Alternatively, models with the expected range of seafloor substrates could be run e.g. with the KRAKEN normal mode model (Acoustic Toolbox from HLS Research with the AcTUP V2.2L interface of Alec Duncan, 2021: <http://cmst.curtin.edu.au/products/underwater/>).

Similar to Formula 4 and 5, $[g(d)]=1$ dB needs to be converted:

$$G(d) = 10^{[g(d)/20]} \quad (8)$$

According to Southall et al. (2019), the SPL_{UW} depends only on the noise signal $p(t,d)$ and the reference pressure for water $p_0 = 10^{-6}$ Pa. SPL_{UW} is defined as:

$$SPL_{UW} = 20 \log_{10} \left[\frac{\max|p(t,d)|}{p_0} \right] \quad (9)$$

Similarly, $SPL_{W,RMS}$ is calculated according to Tougaard (2016):

$$SPL_{W,RMS} = 20 \log_{10} \left[\frac{p_{RMS}(T=125\text{ms})}{p_0} \right] = 20 \log_{10} \left[\frac{\sqrt{\frac{\sum_{t=0}^{t=125\text{ms}} p_W^2(t) \Delta t}{125\text{ms}}}}{p_0} \right] \quad (10)$$

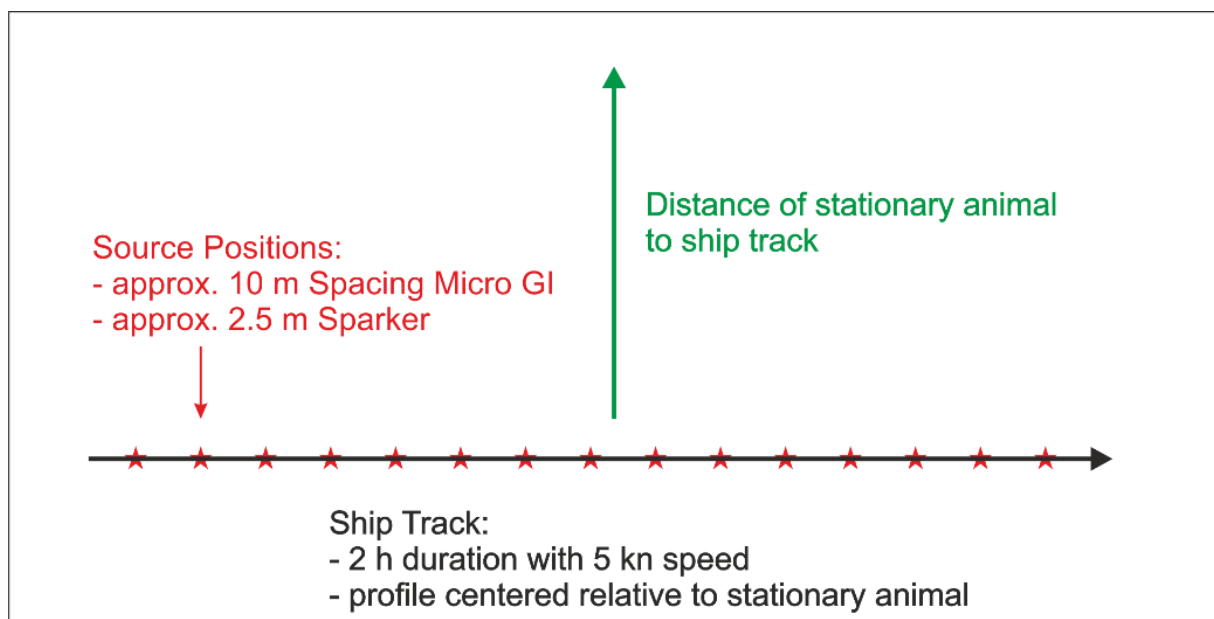


Figure A-2: Set-up of the SEL calculation with the profile crossing a stationary animal at varying distances. Typical values for shot distances and ship speeds for near surface seismic applications are reported. The SEL values are cumulated for the whole profile and should be reported as a function of the distance to the profile line.

As a measure for the onset of PTS and TTS the SEL_W is calculated, which is a cumulated measure for a theoretic profile and a stationary animal as proposed in Tougaard (2016) and shown in Figure A-2. The assumption of a stationary animal is a very conservative estimate, as most animals are likely to be moving during the survey and thus experience less emission to the underwater noise. For the calculation of the SEL_W , the signal spreading, absorption, weighting with the frequency filter of the functional hearing group is applied to the signal as a first step. In a second step, the signals in a certain temporal integration interval T are squared and summed. Finally, the summed signal is cumulated for all shot points of the theoretic profile and then expressed in dB relative to $1 \mu\text{Pa}^2\text{s}$:

$$SEL_W = 10 \log_{10} \left[\frac{\sum_{t=0}^T S_W(t,d)}{p_0^2 s} \right] \quad (11)$$

Data basis for sound metric calculation

The most important basis for the calculation of the noise impact is a calibrated record of the seismic or hydroacoustic source signal. Consequently, those records have to be generated with calibrated hydrophones and calibrated Analog to Digital Converters (ADC). The recording time has to be sufficient to record the full length of the primary source signal, reflections or other secondary effects should not be included. As the hearing capabilities of marine animals exceeds the order of magnitude of 10^5 Hz, the sampling rate should ideally be similarly high and at least sufficient to fulfil the Nyquist criterion. Figure A-3 shows the source signal of a Sercel micro GI gun used at the University of Bremen shot with 130 bars. The source output at a reference distance of 1 m is estimated to be $SPL_{UW}=226 \pm 2$ dB (re $1 \mu\text{Pa}$). The relatively large maximum error of the measurement results from the fact, that the ADC was not calibrated and some connectors had to be added. Nevertheless, this measurement is in good agreement with information by the manufacturer (<https://www.sercel.com/products/Pages/MiniG-Gun.aspx>).

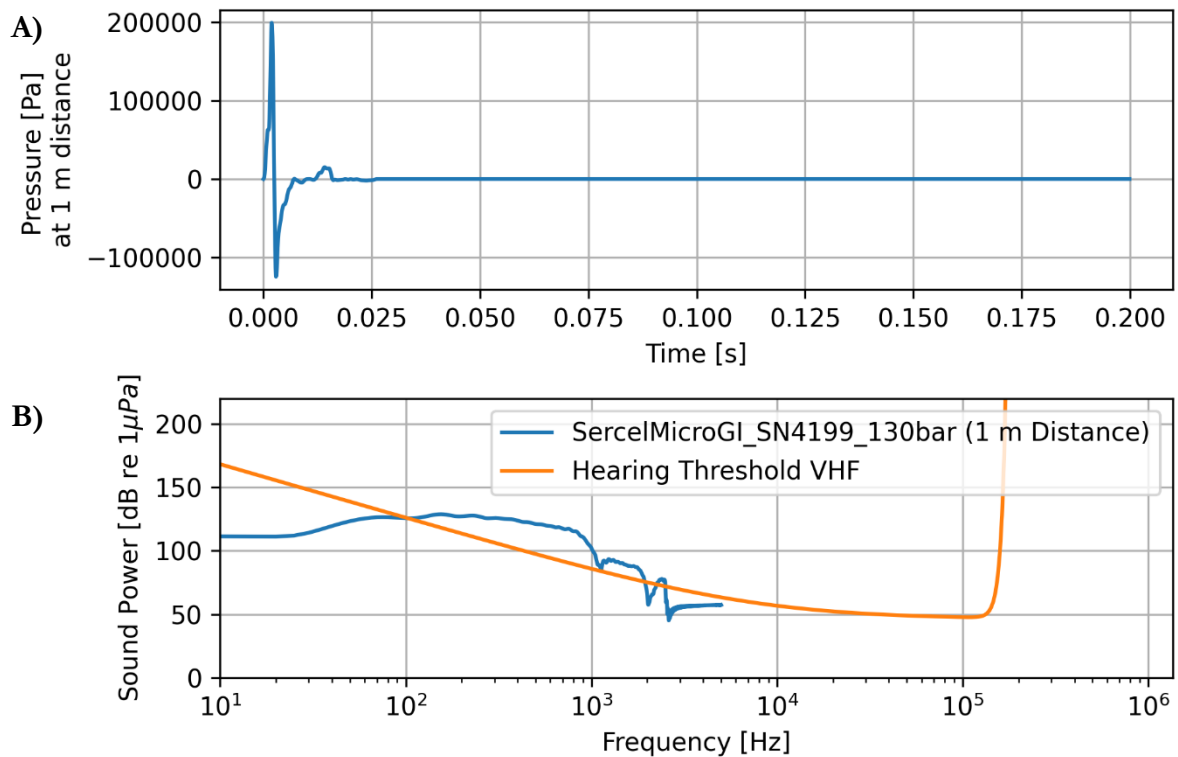


Figure A-3: Source Signal of a Sercel Micro GI gun (SN4199) of the University of Bremen shot with 130 bar shown A) as a time series in the upper panel and B) its Fourier Transform in the lower panel. The hearing threshold of the functional hearing group of Very High Frequency Cetaceans, to which harbour porpoises belong, is calculated according to Southall et al. (2019) and also shown in the lower panel. The hearing threshold curve illustrates, that the frequencies of the best hearing capabilities of VHF are not coinciding with the central frequency of the seismic source.

In the case of point sources, it is sufficient to have a singular record of the far field. Most hydroacoustic sources and some seismic sources are directional sources. In this case it is additionally necessary to determine the directivity. Lurton (2016) gives simplified formulas to model a directionally radiated sound field and also to approximate all sound metrics when only the SPL_{UW} and central frequency are known. Those simplifications are used to determine the underwater noise impact for Single and Multi Beam Echo Sounders in the PYTHON package.

Reporting of underwater noise emissions

Although the noise registry for seismic surveys in the German EEZ is still under development (<https://marinears.bsh.de>), data requirements have been made available to the authors. The data delivery to MarineEars consists of a single, standardised hdf5-file (<https://hdfgroup.org/>). Together with general survey information, detailed information about the sound sources and the

acquired transects have to be put into the file. Currently, there is no established software package to produce this file. Nevertheless, hdf5-files can be produced with PYTHON, so a collection of scripts and functions is supplied (<https://github.com/roestanik/WhaleWatchWorkhorse>) to generate the data report with a minimum of data input.

B.3 Results and Discussion

Workflow Underwater Noise Impact Assessment and Mitigation

After the successful application for three research cruises in Danish and German waters, the following workflow has been established. As a first step, the possible sources of underwater noise such as the seismic and hydroacoustic sources need to be identified. Wavelet records or centre frequency information for echosounders and SPL_{LW} at a reference distance of 1 m are a minimum requirement, it is very beneficial to have calibrated records of the emitted sound. Secondly, the regions of interest and by that the possibly affected animal species need to be identified. Those animals are then grouped in functional hearing groups and the sound exposure limits are determined. It is furthermore needed to gain information on the composition of the seawater to determine the absorption. Typical water depths and seafloor substrates have to be determined to approximate the geometrical spreading. Using those parameters as an input, the models of the underwater noise impact assessments can be conducted and safety distances are determined. Those safety distances are necessary to generate buffers around specially protected areas or to determine the extent of affected areas. As up to six months can be required for permit processes, it is vital to start the work on impact assessments in an early stage of a project.

During the acquisition campaign and as e.g. documented in OSPAR (2016) and JNCC (2017) pre-shooting watch, possibly Passive Acoustic Monitoring and soft start procedures have to be followed. Also procedures for shooting breaks have to be established. The use of mitigation guns or a new soft start after extended breaks are encouraged. After an acquisition campaign, the data necessary has to be submitted to the national noise registries.

Calculation Basics: Auditory Weighting, Absorption and Geometric Spreading

The auditory weighting functions and the geometric spreading approximation have major influence on the noise impact modelling. The hearing threshold shown in Figure A-3 and the filter function in Figure A-4A for VHF form a complementary pair and are determined according to Southall et al. (2019). While the hearing threshold together with the amplitude spectrum of the Micro GI sound source shows, that there is only little overlap between the source spectrum and the hearing capabilities of VHF, the filter function can be used to weight the signal in the frequency domain.

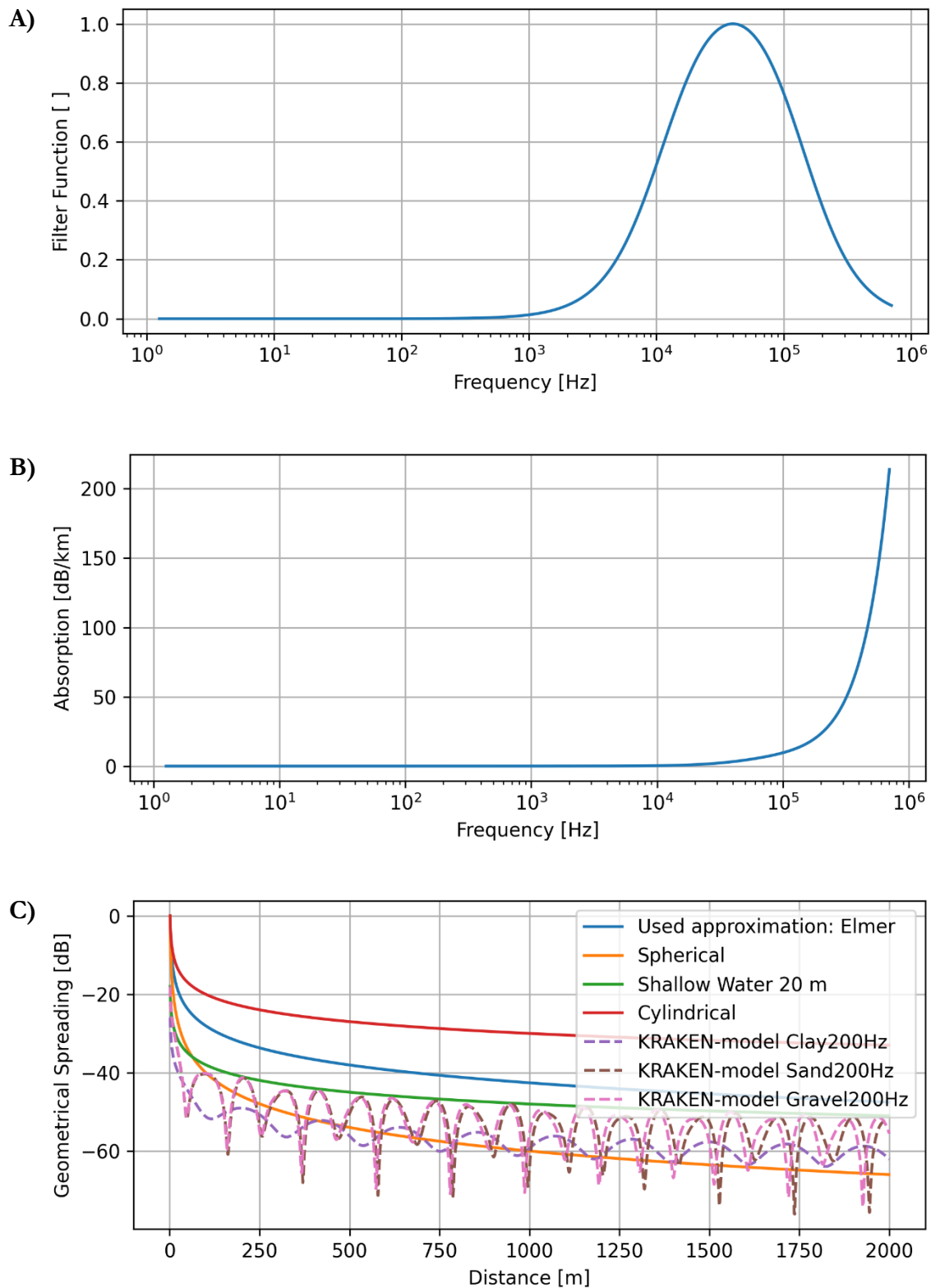


Figure A-4: Calculation basics for the noise impact assessment showing A) the auditory filter function for Very High Frequency Cetaceans (VHF); B) the frequency dependent absorption in a Baltic Sea setting and C) a range of different geometrical spreading functions. Animals in the VHF group have the best hearing capabilities in a frequency range of 10-100 kHz, which is considerably higher than the frequencies commonly used for near surface seismic applications. While the absorption has only little effect on low frequencies, the choice of the geometrical spreading function highly influences the modelling for noise impact assessments.

After weighting and transformation to the time domain as shown in Formula 2, the weighted source signal p_w shows how the signal is perceived by a certain animal. Due to the small overlap of the hearing capabilities and the source signal of a micro-GI, p_w is heavily attenuated relative to p .

According to Ainslie and McColm (1998), the significant absorption mechanism at high frequencies above 100 kHz is viscous absorption, while lower frequencies are mainly attenuated by chemical relaxation effects primarily due to boric acid. Consequently, absorption has only a significant effect in a Baltic Sea Setting at frequencies above 10 kHz as shown in Figure A-4B.

Especially for shallow waters, it is crucial to select a realistic geometrical spreading approximation. In deep waters, the amplitudes of spherically spreading waves are indirectly proportional to the distance to the sound source, see Formula 6 for spherical spreading. In shallow waters, the direct wave is overlapping with the reflections of the signal on the seafloor and the water surface at great distances. This overlap would lead to cylindrical spreading (Formula 7), if there was no loss of the signal into the seafloor or into the air at the reflection points. Shallow water approximations account for this loss. While the approximation of Elmer et al. (2007) is based on measured data, the approximation by Duncan and Parsons (2011) builds on models of a basaltic seafloor. Consequently, the Duncan and Parsons (2011) approximation dramatically underestimates the geometric spreading loss when soft sediments like in the Baltic or North Sea are encountered. As the difference, e.g., between spherical and cylindrical spreading is about 30 dB at a distance of 250 m as shown in Figure A-4C, the choice of the geometrical spreading approximation has a great influence on the impact assessment. For most realistic models it is necessary to run models of the geometrical spreading accounting for topography, water column stratification and seafloor substrate.

Impact of a near surface seismic survey

Safety distances of 60 m to avoid PTS, 140 m to avoid TTS and 260 m to avoid behavioural or likewise physiological changes are determined. According to the BSH standard, the Micro GI with $SPL_{UW}=226\pm 2$ dB (re 1 μ Pa) is classified as a very low energy source and comparing this strength to Table A-2, the sound is too weak to cause mortality of VHF at any distance. Due to the little overlap of the source spectrum with the hearing capabilities (compare Figure A-3), the safety distances for the weighted sound metric SEL_w are lower than for the unweighted SPL_{UW} as shown in Figure A-5A and B. Using the Elmer et al. (2007) geometric spreading approximation, the safety distances are comparatively conservative. KRAKEN models and another shallow water approximation for 20 m water depths (Duncan & Parsons, 2011) are characterised by stronger geometrical spreading losses and thus smaller safety distances.

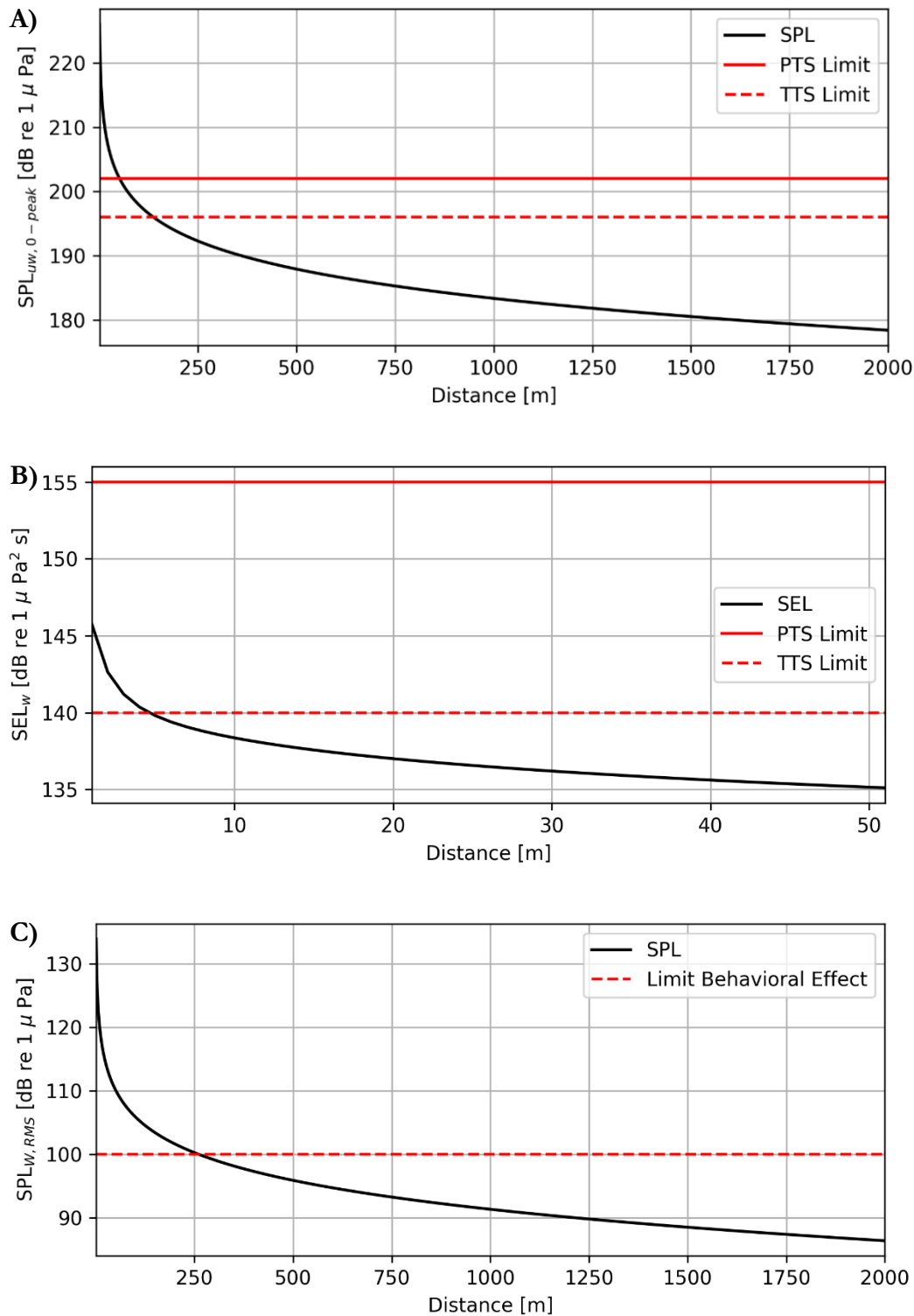


Figure A-5: Results of the noise impact assessment for the Sercel micro-GI shot at 130 bar and Very High Frequency (VHF) cetaceans in a Baltic Sea Setting using the Elmer et al. (2007) geometric spreading approximation including dual exposure metrics for Permanent Threshold Shifts (PTS) and Temporary Threshold Shifts (TTS) with A) the unweighted Sound Pressure Level SPL_{UW} and B) the weighted Sound Exposure Level SEL_w . The resulting safety distances rounded up to the next 10 m are about 60 m for PTS and 140 m for TTS defined by SPL_{UW} as the safety distances by SEL_w are lower. The lowermost panel C) shows the limit for the onset of behavioural effects and the weighted Root Mean Square Sound Pressure Level with an averaging period of 125 ms $SPL_{w,RMS}$ (125 ms). At distances greater than 260 m (result rounded up to the next 10 m) no behavioural or physiological response is to be expected based on the metric.

B.4 Conclusion

Performing an exemplary underwater noise impact assessment for the Sercel Micro GI airgun high resolution seismic source and harbour porpoises, it has been demonstrated, that the impact of noise by such seismic acquisition campaigns on the marine environment is comparatively small. Based on the current state of knowledge on sound exposure metrics, the sound exposure is not sufficient at any distance to cause mortality. Permanent hearing losses are estimated to be possible up to 60 m distance, temporary losses up to 140 m. Behavioural response is modelled to be limited to a distance of 260 m. While absorption is insignificant for low frequencies, the auditory weighting and the geometric spreading model have been found to have the greatest effect on the estimation of safety distances. The presented workflow for assessments and reporting has been implemented in a PYTHON package being available via GITHUB (<https://github.com/roestanik/WhaleWatchWorkhorse>).

The data necessary to perform such impact assessments are not available for all High to Ultra-Ultra High Resolution seismic sources. So, there is the need to establish a broader data basis. Although the impacts by high resolution seismic surveys is comparatively small, possibilities to further decrease the noise emitted during survey should also be investigated. As seismic surveys are conducted within shorter periods of time than e.g. geotechnical surveys, the further uses of seismic inversion products e.g. for offshore wind surveys have to be investigated to decrease the stress on the marine environment.

Acknowledgments

This study was funded through the project ‘SynCore’ (German Ministry of Economics and Energy [BMWi], project number 03EE3020C).

We are much obliged to Jakob Tougaard from the Aarhus University (Denmark) as well as Mads Kløve Hallstrøm, Laura Strøm Magner and Christina Pommer from the Danish Energy Agency for their feedback on our environmental impact assessments for our research cruises to Danish waters.

C Supplementary Material to the Manuscripts

C.1 Receiver Configuration Modelling

In order to evaluate the impact of receiver configuration on the usability of seismic data for inversion, the effect of receiver ghosts and groups is analysed. The receiver ghost can be modelled as a filter function $R_{ghost}(f)$ in the frequency domain. Similar to the source ghost, the receiver ghost is the inverted reflection of a signal, but with the path being “source - reflector - sea surface - receiver”. Following Aytun (1999) and Provenzano et al. (2020), the frequency of the primary ghost notch is determined by:

$$f_0 = \frac{v_w}{2 \cdot d}$$

with the water velocity v_w and the effective receiver depth d and the frequency f . The filter function of the receiver ghost R_{ghost} is then given by:

$$R_{ghost} = 1 + r_{ss} e^{\frac{-i \cdot 2 \cdot \pi \cdot f}{f_0}}$$

with $r_{ss} \approx -1$ quantifying the reflectivity of the sea surface. In a vertical incidence scenario, the depth of the receiver is equal to the effective receiver depth. For non-vertical incidence the angle of the wavefront reflected by the sea surface needs to be considered and consequently the effective depth is larger than the tow depth at non-vertical incidence angles.

The usage of receiver groups introduces a certain directivity. On the one hand, this directivity can be quantified and corrected for in terms of a directivity factor as shown in Riedel & Theilen (2001). On the other hand, the grouping also introduces a change of the received wavelet shape due to the analogue stacking of the received signal at each group sensor, leading to distortions especially at large incidence angles. To quantify both the directivity factor and the wavelet shape change, the effect of receiver grouping has been modelled in a simplistic way. For the model, the output of a receiver group with eight elements is calculated by the sum of all receivers in the group without any NMO correction. So, the signal received at each element of the group was modelled in a convolutional model for a reflector at 40 m depth assuming a NMO velocity of 1500 m/s. The recordings of all group sensors are analysed in terms of the amplitude spectrum and signal strength giving the directivity factor after normalization.

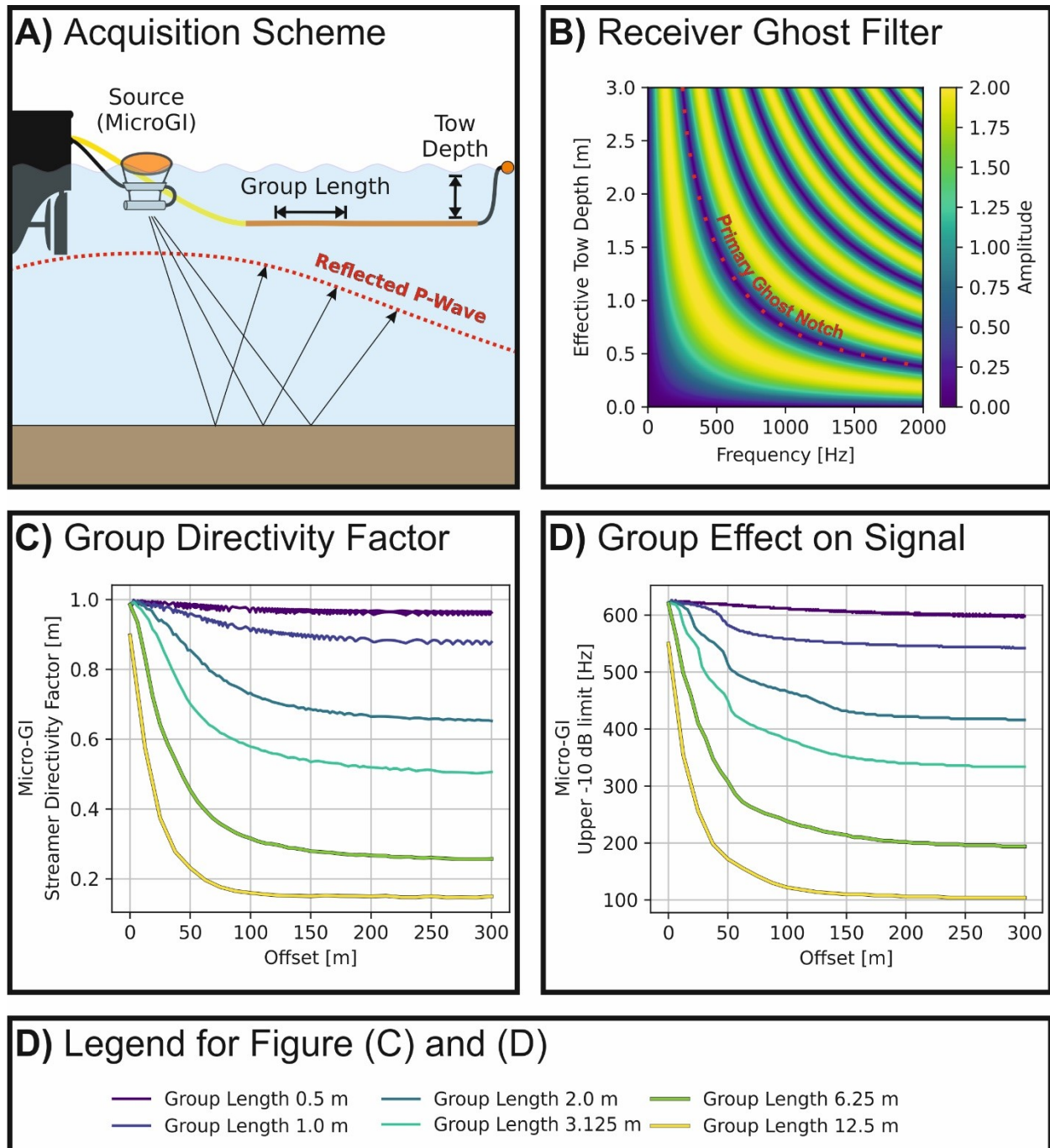


Figure A-6: Effects of the receiver configuration on the seismic data acquisition. A) Schematic illustration of the acquisition scenario and the parameters considered. B) Amplitude of the filter function caused by the receiver ghost depending on the effective tow depth and the frequency considered. The recorded amplitude spectrum can be derived by the multiplication of the source spectrum with the receiver ghost filter at a certain effective tow depth. Consequently, the recorded spectrum can be purposely shaped by the tow depth. The frequency of the primary ghost notch is marked. Groups with eight elements are modelled. Due to the analogue signal summation happening during the data acquisition with groups, no correction for the incident angle of the reflected waves is performed and the recorded signal is both relatively attenuated and distorted. The group effect can be quantified with: C) Streamer directivity factor for common group lengths as a function of the offset for micro-GI airgun shots for a reflector at 40 m depth. This directivity factor quantifies, how much amplitude is recorded by a group compared to the incident amplitude. D) Effect of group length on the received signal illustrated on the upper -10 dB frequency limit of a micro-GI airgun signal for a reflector at 40 m depth. (C) and (D) share the same legend given in (E).

Both the streamer tow depth and the usage of receiver groups have an impact on the data acquisition (Figure A-6). The most pronounced effect of the receiver tow depth is caused by the receiver ghost, which has been modelled by its filter function in the frequency domain (Figure A-6B). Depending on the spectrum of the source and the effective tow depth of the receiver, which is a function of the angle of incidence and the true tow depth, the receiver ghost causes both positive and negative interference and thus acts as a filter, enhances certain frequencies or introduces ghost notches. The frequency of the ghost notch is given in Equation 2 and the amplitude at the notches is zero in the ghost filter function. The amplitudes in between the notches are partially amplified by a factor up to a maximum of two. If a streamer is towed shallowly, the notch at 0 Hz and the primary ghost notch frame the spectrum of the source. So, the high and low frequencies of the source are filtered out, while the central part of the spectrum is enhanced. Towing the streamer at greater depths shifts the primary ghost notch to lower frequencies and the harmonics of the primary notch become increasingly relevant.

The effects of groups on the received signal increases with group length and offset as an increasingly large portion of the signal is lost. This signal loss is explained by the signal summation of all sensors in a group leading to the loss of high-frequency components of the wavelet when seismic wave incidence on the receiver group is non-vertical. The group directivity factor as shown in Figure A-6C (see also Riedel and Theilen, 2001) can be used to quantify the loss and is shown here for a reflector depth of 40 m. At zero offset or likewise vertical incidence, groups up to a length of 6.25 m have only little to no effect on the recorded signal. While small groups with a length smaller than 0.5 m have only little effect on a micro-GI airgun signal in the whole offset range considered up to 300 m, groups of 3.125 m already introduce a factor of about 0.5 at offsets larger than 200 m. Using large groups of 12.5 m length, the directivity factor is <0.2 for offsets larger than ~ 60 m. Furthermore, groups act as a high frequency filter, increasing in effect with both increasing group length and offset. In Figure A-6D, the shift of the upper -10 dB frequency limit of a recorded micro-GI airgun signal caused by receiver groups is shown. At vertical incidence the effect is negligible, but the upper -10 dB frequency limit is reduced to about 100 Hz at large offsets using groups of 12.5 m.

Hydrophone groups introduce both an angle dependent directivity factor and act as a high frequency filter. The significance of those effects depends on both the source signal, the length of the groups and the angle of incidence. We found that the usage of groups larger than 0.5 m introduces an additional angle dependent waveform variation for the micro-GI airgun (Figure A-6) for offsets up to 300 m and 80 m investigation depth. As the effect can be determined, one can also perform a correction for the inversion (Riedel & Theilen, 2001; Provenzano et al., 2017).

Streamer directivity functions mainly depend on the number of hydrophones and the spacing in a group and can be calculated with a measured wavelet or as a function of the incidence angle and frequency (see Appendix B in Riedel & Theilen, 2001). The measured AVA trend has then to be multiplied with the directivity factors to retrieve the corrected AVA trend. Since imaging quality also suffers from the usage of too large groups, we rather suggest the use of single hydrophone streamers.

Another factor is the spacing of the hydrophones or groups in the streamer. The maximum CMP spacing is in the range of 2.1 m (UHR) to 0.26 m (UUHR) for imaging requirements based on the spatial aliasing requirement considering 45° maximum dips and $v_{RMS,max} = 1800$ m/s (Yilmaz, 1991). Ideally, the shot point spacing should be equal to the CMP spacing, with a hydrophone spacing of twice the CMP spacing (4.2 m for UHR and 0.52 m for UUHR). To improve the recovery of AVA trends, the stacking in angle gathers can be considered. To reach a fold of ten in 10° angle gathers, an angle resolution of 1° would be needed. This requirement translates to 3 m minimum spacing in the near and 15 m spacing in the far offsets of 300 m. Consequently, streamers with variable spacing with larger offsets at the tail sections reduce acquisition efforts without limiting AVA inversion possibilities.

It is a general recommendation to optimize the data acquisition to save effort in data processing, especially as the loss of signal due to inadequate acquisition cannot be corrected. If the wavefield is inadequately sampled due to too large receiver spacings or groups or temporal sampling, imaging artefacts such as aliasing will persist after the processing. Similarly, we consider it to be highly beneficial for inversion to tow receivers at an optimum depth range, which is defined by source signal waveform and the receiver ghost filter function (Figure A-6). The optimum can be found by the multiplication of the source spectrum and the filter function as a function of tow depth. Maximum amplitude of the micro-GI airgun signal is reached for effective receiver tow depths of 0.8-1.5 m and ~ 0.3 m for the AADS400 sparker. As shown in Figure A-6B, very shallow towing acts as an undesirable low frequency filter. In an extreme case when the streamer surfaces, all signals are lost. Generally, streamer tow depths for UHR surveying of 0.7-2.4 and for UUHR surveying of 0.4-1.2 appear reasonable, resulting in less than three ghost notches to appear in the recorded data and the streamer is deep enough below the water surface to reduce surfacing issues, e.g., caused by waves. Slanted towing of the streamers inside the optimum window and adopted processing strategies can effectively remove the receiver ghost (Duarte et al., 2017). As shown in Provenzano et al. (2020), unknown and variable receiver tow depth can be deduced from the frequency of the ghost notches and the ghost notch can be attenuated. Nevertheless, the streamer tow depth should ideally be controlled and recorded with suitable devices. The receiver ghost has an additional effect

on the amplitudes and the shape of the recorded wavelet. We have shown in Figure 3-7 and section Figure 3-8 that AVA effects can be smaller than acquisition effects. Therefore, we suggest that it is highly beneficial to tow the streamer at the optimized depth range, directly acquire the best data possible and avoid additional needs for corrections.

C.2 Biot-Stoll Modelling

The sediment properties in Table 3-1 are contrasted with modelling data, to estimate the frequency dependency of attenuation and velocity dispersion. The modelling is based on the formulas given in Hovem (1991), Badiey et al. (1998), Dvorkin et al. (Dvorkin et al., 1999), Breitzke (2006) and Carcione & Picotti (2006). The parameters and results for the different CPT Soil Types are given below.

Table A-3: General Biot-Stoll Modelling Parameters.

Frequency Range	
Minimum Frequency	50 Hz
Maximum Frequency	4000 Hz
Properties of the Pore Fluid	
Bulk Modulus	2.37 GPa
Density	1024 kg/m ³
Viscosity	1.07 10 ⁻³
Properties of the Grains	
Bulk Modulus	21.0 GPa
Density	2670 kg/m ³

Table A-4: Biot Stoll modelling parameters for sensitive, fine grained soils (CPT1).

Sediment Frame Properties	
Bulk Modulus	$5.0 \cdot 10^5 \text{ Pa}$
Shear Modulus	$2.5 \cdot 10^6 \text{ Pa}$
Pore Space Parameters	
Porosity	0.8
Mean Grain Size	$2.0 \cdot 10^{-6} \text{ m}$
Permeability	$7.1 \cdot 10^{-15} \text{ m}^2$
Pore Space Constant	0.5
Pore Shape Factor	5.0 (round)

CPT1: Sensitive, fine grained

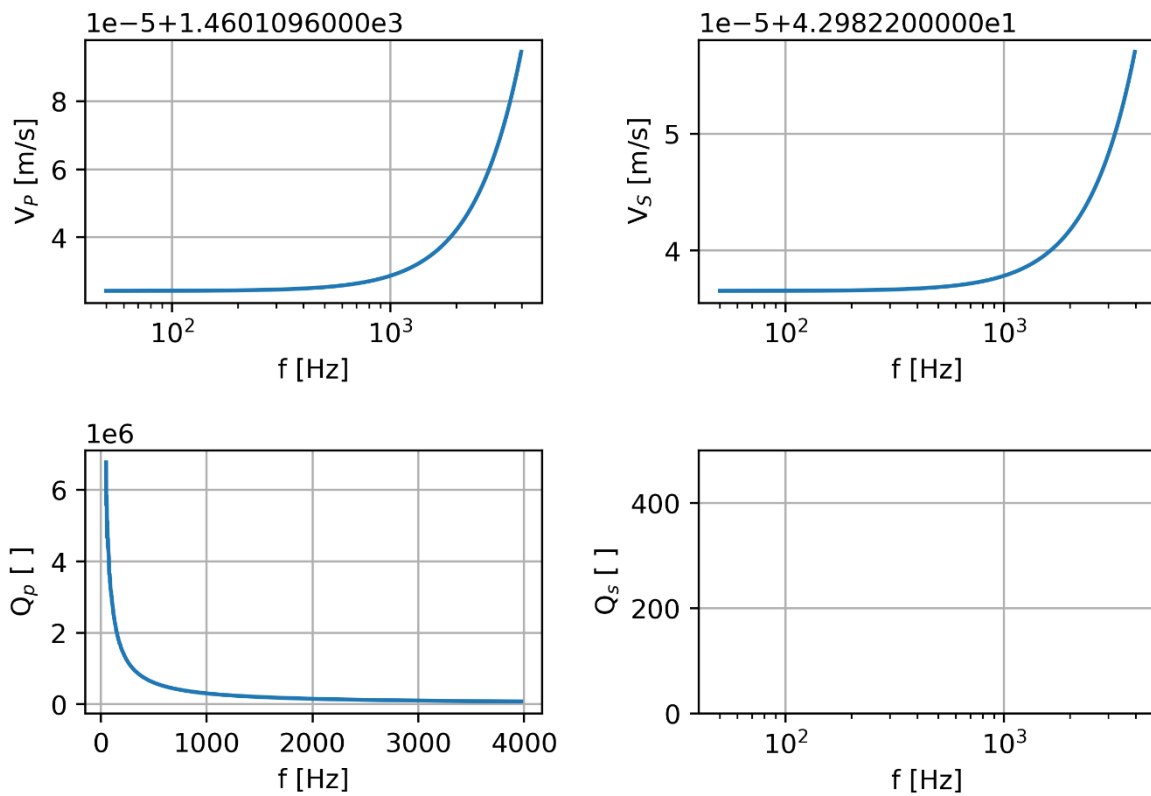


Figure A-7: Biot Stoll model for sensitive, fine grained soils (CPT1)

Table A-5: Biot Stoll modelling parameters for organic soils (CPT2)

Sediment Frame Properties	
Bulk Modulus	$10.0 \cdot 10^5 \text{ Pa}$
Shear Modulus	$5.0 \cdot 10^6 \text{ Pa}$
Pore Space Parameters	
Porosity	0.8
Mean Grain Size	$2.0 \cdot 10^{-6} \text{ m}$
Permeability	$7.1 \cdot 10^{-15} \text{ m}^2$
Pore Space Constant	0.5
Pore Shape Factor	5.0 (round)

CPT2: Organic soils - clay

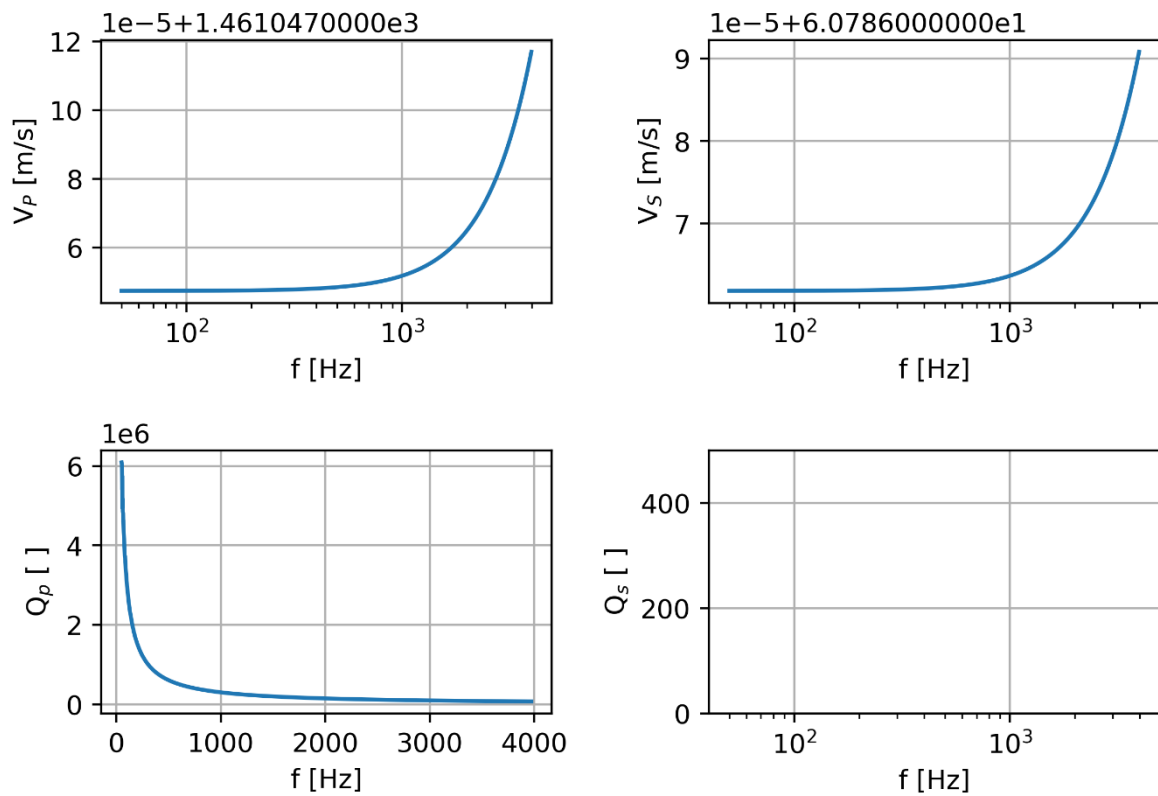


Figure A-8: Biot Stoll model for organic soils and clay (CPT2)

Table A-6: Biot Stoll modelling parameters for clays (CPT3)

Sediment Frame Properties	
Bulk Modulus	$1.0 \cdot 10^7$ Pa
Shear Modulus	$1 \cdot 10^7$ Pa
Pore Space Parameters	
Porosity	0.7
Mean Grain Size	$2.0 \cdot 10^{-6}$ m
Permeability	$7.1 \cdot 10^{-15}$ m ²
Pore Space Constant	0.5
Pore Shape Factor	5.0 (round)

CPT3: Clay - silty clay to clay

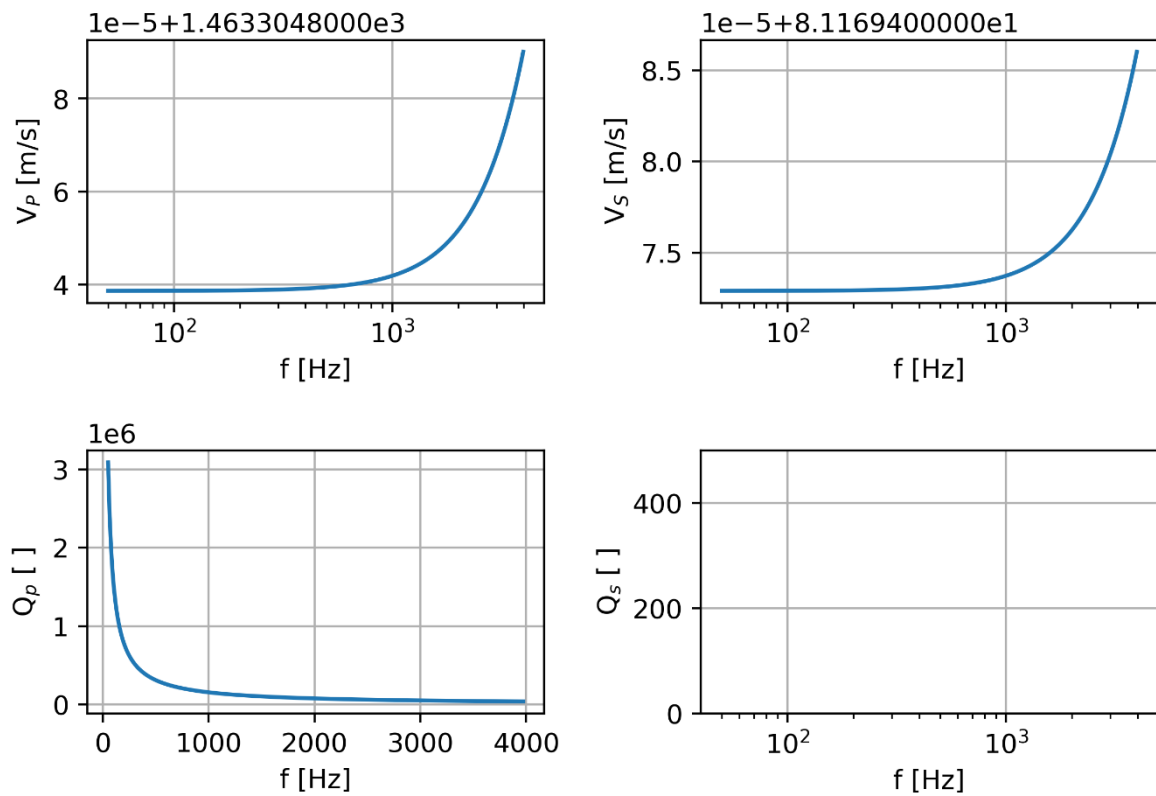


Figure A-9: Biot Stoll model for clays (CPT3)

Table A-7: Biot Stoll modelling parameters for silts (CPT4)

Sediment Frame Properties	
Bulk Modulus	$2.0 \cdot 10^7$ Pa
Shear Modulus	$5.0 \cdot 10^7$ Pa
Pore Space Parameters	
Porosity	0.6
Mean Grain Size	$3.0 \cdot 10^{-5}$ m
Permeability	$2.3 \cdot 10^{-12}$ m ²
Pore Space Constant	0.5
Pore Shape Factor	5.0 (round)

CPT4: Silt mixtures - clayey silt to silty clay

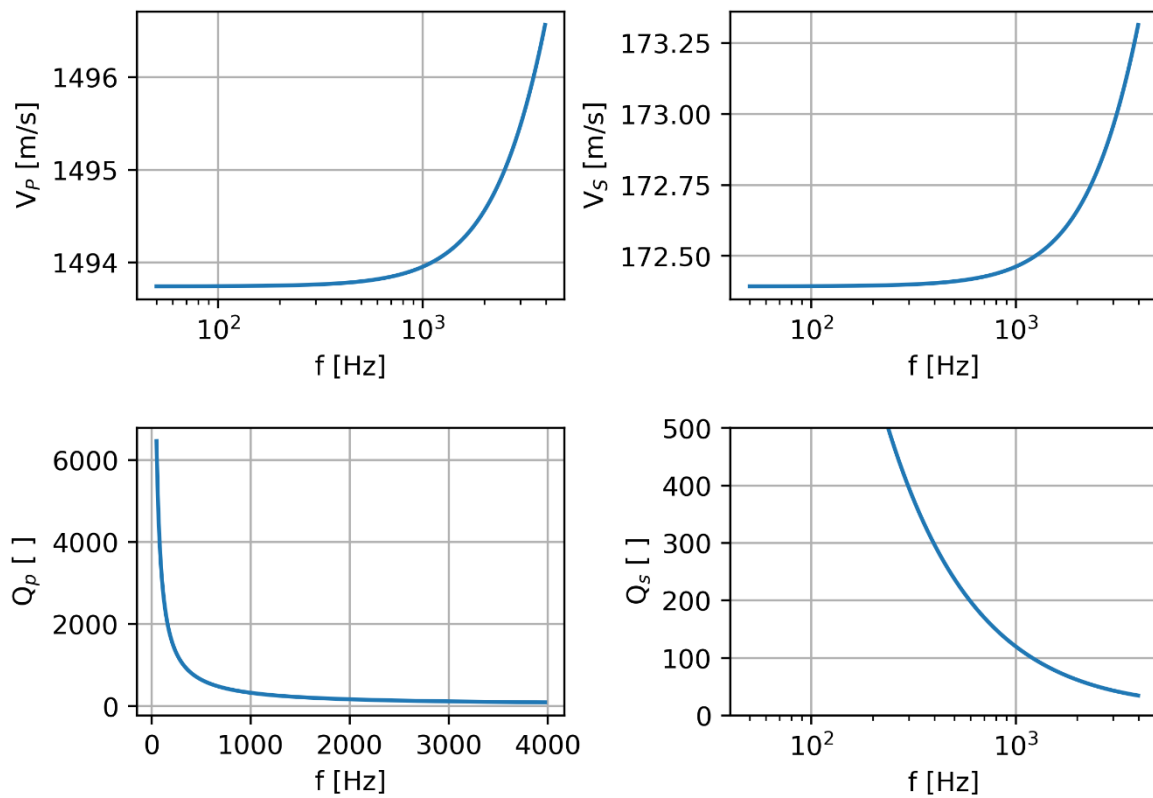


Figure A-10: Biot Stoll model for silts (CPT4)

Table A-8: Biot Stoll modelling parameters for silty sand mixtures (CPT5).

Sediment Frame Properties	
Bulk Modulus	$2.0 \cdot 10^8 \text{ Pa}$
Shear Modulus	$1.0 \cdot 10^8 \text{ Pa}$
Pore Space Parameters	
Porosity	0.5
Mean Grain Size	$8.84 \cdot 10^{-4} \text{ m}$
Permeability	$2.26 \cdot 10^{-11} \text{ m}^2$
Pore Space Constant	0.5
Pore Shape Factor	5.0 (round)

CPT5: Sand mixtures silty sand to sandy silt

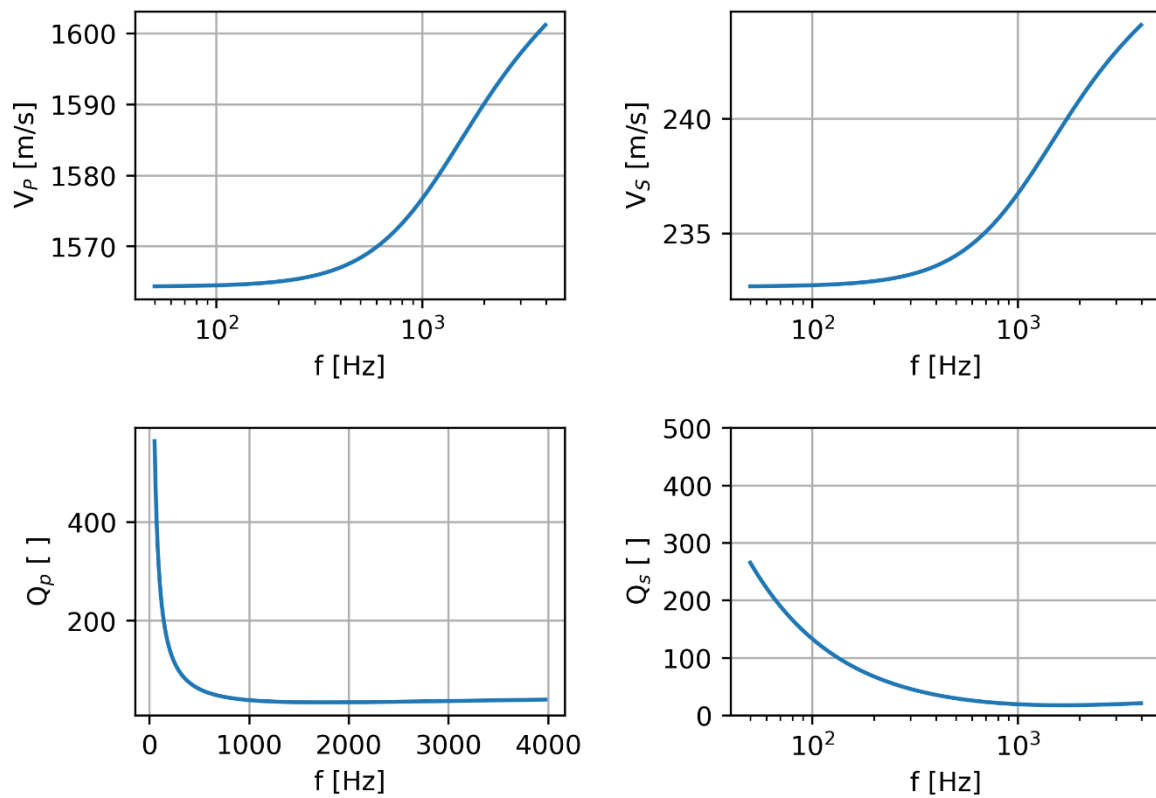


Figure A-11: Biot Stoll model for silty sand mixtures (CPT5).

Table A-9: Biot Stoll modelling parameters for sands (CPT6).

Sediment Frame Properties	
Bulk Modulus	$3.0 \cdot 10^8$ Pa
Shear Modulus	$2.0 \cdot 10^8$ Pa
Pore Space Parameters	
Porosity	0.4
Mean Grain Size	$7.0 \cdot 10^{-5}$ m
Permeability	$5.4 \cdot 10^{-11}$ m ²
Pore Space Constant	0.5
Pore Shape Factor	5.0 (round)

CPT6: Sands - clean sand to silty sand

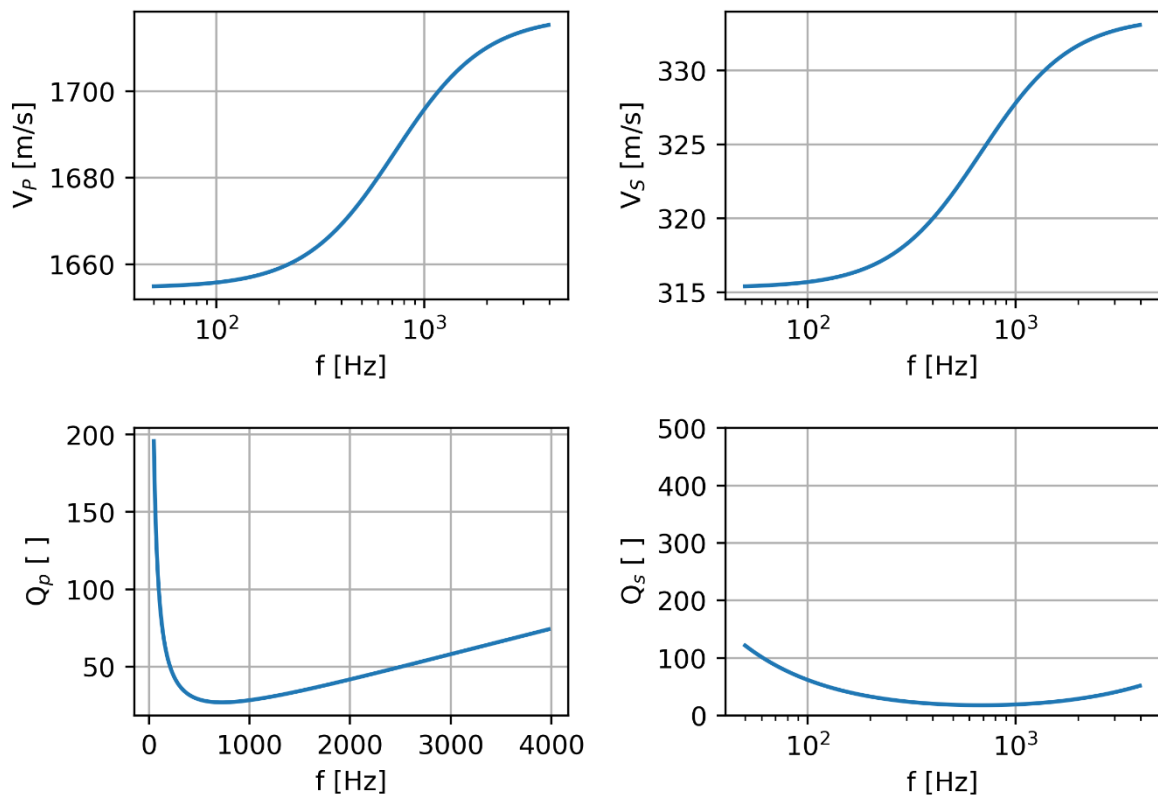


Figure A-12: Biot Stoll model for sands (CPT6).

Table A-10: Biot Stoll modelling parameters for gravely to dense sands (CPT7)

Sediment Frame Properties	
Bulk Modulus	$4.0 \cdot 10^8 \text{ Pa}$
Shear Modulus	$3.0 \cdot 10^8 \text{ Pa}$
Pore Space Parameters	
Porosity	0.4
Mean Grain Size	$5.0 \cdot 10^{-4} \text{ m}$
Permeability	$1.0 \cdot 10^{-10} \text{ m}^2$
Pore Space Constant	0.5
Pore Shape Factor	5.0 (round)

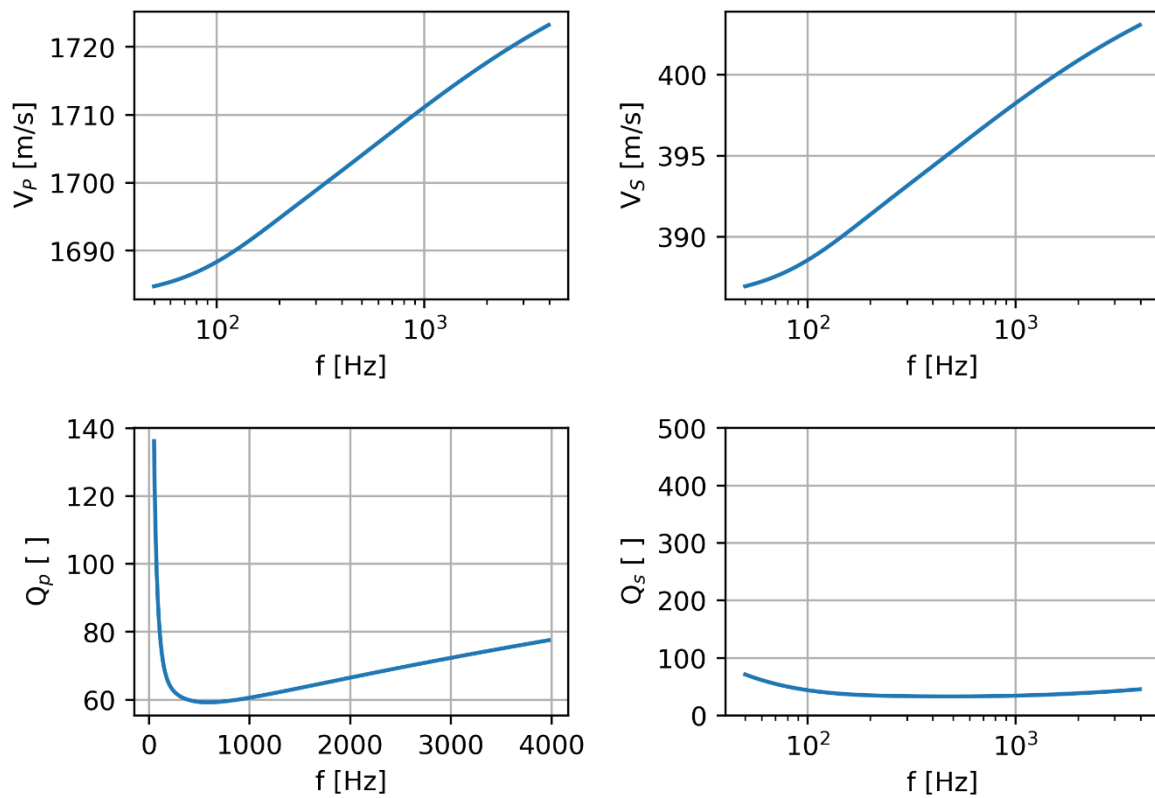
CPT7: Gravelly sand to dense sand**Figure A-13: Biot Stoll model for gravely to dense sands (CPT7).**

Table A-11: Biot Stoll modelling parameters for stiff sand (CPT8).

Sediment Frame Properties	
Bulk Modulus	4.8 10 ⁹ Pa
Shear Modulus	5.7 10 ⁹ Pa
Pore Space Parameters	
Porosity	0.3
Mean Grain Size	8.84 10 ⁻⁵ m
Permeability	9.87 10 ⁻¹³ m ²
Pore Space Constant	0.5
Pore Shape Factor	5.0 (round)

CPT8: very stiff sand to clayey sand (Heavily overconsolidated or cemented)

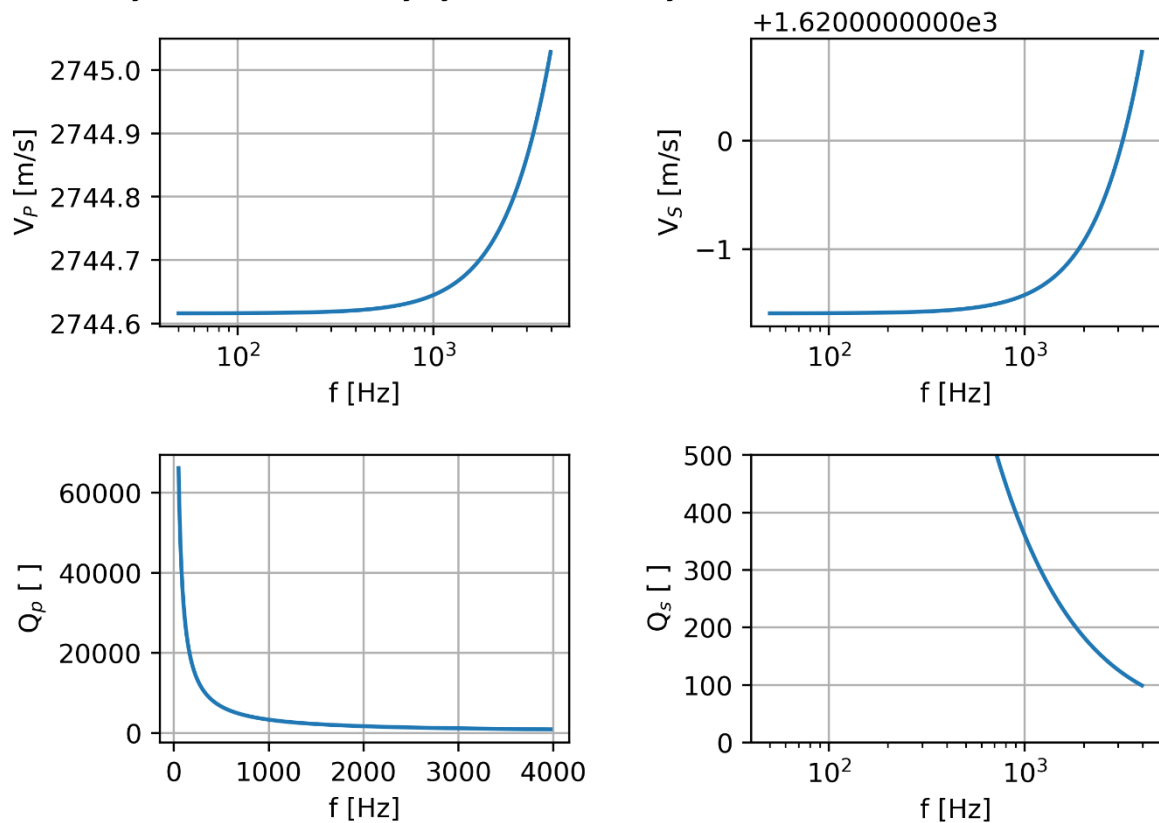
**Figure A-14: Biot Stoll model for stiff sand (CPT8).**

Table A-12: Biot Stoll modelling parameters for stiff fine grained material (CPT9)

Sediment Frame Properties	
Bulk Modulus	$3.3 \cdot 10^9$ Pa
Shear Modulus	$1.2 \cdot 10^9$ Pa
Pore Space Parameters	
Porosity	0.3
Mean Grain Size	$2.0 \cdot 10^{-6}$ m
Permeability	$1.84 \cdot 10^{-17}$ m ²
Pore Space Constant	0.5
Pore Shape Factor	5.0 (round)

CPT9: Very stiff fine grained (Heavily overconsolidated or cemented)

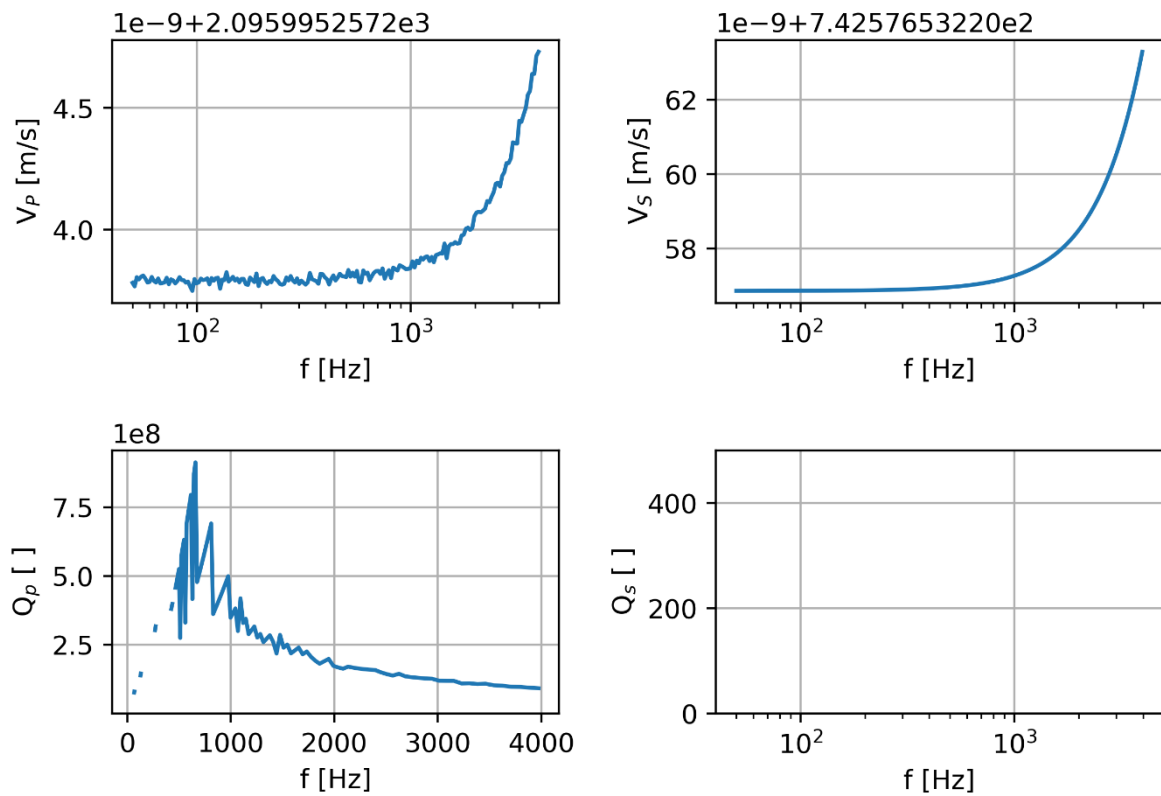


Figure A-15: Biot Stoll model for stiff fine grained material (CPT9).

C.3 Resolution Calculation

Although definitions of resolutions for near surface seismics exist such as ISO 19901-10 (2021), the term resolution often is used inconsistently and vaguely in the literature and for industrial seismic surveys. Therefore, we suggest to follow Kallweit and Wood (1982) who define the temporal resolution T_{res} according to Ricker's resolution criterion to equal the separation between the inflection points of the central lobe of a wavelet. Furthermore, Kallweit and Wood (1982) describe that only for ideal wavelets, such as Ricker or sinc wavelets, the central or peak frequency f_c can be linked to this definition of the T_{res} . In this context, f_c is the frequency with the maximum amplitude in the spectrum. For real, mixed phase wavelets, the inflection point separation has to be determined with a wavelet record. Rayleigh's resolution criterion, in contrast, determines the tuning thickness, which is equal to a quarter of the dominant wavelength $\lambda_d = v_p/f_d$ and determined by the predominant frequency f_d . The parameter f_d is defined as the reciprocal of the width of the central lobe of the wavelet. Migration improves the lateral resolution to λ_d , while the lateral resolution before migration is defined by the radius of the Fresnel zone $r = v_p/2\sqrt{(twt_0/f_d)}$ depending on the zero offset travel time twt_0 (Yilmaz, 1991).

C.4 Sparker Directivity Modelling

Additional modelling of the AADS400 sparker directivity is performed to extend the directivity estimate outside the measurement range, to derive single tip signals and to check the applicability of a convolutional model. The convolutional model is based on the assumptions, that each tip produces the same signal and that the recorded wavelet is the superposition of the signal generated at each tip and its source ghost arriving at different delays at the recording point. Due to the strong negative reflectivity of the water-air boundary, an upgoing signal is reflected and inverted at this boundary. This signal is called ghost reflection and specifically source ghost for the reflection path source-water surface-receiver. Accounting for the spherical spreading, the reflectivity of the sea surface, absorption inside the sparker frame and the traveltimes difference in a filter function, the signal generated at a single tip was approximated by a Wiener Deconvolution of the recorded wavelet with this filter function. The recorded wavelet could then be reproduced with a convolution of the single tip estimate and the filter function.

Sparker Directivity Modelling

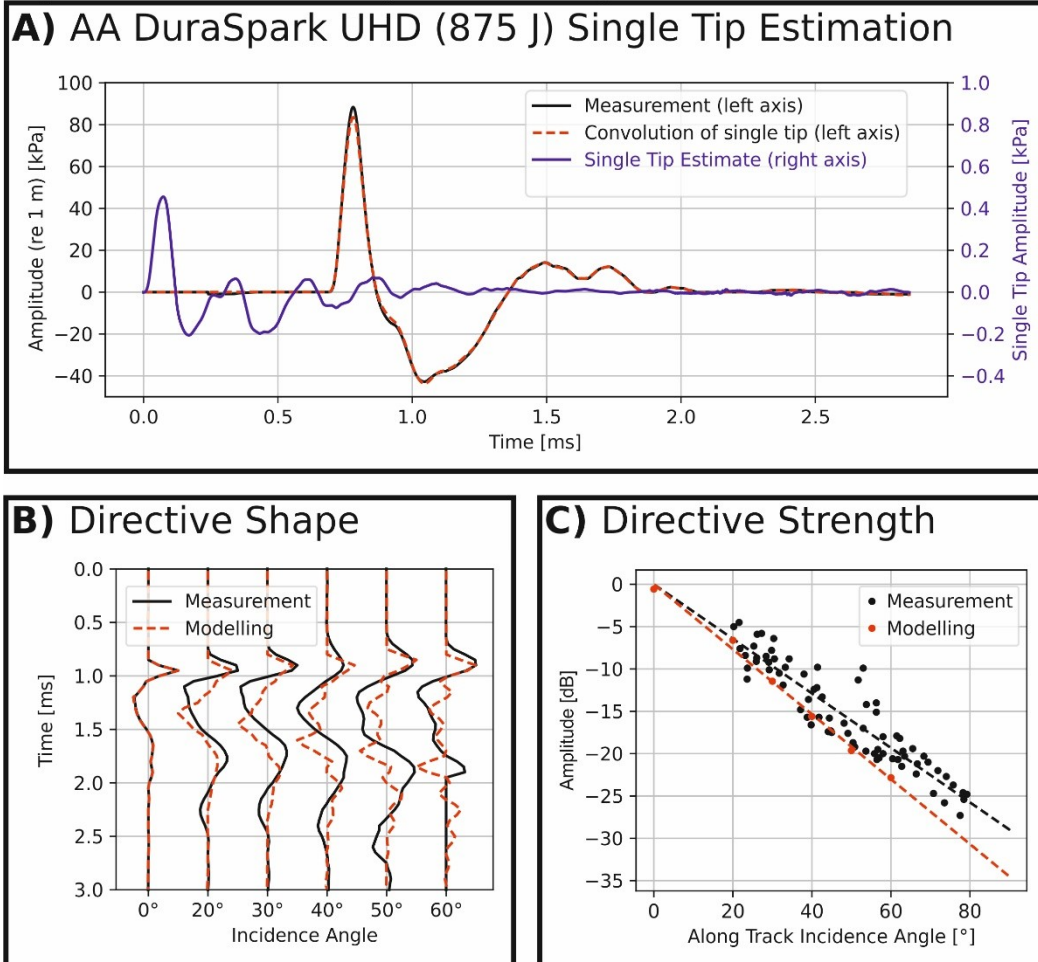


Figure A-16: Convolutional modelling of the directivity of the Applied Acoustics (AA) Dura-Spark UHD 400 sparker (AADS400 sparker). A) Comparison of the wavelet measurements of an AADS400 sparker shot with 875 J recorded 1 m vertically below the tips with the estimated single tip wavelet by deconvolution and the reproduction of the measurement by a convolution of the single tip signal. The single tip estimate and the measured or likewise modelled sparker wavelet share the x-axis, the right axis of the single tip signal has been scaled by a factor of 100 to allow for a better comparison of the signals. B) Comparison of the measured angle gather also shown in Figure 3-4 D and the convolutionally modelled angle gather. C) Scatter plot of the normalized amplitude shown in Figure 3-4 F with an overlay of the modelled directive strength. The dashed line represents the best fit linear function which can be used to determine the source characteristics. Accordingly, the half-beamwidth at a -3 dB level is 9° for the measurements and 8° for the model.

In the simplified AADS400 sparker directivity modelling (see Figure A-16) the source signal is approximated as the convolution of a filter function with a single tip estimate. As not all parameters for the filter function are intrinsically known, some optimization was necessary. An optimum fit of the measurement and the reproduction of the signal via deconvolution and convolution was found for the sea surface reflectivity $r_{ss} = -0.99$, the absorption factor inside the frame of the AADS400 sparker $f_{ul} = 0.59$, the water velocity $v_w = 1470$ m/s and a Signal-to-Noise-Ratio $SNR = 25$ for the Wiener Deconvolution. In Figure A-16A, it is shown that the reproduction with those parameters resembles the measurement of the AADS400 sparker wavelet recorded 1 m vertically

below the source. The single tip estimate is much weaker than measurements, characterized by a slightly higher frequency content and shows some form of damped oscillation. The validity of the simplification is tested with the modelling of the measured directivity (Figure 3-4). As shown in Figure A-16B, there is a good agreement of the modelled traces and the measurements in terms of the peak to trough ratio and for incidence angles up to 40° - 50° in terms of the overall signal shape. Also, the modelled and measured directivity correspond well (Figure A-16C). Performing a line fit of the amplitude to the incidence angle in Figure A-16C, beamwidths can be estimated from the -3 dB intersection of this line. While a half-beamwidth of 9° has been measured, the modelling results in 8° beamwidth.

C.5 Pre-Stack Inversion Parameters

Table A-13: Parameters for the Common Reflection Surface travel time curve inversion with a differential evolution genetic algorithm.

a	$[-3 \cdot 10^{-4}, 3 \cdot 10^4]$
b	$[-5.3 \cdot 10^{-7}, 8.8 \cdot 10^6]$
c	$[2 \cdot 10^{-6}, 1 \cdot 10^{-6}]$
ΔTWT	10 ms
Water Velocity v_0	1485 m/s
Number of individuals per population	50
Number of generations	150
Mutation Rate	0.5
Crossover Rate	0.4

Table A-14: Parameters for the interval velocity determination with a differential evolution genetic algorithm.

Number of individuals per population	30
Number of generations	150
Mutation Rate	0.5
Crossover Rate	0.9
Velocity Search Range	$[1400, 2100] \text{ m/s}$
Maximum Depth	120 m

Table A-15: Parametrisation of the genetic algorithm for impedance inversion and the BLIMP algorithm for the low frequency model merging.

Parameter	Value
Number of repetitions	100
Number of individuals in each generation	2000
Number of generations	750
Crossover Probability	0.6
Mutation Probability	0.001
Probability to be a reflector for initialisation	0.1
Reflectivity Range for initialisation	-58% to 58 %
Number of models for final result	100
Low-pass frequency for the scaling (BLIMP)	300
High-pass frequency for the scaling (BLIMP)	100
Characteristic frequency of the Linkwitz-Riley crossover filter	10

Table A-16: Parameters for the empiric velocity-density relation by Raymer et al. (1980). The parameters were manually optimized to fit to the properties of near surface sediments taken from McCann & McCann (1969), Shumway (1960), Hamilton (1970, 1972), Breitzke (2000), Stevenson et al. (2002), Robb et al. (2006) and the BSH Pinta Data Base (2021) for the wind farms N0307, N0308 and O0103.

Porosity Limit Continuous Rock Matrix: ϕ_R	37%
Porosity Limit Suspension: ϕ_S	53%
P-Velocity Matrix: $v_{p,M}$	3100 m/s
P-Velocity Fluid: $v_{p,F}$	1550 m/s
Density Matrix: ρ_M	2750 kg/m ³
Density Fluid: ρ_F	1000 kg/m ³

Table A-17: Parameters for the S-Wave velocity estimation according to Lee (2006)

Shear Modulus of Quartz	44.0 GPa
Bulk Modulus of Quartz	38.0 GPa
Bulk Modulus of Sea-Water	2.37 GPa
Density of Quartz	2650 kg/m ³
Density of Sea-Water	1024 kg/m ³
Initial Porosity	0.4

C.6 Attenuation Estimation Probability Density Function CMP 492 (He569-GeoB21-033)

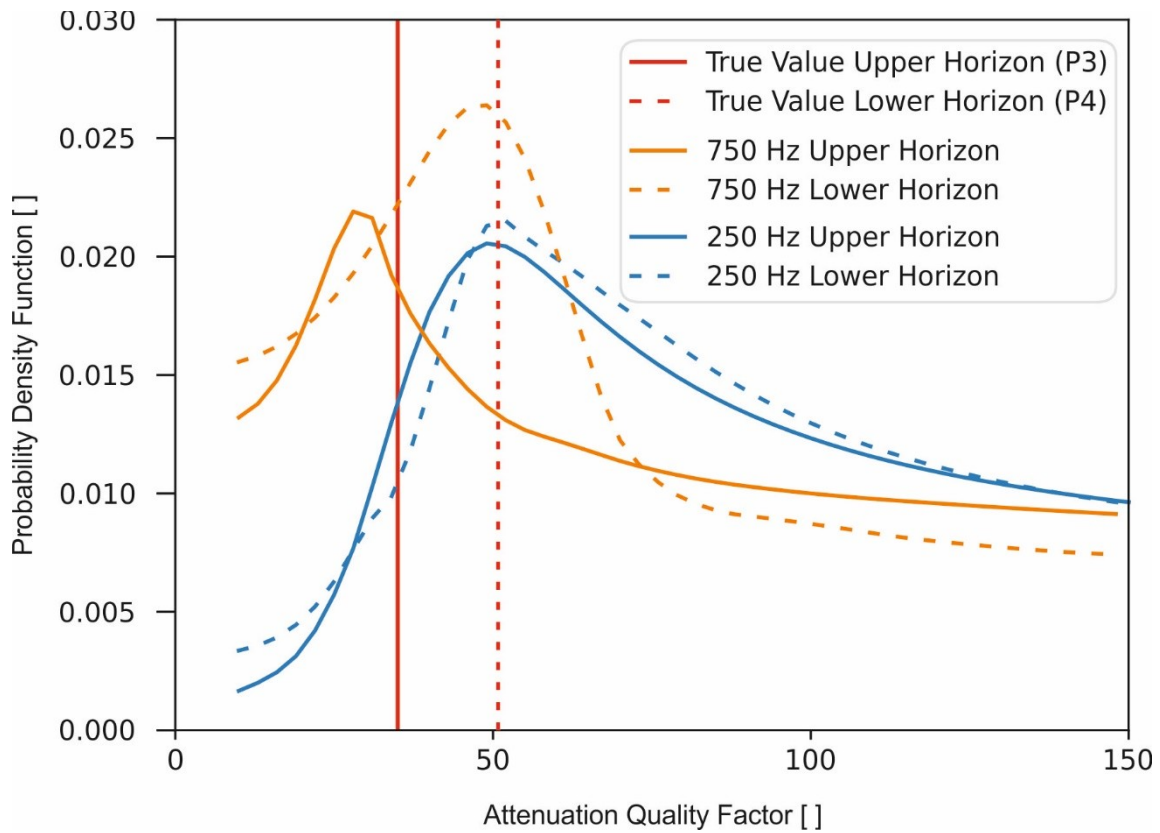


Figure A-17: Sensitivity test of the attenuation estimation with modelled data (see “2.1.4 Synthetic Seismograms”). Synthetic seismic data has been modelled with a 250 Hz and a 750 Hz Ricker wavelet. The attenuation quality factor Q has then been estimated on horizons being equivalent to P3 and P4. The sensitivity test shows that the Q -value at the lower horizon can be well identified and that the probability density function gets narrower and hence the uncertainty is smaller the higher the frequency content of the source.

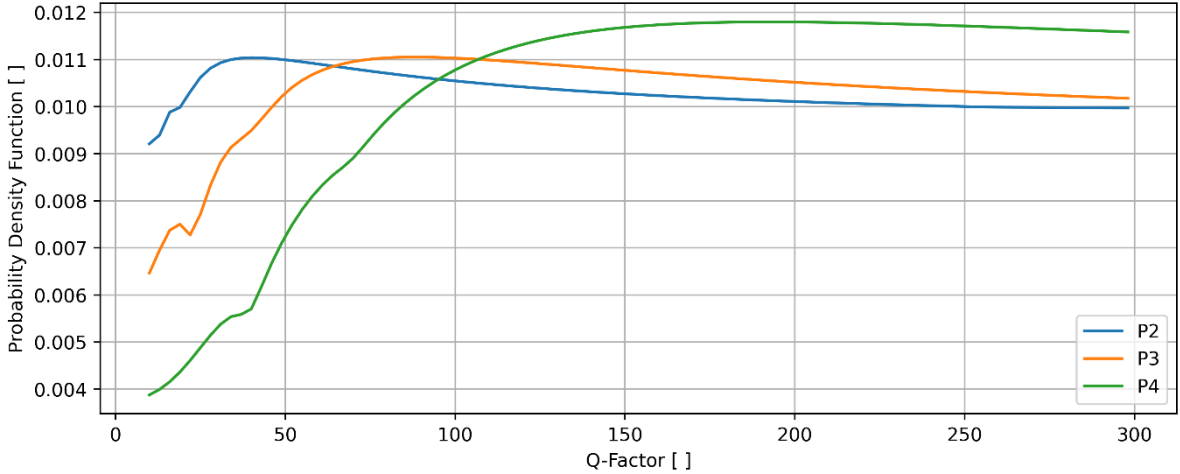


Figure A-18: Probability Density Functions of the Q-Factor estimation for CMP 492 on seismic line He569-GeoB21-033. Due to the relatively low source frequency and shallow penetration, the attenuation has not a strong effect and especially on the deepest Horizon P4 no clear maximum representing the best-guess Q-value can be identified.

C.7 Synthetic Pre-Stack Inversion Test after 60 Iterations

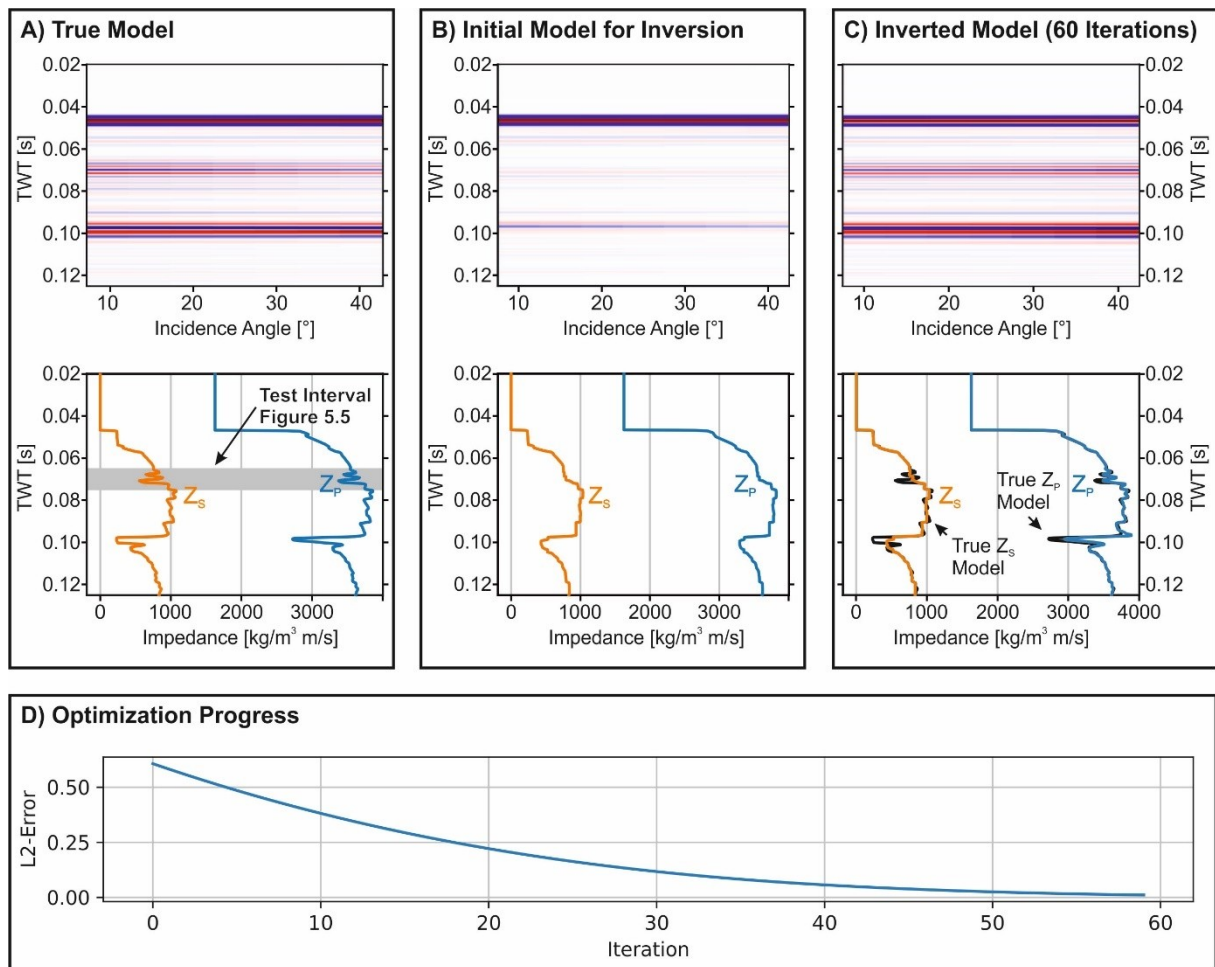


Figure A-19: Pre-stack inversion on synthetic data. The upper panels of (A)-(D) show angle stacks in the range 10° - 40° in 5° steps which are scaled to the same amplitude, while the lower panels of (A)-(D) show the corresponding compressional impedance Z_P as well as the shear impedance Z_S models. A) True model of the synthetic test. The time interval which is used for the sensitivity analysis shown in Figure 5-5 is indicated by a grey bar. B) Initial Model for the inversion, which is the true model in (A) filtered with a 6.25 ms long running median filter. C) Inverted model after 60 iterations. The true impedances are underlying the inverted impedances and are displayed as black lines. D) Optimization progress showing the decreasing L_2 -norm with increasing number of iterations.



CERTIFICATE

Nikolas Römer-Stange

has successfully attended the MARUM / GLOMAR course

Good Scientific Practice

given by

Prof. Dr. Dierk Hebbeln^{1,2}, Jan-Hendrik Hehemann^{2,3} and Dr. Christina Klose²

*1 Faculty of Geosciences, 2 MARUM – Center for Marine Environmental Sciences, University of Bremen,
3 Max Planck Institute for Marine Microbiology, Bremen*

23 June 2021

Good scientific practice, also referred to as research integrity, is essential in all scientific work. It ensures respectful cooperation among scientists and credibility towards the public. The principles of good scientific practice can be violated in many ways. From deliberate falsification or deceit to a lack of care in the application of scientific methods or data handling and documentation.

This course gave an overview over the background of the topic by giving examples of scientific misconduct and explaining the rules of good scientific practice. It provided examples of undeliberate misconduct and of 'grey zones' and how to handle them. Participants had the opportunity to ask questions and discuss their doubts with the lecturers and fellow scientists.

The course included the following topics:

- History of dealing with the topic 'good scientific practice'
- The DFG 'Guidelines for Safeguarding Good Scientific Practice / Code of Conduct'
- Ombudspersons
- Good scientific conduct** and risks of violation, examples of undeliberate falsification of data
- Authorship
- Images and intellectual property rights

Bremen, 23 June 2021

Dr. Christina Klose
Early Career Researcher Support

E Publication List

E.1 Peer Reviewed Publications

Römer-Stange, N., Wenau, S., Bihler, V., Keil, H., Córdova, C. A. R., & Spieß, V. (2022). Boulder Detection in the Shallow Sub-Seafloor by Diffraction Imaging With Beamforming on Ultra-High Resolution Seismic Data—A Feasibility Study. *Earth and Space Science*, 9(6). <https://doi.org/10.1029/2021ea002156>

E.2 Patents

Ramos Córdova, C. A., Preu, B., **Stange, N.**, Keil, H., Spieß, V., & Wenau, S. (2020). Method, device and computer program for detecting one or more objects in the seabed. World Intellectual Property Organization. Retrieved from <https://lens.org/056-259-694-420-530>

Ramos Córdova, C. A., Preu, B., **Stange, N.**, Spieß, V., Wenau, S., & Keil, H. (2021). System, methods and processing module for detecting one or more objects in the seabed. World Intellectual Property Organization. Retrieved from <https://lens.org/018-090-762-834-374>

E.3 Conference Contributions

Wenau, S., **Stange, N.**, Keil, H., Ramos, C., & Spieß, V. (2018). A Seismic Beamforming Approach for the Detection Of Boulders in the Shallow Sub-Seafloor. In 3rd Applied Shallow Marine Geophysics Conference. European Association of Geoscientists & Engineers. <https://doi.org/10.3997/2214-4609.201802672>

Wenau, S., **Römer-Stange, N.**, Keil, H., Spieß, V., & Preu, B. (2020). Sub-Seafloor Object Detection through Dedicated Diffraction Imaging. In NSG2020 4th Applied Shallow Marine Geophysics Conference. European Association of Geoscientists & Engineers. <https://doi.org/10.3997/2214-4609.202020157>

Wenau, S., Bihler, V., Preu, B., **Römer-Stange, N.**, Keil, H., & Spieß, V. (2021). Dedicated diffraction imaging for sub-seafloor object detection. In 2nd Geoscience & Engineering in Energy Transition Conference. European Association of Geoscientists & Engineers. <https://doi.org/10.3997/2214-4609.202121076>

Römer-Stange, N., & Spieß, V. (2022). Requirements and Boundary Conditions for Near Surface Seismic Inversion. In Second EAGE Conference on Seismic Inversion. European Association of Geoscientists & Engineers. <https://doi.org/10.3997/2214-4609.202229012>

Römer-Stange, N., Oguro, A. W., Córdova, C. R., & Spieß, V. (2022). Improving Subsurface Investigations with Acoustic Impedance Inversion: Concept and Example from the German North Sea. In EAGE GET 2022. European Association of Geoscientists & Engineers. <https://doi.org/10.3997/2214-4609.202221057>

Römer-Stange, N., Keil, H., Ogunleye, O., Merl, M., Oguro, A., Ramos Córdova, C., et al. (2023). From Interface to Layer Characterization in the Near Surface by Stochastic Seismic Inversion. Presented as a Poster at the DGG 2023, Bremen, Germany. <https://events.dgg2023.smart-abstract.com/#/event/44645>

Merl, M., **Römer-Stange, N.,** Keil, H., Spieß, V. (2023). Ocean Bottom Nodes in small scale, Ultra High Resolution seismic surveys: QC and first results. Presented as a Talk at the DGG 2023, Bremen, Germany. <https://dgg2023.dgg-tagung.de/deutsch/wissenschaftliches-programm/>

Mhmod, M., Merl, M., Keil, H., **Römer-Stange, N.,** Bihler, V., Spieß, V. (2023). Generating High Resolution Seismic Models to support the development of seismo-acoustic imaging methods for submarine Cable Detection. Presented as a Poster at the DGG 2023, Bremen, Germany. <https://dgg2023.dgg-tagung.de/deutsch/wissenschaftliches-programm/>

Keil, H., Ruhnau, M. Fekete, N., **Römer-Stange, N.,** Merl, M., Spieß, V. (2023). Shallow gas in the Elbe Palaeovalley (German North Sea) imaged by high resolution multichannel seismics – distribution, classification and linkage to the subsurface. Presented as a Poster at the DGG 2023, Bremen, Germany. <https://dgg2023.dgg-tagung.de/deutsch/wissenschaftliches-programm/>

Albers, A. E., **Römer-Stange, N.,** Spieß, V. (2023). High Resolution Seismic Exploration of the Structure and Morphology of a basaltic Carbon Storage Reservoir on the Eastern Juan de Fuca Ridge Flank. Presented as a Poster at the DGG 2023, Bremen, Germany. <https://dgg2023.dgg-tagung.de/deutsch/wissenschaftliches-programm/>

Bihler, V., Wenau, S., Cammarata, D., Schwarz, B., Frielinghaus, G., Ramos Cordova, C. A., **Römer-Stange, N.,** Keil, H., Spieß, V., Preu, B. (2023) Diffraction Imaging for Subsea floor Object Detection: A case study from the German Baltic Sea. Presented as a Talk at the DGG 2023, Bremen, Germany. <https://dgg2023.dgg-tagung.de/deutsch/wissenschaftliches-programm/>

Römer-Stange, N., Spieß, V., Ogunleye, O. Keil, H., Merl, M., Ettrich, N., Morales Hernandez, P. N., Bihler, V., Ramos Córdova, C. A., Oguro, A., Siemann, L., Wilhelm, S., Arnold, P. (2023). Advanced Subsurface Characterization and De-Risking of Offshore Infrastructure Installations or Drillings with High Resolution Marine Seismic Methods. To be Presented as a Poster at the AGU 2023, San Francisco, USA.

Ogunleye, O., **Römer-Stange, N.**, Spieß, V., Keil, H., Morales Hernandez, P. N., Dujardin, J.-R., Pein, T., Sauvin, G., Vanneste, M. (2023). Statistical Boundary Conditions of Subsoil Physical Properties in the Arkona Basin – Delineating Interface-Related and Layer-Based Seismic Attributes for Predicting Near-Surface Geotechnical Parameters. To be Presented as a Poster at the AGU 2023, San Francisco, USA.

Albers, A. E., **Römer-Stange, N.**, Spieß, V. (2023). High-Resolution Seismic Exploration of the Structure and Morphology of the Basaltic Carbon Storage Reservoir on the Eastern Juan de Fuca Ridge Flank. To be Presented as a Poster at the AGU 2023, San Francisco, USA.

Versicherung an Eides Statt / Affirmation in Lieu of an Oath

gem. § 5 Abs. 5 der Promotionsordnung vom 28.04.2021 / *according to § 5 (5) of the Doctoral Degree Rules and Regulations of 28 April 2021*

Ich / I,

Nikolas Römer-Stange

Klagenfurter Straße 2-4, 28359 Bremen

Matr.-Nr.: 2634645

versichere an Eides Statt durch meine Unterschrift, dass ich die vorliegende Dissertation selbständig und ohne fremde Hilfe angefertigt und alle Stellen, die ich wörtlich dem Sinne nach aus Veröffentlichungen entnommen habe, als solche kenntlich gemacht habe, mich auch keiner anderen als der angegebenen Literatur oder sonstiger Hilfsmittel bedient habe und die zu Prüfungszwecken beigelegte elektronische Version (PDF) der Dissertation mit der abgegebenen gedruckten Version identisch ist. / *With my signature I affirm in lieu of an oath that I prepared the submitted dissertation independently and without illicit assistance from third parties, that I appropriately referenced any text or content from other sources, that I used only literature and resources listed in the dissertation, and that the electronic (PDF) and printed versions of the dissertation are identical.*

Ich versichere an Eides Statt, dass ich die vorgenannten Angaben nach bestem Wissen und Gewissen gemacht habe und dass die Angaben der Wahrheit entsprechen und ich nichts verschwiegen habe. / *I affirm in lieu of an oath that the information provided herein to the best of my knowledge is true and complete.*

Die Strafbarkeit einer falschen eidesstattlichen Versicherung ist mir bekannt, namentlich die Strafandrohung gemäß § 156 StGB bis zu drei Jahren Freiheitsstrafe oder Geldstrafe bei vorsätzlicher Begehung der Tat bzw. gemäß § 161 Abs. 1 StGB bis zu einem Jahr Freiheitsstrafe oder Geldstrafe bei fahrlässiger Begehung. / *I am aware that a false affidavit is a criminal offence which is punishable by law in accordance with § 156 of the German Criminal Code (StGB) with up to three years imprisonment or a fine in case of intention, or in accordance with § 161 (1) of the German Criminal Code with up to one year imprisonment or a fine in case of negligence.*

Ort / Place, Datum / Date

Unterschrift / Signature